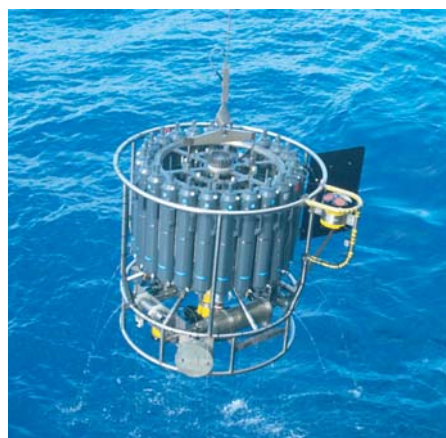




Regional surface albedo characteristics - analysis
of albedo data and application to land-cover
changes for a regional climate model

Swantje Preuschmann



Hinweis

Die Berichte zur Erdsystemforschung werden vom Max-Planck-Institut für Meteorologie in Hamburg in unregelmäßiger Abfolge herausgegeben.

Sie enthalten wissenschaftliche und technische Beiträge, inklusive Dissertationen.

Die Beiträge geben nicht notwendigerweise die Auffassung des Instituts wieder.

Die "Berichte zur Erdsystemforschung" führen die vorherigen Reihen "Reports" und "Examensarbeiten" weiter.



Notice

The Reports on Earth System Science are published by the Max Planck Institute for Meteorology in Hamburg. They appear in irregular intervals.

They contain scientific and technical contributions, including Ph. D. theses.

The Reports do not necessarily reflect the opinion of the Institute.

The "Reports on Earth System Science" continue the former "Reports" and "Examensarbeiten" of the Max Planck Institute.

Anschrift / Address

Max-Planck-Institut für Meteorologie
Bundesstrasse 53
20146 Hamburg
Deutschland

Tel.: +49-(0)40-4 11 73-0
Fax: +49-(0)40-4 11 73-298
Web: www.mpimet.mpg.de

Layout:

Bettina Diallo, PR & Grafik

Titelfotos:

vorne:

Christian Klepp - Jochem Marotzke - Christian Klepp

hinten:

Clotilde Dubois - Christian Klepp - Katsumasa Tanaka

Regional surface albedo characteristics - analysis
of albedo data and application to land-cover
changes for a regional climate model

Swantje Preuschmann

aus Berlin, Deutschland

Hamburg 2012

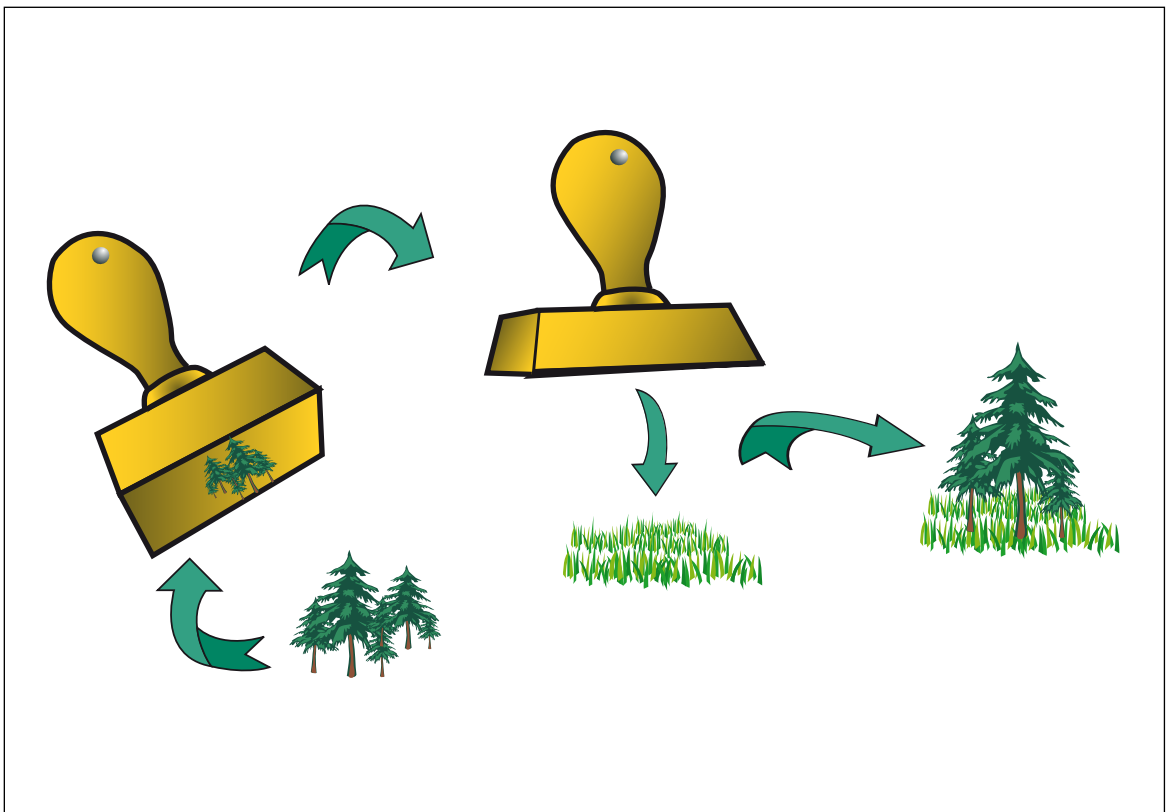
Swantje Preuschmann
Max-Planck-Institut für Meteorologie
Bundesstrasse 53
20146 Hamburg

Als Dissertation angenommen
vom Department Geowissenschaften der Universität Hamburg

auf Grund der Gutachten von
Prof. Dr. Daniela Jacob
und
Prof. Dr. Martin Claußen

Hamburg, den 14. Juni 2012
Prof. Dr. Jürgen Oßenbrügge
Leiter des Departments für Geowissenschaften

Regional surface albedo characteristics - analysis of albedo data and application to land-cover changes for a regional climate model



Swantje Preuschmann

Hamburg 2012

Man kann ein Problem nicht mit den gleichen Denkstrukturen lösen, die zu seiner Entstehung beigetragen haben.

Albert Einstein

Summary

The albedo is one of the most important factor of the energy budget of the Earth surface. This study addresses the question of validating the land surface albedo in a climate model; here the REgional climate MOdel (REMO) is considered. Both the parameterization of albedo in REMO and the remote sensing of albedo are analysed in detail.

In this work an analysis concept for land surface albedo was developed, revealing relevant characteristics of albedo observations. It could be proven that land use types have unique seasonal albedo curves, however, still depending on the region.

Comparisons of the parameterized albedo in REMO with observations showed large differences. The reasons for those are attributable to uncertainties within the albedo parameterization method and the wrong assumption of a linear correlation between vegetation activity and spectrally integrated albedo values. Sensitivity studies showed an impact of spatial and temporal albedo variations on regional climate and support the necessity of a more realistic albedo description for regional climate model simulations.

A new method was introduced, which uses observations to derive albedo characteristics for different land use types. The scheme, called Land Use CHAracter Shifts (LUCHS) allocates land use characters on considered areas for land use change. It is based on the assumption that the courses of mean seasonal albedo cycles are transferable on neighbouring areas, by assuming a persistence in floral, pedological and cultural conditions.

Zusammenfassung

Die Albedo ist eine der wichtigsten Faktoren in der Energiebilanz der Erdoberfläche. Diese Studie setzt sich mit der Validierung der Landoberflächen Albedo in Klimamodellen auseinander; dazu wird hier das atmosphärische REgionale Klima-MOdel (REMO) betrachtet. Beides, die Parameterisierung der Albedo in REMO und die Fernerkundung von Albeden wird im Detail analysiert.

In dieser Arbeit wurde ein Analysekonzept für die Albedo on Landoberflächen entwickelt, welches relevante Charakteristiken der Albedo aufzeigt. Es konnte gezeigt werden, dass Landnutzungstypen einzigartige saisonale Albedo-Kurven aufweisen, indes aber regional abhängig sind.

Vergleiche der parameterisierten Albedo in REMO mit Beobachtungen zeigte große Abweichungen. Gründe dafür konnten Unsicherheiten in der Parameterisierungsmethode und der falschen Annahme einer linearen Korrelation zwischen Vegetationsaktivität und spektral integrierter Albedowerte zugeordnet werden. Sensitivitätsstudien zeigten einen Einfluss von räumlich und zeitlich variierender Albedo auf regionale Klimate und unterstützen damit die Notwendigkeit einer realistischeren Albedo-Beschreibung in regionalen Klimamodellen.

Eine neue Methode wurde vorgestellt, die Beobachtungen nutzt, um daraus Albedo-Charakteristiken verschiedener Landnutzungsklassen abzuleiten. Das Schema namens Land Use CHaracter Shifts (LUCHS) [Landnutzungs-Charakter-Verschiebungen] ordnet Gebieten die einer Landnutzungsänderung unterzogen werden soll, die zu erreichenden Landnutzungs-Charaktere zu. Es basiert auf der Annahme, dass die Verläufe mittlerer saisonaler Albedo-Zyklen auf benachbarte Gebiete übertragbar sind, wenn Persistenzen in den floralen-, bodenkundlichen- und kulturellen Gegebenheiten angenommen werden.

Contents

Summary	i
Zusammenfassung	iii
1. Introduction	1
1.1. Background	1
1.2. Objectives	10
1.3. Structure of the thesis	10
2. Description of the land surface in climate models	13
2.1. Principles of climate modelling including vegetation	13
2.2. Vegetation parameters and its usage in REMO	15
2.3. The lower boundary for the regional model REMO	19
3. Remote Sensing: Albedo data and vegetation indices	27
3.1. Albedo from satellite data	27
3.2. Vegetation indices from satellite data	33
3.3. Used remote sensing data sets	37
3.3.1. Albedomap	37
3.3.2. MODIS data	40
3.3.3. Global Land Cover 2000	42
4. Analysis concepts	45
4.1. The concept of albedo characteristics	45
4.2. The concept of radiative perturbation	48
5. Albedo characteristics	51
5.1. Regional albedo characteristics for different land use types	51
5.2. Albedo characteristics for different fractional contributions to a grid box	55
5.3. Verification by inversion	63
6. Albedo characteristics within the Surface Library for REMO (SL4R)	69
6.1. Comparison of SL4R albedo to observation	70
6.2. Limitations for the use of SL4R albedo for land use change studies	75
6.3. Sensitivity studies with REMO for several albedo characteristics	86
6.3.1. REMO with albedo from SL4R (α_{SL4R}) and white sky broad band albedo of AMAP (α_{amap}) first version (α_{amap_1})	86

6.3.2. REMO with changed LAI and thereby changed albedo	97
6.4. Conclusions for Land Use Change Implementations	109
7. Implementing Land Use Changes with LUCHS	111
7.1. Application of the land use character shifting method	112
7.2. Results of LUCHS	116
8. Conclusions and Outlook	129
8.1. Conclusions	129
8.2. Outlook	130
A. Historical development of MPI-M land surface.	133
B. Explanations to the usage of Beer-Lambert Law and Vegetation Albedo	137
C. Regression of Albedo and Vegetation Index	139
References	147
Acknowledgements	156
Index	158

Symbols and Acronyms

α_{amap}	white sky broad band albedo of AMAP
α_{modis}	MODIS albedo, following Rechid et al. (2008)
α_{SL4R}	albedo from SL4R
APAR	Absorbed Photosynthetically Active Radiation
α_{amap_1}	α_{amap} first version
α_{veg}	surface albedo with active vegetation
α_{soil}	surface albedo with non-active vegetation
albedo-weights	albedo compounds surface albedo with active vegetation (α_{veg}) and surface albedo with non-active vegetation (α_{soil}) as weighting factors in the albedo parameterization in the SL4R
LAI_d	Leaf Area Index for dormancy season $\Leftrightarrow LAI_{min}$
LAI_g	Leaf Area Index for growing season $\Leftrightarrow LAI_{max}$
c_v	Vegetation Ratio
c_{vd}	Vegetation Ratio for dormancy season
c_{vg}	Vegetation Ratio for growing season
c_f	Forest Fraction
CO_2	carbon dioxide
f_{apar}	Fraction of Absorbed Photosynthetic Active Radiation
f_i	Growing Factor
z_0	Roughness Length
z_{0veg}	Roughness Length of vegetation
PAR	Photosynthetically Active Radiation
VI_{amap}	White Sky MERIS Vegetation Index of AMAP
w_{ava}	Water holding capacity of soil
Albedomap	albedo data product of MERIS
AMAP	adapted Albedomap data product of MERIS
AVHRR	Advanced Very High Resolution Radiometer
Aqua	Multi-national NASA scientific research satellite
BRDF	Bidirectional Reflectance Distribution Function

ECHAM	GCM, namely the ECMWF model in the MPI-M Hamburg version.
ENVISAT	Environmental Satellite
EOS	Earth Observing System
EROS	National Center for Earth Resources Observation and Science
ESA	European Space Agency
GCM	General Circulation Model
GET	Global Ecosystem Types
GLC2000	Global Land Cover 2000
JRC	Joint Research Centre of the European Commission
JSBACH	Jena Scheme for Biosphere-Atmosphere Coupling in Hamburg
LAI	Leaf Area Index
LSPII	Land Surface Parameter data set second version
LUCHS	Land Use CHaracter Shifts
MERIS	Medium Resolution Imaging Spectrometer
MODIS	Moderate Resolution Imaging Spectroradiometer
NASA	National Aeronautics and Space Administration
NDVI	Normalized Difference Vegetation Index
LUH-P	Land Use Harmonization Protocol
NIR	Near Infrared
NOAA	National Oceanic and Atmospheric Administration
REMO	Regional Model
SL4R	Surface Library for REMO
Terra	Multi-national NASA scientific research satellite - flagship of EOS
TOA	Top Of Atmosphere
USGS	U.S. Geological Survey
VIS	Visible

1. Introduction

1.1. Background

Mankind influences the Earth's climate system. The extent of the human impact on climate is still under debate - for the past and for the future.

The human influence on vegetation cover is a recent scientific aim (RCP-Database, 2009) in the climate modelling community. Vegetation is a major factor for land-atmosphere interaction, the anthropogenic shaping of the land surface is influencing the Earth's climate. In the last years the investigations of biogeochemical and biogeophysical aspects of vegetation are increasing. The importance of vegetation parameters and their influence on climate are part of many studies (e.g.: Sellers, 1987; Betts et al., 1996; Eltahir, 1996; Crowley and Baum, 1997; Kleidon et al., 2000; Knorr et al., 2001; Claussen et al., 2001; Pitman, 2003; Lawrence and Slingo, 2004; Oleson et al., 2004; Brovkin et al., 2006; Rechid and Jacob, 2006; Betts et al., 2007; Miguez et al., 2007; Pielke et al., 2007; Reick et al., 2010).

A biogeochemical impact of vegetation is related to the carbon cycle. Plants can act as a carbon pool by storing carbon dioxide (CO_2), which influences the CO_2 concentration in the atmosphere and thereby the greenhouse effect of the atmosphere. Many efforts were undertaken to estimate the influence of vegetation on the carbon cycle (e.g., Dixon et al., 1994; Brovkin et al., 2002; Pongratz et al., 2009b).

A biogeophysical aspect is the influence of vegetation on the Earth's heat budget. The heat budget is "the concept of equilibrium [at the surface] which refers to the incoming solar radiation received by the atmosphere and the Earth in relation to the outgoing re-radiated or reflected heat" (Whittow, 2000).

$$R_n + S + L + G + F = 0 \quad (1.1)$$

The net radiation (R_n), sensible heat flux (S), latent heat flux (L), the ground heat flux (G) and chemical energy (F) must be balanced (Pitman, 2003). The heat transfer processes into the atmosphere are described by sensible and latent heat fluxes. The ground heat flux is indicating a heat transport into the Earth or ocean. The chemical energy F represents the part of energy stored during photosynthesis, which is released by respiration. This term is often omitted in climate models, as the amount is very low (Pitman, 2003).

Vegetation's evapotranspiration processes have an impact on sensible and latent heat fluxes. The net radiation is directly linked to the reflectivity of the surface. As vegetation often covers the surface, it is impacting the net radiation. Different vegetation covers or other surfaces have different reflectivities and are influencing the heat balance of the Earth's surface, as sketched in figure 1.1.

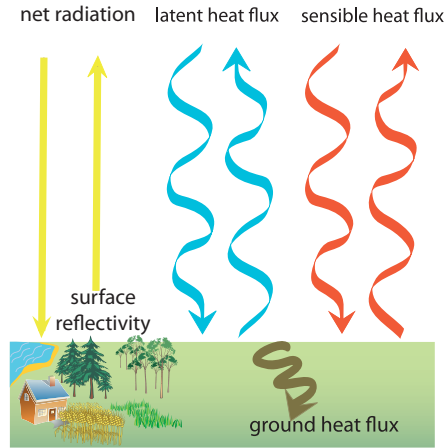


Figure 1.1.: Simplified surface heat balance model, omitting F in equation 1.1.

The radiation can be separated into a shortwave¹ part and a longwave² part. Altogether, the total net radiation balance (R_n) at the surface, can be formulated by equation 1.2. The outgoing longwave radiation, also cited as thermal or terrestrial radiation, can be estimated after Stefan-Boltzmann as $\epsilon\sigma T_S^4$, where T_S is the surface temperature, and ϵ is representing the emissivity of the surface and σ the Stefan-Boltzmann constant.

$$R_n = \underbrace{S - \alpha S}_{\text{shortwave radiation balance}} + \underbrace{L - \epsilon\sigma T_S^4}_{\text{longwave radiation balance}} \quad (1.2)$$

with

- R_n : net surface radiation [W/m^2]
- S : incoming shortwave radiation at surface [W/m^2]
- α : surface albedo [dimensionless]
- L : incoming longwave radiation at surface [W/m^2]
- $\epsilon\sigma T_S^4$: thermal outgoing radiation of the surface [W/m^2]

The albedo (α) is defined as the ratio between backscattered solar radiation flux density and the incoming solar radiation flux density (often called global radiation); detail of the albedo definition are given in chapter 3. Altogether it is a measure for the reflectivity of shortwave radiation by a surface (Whittow, 2000). For example, a surface of snow reflects much more of the incoming shortwave radiation as grassland, which reflects more than a forested surface.

The net shortwave radiation balance is calculated as the portion of incoming shortwave radiation minus the reflected part ($S - \alpha S$). Therefore, the surface albedo is the driving factor within the shortwave radiation balance. The vegetation's influence on net radiation originates from the canopy's reflectivity in the shortwave radiation.

¹Ultraviolet, visible and near infrared of the solar spectrum, wavelength up to $\approx 3.5 \mu m$

²Infrared (thermal) part of the solar spectrum, wavelength $> 3.5 \mu m$

Due to changes in the radiation balance several climatic parameters are affected. The temperature is directly influenced by radiation, and temperature drives convective processes and also cloud development.

Estimating the surface temperature by using the simplest Earth energy budget model without atmosphere:

$$(1 - \alpha) \frac{S_c}{4} - \sigma T_E^4 = 0 \quad (1.3)$$

with a solar constant $S_c = 1366 \text{ W/m}^2$ as incoming radiation, the Stefan-Boltzmann constant $\sigma = 5.670373 \cdot 10^{-8} \text{ W/m}^2\text{K}^4$ and an albedo $\alpha = 0.3$, the Earth surface temperature (T_E) is about 255 K. This temperature would increase about 4 K if an albedo of 0.25 is used and decrease about 5 K for an albedo about 0.35. Compared to an estimated climate sensitivity of climate models by about 2 K in case of a doubling of the carbon dioxide concentration in Earth's atmosphere (IPCC, 2007b), the effect of surface albedo changes can not be neglected in climate models.

The demand for estimating regional climate change effects due to anthropogenic influences is increasing. Therefore, the importance of regional specification and realistic description of the surface albedo characteristics is increasing.

Myhre and Myhre (2003) mention the problematic of regional and seasonal differences in surface albedo values for vegetation classes. For land use change studies with regional climate models, regional accuracy is a problematic issue. The horizontal scale in global climate model simulations is often about 200 x 200 km (spectral resolution of T63). A grid box in such a resolution represents an area of the size of Switzerland. Climatic conditions, as well as the vegetation cover, depend on regional specifications which are not necessarily homogeneous within 40.000 km². In the context of regional mitigation and adaptation strategies to climate change, more detailed information e.g. for at least a Swiss Canton is needed.

Information on land use changes exists, but often only with 0.5° resolution (e.g., Ramankutty and Foley, 1999; Goldewijk, 2001; Hurtt et al., 2006).

For regional climate models, calculating on a grid with a resolution of about 10 km, the data need to be downscaled. Transferring coarse resolution information into finer resolved information leads to uncertainties. For regional aspects, these uncertainties can be of the same order as natural variations. This is, for example, the case for albedo data sets.

Land use changes are affecting the albedo and therefore the heat budget. Variation in the surface's cover result in different albedo values - no matter whether the variation is induced by seasonality or by different surface covers. For land use change studies, it is crucial to know about the horizontal distribution of different surface covers, the typical seasonal changes for these surface covers, and how the albedo would change in case of changes in the surface cover.

Establishing a reliable distribution for surface covers for regional modelling is already complex, as there are different definitions and applications. Land use and land use change and its climatic relevance, is given by the glossary of Working Group I of the IPCC (2007b): "**Land use** refers

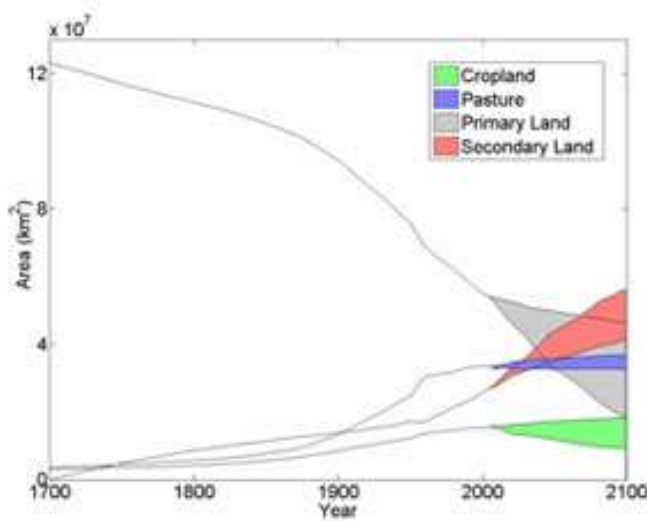


Figure 1.2: Global land area in km^2 . Recapulated for the years 1700-2000 and estimated developments for 2001-2100 showing the range of future IAM scenarios and smooth transitions in the harmonization year (2005); Global Ecosystem Laboratory, University of New Hampshire, <http://gel.sr.unh.edu/>.

to the total of arrangements, activities and inputs undertaken in a certain land cover type (a set of human actions). The term land use is also used in the sense of the social and economic purposes for which land is managed (e.g., grazing, timber extraction and conservation). **Land use change** refers to a change in the use or management of land by humans, which may lead to a change in land cover. Land cover and land use change may have an impact on the surface albedo, evapotranspiration, sources and sinks of greenhouse gases, or other properties of the climate system and may thus have a radiative forcing and/or other impacts on climate, locally or globally. [...].”

Land use is therewith a description of how humans are using a specific part of the Earth surface. In contrast to land use, **land cover** is an explicit description of the physical material which is covering the land surface. This can be coverages such as maize, wheat, grass, bare soil, water, asphalt, and so on.

For the new fifth Assessment Report (AR5) of the IPCC, the global climate modelling community agreed, to include land use changes in order to investigate mainly the influence of the atmospheric carbon concentration due to human activity through land use changes. A harmonized land use change description, the so-called Land Use Harmonization Protocol (LUH-P) of the Global Ecosystem Laboratory, University of New Hampshire (Hurtt et al., 2006) exists. For that reason, different Integrated Assessment Models (IAM) simulated a development of land usage with respect to human population for the past and future. The model output distinguishes between five categories of land usage: Cropland, Pasture, Primary Land, Secondary Land, and Urban. Changes are given as fractional area transitions from one class into another. As shown in figure 1.2 the information is given as areal amounts. The assessment models do not allocate explicit vegetation parameters etc. for a physical characterization of a class like “Secondary Land”. The LUH-P scenarios need adaptations to fit the existing land surface scheme of each model. The methods for the implementation are open.

Land use change

Besides all differences of land surface representations in numerical climate models, the land surface after a land use change should represent the new land surface and its corresponding physical properties. For example, by a replacement of agricultural land into forest, the parameters after a change must be a parameterized equivalent to a forest. The concept of land use change is shown in figure 1.3, where a hypothetical expansion of urban areas, forests and pasture (grassland) at the expense of cropland is demonstrated.



Figure 1.3.: Hypothetical appearance of land use change. In the original appearance, the orange box indicates a 100 m grid box (left). Same area with extensions of forest, grassland and urban areas (right) [Google Maps - ©2011 Google, adapted].

Compared to the original state, it is obvious that the annual cycle of the albedo in the changed areas will behave completely different compared to the original annual cycle of albedo. We assume that the forested area has an overall lower and less varying annual albedo cycle. Also for the urban and grassland areas, we expect the annual albedo cycle to behave differently in its absolute extremes and its shape over time. But we do not know the exact albedo change due to that scenario. Therefore, two aspects have to be addressed:

1. Land cover appearances for different horizontal resolutions
2. Regional aspects in land covers

Land cover appearances in different horizontal resolutions

Land cover represented in grid boxes of several square kilometres comprise several land use types. The heterogeneity of land use type composition rises, the coarser the horizontal resolution. Imagine to zoom out from the detailed view on the region, shown in figure 1.3. It is repeated in figure 1.4 top left, whereby the orange box on the left side is indicating a grid box of 100 x 100 m^2 . Here a pure allocation of land use types could be done, for example for urban (artificial), pasture,

forest, and even pure maize, wheat, hop etc.. Figure 1.4 shows views on the same area in different zooming factors. Already after a one step zoom out, a one kilometre grid cell is representing a heterogeneous mixture of cropland, pasture and forest (figure 1.4, second row, left). Further zooming out (second row, right) a five kilometre horizontal model resolution could be adjoined to pure forest, but not anymore to pure maize, grassland or built-up areas. For 5 km horizontal resolution, generalized descriptions are already needed, and still, the horizontal resolution is lower than commonly used in regional climate modelling. Often the horizontal resolutions used for REMO, are between 10 km and 50 km. In figure 1.4 third row, for 10 km resolution the local aspects are still visible, while for 50 km only general regional aspects are prominent as topographical and geological features. The agricultural area within the Rhine valley (underneath the 50 km sign) is well distinguishable compared to the hilly areas of the Blackforest and Vosges, where agriculture is not as cost-efficient. Taunus, Bavarian Forest and Harz are observable as major forested areas, following their geomorphological structure (Harz: top middle, Bavarian Forest: centre, Taunus: right above 50 km sign). For resolutions of about 200 km even those aspects are too fine to be resolvable. A grid cell of 200 km, can only represent a mixture of different land cover types. Even though homogeneous patterns of several hundreds of kilometres globally exist, they are rare for inhabited areas. Definitely, information based on such rough horizontal grid spacing is not usable for regional land use change studies.

Regional aspects in land covers

Human cultural habits, infrastructure, geomorphological aspects, floral characteristics due to pedological properties, all this can influence the appearance of a land cover. For example cropland in different areas and cultures may appear different. Figure 1.5 is showing the already used example of a German cropland area in comparison to one in central Spain and one in South Dakota of the United States of America. The pictures have the same horizontal spacing, the orange box represents a $5 \times 5 \text{ km}^2$ grid box. While the German cropland area is often riddled by forested areas, these are rare in the Spanish and the American examples. The albedo of mixed areas is lowered, compared to a non dissected cropland area.

Another issue is the importance of the pedological characteristics, which seems to be more evident in the Spanish area. In this example the "soil colour" of the south-western part of the Spanish example is brighter than the remaining area³. In this case it could be that upper darker sediments got eroded, so that lighter sediments appear. Nevertheless, a pedological dependency is obvious in this example. Comparing the Spanish and US-American examples, human impact on plant activity gets obvious. In the Spanish cropland area, only some circular irrigation fields are observable, whereby these circular patterns exist quite often in the example of the US-American cropland area.

³The pictures chosen here are coincidental examples. Google Maps is using different satellite observations. The photographical view (RGB-view) is an artificial satellite product, there is no rely on the colours. Nevertheless, the RGB-views can be used as indicators for differences.

It is a human impact, which definitely prolongs, or even allows plant photosynthetic activity and therefore, as explained in section 1.1, affects the local radiation budget. The examples in figure 1.5 show differences which are related to cultural habits, occupation and settlement of land.

The claim for higher horizontal resolution of land cover descriptions, due to the heterogeneity of land covers is certainly justified. The mentioned facets of scale and regionality are leading to a statement, crucial for this work:

- ▷ a realistic representation of land surface parameters, such as albedo, is important for reliable climate change simulations.

1. Introduction

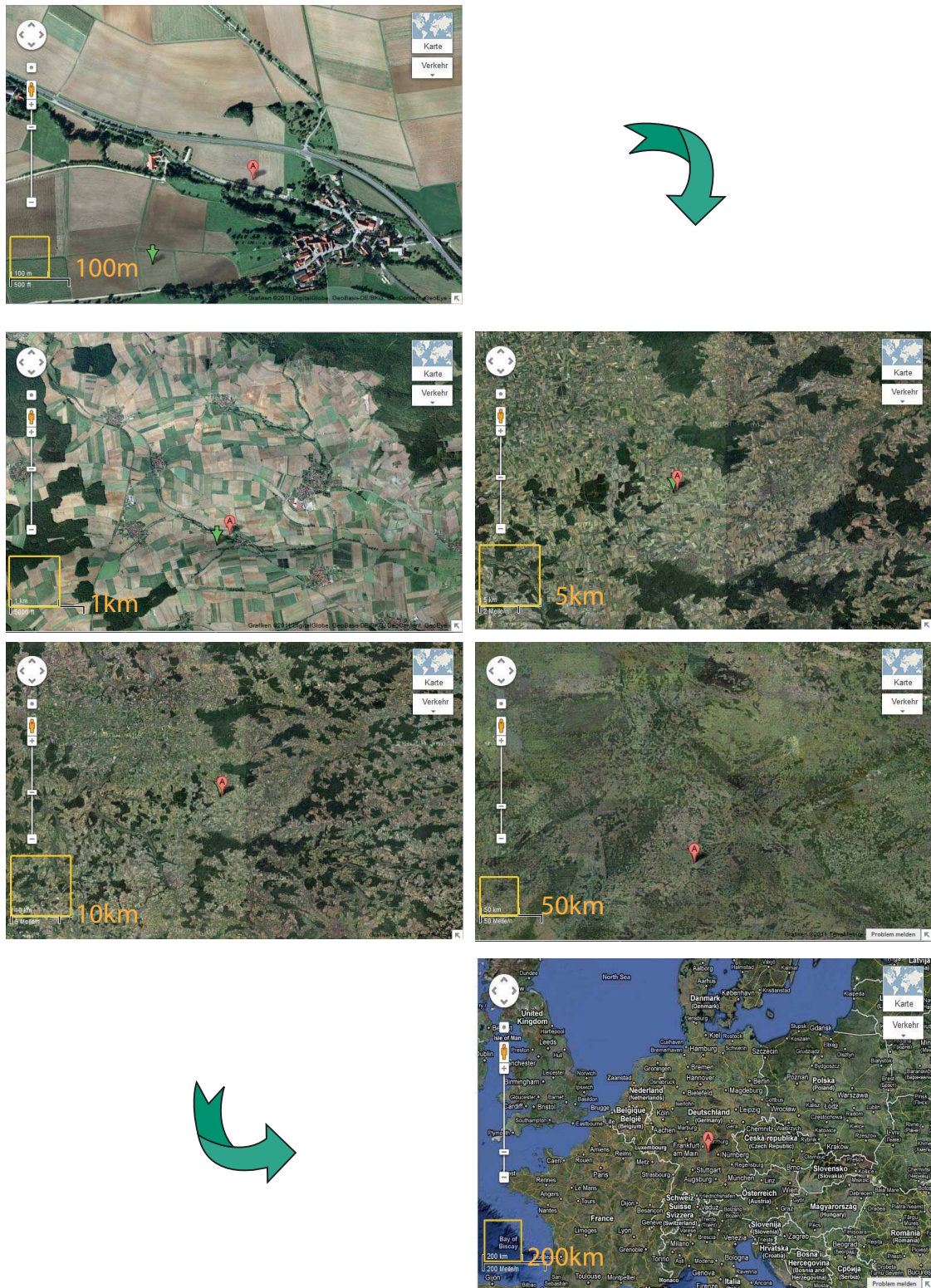


Figure 1.4.: Land cover appearance for different zoom factors fixed to the red pin A. Orange boxes indicate the size of a model grid box in the assigned horizontal approximate resolution. [Google Maps - ©2011 Google, adapted]



Figure 1.5.: Regional-specific appearances of cropland. South Germany (top), Central Spain (centre), South Dakota USA (bottom). Orange boxes indicate the size of a model grid box for 5 km horizontal resolution. [Google Maps - ©2011 Google, adapted]

1.2. Objectives

Regional climate model simulations with land use change scenarios, are trying to answer questions which are useful for regional adaptation and mitigation strategies. If REMO simulations shall be interpreted for such applications, we have to be sure that we can represent region-specific, climate-relevant aspects of vegetation.

Major questions are guiding this PhD-Thesis and will be answered:

- ▷ What are climate effective characteristics of the land surface albedo?
- ▷ Does specific land use types have characteristical mean seasonal albedo cycles?
- ▷ Can climate effective characteristics of the land surface albedo be represented with the recent land surface scheme for REMO (SL4R)?
- ▷ Does albedo changes of some percent influence regional climate?
- ▷ Does albedo changes of some percent indicate land use changes?

Finally the investigations on land use characteristics led to the development of a new easily applicable method for implementing albedo changes due to land use changes, based on satellite observation data sets.

1.3. Structure of the thesis

Terms and definitions for representing vegetation in climate models are given in Chapter 2 **Description of the land surface in climate models**. First background information about climate modelling techniques with respect to vegetation are mentioned in section 2.1 **Principles of climate modelling including vegetation**. The most important parameters for describing vegetation in climate models are introduced in section 2.2 **Vegetation parameters and its usage in REMO**. As this thesis came into existence by working with the Regional Model (REMO), section 2.3 **The lower boundary for the regional model REMO** is presenting in detail how the lower boundary information is constructed with the Surface Library for REMO (SL4R).

Chapter 3 **Remote Sensing: Albedo data and vegetation indices** is outlining the derivation of albedo and vegetation indices by remote sensing techniques. The basic remote sensing data sets used in this work are introduced in section 3.3 **Used remote sensing data sets**.

Chapter 4 **Analysis concepts** introduces basic concepts for approaching the complex themes of comparing different albedos and estimating the effects of albedo differences on the radiation budget. For the albedo comparison, section 4.1 **The concept of albedo characteristics** is giving the relevant terminologies. Section 4.2 **The concept of radiative perturbation** is introducing a method for estimating the albedo impact on the radiation budget by using regional typical incoming radiation.

In chapter 5 **Albedo characteristics** it is shown and discussed, that different land use types have

unique region-specific albedo characteristics (section 5.1 **Regional albedo characteristics for different land use types**)

Section 5.2 **Albedo characteristics for different fractional contributions to a grid box** and section **Verification by inversion**, are discussing the basic theory for validating the idea of albedo characteristics.

In chapter 6 **Albedo characteristics within the Surface Library for REMO (SL4R)**, the concept of albedo characteristics is applied to the albedo used in REMO. The albedo of the SL4R is compared to observations in section 6.1 **Comparison of SL4R albedo to observation**, whereby the reasons for discrepancies of the albedo of SL4R is explained in section 6.2 **Limitations for the use of SL4R albedo for land use change studies**. This is followed by the demonstration of two sensitivity studies, to reveal the importance of correct regional albedo descriptions in section 6.3 **Sensitivity studies with REMO for several albedo characteristics**.

Based on these results, a new scheme for implementing albedo changes due to land use changes is developed and introduced in chapter 7 **Implementing Land Use Changes with LUCHS**. LUCHS is explained by implementing a reforestation for two regions: the Iberian Peninsula and Central Europe section 7.1 **Application of the land use character shifting method**. The results concerning the albedo characteristics are shown in section 7.2 **Results of LUCHS**.

Finally in chapter 8 **Conclusion and Outlook**, the important aspects of regional albedo characteristics are summarized and future applications are outlined.

2. Description of the land surface in climate models

At the Earth's surface the solid or liquid part is directly in contact with the atmosphere. It is the interface where physical, biological and also chemical exchange processes between surface and atmosphere as well as the energy exchange take place. Several physical and dynamical processes in a model need information, directly connected to this interface. Therefore, any atmospheric climate model (like REMO) needs a parameterized representation of the Earth's surface. The set of physical parameters, which are describing the Earth's surface for atmospheric circulation models is called lower boundary.

This chapter gives a short introduction on lower boundary descriptions for such models. First, some more general definitions and principles in climate modelling are given in section 2.1. As this work focuses on the impact of land use changes by vegetation, specific terms concerning vegetation parameters are explained in section 2.2. The lower boundary for REMO is explained in more detail in section 2.3.

2.1. Principles of climate modelling including vegetation

Interaction of climate processes

Numerical solutions of the time-dependent partial differential equations for large-scale flows and parameterizations for sub-grid-scale physical processes are the basis to describe atmospheric processes in a climate model (see figure 2.2). Stensrud (2007) states that parameterization in numerical climate models are to “represent subgrid physical processes for which the model has no direct information”. Modellers are using the expression parameterizations not only for sub-scale processes but also, in case of a necessary simplification.

Multiple single processes are interlocked by using output variables of other processes as input variables. For example the movement of an airmass comprises the gaseous conditions on temperature and pressure. Therefore, the actual surface temperature is an important factor, which is among others influenced by radiation processes. As the albedo is a controlling factor for the calculation of the radiation balance at the surface, surface albedo is involved when computing ground temperature, which again influences the parameterization of sensible heat fluxes. This influences the temperature in other model levels and further other diabatic processes, which are leading to adiabatic processes e.g. through pressure changes. This loop is highlighted with yellowish arrows in figure 2.1, which represents the interaction of single diabatic processes for modelling adiabatic processes in ECHAM3.

The principles of physical process interactions for newer ECHAM versions or even other models

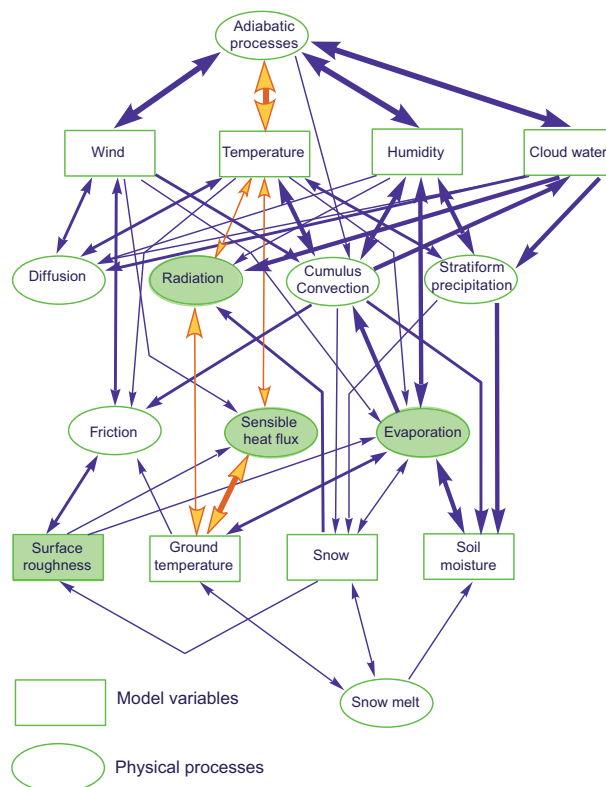


Figure 2.1.: Schematic representation of physical process interaction in the ECHAM3 model, (DKRZ, 1993) (adapted). The yellowish arrows indicate the loop where the surface albedo is directly involved.

are the same. For the numerical descriptions of processes, measurable variables are used, which are called parameters. Concerning this work, green boxes indicate processes where vegetation parameters as albedo, Leaf Area Index (LAI), Vegetation Ratio (c_v) and Roughness Length (z_0) are involved. They are defined in section 2.2. Changes in those parameters are affecting directly or indirectly model variables as wind, temperature, humidity and cloud water.

Land surface treatment in atmospheric climate models

A set of physical parameters within in the lower boundary conditions of atmospheric circulation models is used for the description of the land surface properties. Typically, but not necessarily it comprises parameters such as:

- ▷ orography
- ▷ roughness length
- ▷ albedo
- ▷ vegetation

▷ soil texture

The parameters are values which are describing the actual status of the Earth's surface as input for the atmosphere, for every time step in every grid box. They are used within the equations which are representing the climate processes. For gridded climate models, the surface information must be a gridded information, so that a parameterized surface representation can be allocated individually in every grid box. Temporally constant representations for the lower boundary are represented by a set of gridded maps. Figure 2.2 is demonstrating the pathway of different surface

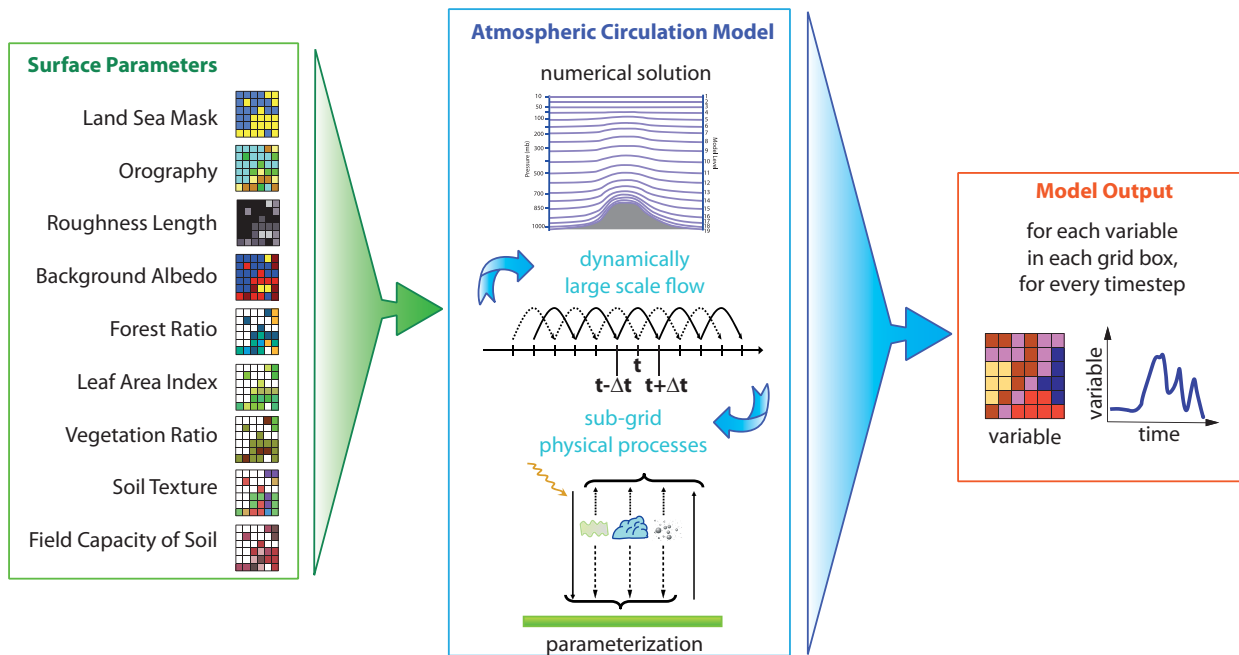


Figure 2.2.: Surface parameters as input for Atmospheric Circulation Models to receive model output data.

data as lower boundary condition for an atmospheric circulation, needed for a consistent model output. Different gridded data sets are used as input for the dynamical and physical processes in a climate model. Finally the model outputs are the results of the interacting calculations, and are representing e.g. three-dimensional fields of temperature, precipitation or wind for every time step and every grid box. The analysis of the model output is often a statistical analysis, whereby the output variables are used as populations which can then be described by statistical parameters such as means, standard deviation, extremes or trends.

2.2. Vegetation parameters and its usage in REMO

Nearly thirty percent of the Earth surface is covered by land and roughly 60% of the land surface is vegetated (Haggett, 1991). A parameterization of vegetation is needed to describe the physical

characteristic of the land surface. Therefore, the vegetation characteristics need to be translated into information, which can be numerically used. Commonly used vegetation parameters are:

- ▷ albedo
- ▷ forest ratio
- ▷ leaf area index (LAI)
- ▷ vegetation ratio (c_v)
- ▷ roughness length.

In the parameterization of atmospheric processes, vegetation is affecting mainly the following parameterizations: radiation, evaporation and vertical diffusion.

Radiation-influencing vegetation parameters

Concerning the heat balance, as explained in section 1.1, the surface albedo has a major role within the shortwave radiation budget.

The **albedo** (α) is a relative measure for the reflectivity of a surface for solar radiation (a detailed albedo definition is given in chapter 3). It is a dimensionless term which is principally ranging between zero and one, in case of a perfect reflection it would be one and for a black body zero. In the glossary of the IPCC of the working group I (IPCC, 2007b) the albedo is defined as: “The fraction of solar radiation reflected by a surface or object, often expressed as a percentage. Snow-covered surfaces have a high albedo, the surface albedo of soils ranges from high to low, and vegetation-covered surfaces and oceans have a low albedo. The Earth’s planetary albedo varies mainly through varying cloudiness, snow, ice, leaf area¹ and land cover changes.” Whereby high albedo values for fresh snow cover are around 0.8 (80%). Very dark areas over land might have an albedo of around 0.1 (10%).

In this work, only the albedo of the land surface is of interest; even more detailed, only the surface albedo without a snow cover. In atmospheric circulation models, the surface albedo can have two values, a **background albedo** without snow and a **surface albedo**, during snow cover. The background albedo within REMO, is defined as the land surface albedo without the snow cover. Together with a simulated snow cover it is representing the “total” surface albedo within the model. Hence, the “surface albedo” is a climate model result. For simplification the term “background albedo” is referred to in the following as “albedo” only.

However, a further vegetation parameter is used in REMO for the calculation of the surface albedo with snow cover. To capture the so-called **snow albedo**, the **forest ratio** (c_f) is used. It identifies for every grid box the forested fraction. How to calculate snow albedo is documented in DKRZ (1993), but the principle is introduced here as an example. Within a forest, snow covers trees not

¹In IPCC’s definition the role of the Leaf Area is mentioned. A dependence of the albedo on vegetation is obvious, but the reflection of vegetation is not primarily depending on the leaf size. For example in autumn, dying leaves have the same size as in summer, but have a different reflectivity.

always as well as the ground. In fact, the snow cover in a forest is never continuous and therefore, the albedo is often strongly lowered in comparison to a fully snow covered flat area. To capture the effect of a lowered albedo over forested areas a measure for the horizontal extension a forest is used. In REMO this variable is a theoretical value, which is attributed to each land cover class. So, the attributed forest ratio to the class Urban is 0, whereby to the Coniferous Forest class a forest ratio of 0.9 is attributed.

Evaporation-influencing vegetation parameters

Turbulent exchange processes close to the surface like latent heat flux, are parameterized by vertical diffusion processes. In the parameterization of evaporation over land, the moisture fluxes are calculated on fractions for each grid cell: covered with vegetation, covered with water in skin reservoir, covered with bare soil and covered with snow.

First, **Vegetation Ratio** (c_v) is used in order to define the vegetated fraction of each grid box. A dense plant community in a tropical rain forest has a much higher vegetation ratio compared to a semi-desert plant community. C_v accounts for the amount of bare soil, which would be visible for nadir view. This is shown in figure 2.3, which is also showing how this information is translated

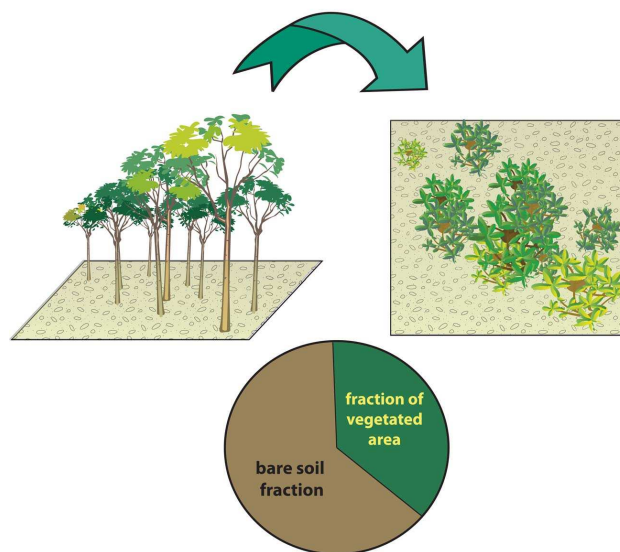


Figure 2.3.: Vegetation Ratio (c_v): 3D-view, nadir view and resulting estimation of vegetation and bare soil fraction.

into a variable, explicitly into a parameter for a climate model. Measurements of such a variable are more difficult, due to the fact that plants are usually structured in overlapping levels. C_v can hardly be verified for dense vegetations by measurements, for example by remote sensing.

Calculating the wet skin fraction in REMO, c_v and a **Leaf Area Index (LAI)** are used. The



Figure 2.4: A hemispheric photo of a boreal forest. These photos are used to calculate estimates of LAI, <http://www.whrc.org/ecosystem/boreal/fieldmeasurements.html>.

interception layer describes the ability of plants to store precipitation water on short-term on their leaves, from where evaporation of precipitation water takes place, until this skin reservoir is emptied. In case of a dry wet skin fraction, the LAI is part in the parameterization of evaporation efficiency from dry vegetation, as a factor within the calculation of stomatal resistance (DKRZ, 1993).

The Leaf Area Index (LAI) is defined within the glossary of the Workpackage 2 of the fourth report of the Intergovernmental Panel on Climate Change (IPCC, 2007a) as: “The ratio between the total leaf surface area of a plant and the ground area covered by its leaves. Commonly the sum of the upper leaf surface of the vegetation for the total columns height, is taken into account, and then divided by the surface area on which the vegetation is spread.” The LAI is a dimensionless index. For bare ground it is equal to zero, in contrast to dense vegetation, which has a leaf area of at least three to six times the area of the ground.

The Leaf Area Index is usually measured on site, by sampling and counting of plant leaves. Another method is done by a photogrammetric method, using a 360° spherical camera on ground directed into sky, shown in figure 2.4. The contrast of sky to tree covered fraction delivers an estimated LAI. The LAI is also a variable which can be obtained by remote sensing, described in section 3.2.

In the calculation of vertical diffusion, turbulent fluxes uses the **Roughness Length** (z_0) of a surface. It can be seen as a variable which can decelerate or accelerate the vertical diffusion and also may influence major directions of regional wind systems. The roughness length is representing the height where the mean wind speed becomes zero, if the vertical wind profile is logarithmic. As vegetation does have characteristic heights, the roughness length over land is varies with its cover. Therefore, the roughness of the land surface is also influenced by vegetation, besides a surface roughness due to orography.

Additionally, also hydrological parameters are influencing evaporation like soil water, and the ability of vegetation to evaporate water from the soils. The soil water representation in the current REMO version is a so-called bucket scheme. It is connected to the vegetation, as the maximum and minimum depth of the bucket depends on vegetation types of the Global Ecosystem Types (GET)

called **water holding capacity** and **permanent wilting point**.

Seasonal variations in vegetation parameters

Some vegetation parameters are time dependent. They do have annual cycles, and also their spatial distribution can change over time.

Seasonality of vegetation is very obvious in many areas of the world. The life cycle of vegetation (phenology) is driven by temperature, moisture and sunlight. The plants' strategy is to adapt to the climate conditions. The differences between growing and dormancy season do impact the physical processes. The factors which are mainly indicating a change in the plant status are changes in plant size (c_v) or leaf size (LAI) and colour (connected to the albedo). With a colour change the radiative transfer is changed, with a change in the leaf size and vegetation ratio the evaporation processes are influenced. The life cycles of plants in climate models without an own phenology parameterization may be expressed as a given annual cycle of the vegetation ratio, leaf area index and albedo.

A seasonal variation in the vegetation ratio describes leaf growth and decay and leads to a changed horizontal distribution. Schematically this is shown in figure 2.5. The upper part is representing a typical vegetation ratio annual cycle as a mean of an area. A corresponding illustration of plant growth for some month is shown in the middle part. Within the grid boxes of a climate model, single plants and their size can not explicitly be resolved. The expansion of vegetation within a model, is also not meant by giving a position of a plant within a grid box. The information has to be seen as a simple subgrid information for each model grid box, as demonstrated in the bottom part of figure 2.5.

The annual cycle of the Leaf Area Index can be seen as a vertically resolved information, in contrast to the horizontal information of the c_v . The LAI may be larger than the ground area underneath. A value of 1.3 for the LAI in January, means that the represented area has a leaf area which is 1.3 times higher than its ground surface. Figure 2.6 shows an annual cycle of the LAI, corresponding to figure 2.5 for c_v . This vertical distribution of LAI is important to estimate the amount of water which can be stored on the plant surface in the wet skin fraction as explained above.

2.3. The lower boundary for the regional model REMO

The Regional Model REMO

The Regional Model (REMO) is an atmospheric circulation model for a limited area, used to dynamically downscale global model data (Jacob et al., 2007; Jacob, 2009).

For this downscaling results of a General Circulation Model (GCM) or reanalysis data are used (often in resolution about 200 km) as lateral driving data. The aim of dynamical downscaling is to

2. Description of the land surface in climate models

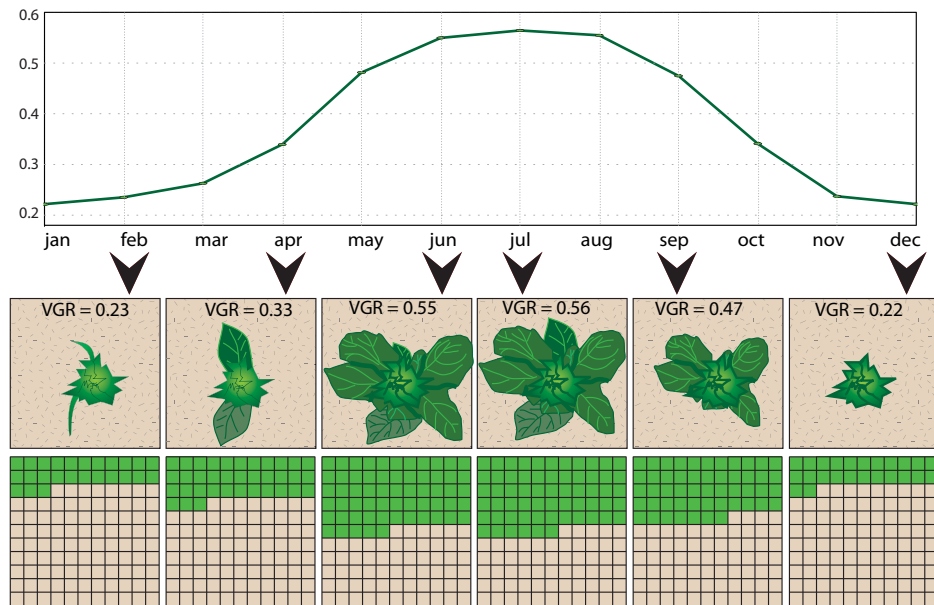


Figure 2.5.: Schematic representation of the annual cycle of the Vegetation Ratio (c_v) (horizontal character).

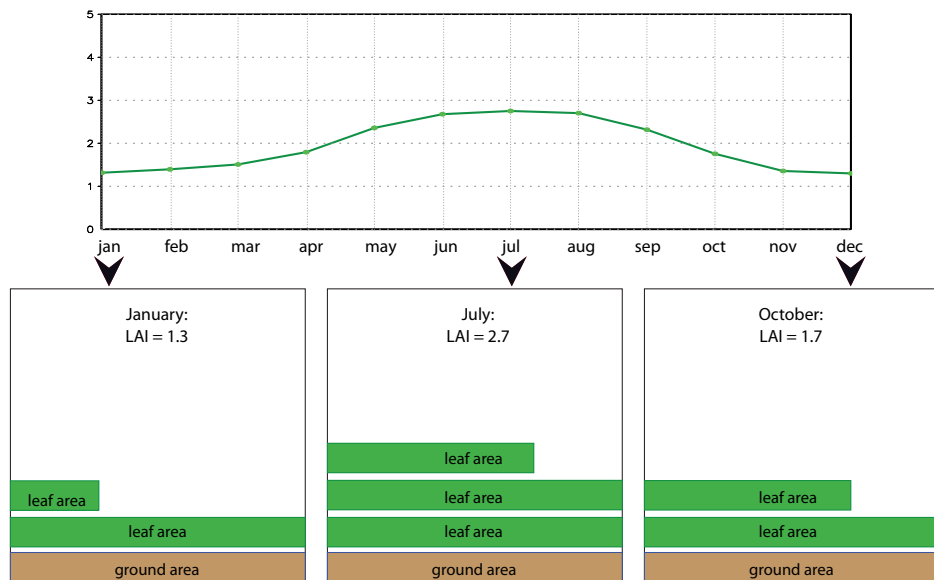


Figure 2.6.: Vertical character of LAI cycle.

receive a spatially more accurate climate information. The higher the horizontal resolution, the less information needs to be generalized. Therefore, simulations of climate processes which are depending on orographic structures, as wind and precipitation, are simulated more accurate for e.g. in 50 km resolution.

This downscaling is called one way nesting. To simulate circulation for an even more detailed resolution (e.g. ≤ 10 km), it is common to use the results of the first nesting step for a second nesting step, then called double nesting. Usually, there is no feedback of the nested area to the outer area. A two way nesting method, in which information of the nested area is also influencing the parent information, is technically possible for REMO (Lorenz and Jacob, 2005).

The Surface Library for REMO (SL4R)

The SL4R is the parameterized description of the earth-atmosphere interface in REMO. Originally it has been developed for the global models ECHAM4 and ECHAM5 (e.g., Hagemann et al., 1999, 2001; Rechid et al., 2008). As the SL4R is based on a global, only roughly resolved description of the lower boundary, it must have some deficiencies in representing details for resolutions lower than 0.5° . Extending information from the global to the regional scale might lead to uncertainties in the results of climate change simulations (Giorgi, 2005). Especially the parameterized albedo within SL4R shows inaccuracies in comparison to satellite albedo observation.

Vegetation independent parameters as:

1. Orography
2. Land sea mask
3. Soil texture

are used in the SL4R directly as constant maps. The orography and the land sea mask are coming from a global Digital Elevation Model (DEM) with a horizontal grid spacing of 30 arc seconds (U.S.Geological-Survey, 1996). As soil texture the “Soil Maps of the World” in 1:5 million scale in a 0.5° version of FAO (1971-1981) are used. These data sets are simply remapped by a nearest neighbour method for the region in the target resolution.

Maps of the Global Ecosystem Types (GET) from Olson (1994) in 1 km spatial resolution are used to achieve a horizontal distribution of parameters connected to vegetation. To each GET type distinct vegetation parameters are allocated. This allocation is a look up table called Land Surface Parameter data set second version (LSP2) (Hagemann, 2002), for the following parameters used in REMO:

1. Roughness Length of vegetation (z_{0veg})
2. Vegetation Ratio for growing season (c_{vg})
3. Vegetation Ratio for dormancy season (c_{vd})
4. Leaf Area Index for growing season $\Leftrightarrow LAI_{max}$ (LAI_g)
5. Leaf Area Index for dormancy season $\Leftrightarrow LAI_{min}$ (LAI_d)

6. Forest Fraction (c_f)
7. Water holding capacity of soil (w_{ava})

As REMO is calculating in resolution between 0.088° (≈ 10 km) up to 0.5° (≈ 55 km), the allocated parameters to the GET in 1 km resolution are upscaled. Therefore, it is assumed that for every coarser spatial resolution, the distribution of the chosen parameter can be seen as a linear combination of every contributing fraction of ecosystem type. More detailed for every grid box and every parameter X (e.g. $X=LAI_g$) the fractional mean \bar{X} can be calculated with equation 2.1:

$$\bar{X} = \sum_{i=1}^{100} f_{GETi} * X_{GETi}. \quad (2.1)$$

f_{GETi} is the fraction of the i'th GET class, and X_{GETi} the allocated parameter for i'th GET class. The result is a horizontal distribution of each parameter for the target resolution. Indeed, the means from equation 2.1 are no longer attributable to certain ecosystem types. The means are not reversible to GETs.

The first row in figure 2.7 is representing schematically the procedure of using the GET maps, while allocating and calculating the fractional means in the target resolution for the parameters.

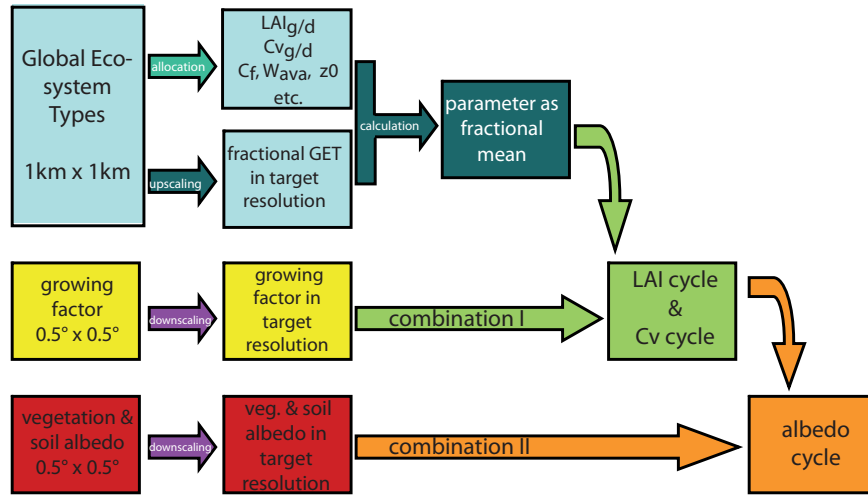


Figure 2.7.: Processing chain of Soil library for REMO

The growing factor and the LAI/ c_v annual cycles

The parameters

1. Leaf Area Index (LAI)
2. Vegetation Ratio (c_v)
3. Backgroundalbedo² (α)

²Further only referred to as albedo.

are treated in the SL4R separately in order to construct an annual cycle for those parameters. This is based on the combination of different data sets, but includes a phenological component in the SL4R output. The connection of these different types of data is shown in the second and third row of figure 2.7, and is documented in the following.

In order to obtain a seasonality for the leaf area index and the vegetation ratio, a so-called Growing Factor (f_i), also referred to as limitation factor, is used. Therefore, the LASUR GVI³ product (Berthelot et al., 1994) was taken as a Fraction of Absorbed Photosynthetic Active Radiation ($fapar$) (compare chapter 3.2) data set. This $fapar$ data set was used to acquire the climatology index for grid boxes between 40° North and 40° South. For the remaining higher latitudes a monthly 2 m temperature climatology of Legates and Willmott (1990) was used. The detailed generation of f_i is documented in Hagemann (2002). It results in maps of f_i in 0.5° resolution for 12 months. For the REMO simulation in case of a chosen resolution under 0.5°, f_i gets downscaled and simultaneously rotated (interpolated) to the target resolution.

The monthly growth factors are then combined with the maps of LAI_g and LAI_d to obtain an annual cycle for the LAI (same for c_{vg} and c_{vd}). For every month i the leaf area index in every grid box is calculated by:

$$LAI_i = LAI_d + f_i * (LAI_g - LAI_d) \quad (2.2)$$

In figure 2.7 the procedure is shown in the middle part, whereby the yellow part is representing the interpolation of the 0.5° climatology map of f_i onto the target resolution. The greenish part indicates the combination of the f_i cycle with the c_v and LAI cycles.

The annual cycle of albedo

In the SL4R, a Moderate Resolution Imaging Spectroradiometer (MODIS) albedo is used for desert areas, where no ground variability is assumed. For areas, where albedo shows an annual cycle, a dependence on vegetation activity is constructed. As vegetation is influencing the surface albedo, it was a major aim to derive a seasonal albedo cycle controlled by vegetation. From observations it was known that the albedo cycle does not always be in phase with the vegetation cycles. It was suggested that the reason for this offset is attributable to the fact that vegetation elevates the albedo in case of dark soils, whereby it is damping the albedo in case of bright soils (Lambers et al., 1998). To adjoin annual albedo cycles, which can evolve off phase to the vegetational annual cycles, a technical trick for generating annual albedo cycles is developed. It is explained in the following, and marked in the bottom line of figure 2.7, where the usage of another new data set is involved and indicated by red boxes (bottom left).

In order to provide a flexible development of the albedo cycle, Rechid et al. (2008) are introducing a procedure, which partitions a MODIS albedo product into a vegetation albedo part and a soil

³Land Surface Reflectance (LASUR) is a postprocessing of the NOAA/AVHRR Global Vegetation Index (GVI) product.

albedo part. Therefore, they are assuming a linear relationship between the $fapar$ and the spectral integrated albedo. The method used is a correlation of the MODIS product FPAR⁴/LAI called MOD15A2 (Myneni et al., 2002) to the MODIS albedo product called MOD43C1 (Schaaf et al., 2000)⁵.

Three years of data were for the period March 2001-2004 were used for the correlation. Both data sets contain 16 day means. For the correlation they were both upscaled to a 0.5° resolution. Albedo grid boxes with snow were excluded, for obtaining a background albedo only (see section 2.2).

Rechid et al. (2008) are stating “In our method, the $fapar$ value is used as an indicator of the presence of vegetation. The total background surface albedo α results from the vegetation albedo (α_{canopy}), where vegetation is present, and the albedo of the soil (α_{soil}), where the underlying surface is visible:

$$\alpha = \alpha_{canopy}fapar + (1 - fapar) \alpha_{soil} \quad (2.3)$$

By linear regression of MODIS $fapar$ and total surface albedo data the vegetation albedo and soil albedo can be estimated. If there is no vegetation ($fapar=0$), surface albedo is equal to soil albedo. If vegetation is present, the contrast between vegetation albedo and soil albedo defines the slope of albedo change.”

This statement needs some explanations concerning its arithmetic background, as it is a major reason for limitations to adapt the SL4R routines for land use changes:

The equation 2.3 can be transformed in the slope-intercept form $f(x) = mx + b$, whereby the $fapar$ is now taken as x .

$$\alpha(x) = \alpha_{veg}x + (1 - x)\alpha_{soil} \quad (2.4)$$

$$\iff \alpha(x) = \alpha_{veg}x + \alpha_{soil} - \alpha_{soil}x \quad (2.5)$$

$$\iff \alpha(x) = (\alpha_{veg} - \alpha_{soil})x + \alpha_{soil} \quad (2.6)$$

α_{canopy} is equal to α_{veg} , as used here. Technically the regression of the MODIS albedo to the MODIS $fapar$ products was only used for grid boxes in which

1. the total amount of valid regression pairs was higher than 3,
2. the differences of each $fapar$ value per grid box over time was higher than 0.1,
3. when $fapar$ was lower than 0.8.

For every grid box the linear regression of the paired values over time resulted in a linear equation, representing the best-fit line through the cloud of value pairs. It is assumed that a linear correlation between albedo and $fapar$ exists. Hence, the best-fit line is equivalent to the idea of:

$$\alpha(fapar) = m * fapar + b \quad (2.7)$$

⁴FPAR= $fapar$

⁵Both products are introduced more detailed in chapter 3.3.2

Figure 2.8 shows an example for one grid box. The blue best-fit line is the calculated linear regression model for the albedo $fapar$ dependency in this grid box. The arithmetic translation is therefore:

$$y = -0.1 * x + 0.25 \quad (2.8)$$

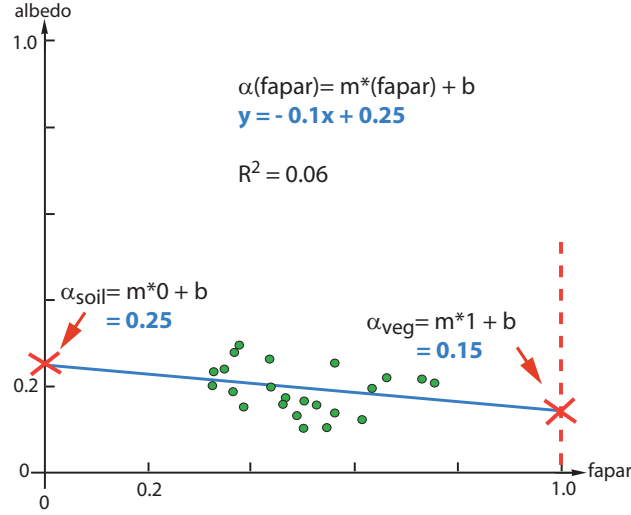


Figure 2.8.: Principle of α_{veg} and α_{soil} separation by linear regression of MODIS albedo to MODIS $fapar$.

As figure 2.8 is indicating, the y-intercept of the regression line is now taken as soil-albedo:

$$b = \alpha_{soil} \quad (2.9)$$

which is confirmed by the statement: “If there is no vegetation ($fapar=0$), surface albedo is equal to soil albedo” (Rechid et al., 2008). This gets interpreted as:

$$\alpha(fapar = 0) = m * 0 + b \quad (2.10)$$

Taking equation 2.6 we can equate the slope ($\alpha_{veg} - \alpha_{soil}$) with the calculated slope of the regression m . A transformation, by using 2.9, leads to a calculated α_{veg} :

$$m = \alpha_{veg} - \alpha_{soil} \quad (2.11)$$

$$\iff \alpha_{veg} = m + \alpha_{soil} \quad (2.12)$$

$$\iff \alpha_{veg} = m + b \quad (2.13)$$

The result for α_{veg} is the addition of slope m and intercept b of the regression. It is identical to $fapar = 1$, also shown in figure 2.8.

Altogether it results in two maps in 0.5° resolution for α_{veg} and α_{soil} , for the usage in equation 2.3. The two weighting factors are summarized in the following as albedo-weights. They are denoted as

2. Description of the land surface in climate models

α_{veg} and α_{soil} , and are shown for parts of Europe and North Africa as well as parts of the near East in figure 2.9.

The connection to vegetation of the LSPII is done by substituting $fapar$ with equation 2.14. The argumentation relies to Monsi and Saeki (1953) who adapted the Beer-Lambert law to vegetation

$$fapar = 1 - e^{-k*LAI} \quad (2.14)$$

with $k = 0.5$ as extinction factor (Dickinson, 1983). For detailed information on the derivation of formula 2.14 by using the Beer-Lambert law, see appendix B.

Then equation in 2.3 turns into:

$$\alpha = \alpha_{veg}(1 - e^{-k*LAI}) + (e^{-k*LAI})\alpha_{soil} \quad (2.15)$$

and relates to LAI. In the SL4R the annual cycle of LAI is calculated first with equation 2.2 for every grid box. Then, for every month i , the LAI_i from equation 6.3.2 is used to calculate the annual cycle of albedo in every grid box.

It is very important to realize that by using the two albedo-weights in combination with the LAI annual cycle, the constructed annual albedo cycles can only be in or off phase to the LAI annual cycles. In case of $\alpha_{veg} > \alpha_{soil}$, it produces annual albedo cycles which are in phase (both annual cycles have their maximum and minimum at the same dates) to the LAI cycle. If $\alpha_{veg} < \alpha_{soil}$, the albedo cycle is exactly off phase, and the LAI maximum is equivalent to an albedo minimum.

If needed to distinguish the background albedo of the SL4R, it will be referred to as α_{SL4R} .

In a further development by Rechid (2008) the temperature and water content were used to derive a climatology for the LAI. This could be used as growing factor and might replace the fixed annual cycles in connection to the growing factor. It would not counteract the fact of having an albedo cycle which is in or off phase to the vegetational cycles of LAI and c_v .

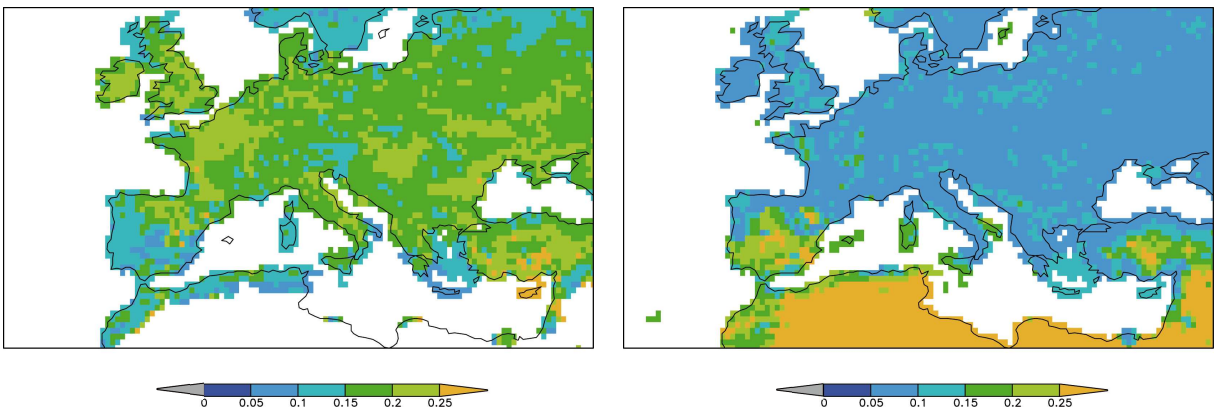


Figure 2.9.: Albedo-weights for west to eastern Europe and north Africa, in 0.5° horizontal resolution; α_{veg} (left), α_{soil} (right).

3. Remote Sensing: Albedo data and vegetation indices

The measure for the reflectivity of a surface is the albedo. In section 2.2 it was defined as the ratio of outgoing to incoming radiation flux density. However, the albedo varies with wavelength and the directional distribution of the incoming radiation. Since the sun emits electromagnetic radiation in different intensities (see figure 3.2), and illumination angles are depending on the sun's position, it is common to use the spectral albedo. "The spectral albedo of a surface is a dimensionless ratio of the radiant energy scattered away from the surface to that received by the surface at a particular wave band."(d'Entremont et al., 1999):

$$\alpha(\lambda) = \frac{E \uparrow (\Lambda)}{E \downarrow (\Lambda)} \quad (3.1)$$

Whereby $E \uparrow (\Lambda)$ is the upwelling radiant energy flux density from the surface for the wave band Λ , and $E \downarrow (\Lambda)$ is the downwelling radiant energy flux density for the wave band Λ .

If we are using albedo data from satellites, we need to understand, how the radiation observation and the data retrieval works. Moreover, we have to accept what Myhre and Myhre (2003) pointed out that no "most realistic" remote sensing albedo data set can be given.

3.1. Albedo from satellite data

Spectrometers orbiting our Earth on a satellite platform, receive Earth's upwelling radiance, technically from Top Of Atmosphere (TOA). Since illumination and view angles and multiple scattering in the atmosphere and at the Earth's surface are influencing the satellite radiances, these processes have to be taken into account for surface albedo retrievals (see figure 3.1). For its usage in climate modelling, three procedures should be known:

1. elimination of radiation angle dependencies by retrieving a **white-sky albedo**
2. elimination of atmospheric disturbances by **atmospheric corrections**
3. spectral dependencies by using a **spectrally integrated albedo**

White-Sky Albedo

As the Earth's surface scatters radiation into all directions and differently at different wavelengths. The Bidirectional Reflectance Distribution Function (BRDF) has been introduced, describing how radiation is reflected at a surface, as a function of illumination and view angles in a particular wave

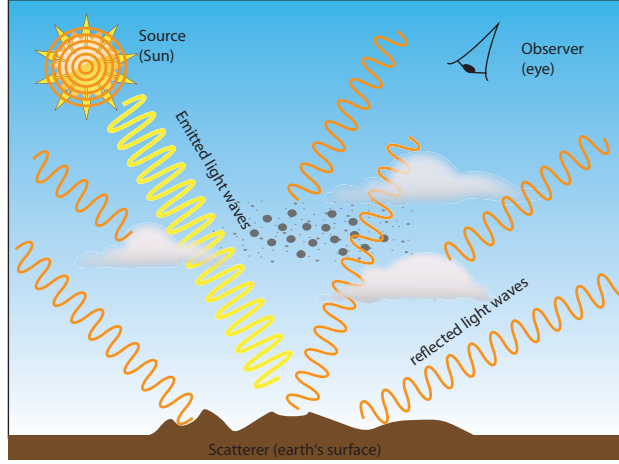


Figure 3.1.: Satellite albedo observation: The source's (Sun) radiation as parallel-beam irradiance, the scatterer (Earth, clouds, aerosols, etc.) reflects radiation in all directions, the observer (eye) receives radiation from scatterer in viewing direction per field of view. Adapted from: NASA <http://southport.jpl.nasa.gov/cdrom/sirced03/cdrom/DOCUMENT/HTML/TEACHERS/MODULE02/MOD2SECA.HTM>.

band:

$$brdf(\vartheta_i, \phi_i; \vartheta_v, \phi_v; \Lambda) = \frac{dL_r(\vartheta_i, \phi_i; \vartheta_v, \phi_v; E_i; \Lambda)}{dE(\vartheta_i, \phi_i; \Lambda)} \quad (3.2)$$

where $brdf(\vartheta_i, \phi_i; \vartheta_v, \phi_v; \Lambda)$ is the BRDF in $[sr^{-1}]$ in wave band Λ ; ϑ_i, ϕ_i and ϑ_v, ϕ_v are zenith and azimuth angles of the direction of irradiance and viewing; $E(\vartheta_i, \phi_i; \Lambda)$ in $[W m^{-2} \mu m^{-1}]$ is the parallel-beam monochromatic irradiance from the illumination direction in wave band Λ ; therefore, $dL_v(\vartheta_i, \phi_i; \vartheta_v, \phi_v; E_i)$ is the monochromatic radiance $[W m^{-2} \mu m^{-1} sr^{-1}]$ in the view direction in wave band Λ under the conditions of illumination E_i (d'Entremont et al., 1999). Note, radiance is the amount of radiation emitted from a particular area within a given solid angle in a specified direction ($L_i(\vartheta_i, \phi_i)$), whereby the power of electromagnetic radiation per unit area (radiative flux density) incident on a surface, is often called irradiance ($E_i = \int_{\Omega} L_i(\vartheta_i, \phi_i) d\Omega$ \wedge Ω denotes hemispherical illumination directions).

Strictly spoken, equation 3.1 is the spectral albedo, a ratio of radiation flux densities, integrated over all illumination and viewing angles:

$$\alpha(\Lambda) = \frac{\int_0^{2\pi} \int_0^{\pi/2} L \uparrow(\vartheta_v, \phi_v; \Lambda) \sin\vartheta_v \cos\vartheta_v d\vartheta_v d\phi_v}{\int_0^{2\pi} \int_0^{\pi/2} L \downarrow(\vartheta_i, \phi_i; \Lambda) \sin\vartheta_i \cos\vartheta_i d\vartheta_i d\phi_i} \quad (3.3)$$

where $\alpha(\Lambda)$ is the spectral albedo (dimensionless) in wave band Λ ; $L \uparrow(\vartheta_v, \phi_v; \Lambda)$ is the upwelling radiance in direction ϑ_v, ϕ_v in wave band Λ ; and $L \downarrow(\vartheta_i, \phi_i; \Lambda)$ is the downwelling radiance in direction ϑ_i, ϕ_i in wave band Λ (d'Entremont et al., 1999).

Relfectances independent of illumination and viewing angles are referred to as white-sky and black-sky albedo. The white-sky albedo is a bi-hemispherical reflectance where the illumination

and the reflectance is equally distributed in all directions. The black-sky albedo is the directional-hemispheric reflectance where the incoming radiation of a certain direction is equally reflected into all directions.

No further details will be given here for sensor specific BRDFs, as the details are not necessary for understanding this thesis, details are documented in (e.g., Ranson et al., 1991; d’Entremont et al., 1999; Lucht et al., 2000; Schaaf et al., 2000, 2002; Strugnell and Lucht, 2001; Maignan et al., 2004).

Atmospheric Corrections

While passing the atmosphere, the radiation gets absorbed, reflected and scattered by different gases and particles. Due to the variability in the concentrations of these, the incoming radiation flux density at the surface is also variable, and the reflected radiation flux density as well. In order to have constant conditions, the contribution of the atmosphere to the radiance received at the satellite has to be removed. These atmospheric corrections are done with radiative transfer models. They are simulating the optical properties of the atmosphere (e.g., de Haan et al., 1991; Vermote et al., 1997; Fell and Fischer, 2001; Schroeder et al., 2005).

Besides cloudy pixels needs to be eliminated for surface albedo estimates. Special techniques are used for so-called cloud masking (Reuter, 2005).

Atmospheric corrections and cloud masking are challenging topics in remote sensing. For satellite sensor different algorithms and techniques are used. Often different remote sensing products are combined to receive more sufficient information. Still no product is perfect, and still many investigations and developments are ongoing in remote sensing.

The satellite data used for this thesis are described in detail in section 3.3.

Spectrally Integrated Albedo

The downwelling sky radiance distribution at the Earth’s surface is determined by absorption of different gases in the atmosphere and multiple scattering by aerosol particles (Rayleigh and Mie scattering). Spectral irradiances at top of the atmosphere and at sea level are shown in figure 3.2.

The commonly used term “albedo” is therefore, the spectral albedo integrated over all wavelengths (λ), in consideration of the spectral’ irradiance distribution at the surface (E_λ) (Kriebel and Koepke, 1985):

$$\alpha = \frac{\int_0^\infty \alpha(\lambda) E_\lambda d\lambda}{\int_0^\infty E_\lambda d\lambda} \quad (3.4)$$

Note, first (in eq. 3.3) the radiances are integrated over all angles in a hemisphere and become irradiances. Then the irradiances gets integrated over all wavelengths. The ratio is the dimensionless measure for surface reflectivity, independent of illumination and observation angles.

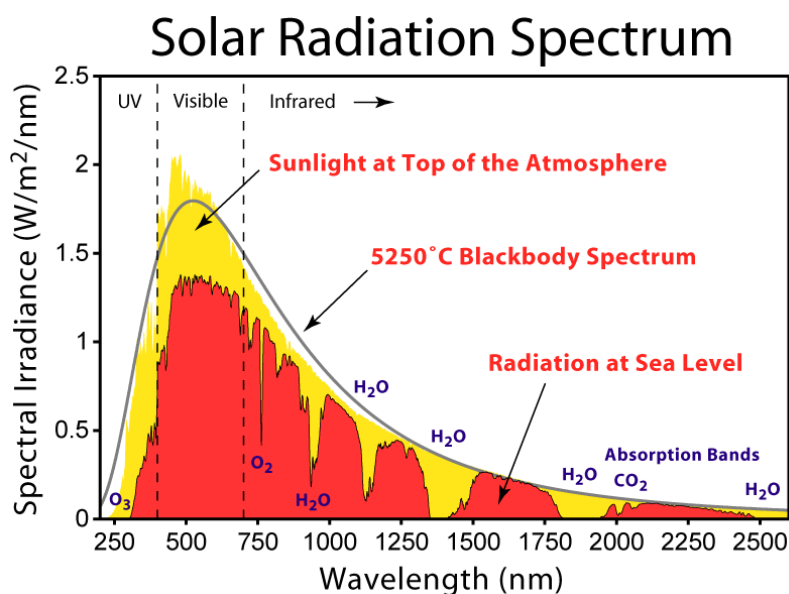


Figure 3.2.: “This figure shows the solar radiation spectrum for direct light at both the top of the Earth’s atmosphere and at sea level. The sun produces light with a distribution similar to what would be expected from a 5525 K (5250 °C) blackbody, which is approximately the sun’s surface temperature. As light passes through the atmosphere, some is absorbed by greenhouse gases with specific absorption bands. Additional light is redistributed by Rayleigh scattering, which is responsible for the atmosphere’s blue color. [...] Regions for ultraviolet, visible and infrared light are indicated.” Image and caption created by Robert A. Rohde / Global Warming Art: http://www.globalwarmingart.com/wiki/File:Solar_Spectrum_png.

As this work focuses on the role of vegetation and its impact on the shortwave radiation budget, as mentioned in section 1.1, some aspects concerning the electromagnetic spectrum are important for this thesis.

As shown in figure 3.2 the relevant solar irradiance starts at around 250 nm up to 2500 nm, with a maximum intensity in the visible spectral range between 400 nm and 700 nm (VIS). When looking to spectrally resolved albedo curves for different surfaces, the albedo changes strongly with wavelength. The spectral albedo is shown in figure 3.3 for five different surfaces. They demonstrate completely different but very typical spectral albedo curves. Comparing dry silt, dry sand and wet sand (note that silt and sand describe grain sizes and not soil types), the texture and condition of a surface is influencing the reflectivity.

The interesting aspect of snow surfaces is the strong reflection in the visible spectra. The ability of vegetation to absorb especially in the visible spectrum, and the characteristic high reflectivity in the Near Infrared (NIR) (700-1300 nm) is also demonstrated in the example for a broadleaf. As will be shown in section 3.2 this effect is used to derive vegetation indices.

After integration of the spectral albedo over all wavelengths only one single albedo value is then representing the reflectivity of a surface. The spectrally integrated albedo might be similar, even

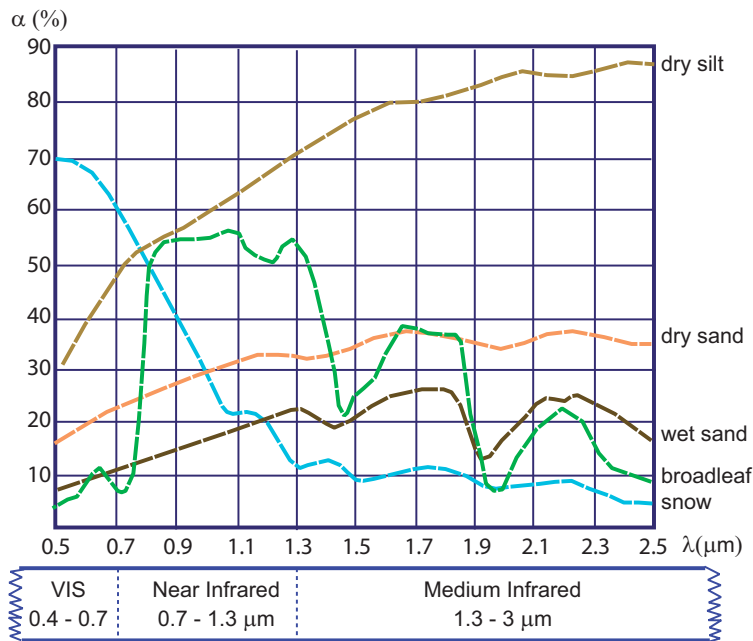


Figure 3.3.: Spectral albedo for different surfaces, from Kraus (1988) (adapted).

if the spectrally resolved albedo shows differing curves. Figure 3.3 can be compared to table 3.1, where spectrally integrated values are given. The given ranges of the albedo values in table 3.1 denote the high variability of surface albedos. Not even mentioned are seasonal variations for the albedo, which are roughly estimated around 5%. Moreover, often neglected are albedo variations for the same vegetation types in different regions (Mediterranean evergreen oak versus Macedonian oak) or for different plants of the same tree type (e.g. for broad leaf forest: maple, oak, birch).

As long as we do not know what type of instrument was used, and which external conditions contributed to the measurements (viewing and illumination angles, exact amount of incoming

Table 3.1.: Typical surfaces and contributed ranges of spectrally integrated albedo values, from: von Storch et al. (1999).

surface	range of spectrally integrated albedo
unvegetated cambisol	0.07 - 0.23
dry sand	0.3 - 0.45
wet sand	0.2 - 0.3
broad leaf forest	0.1 - 0.2
needle leaf forest	0.05 - 0.15
fresh snow cover	0.7 - 0.95
old snow cover	0.4 - 0.7

irradiance), the albedo values can be seen as an informal value but not as an exact description for the reflectivity of a special surface.

For the albedos of vegetated areas the process of determining a plant canopy albedo is even more complex. Dickinson (1983) states that the albedo of a vegetation cover is not strongly correlated to the albedos of single leaves. The canopy albedo is determined by light trapping which is the effect of shadowing by other leaves. The higher the trapping of light by ordering of leaves, the lower the albedos. Further, besides the spectral composition and direction of incoming radiation, vegetation canopy albedos are determined by three aspects: first the “optical properties of individual leaves”, second, “the structure of the canopy”, which are inhomogeneities in the horizontal distribution as well as vegetation heights. Finally the “orientation of plant leaves” is influencing the vegetation albedo. All these processes explain the high variability in plant canopy albedo measurements.

Narrow to broadband conversion in Remote Sensing

Remote Sensing of albedo with satellite platforms, usually detects only certain spectral bands, with radio or imaging spectrometers. Every scanner is tuned to observe a spectrally defined range. The number of detected wavebands and the definition of the bandwidths is characteristic for each scanner. For example the Medium Resolution Imaging Spectrometer (MERIS) on ESA’s Environmental Satellite (ENVISAT) has 15 spectral channels in the shortwave to near infrared spectrum, listed in table 3.3.1. The first version of the AVHRR sensor has four defined channels, covering the shortwave radiation from 0.580-0.68 μm , near infrared range from 0.725-1.10 μm , and two more in the thermal infrared at 3.550-3.93 μm and 10.5-11.5 μm . MODIS, VEGETATION, and others are all instruments for albedo detection and all of them observe in different wave bands.

Usually a BRDF is used for a certain surface type and atmospheric corrections are applied, which results in spectral albedos (e.g. as white-sky albedos) for a defined wave band. To receive a spectrally integrated albedo in respect to spectral irradiance, approximation are used. Basically, appropriate linear combinations of spectral albedos represent a spectrally integrated albedo. This method is called spectral to broad band conversion. The methods of how to make the integration might differ. The spectral to broad band conversion for the albedo data product of MERIS (Albedomap) is explained in section 3.3.1.

Figure 3.4 displays for one pixel on the Iberian Peninsula the white-sky spectral albedo curves of 13 MERIS wave bands between 0.4-0.9 μm (400-900 nm) for 16 day mean time interval (left) and the annual cycle of spectrally integrated albedo for the same MERIS pixel (right). The curves of figure 3.4 are clearly representing bare soil and vegetation spectral albedo curves. The contributing spectrally integrated albedo of Albedomap is plotted with the same colour scheme as for the annual cycle in figure 3.4. Obviously, the spectrally integrated albedo in spring and summer can have the same value. Even though the profiles of the spectrally resolved albedo might explicitly show a major difference: active or non-active vegetation.

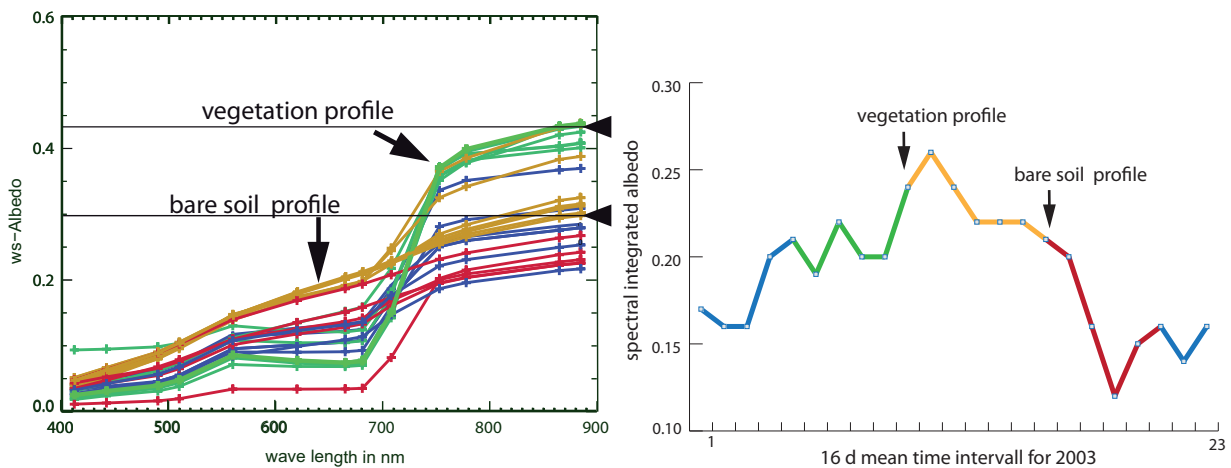


Figure 3.4.: Left: Spectral albedo (white-sky) of one Albedomap data pixel near to Cordoba (Spain) for each 16 day mean of 2003. Marked with arrows, are the typical profiles for vegetation and bare soil. Right: the annual cycle of spectrally integrated albedo for the same pixel. Marked with arrows, are the two time points, equivalent to marked spectral albedo profiles. The colours represent seasons: blue = winter, green = spring, yellow = summer, red = autumn.

The danger of spectral to broad band conversion is therefore, the elimination of any secondary information, i.e. active vegetation or no active vegetation. Since the spectrally integrated albedo is unable to reveal the status of vegetation for the observed pixel, the annual albedo cycle can not make any statement about vegetation activity.

3.2. Vegetation indices from satellite data

Vegetation indices derived from albedo observation are all using one special ability of plants: For photosynthesis, plants can only use photons between 350 and 750 nm wavelength (McCree, 1972) (declarations for the photosynthetic active waveband differs in the literature). Basically, photosynthesis is the process where plants are using light in order to transform carbon dioxide (CO_2) and water to sugar and oxygen. Therefore, the pigment chlorophyll absorbs energy in the wavelength between ≈ 0.35 to $0.75 \mu\text{m}$. On the other hand, in the spectral range from ≈ 0.75 to $1.3 \mu\text{m}$, plants have a high ability for reflection. It is mainly the plant's physiological status, which affects the amount of absorption and reflection. The higher the chlorophyll activity, the more light can be absorbed. In contrast, the presence of wax layers, short white hairs, or salt crystals on the leaf's skin, can also lead to high reflections at lower wavelengths (e.g. Lambers et al., 1998). Equally, the plant's vitality, driven by its water content, influences reflection. Young leaves have a higher water content than old leaves. This is influencing the reflection in the Near Infrared (NIR) range. A fresh plant leaf reflects more in the NIR than the same leaf in a dried condition (e.g. Woolley, 1971).

The contrast between strong absorption in the red spectral range and high reflection in the NIR

range, is called red-edge. It can be used to measure the vitality of a plant or the photosynthesis activity.

Normalized Difference Vegetation Index

The most famous vegetation index which is using this red-edge information is the Normalized Difference Vegetation Index (NDVI). It is an index, developed for the Advanced Very High Resolution Radiometer (AVHRR) instrument of the National Oceanic and Atmospheric Administration (NOAA), first published by Rouse et al. (1973). Therefore, the difference of the reflectance in the near infrared spectral range to the reflectance in the red spectral range gets normalized through their sum:

$$NDVI = \frac{NIR - RED}{NIR + RED} \quad (3.5)$$

The spectral bandwidth for the RED channel of AVHRR is 0.580-0.68 μm . For the NIR channel the spectral bandwidth is 0.752-1.10 μm . Even though the NDVI is originally defined for the AVHRR instrument, many other instruments are using the same equation, to derive a vegetation activity index. As the spectral bandwidths for every instrument are individually set, the vegetation indices of the instruments are not necessarily comparable in their absolute values. Still all vegetation indices from different instruments try to use channels which are able to capture the red-edge difference.

The principle of using the red-edge for the calculation of Vegetation Indices (VI) is demonstrated in figure 3.5. The difference of the red and near infrared channel is indicated for one typical reflectivity curve in comparison to one typical bare soil curve (the same profiles of figure 3.4 and their spectrally integrated value in the annual cycle of figure 3.4). The NDVI rises with growing contrast between RED and NIR. The potential maximum for NDVI is one. A NDVI value lower than 0.125 roughly indicates the absence of vegetation (Knyazikhin et al., 1999). The variations in this red-edge jump is visible in figure 3.4 left. Especially for the spring season (green) the typical spectral albedo curve for active vegetation is prominent, even though they are not identical for each 16 day mean. For some summer profiles, the typical curve for vegetation is missing. Therefore, a bare soil curve is reached which is a hint for the cessation of photosynthesis.

Fraction of Absorbed Photosynthetic Active Radiation

For photosynthesis, plants are using incoming radiation with wavelengths between 0.4-0.7 μm . The incident radiation within this spectral band above the canopy is called Photosynthetically Active Radiation (PAR), given in W/m^2 .

The amount of radiation absorbed by vegetation is called the Absorbed Photosynthetically Active Radiation (APAR), given in W/m^2 . Neglecting the radiation which is transmitted by the canopy and radiation which is reflected directly by the surface, the APAR is represented by subtracting

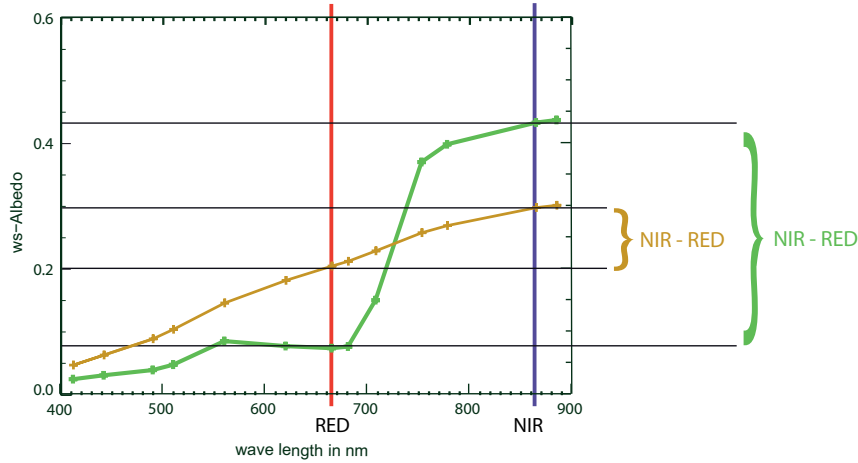


Figure 3.5.: Red-Edge jump as principle for the calculation of Vegetation Indices as the NDVI. Green curve: Albedomap white-sky spectral albedo over active vegetation. Yellow curve: Albedomap white-sky spectral albedo over non-active vegetation / bare soil. Red: Position of MERIS channel 7 (RED), Blue: Position of MERIS channel 13 (NIR). Assigned are the differences of NIR minus RED for each spectral albedo curve. The Vegetation Index following equation 3.5 for the curve with active vegetation is ≈ 0.73 , for the curve with non-active vegetation ≈ 0.25 .

the reflected radiation of the canopy ($rPAR_{canopy}$) from PAR (Epiphanio and Huete, 1995), shown in equation 3.6:

$$APAR = PAR - rPAR_{canopy} \quad (3.6)$$

The ratio of APAR to PAR denotes the dimensionless measure of Fraction of Absorbed Photosynthetic Active Radiation ($fapar$) within the spectral band between 0.4-0.7 μm , which can also be expressed by using equation 3.6 with the canopies reflectivity in equation 3.8:

$$fapar = \frac{APAR}{PAR} \quad (3.7)$$

$$= 1 - \frac{rPAR_{canopy}}{PAR} \quad (3.8)$$

Please note that $rPAR_{canopy}/PAR$ can be seen as an albedo of canopy for wavelengths between 0.4-0.7 μm (compare also appendix B).

Figure 3.6 is visualizing the basic idea of the $fapar$ index, by using the solar radiation spectrum at sea level of figure 3.2 as incoming radiation above canopy and one spectral albedo of figure 3.4 (left).

Different studies have shown a well correlation of $fapar$ and the NDVI (e.g., Myneni and Williams, 1994; Knyazikhin et al., 1999; Gobron et al., 2004, 2005). Therefore, within the method of converting satellite data of spectral reflectances into $fapar$ values, basically the same red-edge information is used. Depending on the method, information on the reflectivity decrease between 550 to 700 nm are added, in order to be more accurate in distinguishing active vegetation.

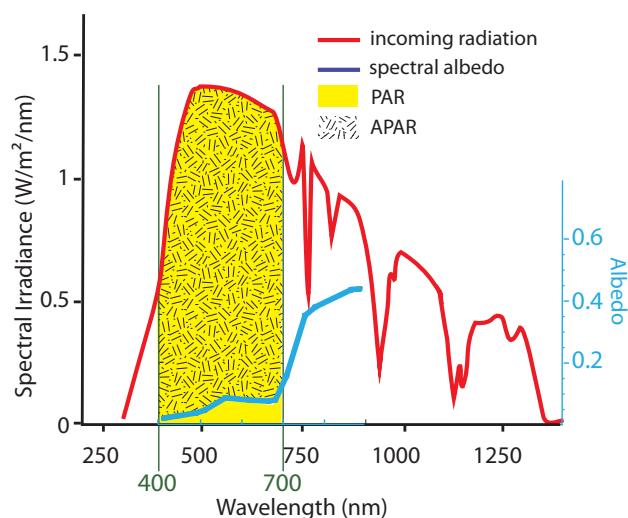


Figure 3.6.: Principle of *fapar*: According to the incoming radiation above the canopy (red curve), the yellow part indicates the Photosynthetically Active Radiation (PAR) as defined between 400 to 700 nm. The spectral albedo (blue curve), is representing the reflectivity of a vegetation cover in each wavelength between 400 to 900 nm. The speckled area indicates the Absorbed Photosynthetically Active Radiation (APAR). The Fraction of Absorbed Photosynthetically Active Radiation (*fapar*) is the proportion of the speckled area to yellow area, whereby the yellow non-speckled area beneath the blue curve is representing $rPAR_{canopy}/PAR$.

For the *fapar* retrieval, information on leaf density distribution (sparse to dense) and the leaves orientation (i.e. erectophile or planophile) are influencing parameters. However, it is important to define a biome type in order to simulate the radiation transport within the vegetation cover. This enables “the *fapar* value act[ing] as an indicator of the presence and state of the vegetation [...]” (Gobron et al., 2007).

LAI from Remote Sensing

“Leaf Area Index (LAI) quantifies the amount of leaf material in an ecosystem, and is a measure of the potential of the vegetation for photosynthesis, respiration, rain interception, and other processes that link vegetation to climate.” (Manninen et al., 2009). As every Vegetation Index the retrieval for the LAI is using information about the red-edge (Myneni et al., 1997). Hence, the LAI can be used as biomass translation for *fapar* or also for NDVI, if the according vegetation type is known. No matter if it is an algorithm or a look up table, principally, for different biomes, a typical LAI and *fapar* are allocated to observed NDVI values (Knyazikhin et al., 1999).

Although there is a strong correlation between LAIs and NDVIs, improved methods are needed, to refer to seasonal and inter-annual variations for the LAI retrieval (Wang et al., 2005).

3.3. Used remote sensing data sets

Three different remote sensing data sets are used within this thesis. Some necessary information about these data sets are given in the following part. A major focus here is on Albedomap data, as it is used within the development of LUCHS. The MODIS data will be introduced only shortly, as they are used for comparisons only. The method LUCHS is using a land use classification. For completeness, the Global Land Cover data set Global Land Cover 2000 (GLC2000) is also introduced here.

3.3.1. Albedomap

Albedomap is an intermediate, not officially released albedo retrieval of the MERIS instrument, for the years 2003, 2004 and 2005 documented in Fischer et al. (2007). MERIS is one of ten sensors on board the ENVISAT of the European Space Agency (ESA). The ENVISAT project was designed for monitoring the climate of ocean and land surface. The satellite was launched on first of March 2002 by an Ariane-5 rocket from space mission launch centre Kourou in French Guyana. The satellite is in a Sun synchronous polar orbit with an altitude of 790 km (± 10 km), whereby one orbit is completed within about 100 minutes. The satellite reaches exactly the same position over the Earth after 35 days. The scanwidth of MERIS is about 1150 km. A global coverage of the Earth is reached every 3 days with a horizontal resolution of 300 m per pixel.

The MERIS instrument is a wide angle pushbroom¹ imaging spectrometer, with 15 spectral bands between 400 and 900 nm (visible and near infrared). The specifications of the 15 channels are listed in table 3.2.

The spectral white-sky and black-sky albedo are processed for 13 of the 15 MERIS channels by using the MODIS BRDF. Data basis is the MERIS level 2 data, which are Rayleigh and ozone corrected reflectances, and got further processed by cloud screening and aerosol corrections. The final white-sky and black-sky albedo products for the 13 channels, are in a spatial resolution of 0.05° (≈ 5 km), representing 16 day means.

In this thesis only the white-sky albedos are used, as in climate models such as REMO, diffuse conditions are assumed. Therefore, the white-sky albedo from satellite products are mainly used for comparisons and satellite data assimilations in climate models.

The narrow to broadband conversion is done by a linear combination of the white-sky albedos for the channels 3, 5, 7 and 13. The used conversion factors are documented in Gao et al. (2003). The conversion for Albedomap is calculated as:

$$X_{bb} = b * ch03 + g * ch05 + r * ch07 + n * ch13 + c \quad (3.9)$$

¹The line scanner works as a digital camera, with only one picture line. As the instrument is moving, the surface gets scanned line by line.

Table 3.2.: Specification of the 15 MERIS channels recommended by the Science Advisory Group (SAG) (<http://wdc.dlr.de/sensors/meris/>).

MERIS Channel Number	Centre Wavelength \pm Bandwidth (nm)	Application
01	412.5 \pm 10	Yellow substance and detrial pigments
02	452.5 \pm 10	Chlorophyll absorption maximum
03	490 \pm 10	Chlorophyll and other pigments
04	510 \pm 10	Suspended sediments, red tides
05	560 \pm 10	Chlorophyll absorption minimum
06	620 \pm 10	Suspended sediments
07	665 \pm 10	Chlorophyll absorption and fluorescence reference
08	681.25 \pm 7.5	Chlorophyll fluorescence peak
09	708.75 \pm 10	Fluorescence reference, atmospheric corrections
10	753.75 \pm 7.5	Vegetation, cloud
11	760.625 \pm 3.75	Oxygen absorption R-branch
12	778.75 \pm 15	Atmosphere corrections
13	865 \pm 20	Vegetation, water vapour reference
14	885 \pm 10	Atmosphere corrections
15	900 \pm 10	Water vapour, land

Table 3.3.: Narrow to broad band conversion factors of spectral white-sky albedos in order to remain visible broadband (VIS-bb), near infrared broadband (NIR-bb), and shortwave broadband (SW-bb) albedos.

	VIS-bb (0 .4-0 .7 μ m)	NIR-bb (0 .7-3 μ m)	SW-bb (0 .4-3 μ m)
b (blue - ch03)	0.3511	0.0	0.1587
g (green - ch05)	0.3923	0.0	-0.2463
r (red - ch07)	0.2603	0.0	0.5442
n (NIR - ch13)	0.0	0.6088	0.3748
c (correction factor)	-0.003	0.1442	0.0149

Table 3.4.: Criterion for exclusion

categories	spectral test
good pixel without clouds	$0 \leq \text{ch03} \leq 0.3$ $0 \leq \text{ch05} \leq 1$ $0 \leq \text{ch07} \leq 0.5$ $0 \leq \text{ch13} \leq 0.7$ $0 \leq \text{ch14} \leq 1$
no vegetation possibly snow	$\frac{\text{ch13}-\text{ch07}}{\text{ch13}+\text{ch07}} \leq 0.1$ $\wedge \frac{\text{ch13}-\text{ch14}}{\text{ch13}+\text{ch14}} \geq 0$
allow bright surfaces	if no vegetation, but possible snow appears for areas lower than climatological snow heights

There are broadband conversion schemes for the visible, the near infrared and the full shortwave band. The constants for b, g, r, and n are different for each broadband conversion. They are listed in table 3.3.

Further adaptations

Even though cloud and snow already have been eliminated within the postprocessing of Albedomap, personal additional adaptations are applied, to avoid artefacts caused by cloud and snow. The Albedomap data in the adapted version will be referred to as adapted Albedomap data product of MERIS (AMAP). To exclude remaining clouds and other disturbances by bright surfaces, a channel dependent exclusion method was applied. It refers to the ability of clouds having a strong reflectance in specific spectral bands (Gobron et al., 2001). First, as listed in the first row of table 3.4, only positive pixels were allowed. Constraints for the higher reflectance were made as indicated, for the blue, red and NIR channels.

For the personal data processing only “good pixel without clouds” were allowed. If one of the conditions was not true, the pixel was excluded. Additional masking for snowy areas was done,

with the following strategy: Snow and vegetation have both high reflectance for channels 13 and 14 (between 865 to 900 nm) but have contrasting slopes. This can be used to exclude pixels, if the “no vegetation/possibly snow” condition was true (second row of table 3.4). This masking excludes all bright pixels - including very bright areas in deserts or salt pan areas. To avoid a too strong exclusion of bright pixels, a special technique was applied, which allows bright surfaces if snow is very unlikely. Therefore, a coarse map of climatological snow heights was constructed. It is an application of the climatological snow heights estimations of Paschinger (1911) on a 0.05° horizontal resolved orography. The two masks “no vegetation/possible snow” and “allow bright surfaces” were used simultaneously on the integrated albedo.

The AMAP shortwave broadband albedo: α_{amap}

The shortwave broadband albedo was calculated with the remaining pixels using equation 3.9 with the shortwave broadband conversion factors (SW-bb) from table 3.3. This albedo will be referred to as white sky broad band albedo of AMAP (α_{amap}). As it the albedo without snow cover, it is representing the so-called background albedo. For comparison reasons and for the usage in LUCHS, the three year 16 day mean was transformed into the monthly mean annual cycle.

The AMAP vegetation index: VI_{amap}

To generate a corresponding vegetation parameter, the white sky albedos of MERIS channel 13 (at ≈ 865 nm) as NIR and 07 (at ≈ 665 nm) as RED have been used, following equation 3.5:

$$VI_{amap} = \frac{ch13 - ch7}{ch13 + ch7} \quad (3.10)$$

The received parameter is referred to as White Sky MERIS Vegetation Index of AMAP (VI_{amap}).

Additional comment:

Following Jan-Peter Muller (personal communication in November 2010), the Albedomap data are inaccurate for latitudes above 60° north due to a mistake in the aerosol retrieval. A new data set GLOBALBEDO is in preparation, but was not available for this work on time. Therefore, only results for up to $\pm 60^\circ$ latitude are shown.

3.3.2. MODIS data

Two Moderate Resolution Imaging Spectroradiometer (MODIS) products are often mentioned in this work. First, a MODIS albedo product and second, a MODIS FPAR/LAI product. For both data sets, three years of data were used from March 2001 to March 2004.

Both products are derived from data of two different MODISs on board two satellites. Both are

across-track wide-field-of-view scanners of NASA², in the EOS³ mission. One is on board of the Terra⁴ the other on the Aqua⁵.

MODIS albedo

The broadband MODIS albedo product MOD43B3 (Schaaf et al., 2000) is a 16 day mean on a global 1 km grid. For the broadband conversion the method of Liang et al. (1999) is used. In the online documentation (<http://www-modis.bu.edu/brdf/userguide/albedo.html>) it is explicitly mentioned: “Liang et al. (1999) used observed spectra and numerical simulations to produce the conversion coefficients for MODIS and MISR used by the operational algorithm. One should keep in mind that spectral-to-broadband conversion is a function of atmospheric state to the extent that the spectral distribution of the solar downwelling flux depends on atmospheric properties and the solar zenith angle. The conversion coefficients computed by Liang et al. (1999) are derived for typical average cases. Variations of the exact results with aerosol optical depth and solar zenith angle are small but affect retrieval accuracies on the level of a few percent”.

For comparisons in this work, the adapted MODIS albedo product by Rechid et al. (2008) is used. It is valid for surfaces without snow cover and was also transformed into a one year monthly mean annual cycle. Therefore, it is as well a background albedo. To indicate the usage of an adapted MODIS albedo data set it is referred to as MODIS albedo, following Rechid et al. (2008) (α_{modis}).

MODIS fapar

The MODIS vegetation index is the MOD15A2 product (Myneni et al., 2002), representing a FPAR and a LAI. The terms FPAR and *fapar* are often used equivalent in the literature. These two parameters for the MOD15A2 are documented as: “FPAR[...] is the fraction of [...] photosynthetically active radiation that a plant canopy absorbs for photosynthesis and growth in the 0.4-0.7 [μ]m spectral range. FPAR is expressed as a unitless fraction of the incoming radiation received by the land surface. [The] Leaf area index [LAI] is the biomass equivalent of FPAR, and is also a dimensionless ratio (m^2/m^2) of the leaf area covering a unit of [surface] area. Both of these variables are computed daily at 1 km [resolution] from MODIS spectral reflectances for all vegetated land surface[s] globally” ([with several corrections], http://modis.gsfc.nasa.gov/data/dataproduct/dataproducts.php?MOD_NUMBER=15).

²National Aeronautics and Space Administration (NASA)

³Earth Observing System (EOS)

⁴Multi-national NASA scientific research satellite - flagship of EOS (Terra)

⁵Multi-national NASA scientific research satellite (Aqua)

3.3.3. Global Land Cover 2000

A land cover data set used for this thesis, is the GLC2000 product (Bartholome and Belward, 2005). The GLC2000 data are available free of charge for all non-commercial applications from <http://www.gvm.jrc.it/glc2000>. It is based on satellite observations coming from the VEGETATION sensor on-board SPOT 4. The detailed database for the European continent and North Africa was used. The data is available at 1 km horizontal resolution.

The general objective of GLC2000 was to provide for the year 2000 a harmonized land cover database of the whole globe. Therefore, the United Nation's Ecosystem-related International Conventions were applied: "The UN Land Cover Classification System (LCCS) is an international standard for the classification of land cover information. It is a universally applicable system by following a standardised, systematic and multipurpose approach. It enables a comparison of land cover classes regardless of data source, economic sector or country" (http://ionia1.esrin.esa.int/news/_faq.asp?id=30).

All such 22 land cover classes are presented in table 3.5.

Table 3.5.: GLC2000 legend

Type	Label
11	Post-flooding or irrigated croplands (or aquatic)
14	Rain-fed croplands
20	Mosaic cropland (50-70%) / vegetation (grassland/shrubland/forest) (20-50%)
30	Mosaic vegetation (grassland/shrubland/forest) (50-70%) / cropland (20-50%)
40	Closed to open (>15%) broadleaf evergreen or semi-deciduous forest (>5m)
50	Closed (>40%) broadleaf deciduous forest (>5m)
60	Open (15-40%) broadleaf deciduous forest/woodland (>5m)
70	Closed (>40%) needleleaf evergreen forest (>5m)
90	Open (15-40%) needleleaf deciduous or evergreen forest (>5m)
100	Closed to open (>15%) mixed broadleaf and needleleaf forest (>5m)
110	Mosaic forest or shrubland (50-70%) / grassland (20-50%)
120	Mosaic grassland (50-70%) / forest or shrubland (20-50%)
130	Closed to open (>15%) (broadleaf or needleleaf, evergreen or deciduous) shrubland (<5m)
140	Closed to open (>15%) herbaceous vegetation (grassland, savannas or lichens/mosses)
150	Sparse (<15%) vegetation
160	Closed to open (>15%) broadleaf forest regularly flooded (semi-permanently or temporarily) - Fresh or brackish water
170	Closed (>40%) broadleaf forest or shrubland permanently flooded Saline or brackish water
180	Closed to open (>15%) grassland or woody vegetation on regularly flooded or waterlogged soil - Fresh, brackish or saline water
190	Artificial surfaces and associated areas (Urban areas >50%)
200	Bare areas
210	Water bodies
220	Permanent snow and ice
230	No data (burnt areas, clouds, etc.)

4. Analysis concepts

4.1. The concept of albedo characteristics

Due to the complex retrieval algorithms, albedo data and also vegetation indices from different satellite products are not necessarily comparable in their absolute values. Therefore, a method has to be developed which allows comparisons. Since the annual cycle of albedo is observable, it can be used for comparison. If one instrument observes an increasing albedo for one location, another instrument will also observe an increase for the same location, though the absolute values might differ substantially. One can assume that the shape of the albedo's annual cycle for one vegetation cover is similar for different satellite instruments. The characteristic information can be used like a fingerprint for the observed vegetation cover.

An annual cycle has three main characteristic features:

1. Amplitude: difference between albedo maximum and albedo minimum
2. Phase: date of albedo maximum and albedo minimum
3. Minimum level: absolute minimum of the albedo during a year

The amplitude is seen as a peak-to-peak amplitude and reflects the seasonal variability. The phase refers to the shape of the annual cycle. The dates for the minimum and maximum are important for the radiation budget. The absolute minimum level is important for a categorical classification. Summarizing these three aspects for the albedo, the expression **albedo characteristics** is used in this work. All three aspects are schematically demonstrated in figure 4.1. Annual albedo amplitude,

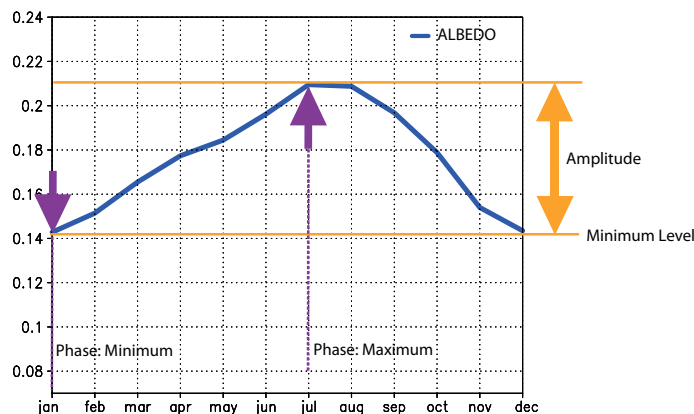


Figure 4.1.: Schematic of albedo characteristics.

phase and albedo minimum of α_{amap} are shown as an example for large parts of Europe and parts of North Africa in figure 4.2.

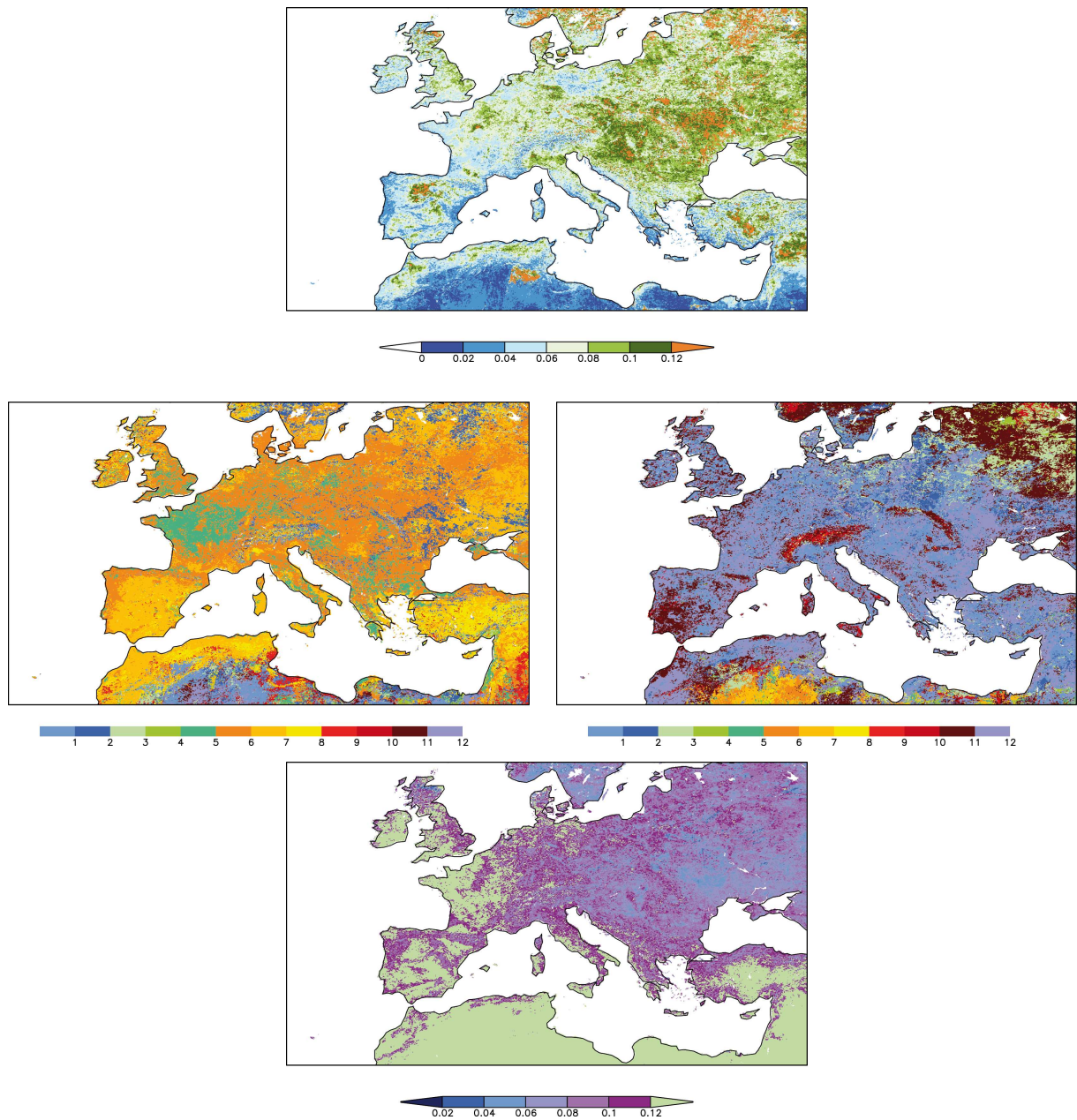


Figure 4.2.: Visualization principle for Amplitude (top), Phase: month of maximum (centre left), month of minimum (centre right), Minimum Level (bottom), of α_{ama} .

The albedo characteristics are regional specific. For example cropland in different regions has different shapes of the annual cycle of albedo. In figure 4.3, the annual cycle of albedo from AMAP (α_{ama}), MODIS (α_{modis}) and from SL4R (α_{SL4R}) are compared. For both regions, the Land Use Harmonization Protocol (LUH-P) with more than 50% fractional contributions of crop is used as a mask in 0.5° horizontal resolution. For the α_{ama} data, the LUH-P (see section 3.3) crop mask was conservatively remapped on 0.05° horizontal resolution. Therefore, the remapped mask on the

α_{amap} data in 0.05° is representing the same area.

The focus of figure 4.3 is the comparison between the two regions and the different albedo data sets. First, the characteristics (amplitude, phase and level) of the observational data (AMAP and MODIS) are completely different for the two regions. Second, it is important to realize that the albedo of the SL4R which is used so far in REMO, shows almost no differences for the two regions. The large differences to observations are related to the way of the albedo parameterization in SL4R, as explained in section 6.2. The large offset in the two albedo observations α_{amap} and α_{modis} , can be attributed to differing post processing methods. The data sets also cover different periods (α_{amap} : 2003-2005; α_{modis} : 2001-2004), both originally for 16-day mean. Additionally, the original MOD43B3 product has 0.05° horizontal resolution and was upscaled to 0.5° horizontal resolution. Altogether this can lead to a loss in albedo amplitude and shifts in the phase of the mean annual cycle.

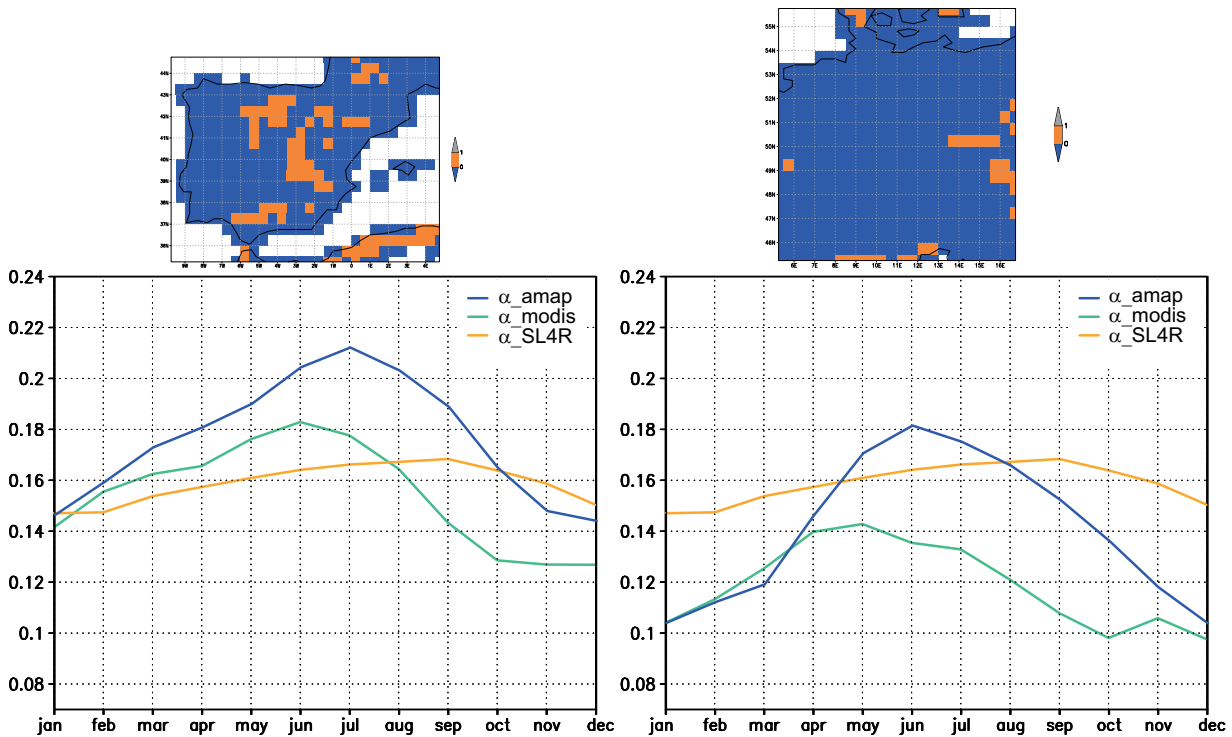


Figure 4.3.: Annual cycle of surface albedos α_{amap} , α_{modis} and α_{SL4R} for the orange grid boxes, which are indicating where the LUH-P crop class covers more than 50% (top). Left: Iberian Peninsula, right: Central Europe.

4.2. The concept of radiative perturbation

Estimating the climate effect due to surface albedo changes on one single variable is not simple. Therefore, the concept of radiative forcing is often used. Radiative forcing is a term, denoting an “externally imposed perturbation in the radiative energy budget of the Earth’s climate system” (IPCC, 2001), expressed as an energy flux density given in W/m^2 .

Model simulations have investigated the influence of land cover changes due to expanding human population on the radiative forcing. The mean global radiative forcing due to surface albedo change since 1750 estimated to be $-0.2 W/m^2$ (Pongratz et al., 2009a). By accounting for deforestation, the resulting changes in radiative forcing caused a cooling of about 1-2 K for the northern mid-latitudes (Betts et al., 2007). The radiative forcing of the surface albedo change (≈ -0.2 to $0.1 W/m^2$) is lower than the radiative forcing of CO_2 ($\approx 1.66 W/m^2$) or the cloud albedo effect ($\approx -0.7 W/m^2$) (IPCC, 2007b).

Dickinson (1983) states that an albedo decrease leading to $8 W/m^2$ more absorption of solar radiation results in a temperature increase of $1^\circ C$, could cause in combination with corresponding changes in latent and sensible heat fluxes a total heating of $80 W/m^2$. “The additional radiation would correspond to an increased downward flux of thermal infrared radiation and the decreased sensible and latent heat fluxes due to a warmer atmosphere containing more water vapour (Dickinson, 1983)”. Even small changes of the albedo are impacting climate by affecting the shortwave radiation budget (see chapter 1.1). To get a more intuitive perspective on the impact of albedo changes, a concept of radiative perturbation is developed and used here. It is an ‘a posteriori’ calculation, independent of using the experimental set up of a radiative forcing experiment with fixed atmospheric condition. Although it is also not comparable to radiative forcing values, it has a similar meaning.

For the calculation of radiative perturbation, a fixed annual cycle of global radiation for every grid box is needed. Global radiation is defined as the incoming shortwave radiation at the surface after it has passed the atmosphere. While passing the atmosphere the solar radiation is partly scattered and absorbed by gases and aerosols (see also chapter 3). As shown in figure 4.4, the global radiation is the sum of the remaining radiation on the surface, in W/m^2 .

The reflection of the incoming solar radiation at surface is determined by the reflectivity of the surface. Therefore, the albedo multiplied with the global radiation is the solar radiation at the surface in upward direction in W/m^2 . In atmospheric climate models, the processes of absorption and scattering of the solar (shortwave) radiation within the atmosphere is parameterized by a radiation transfer model for that radiation band (e.g. Roeckner et al., 1996). The net incoming solar radiation at the surface, is calculated in accounting for atmospheric processes. The outgoing solar radiation at the surface is depending on the prescribed surface albedo within the radiation scheme. Both variables are model output variables of REMO. The global radiation is calculated internally within the radiation transfer scheme.

As it is for comparison only, a one year monthly mean annual cycle of the global radiation should

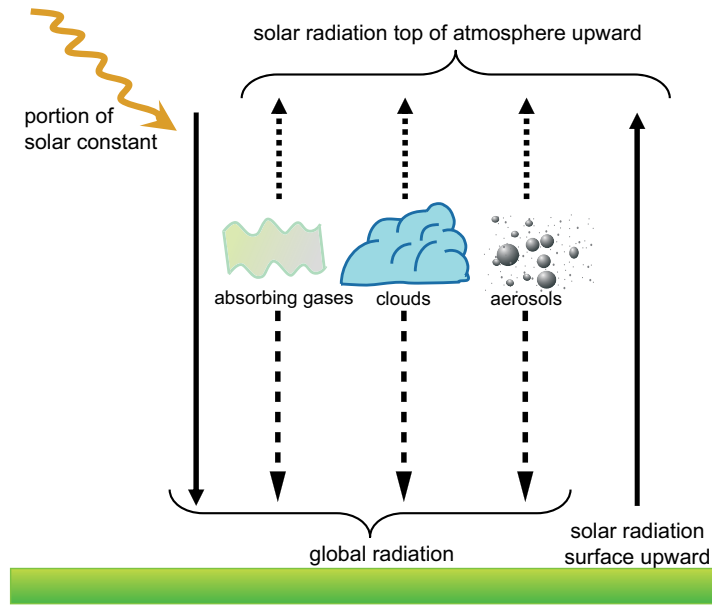


Figure 4.4.: Pathways of solar radiation (= shortwave radiation).

be calculated, for every grid box. It is referred to as G_{ref} in the following. For two experiments with different albedo characteristics, the radiative perturbation can be calculated by using the fixed global radiation distribution of G_{ref} , α_A for the albedo of case A, and α_B for case B:

$$RadiativePerturbation = (G_{ref} * \alpha_A) - (G_{ref} * \alpha_B) \quad (4.1)$$

The radiative perturbation in W/m^2 is representing the irradiation difference into the atmosphere. It is according to a mean radiation status for every grid box, and reflects typical conditions in the radiation regime. Positive radiative perturbation indicates less absorption of solar radiation at the surface.

Within this study a mean global radiation annual cycle of global radiation will be referred as: G_{001524} . It is taken from for the period 1990-1994, of an experiment with the internal number: e001524 at 0.11° horizontal resolution over Europe, with ERA-Interim boundary data (Simmons, 2006).

Figure 4.5 shows the five year mean for all seasons of G_{001524} in the horizontal resolution of 0.11° . The discrepancy at the left border is related to the inflow of driving data and is not relevant. A latitudinal dependency of the global radiation is obvious. For the south-west of the Iberian Peninsula the in all seasons higher in global radiation is caused by statistically high probability for the absence of clouds. Altogether, incoming radiation differs regionally.

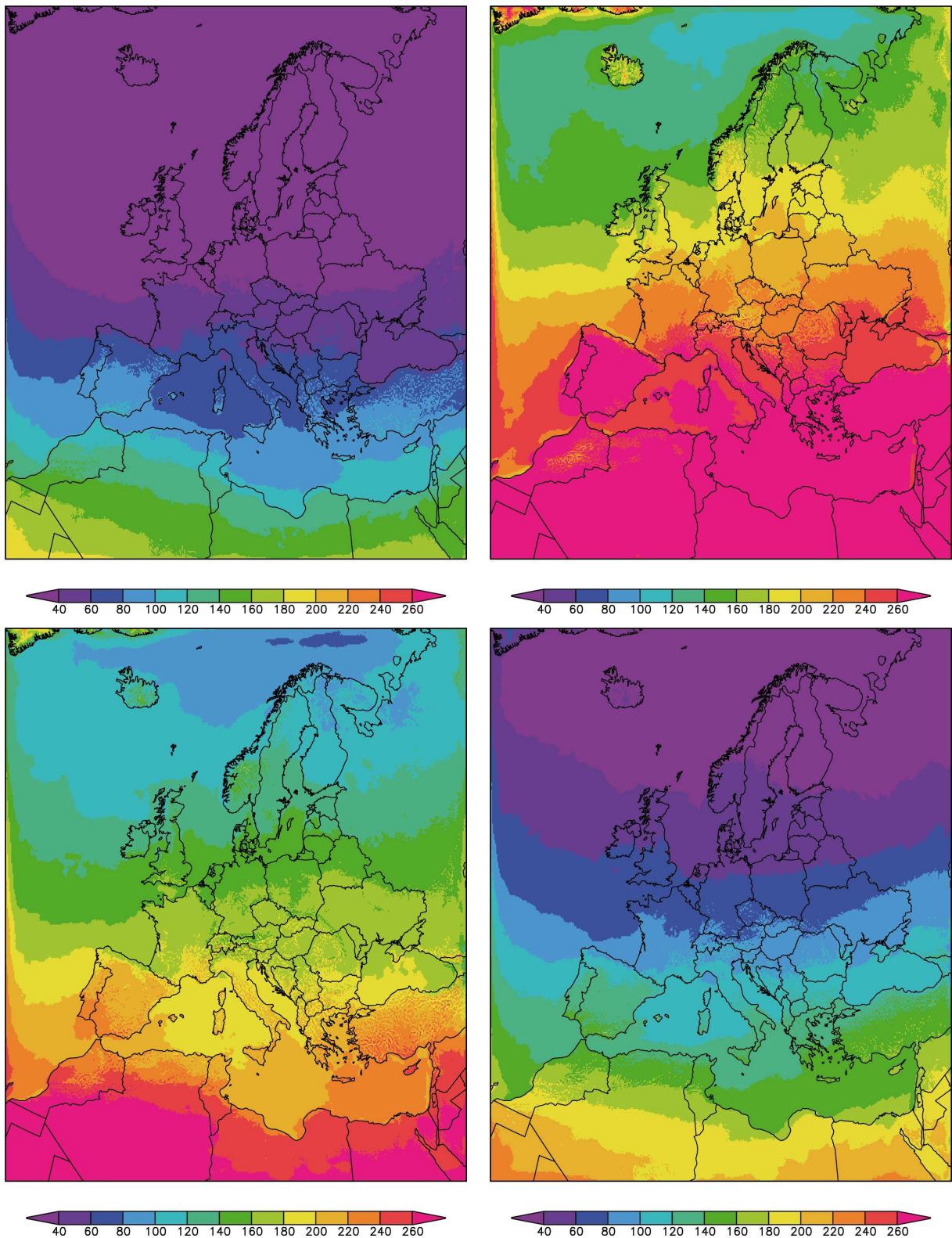


Figure 4.5.: Global Radiation G_{001524} in W/m^2 for seasonal means: DJF (top left), JJA (top right), MAM (bottom left), SON (bottom right).

5. Albedo characteristics

5.1. Regional albedo characteristics for different land use types

The method of analysing regional albedo characteristics resembles the idea of spectral unmixing in remote sensing (e.g., Keshava and Mustard, 2002; Probeck et al., 2004). Here it is not an unmixing of the spectral albedo curves but a separation of the annual cycle of shortwave broadband surface albedo for known land use classes.

Figure 5.1 shows the orography of the regions chosen for analysing albedo characteristics for different land use types: the Iberian Peninsula (further referred to as Iberia) and Central Europe.

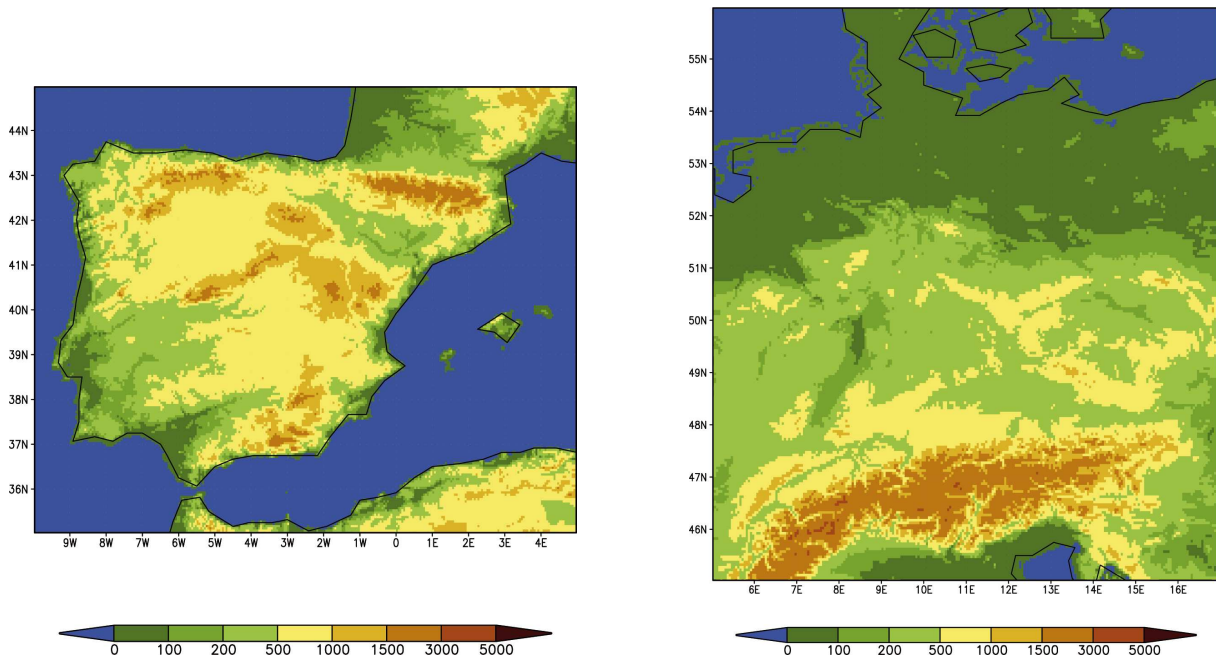


Figure 5.1.: Topography of the regions at 0.05° horizontal resolution: Iberia (left), Central Europe (right).

The annual albedo cycle of the surface albedo is derived for different land cover classes of the Global Land Cover 2000 (GLC2000) data set (see section 3.3), using the GLC2000 types Rain-fed Crop, Deciduous Forest, Needle Leaf Forest, Sparse Vegetation and Artificial. The fractional contribution per grid box in 0.05° horizontal resolution for both areas is shown in figures 5.2 and 5.3. Therefore, in yellow marked grid boxes the fraction of the shown land cover types is higher than 75%, in light green it is higher than 50% and so on.

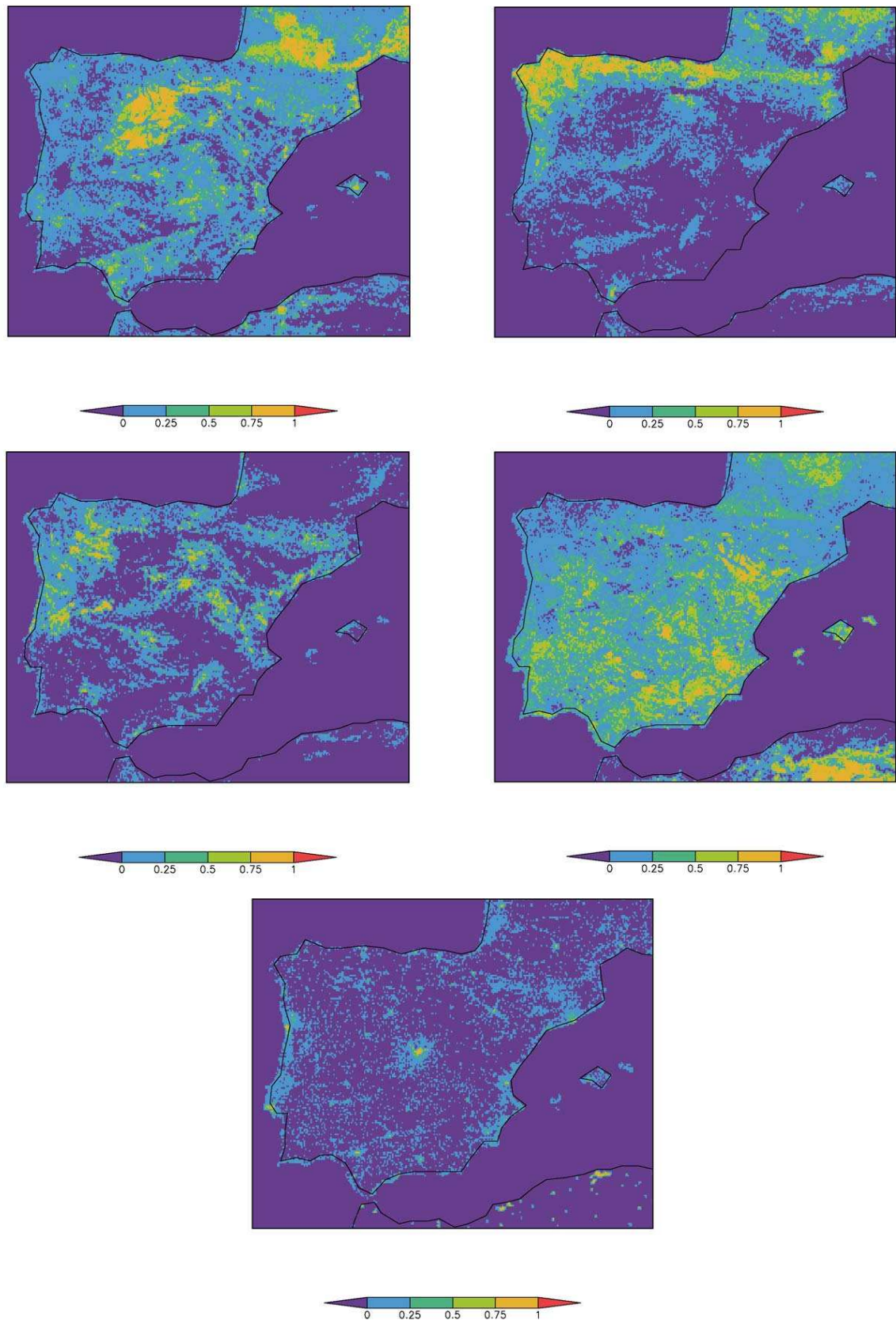


Figure 5.2.: Fractional contribution per 0.05° grid box of GLC types for the Iberia region. Top left: GLC14 Rain-fed Crops, top right: GLC50 Deciduous Forest, centre left: GLC70 Needle Leaf Forest, centre right: GLC150 Sparse Vegetation, bottom left: GLC190 Artificial.

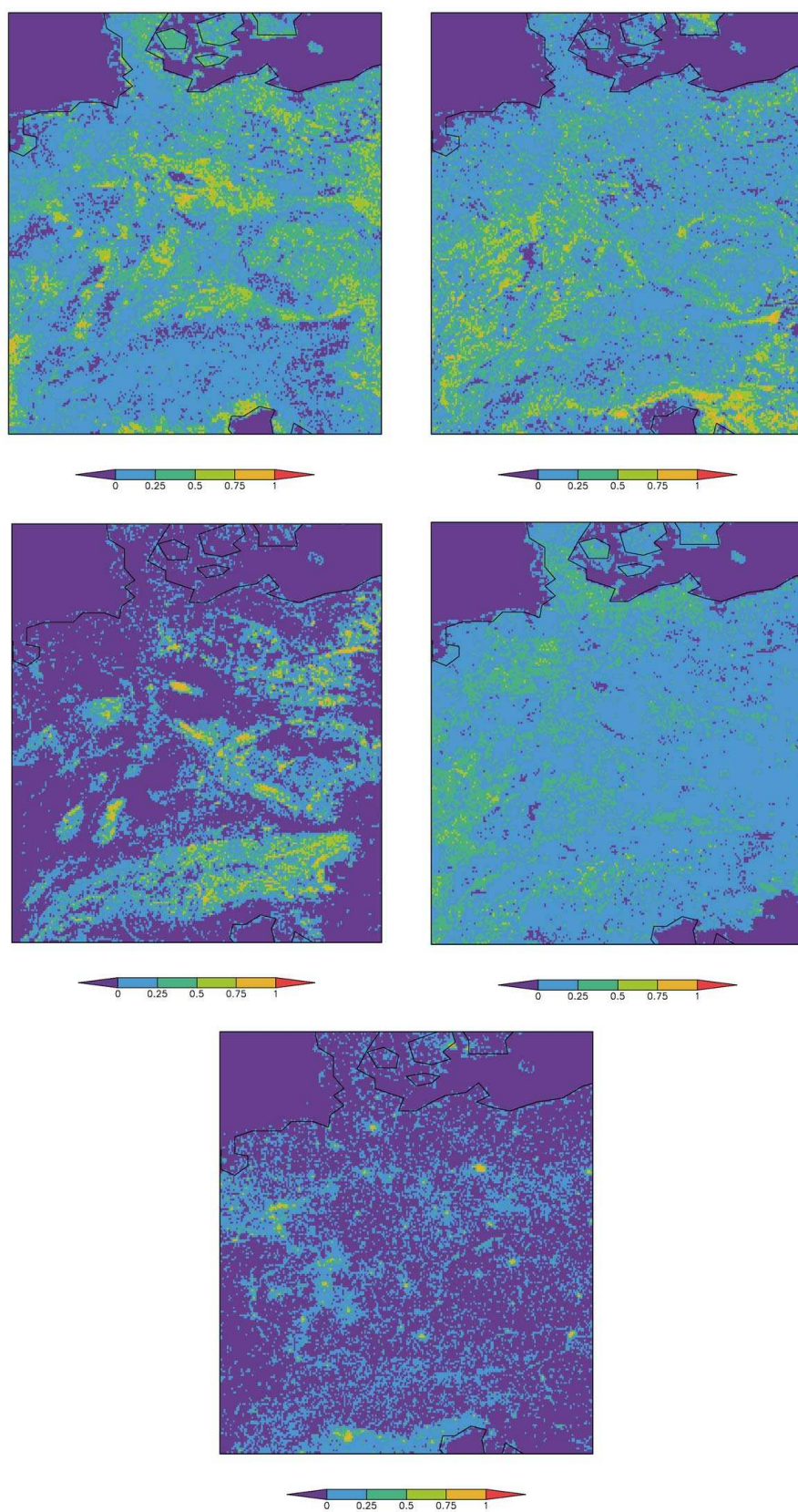


Figure 5.3.: Fractional contribution per 0.05° grid box of GLC types for Central Europe. Top left: GLC14 Rain-fed Crops, top right: GLC50 Deciduous Forest, centre left: GLC70 Needle Leaf Forest, centre right: GLC150 Sparse Vegetation, bottom left: GLC190 Artificial.

While applying the GLC2000 masks on α_{amap} , it is obvious that the albedo climatologies differ for each class. There are characteristic shapes in the climatologies, as can be seen in figure 5.4 for different land cover types of the Iberian region (left) and for Central Europe (right).

Figure 5.4 shows the mean α_{amap} annual cycle for the five introduced land cover classes.

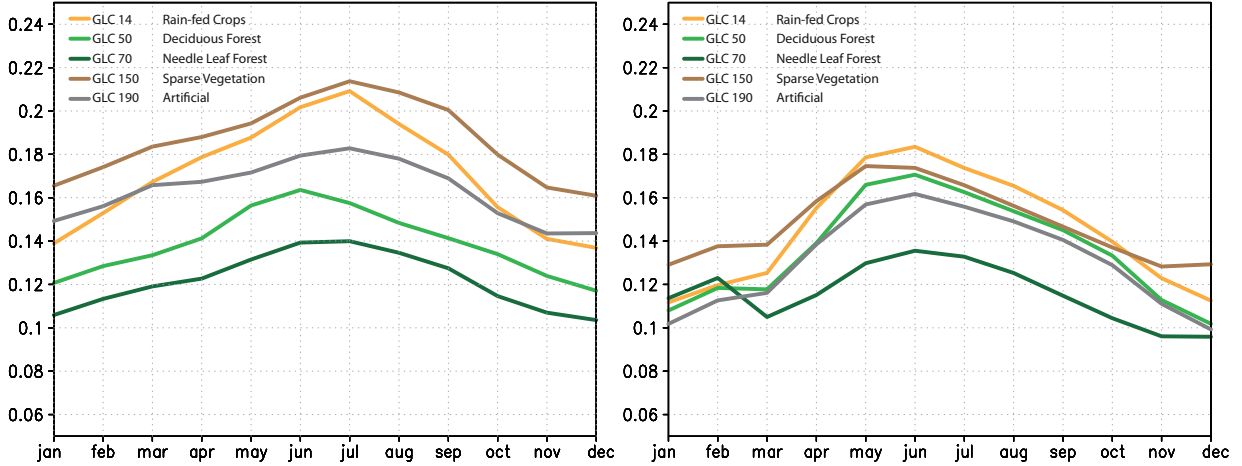


Figure 5.4.: Annual cycle of AMAP albedo (α_{amap}) for areas with more than 50% fractional contribution per grid box of GLC-types 14 (Rain-fed Crop) , 50 (Deciduous Forest), 70 (Needle Leaf Forest), 150 (Sparse Vegetation), 190 (Artificial). For Iberia region (left), Central Europe (right).

In both regions the amplitudes for all land cover types differ. In Iberia different minimum albedo levels are well discernible for each land cover class. This is also true for the Central European region, even though the absolute albedo minima are much closer to each other. In both regions the albedo maxima appear in different months. The maximum for deciduous forest appears for Iberia one month earlier than the maxima of the other classes. The maximum for sparse vegetated areas appears one month earlier for Central Europe than the others. Over all, the maxima in Central Europa appear one month earlier than the maxima for Iberia.

In both regions the annual cycle of surface albedo for Needle Leaf Forest has the lowest minimum and has the smallest amplitude. For Central European the annual cycle of surface albedo for Needle Leaf Forest has a second peak in February. It might be a remaining data artefact due to snow, but can also indicate a waxy conifer cuticle to protect against frost (Lambers et al., 1998). Further investigation should be made, but as snowy and cloudy pixels were removed quite restrictively, it could also be a hint on a characteristic albedo behaviour for Needle Leaf Forests in Central Europe, as it is obvious that the February peak for the Central European Needle Leaf Forest occurs for different contributing area fractions (see figure 5.12).

5.2. Albedo characteristics for different fractional contributions to a grid box

Verifying the characteristic albedo climatologies, the fractional contribution per grid box might lead to different results. The question is, whether the characteristic albedo curve changes with area sizes. The real area size is correlated to the sample size numbers. The number of grid boxes is increasing, the lower the fractional contribution per grid box of the GLC2000 is chosen. If it would be so, it would point out that the albedo curve is just a product of the statistical mean, but can not be seen as a characteristic representation for the land cover class.

Therefore, the annual cycle of albedo α_{amap} was analysed for each GLC2000 class (14, 50, 70, 150, 190) for three different fractional contributions per grid box. Only boxes with more than 25%, (> 50%, > 75%) coverage of the GLC2000 class were chosen. In figures 5.5-5.9 and 5.10-5.14 α_{amap} is shown in blue curves in the top row with rising fractional contributions per grid box from left to right.

In the same figures the equivalent annual cycle of VI_{amap} is shown in green curves beneath the albedo curves for the same fractional contributions. As the albedo is depending on the vegetation cover, the correlation of vegetation activity with the annual cycle of broadband albedo is of major interest. It is shown here in order to point out that seasonal variations in vegetation activity and albedo do not have the same time dependence, which hinders the assumption of a linear correlation between background albedo and f_{apar} , as will be discussed further in section 6.2.

The tables contained in the figures give mean values of α_{amap} for different fractional contributions of one surface type. Analysis factors are: the albedo amplitude per year, the absolute albedo maximum (max), the absolute albedo minimum (min), the annual mean (mean). The 10th percentile (10thpctl) shows the average of 10% lowest values. The columns 'month of max' and 'month of min' indicate the 50th percentile. The last column 'number of cells' gives the number of pixels included in the analysis.

Altogether the α_{amap} and VI_{amap} annual cycles for the different fractional contributions per grid box of the land cover classes do not change their shape strongly. Amplitudes and mean level change strongly. The differences for the fractional contribution is much smaller than the difference to other classes. Of course, the curves are still a mean from all contributing pixel, and for each pixel the annual cycle might differ more than the average shown.

It can be concluded that land cover class masks with 50% fractional contribution are sufficient for the annual cycle of albedo.

Land use characteristics for all GLC classes

All GLC2000 classes shows clearly distinguishable values. As the 50% fractional contribution pixels have shown acceptable results, table 5.1 lists the complete analysis for the Iberian Peninsula for this 50% contribution. In table 5.2 the same is presented for the Central Europe.

Please note, α_{amap} is an albedo data set without snow cover. The presented albedo characteristics of snow, ice in table 5.2 are showing pixels, where the GLC class assumes grid boxes with more than 50% fraction of glaciers. Represented are values in such areas if there is no snow. In both regions, the GLC water pixels are including coastal areas and land mixed with more than 50% fraction of lakes. The albedo over the ocean is not included in α_{amap} , and pixels are excluded for fractional contributions of lakes with more than 80%. Therefore, the values here are not representative for water.

Albedo and correlation to vegetation activity

Comparing the shapes of the shortwave broadband albedo α_{amap} to the annual cycle of vegetation activity VI_{amap} an important fact can be observed. For all land cover types in the figures 5.5 - 5.9 and 5.10 - 5.14, the annual cycle of vegetation index and annual albedo cycle do not follow a particular co-variation. This will be crucial for the parameterization of the albedo in combination with vegetation activity.

Conclusion

Shifts of albedo in space and time can be attributed to land cover changes.

5.2. Albedo characteristics for different fractional contributions to a grid box

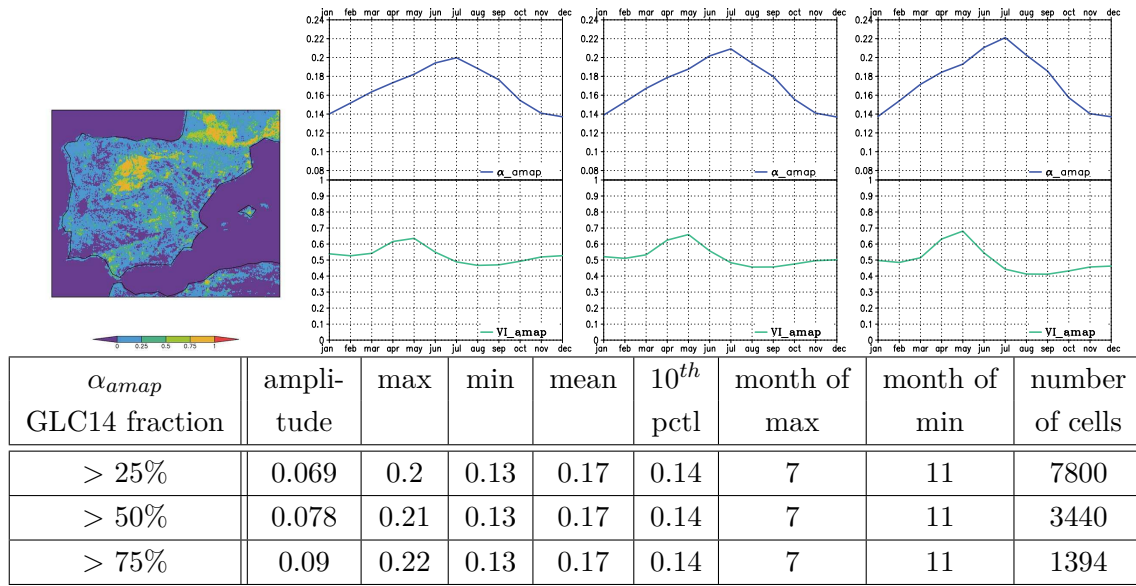


Figure 5.5.: Analysis for GLC14 - Rain-fed Crops. Top left: fraction in Iberia, top middle to right: α_{amap} (blue) and VI_{amap} (green) annual cycles for fractions > 25%, > 50%, > 75%.

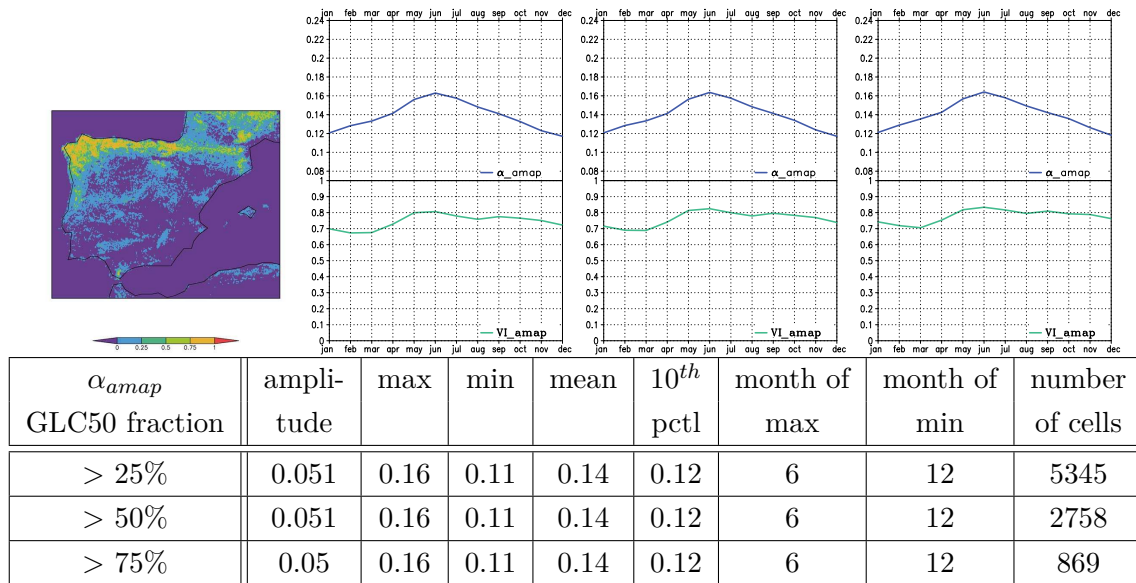


Figure 5.6.: As figure 5.5 but for GLC50.

5. Albedo characteristics

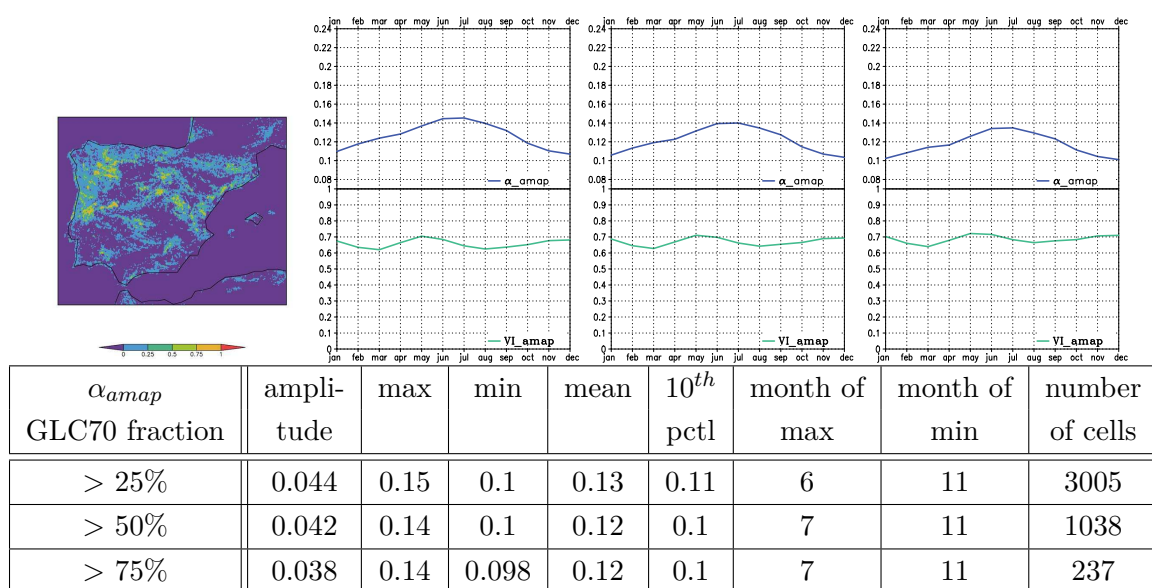


Figure 5.7.: As figure 5.5 but for GLC70.

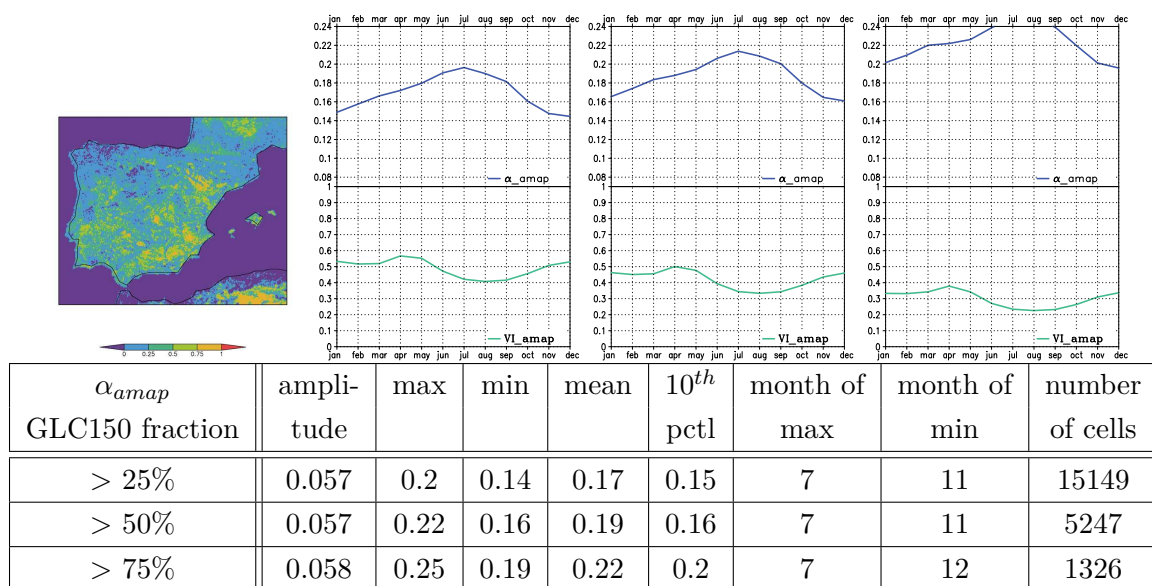


Figure 5.8.: As figure 5.5 but for GLC150.

5.2. Albedo characteristics for different fractional contributions to a grid box

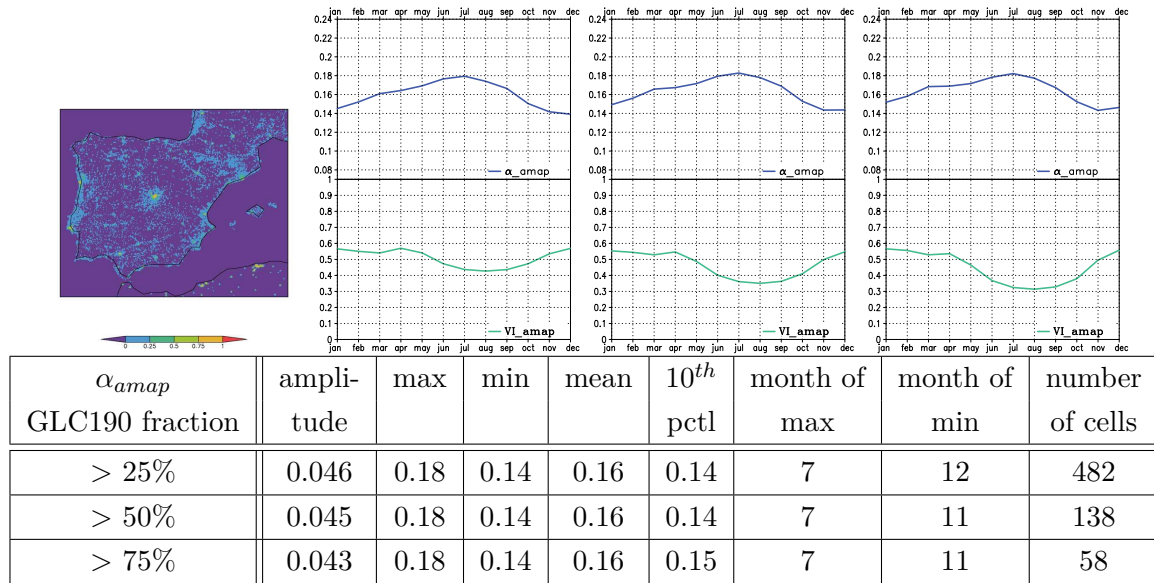


Figure 5.9.: As figure 5.5 but for GLC190.

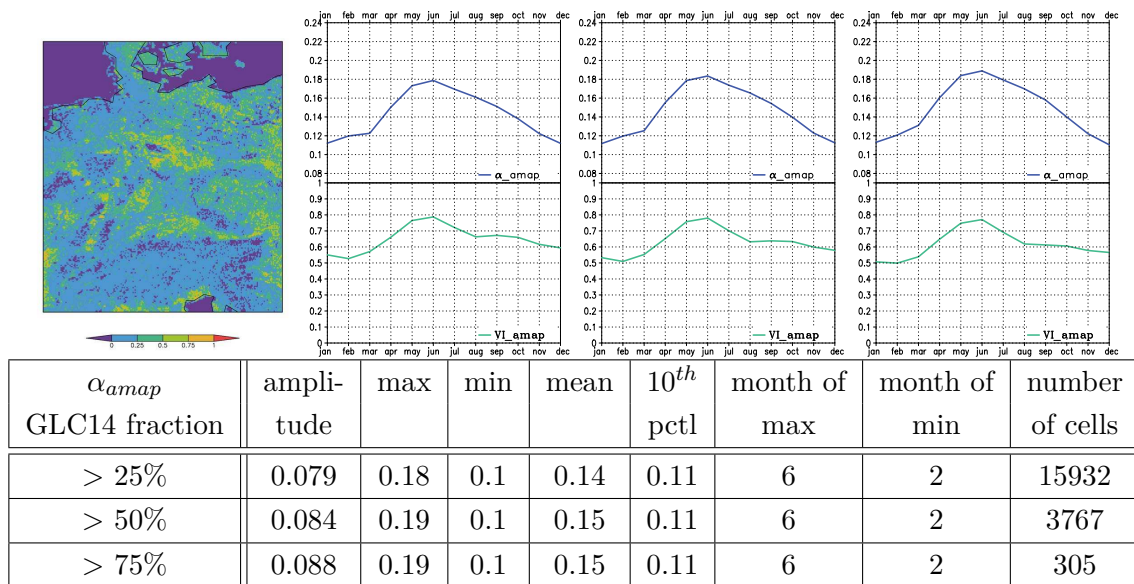


Figure 5.10.: Analysis for GLC14 - Rain-fed Crops. Top left: fraction in Central Europe, top middle to right: α_{amaap} (blue) and VI_{amaap} (green) annual cycles for fractions > 25%, > 50%, > 75%.

5. Albedo characteristics

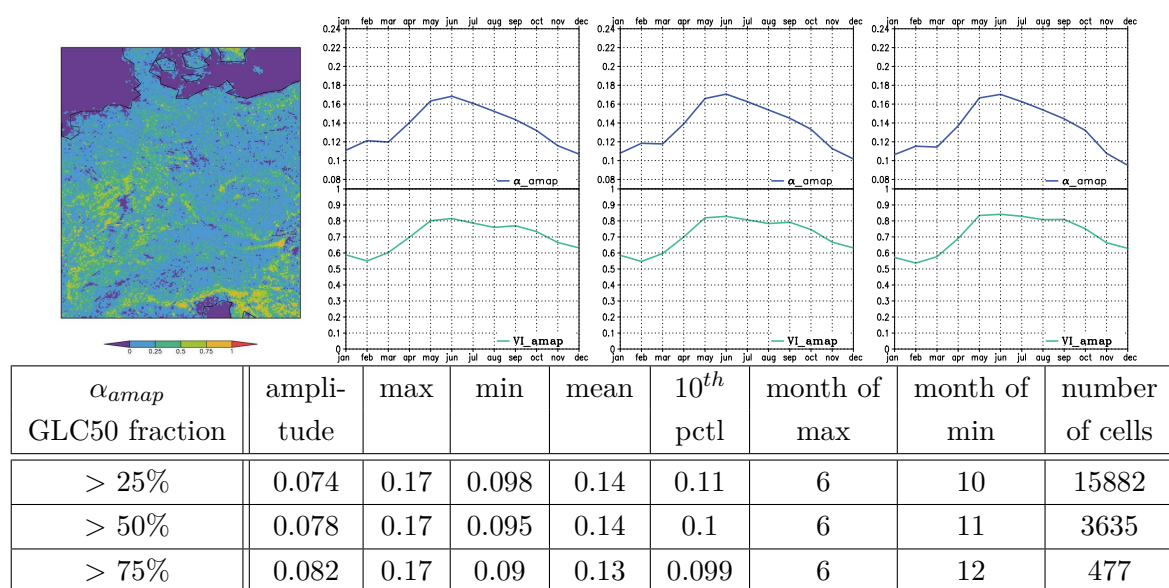


Figure 5.11.: As figure 5.10 but for GLC50.

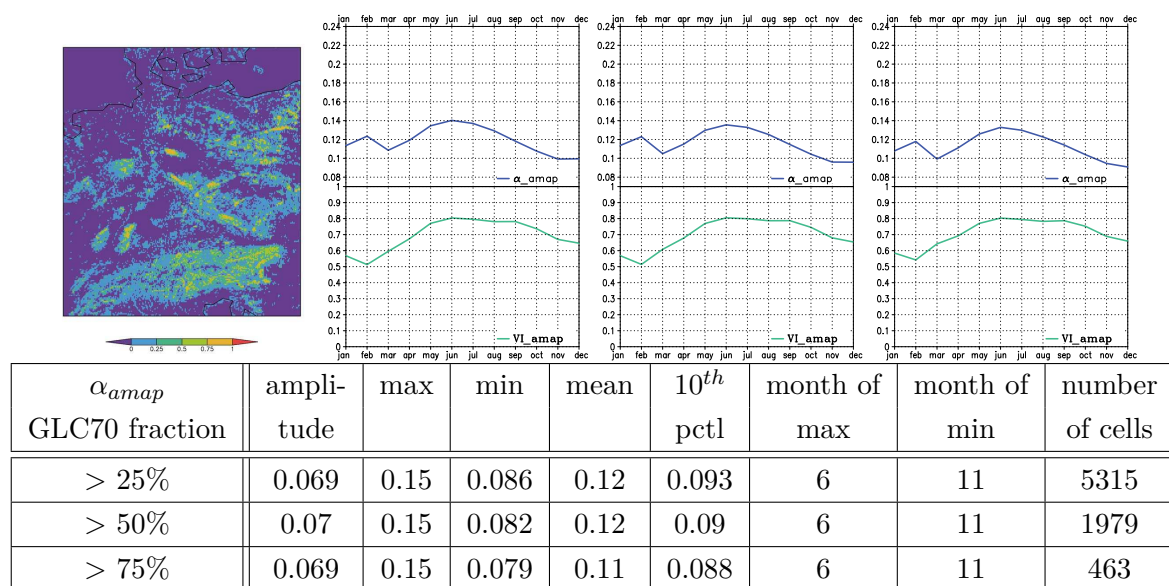


Figure 5.12.: As figure 5.10 but for GLC70.

5.2. Albedo characteristics for different fractional contributions to a grid box

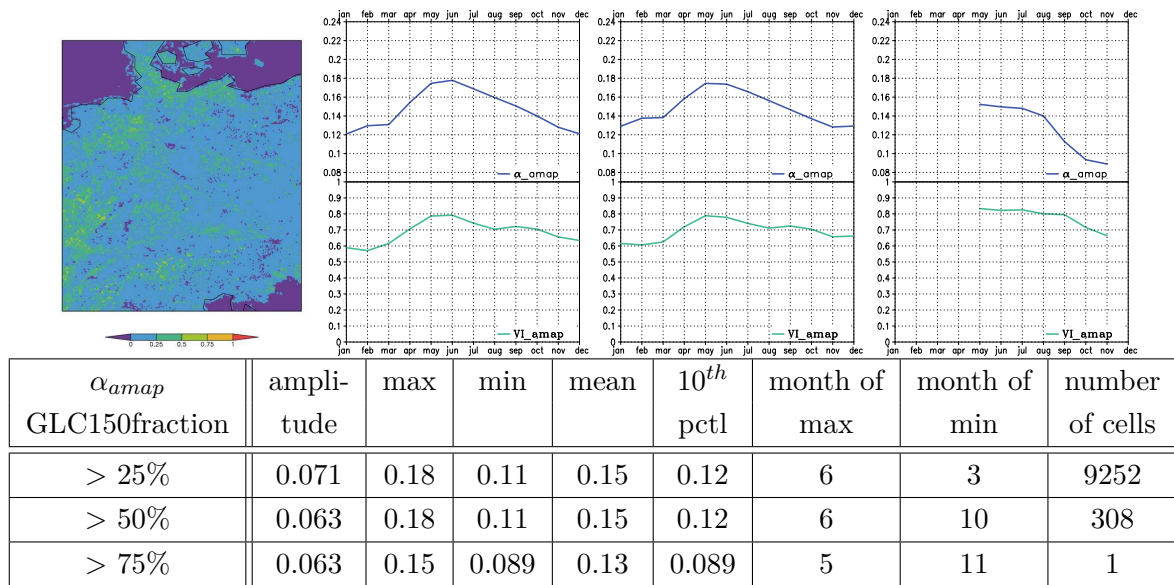


Figure 5.13.: As figure 5.10 but for GLC150.

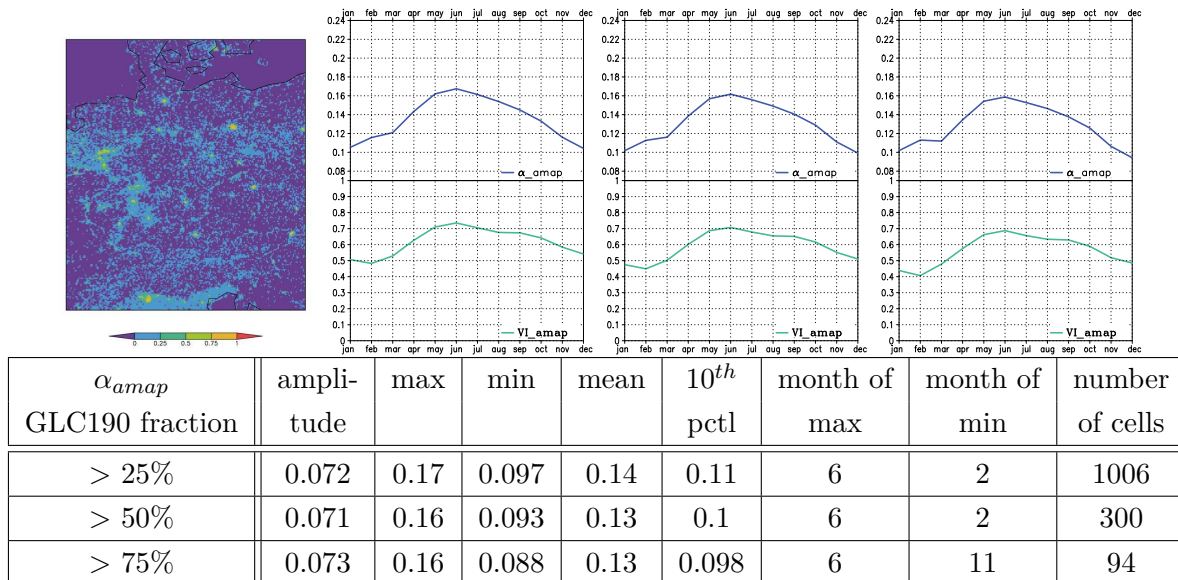


Figure 5.14.: As figure 5.10 but for GLC190.

5. Albedo characteristics

Table 5.1.: α_{amap} for Iberia, derived from at least 50% cover of each land cover class: close (c), open (o), close to open (c2o), mosaik (m), evergreen (eg).

GLC type	shortname	amplitude	max	min	mean	10 th pctl	month of max	month of min	number of cells
GLC 11	Irrigated Crop	0.068	0.21	0.14	0.18	0.15	7	11	266
GLC 14	Rain-fed Crop	0.078	0.21	0.13	0.17	0.14	7	11	3440
GLC 20	Cropland (m)	0.066	0.2	0.14	0.17	0.14	7	11	1191
GLC 30	Broadl. eg (c)	0.064	0.21	0.15	0.18	0.15	7	12	777
GLC 40	Broadl. eg (c2o)	-	-	-	-	-	-	-	0
GLC 50	Broadl. (c)	0.051	0.16	0.11	0.14	0.12	6	12	2758
GLC 60	Broadl. (o)	-	-	-	-	-	-	-	0
GLC 70	Needlel. (c)	0.042	0.14	0.1	0.12	0.1	7	11	1038
GLC 90	Needlel. (o)	0.042	0.14	0.095	0.12	0.1	6	12	30
GLC 100	Mixed Forest (c2o)	0.041	0.14	0.1	0.12	0.11	6	12	77
GLC 110	Forest/Shrub (m)	0.047	0.19	0.14	0.17	0.15	7	12	108
GLC 120	Grass (m)	0.049	0.19	0.14	0.16	0.14	8	12	1
GLC 130	Shrub (c2o)	0.045	0.16	0.11	0.14	0.12	7	11	1720
GLC 140	Herbaceous (c2o)	0.053	0.19	0.13	0.16	0.14	6	11	8
GLC 150	Sparse Veg.	0.057	0.22	0.16	0.19	0.16	7	11	5247
GLC 170	Shrub saline (c2o)	-	-	-	-	-	-	-	0
GLC 180	Grass Woody (c2o)	-	-	-	-	-	-	-	0
GLC 190	Artificial	0.045	0.18	0.14	0.16	0.14	7	11	138
GLC 200	Bare areas	0.059	0.31	0.25	0.28	0.26	8	12	222
GLC 210	Water	0.039	0.16	0.12	0.14	0.12	6	11	25599
GLC 220	Snow, Ice	-	-	-	-	-	-	-	0
GLC 230	No data	-	-	-	-	-	-	-	0

Table 5.2.: As table 5.1 but for Central Europe.

GLC type	shortname	amplitude	max	min	mean	10 th pctl	month of max	month of min	number of cells
GLC 11	Irrigated Crop	0.11	0.2	0.084	0.13	0.089	8	1	54
GLC 14	Rain-fed Crop	0.084	0.19	0.1	0.15	0.11	6	2	3767
GLC 20	Cropland (m)	0.088	0.18	0.097	0.14	0.11	6	1	441
GLC 30	Broadl. eg (c)	0.09	0.18	0.09	0.14	0.1	5	1	14
GLC 40	Broadl. eg (c2o)	-	-	-	-	-	-	-	0
GLC 50	Broadl. (c)	0.078	0.17	0.095	0.14	0.1	6	11	3635
GLC 60	Broadl. (o)	-	-	-	-	-	-	-	0
GLC 70	Needlel. (c)	0.07	0.15	0.082	0.12	0.09	6	11	1979
GLC 90	Needlel. (o)	0.047	0.13	0.087	0.11	0.096	6	3	4
GLC 100	Mixed Forest (c2o)	0.067	0.16	0.089	0.12	0.097	6	3	274
GLC 110	Forest/Shrub (m)	0.063	0.17	0.1	0.14	0.12	6	12	5
GLC 120	Grass (m)	0.1	0.19	0.089	0.14	0.095	6	1	2
GLC 130	Shrub (c2o)	-	-	-	-	-	-	-	0
GLC 140	Herbaceous (c2o)	0.069	0.19	0.12	0.16	0.13	6	2	744
GLC 150	Sparse Veg.	0.063	0.18	0.11	0.15	0.12	6	10	308
GLC 170	Shrub saline (c2o)	-	-	-	-	-	-	-	0
GLC 180	Grass Woody (c2o)	0.073	0.18	0.1	0.14	0.11	6	3	56
GLC 190	Artificial	0.071	0.16	0.093	0.13	0.1	6	2	300
GLC 200	Bare areas	0.04	0.14	0.1	0.12	0.1	6	10	42
GLC 210	Water	0.064	0.17	0.1	0.13	0.11	6	7	8440
GLC 220	Snow, Ice	0.04	0.14	0.1	0.12	0.1	6	10	85
GLC 230	No data	-	-	-	-	-	-	-	0

5.3. Verification by inversion

The climatologies for different land use classes can be distinguished, as shown in chapter 5.1. However, for specific land cover classes, the white sky broad band albedo of AMAP (α_{amap}) might not be unique for each land cover class. For verification it must be possible to localize the areas for one land cover class. If albedo characteristics are unique for specific land cover classes, this information can be used for land use change studies.

For the localization only two aspects are used: the amplitude and the absolute maximum of albedo. The inversion method is performed for the GLC2000, whereby 50% fraction to a grid box in 0.05° horizontal resolution are used as masks on the α_{amap} in 0.05° horizontal resolution.

First, a box-and-whisker diagram for the absolute maximum and the amplitude is plotted for each land cover class in both regions, in figure 5.15 for the Iberian Peninsula and in figure 5.16 for Central Europe. The upper part shows the box-plots of the absolute maximum of the annual cycle for some GLC2000 classes, whereby the box-plots for the amplitude is shown in each figure at the bottom. The coloured boxes are indicating the lower and upper quartiles (25th- and 75th-percentiles) for same land cover classes. The median is drawn as a dashed purple line and the whiskers extend to the most extreme data point within the extended interquartile range. The pixels used per box-plot are indicated in the tables of figures 5.5-5.14.

A specific range for the albedo maximum and albedo amplitude was chosen for each class for a successful localisation using so-called expert knowledge. The blue and lilac boxes in figures 5.15 and 5.16 assign the chosen ranges for inversion. For the inversion itself, a selection criterion is set: Grid boxes belong to a certain class if the amplitude and maximum of albedo cycle fit the chosen ranges as indicated in figures 5.15 and 5.16. If both conditions are fulfilled at the same time that grid box was assigned to the belonging land cover class.

As an example grid boxes of α_{amap} in the Iberian region with an absolute albedo maximum ranges between 0 and 0.15 (0 to 75thpctl) and an amplitude between 0.03 to 0.038 (25thpctl to 50thpctl) indicate Needle Leaf Forest for Iberia.

The distributions so found for each land cover class are then compared to the original distribution of the GLC2000- 50% fraction per 0.5° grid box.

The results of the inversion method and its comparison to the original distribution are shown for Iberia in figure 5.17 and for Central Europe in figure 5.18, where always the GLC2000 class on the left is opposed to the maskings on the reference AMAP albedo α_{amap} . For the Iberian Peninsula, the distribution of Rain-fed Crops (fig. 5.17: mask 14, top left), is well captured. Also the grid boxes with presumably Needle Leaf Forest (mask 70) are showing similar structures as the observed distribution of the GLC2000 map. The same holds for Sparse Vegetation (150). The distribution for Deciduous Forest (50) shows clearly more grid boxes with an albedo maximum between 0.15 to 0.16 and an amplitude between 0.037 to 0.061, but still has faint similarities to the observation. The Artificial (190) class seems to be overestimated.

The distributions after inversion for Central Europe show similar structural distributions for Rain-fed Crops (14) and Needle Leaf Forest (70) (fig. 5.18). Less similarities can be seen for Deciduous Forest (50), and with considerable inaccuracies but structural similarities for the Artificial (190) land cover class. However, the land cover class 'Sparse Vegetation (150)' is not captured well.

The ranges and conditions for this inversion method could be further developed to get more appropriate results. For example the month of maximum could be used as an additional criterion. For Needle Leaf Forest, the existence of a second peak in the annual cycle, as it can be observed for Central Europe in figure 5.4, could be a further criterion for that class.

Nevertheless the results of this inversion show that several criterion of an annual albedo cycle are able to characterize different land cover classes.

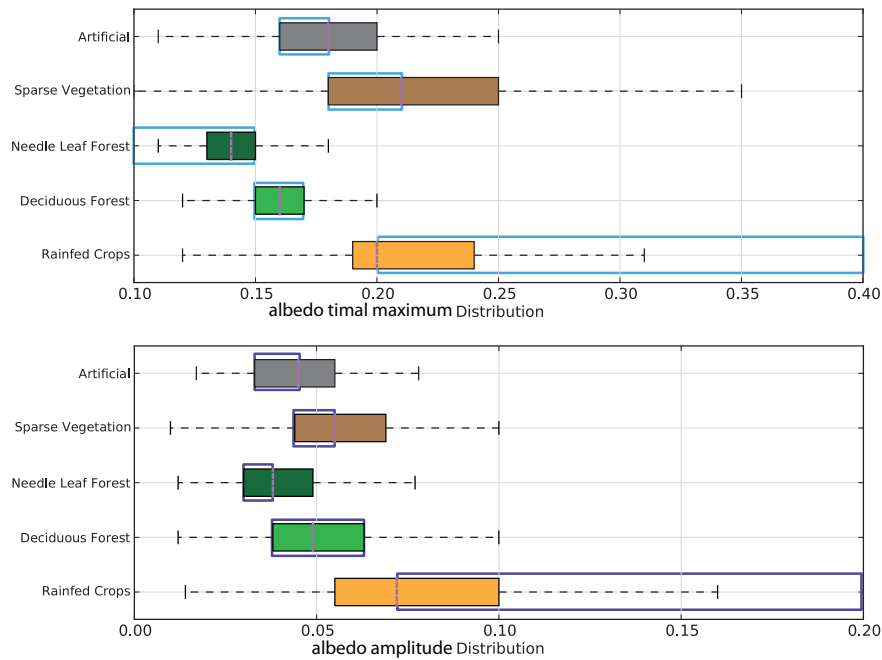


Figure 5.15.: Quartile plot of albedo parameters for some GLC2000 types in Iberia, blue and lilac boxes indicate ranges for inversion method; top: albedo amplitude, bottom: albedo maximum.

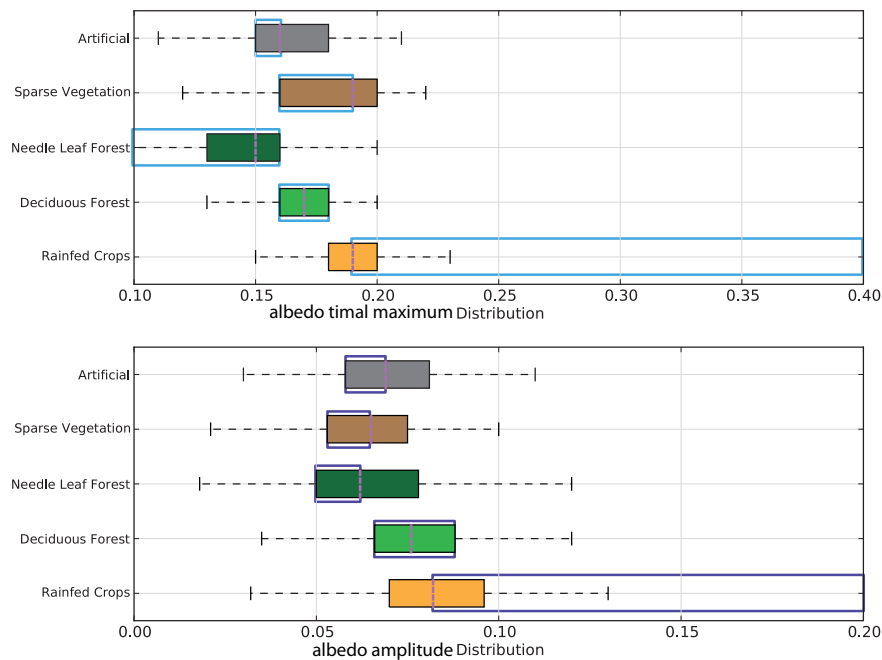


Figure 5.16.: As figure 5.15, but for Central Europe.

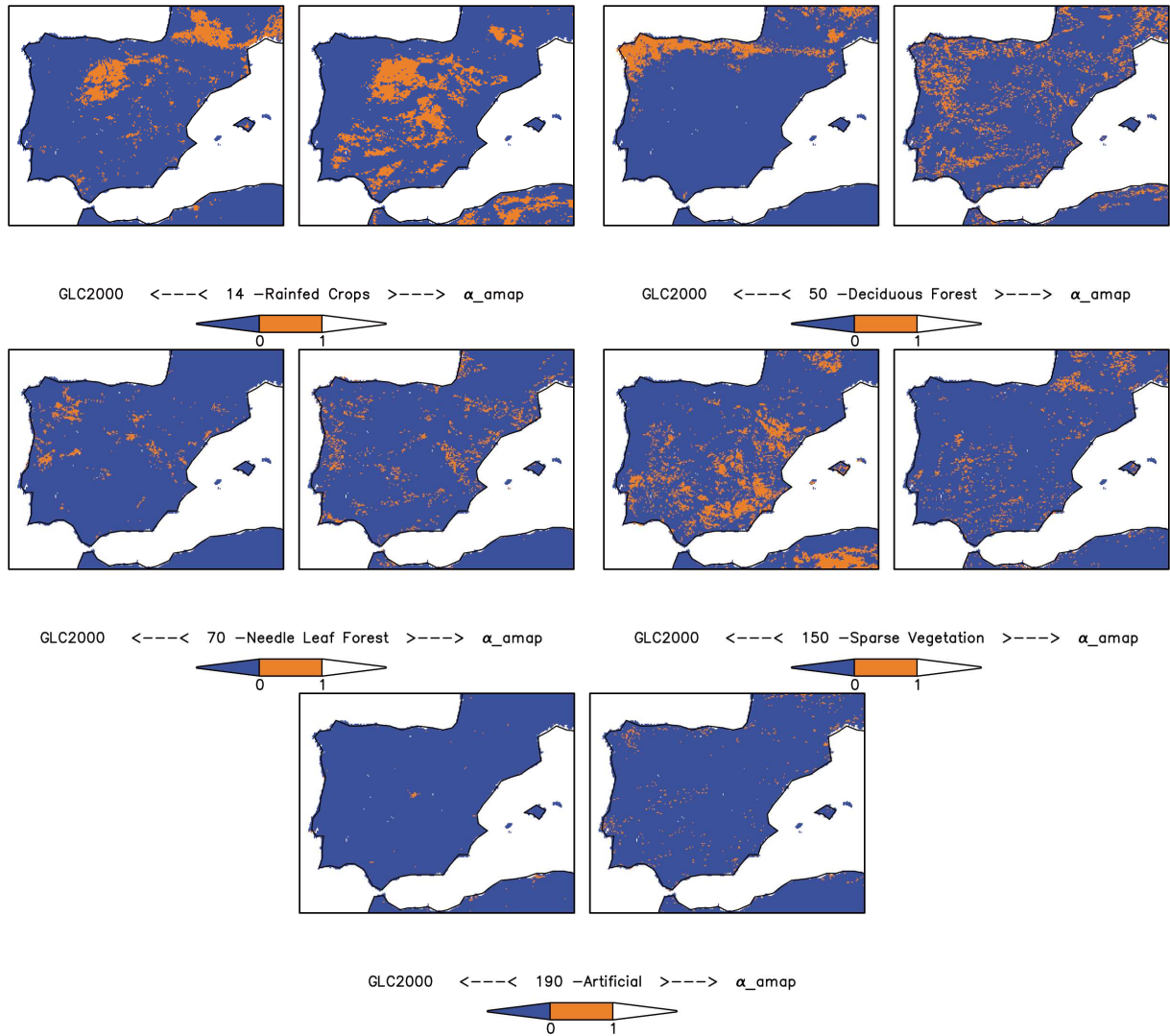


Figure 5.17.: Comparison of distributions for Iberia of 5 GLC2000-types for the >50% fraction per 0.05° grid box (left) to relocation by inversion method on α_{omap} (right).

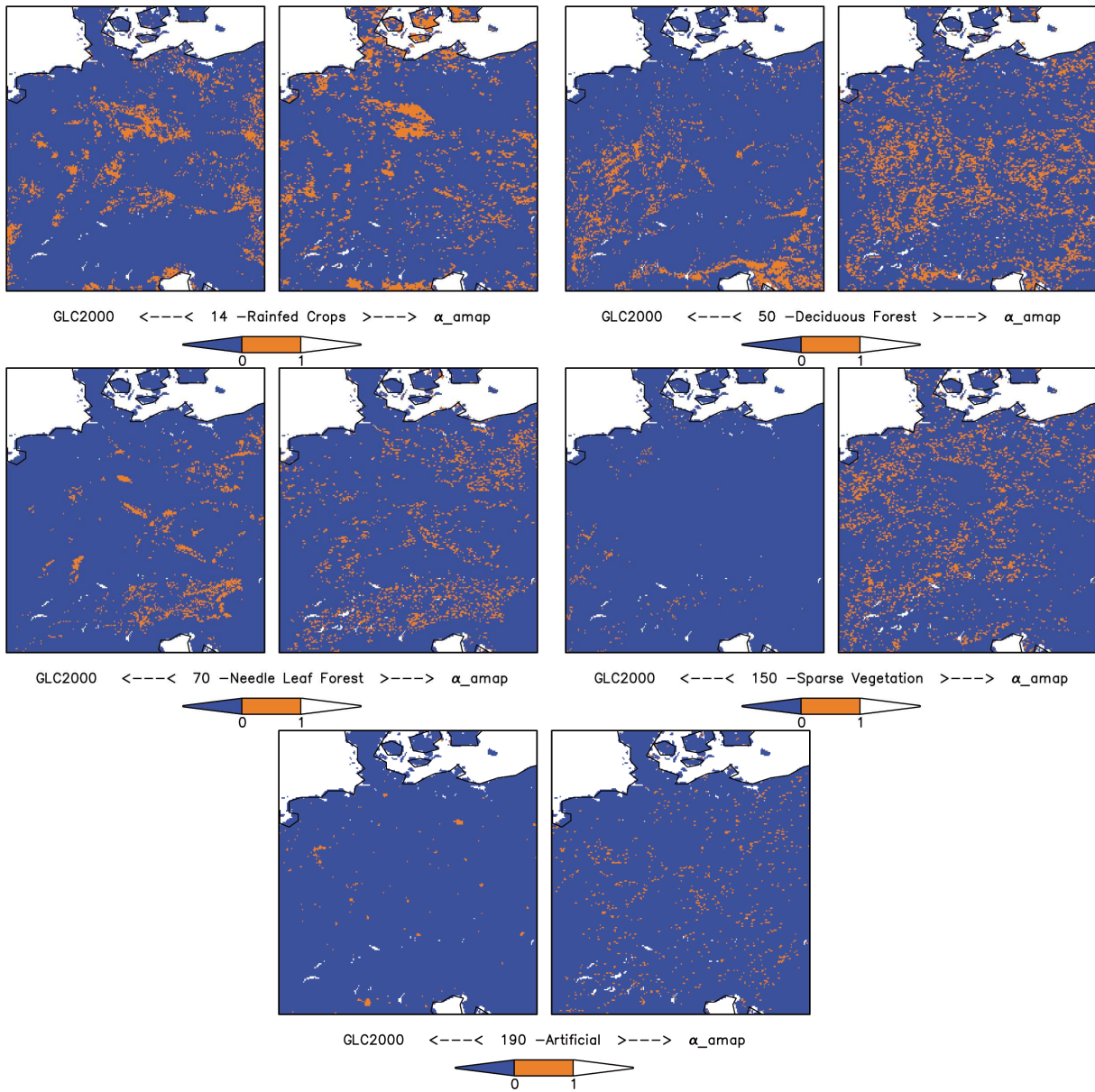


Figure 5.18.: As figure 5.17 but for Central Europe.

6. Albedo characteristics within the Surface Library for REMO (SL4R)

The albedo parameterization for a climate simulation must serve the needs of the scientific question of the climate simulation. Depending on the scientific question a surface albedo must not necessarily represent exact values or exact seasonal specifications. For climate scenario simulations searching for impacts of different greenhouse gas concentrations on climate, a simple seasonal albedo value is sufficient, as the regional specific radiative impact of the land surface is not the major topic. However, in case of land use change studies the albedo should be regionally as exact as possible. Especially the albedo differences for different land covers and the corresponding variability due to vegetation activity are important information. The heat balance in REMO is reacting on small changes in the radiation budget, as is already shown by Rechid and Jacob (2006).

Albedo differences for different land covers are often as small as the annual cycle of albedo. As an overview table 6.1 is presenting the standard deviation for white sky broad band albedo of AMAP (α_{amap}), MODIS albedo, following Rechid et al. (2008) (α_{modis}) and albedo from SL4R (α_{SL4R}) for Europe. The statistical variability in the albedo pattern does vary around 10% for all three data sets (column two). The third column is representing a threshold for a seasonal albedo variability. In both observation data sets, it is about 2%. The result for the parameterized albedo from SL4R is with 0.06% much smaller, almost by a factor of three.

The values for the observation data in table 6.1 are summarizing two issues. First, the seasonal variability is a small variable, of about 0.01 to 0.02 albedo percent points. Second, the variability in the horizontal pattern is by a factor of four to six higher, than the seasonal variability.

Table 6.1.: Standard deviation of albedo data sets for Europe.

	⊙ spatial deviation	⊙ temporal deviation
α_{amap}	0.093	0.021
α_{modis}	0.102	0.015
α_{SL4R}	0.086	0.006

Table 6.1 hints at some deficiencies of the SL4R albedo data set. Even though the horizontal variability is about 0.1, it has with 0.086 the lowest spatial albedo variability. The mean seasonal variability is extremely low, even under 1%. Within α_{SL4R} the spatial variability is by a factor of 14 higher than the temporal variability.

The main hypothesis for this work is that the current scheme of the Surface Library for REMO (SL4R) is not sufficiently accurate to represent the albedo characteristics for different land cover classes.

Therefore, some investigations on the limitations in the albedo representation of the current SL4R scheme will be part of this section.

The albedo α_{SL4R} for two horizontal resolutions (0.088° and 0.5°) is first compared to observed data. The α_{SL4R} data for 0.088° resolution are compared to the α_{amap} in 0.05° and the coarser resolution data are compared to α_{modis} in the same resolution.

6.1. Comparison of SL4R albedo to observation

Albedo amplitude

Comparing the albedo amplitude, an overall lower amplitude in the α_{SL4R} can be seen in figure 6.1 for both horizontal resolutions. The amplitude does not exceed values of 0.06. In the comparison of the two observation data sets the values are also not identical; nevertheless, the overall pattern of both observation data sets is similar. The horizontal patterns of the albedo amplitude for α_{amap} and α_{modis} are showing similarities, even in different resolution. A good coherency in pattern can be seen, especially for points with a large albedo amplitude in Spain and Turkey. A low albedo amplitude for the Alps is also common in both observations. Altogether both data sets show an increase of the albedo amplitude eastward. Also the decrease in the albedo amplitude from north to south for the north African coast is similar. Especially for the Mediterranean areas and also for central Europe, even details are captured well and show a very similar degree of amplitude variability in the observations. The green to orange spots on the Iberian Peninsula and Turkey are showing an albedo amplitude above 0.1. These spots are missing in the SL4R data. In contrary they show an amplitude of only 0.02.

The white parts in Northern Africa and Scandinavia for the SL4R data, especially in the resolution of 0.088° are indicating constant albedo values. Altogether, the annual cycle of albedo as input parameter for REMO does rarely exceed 0.08 for Europe. The parameterized albedo cycle is compressed.

The loss in temporal variability in α_{SL4R} can be attributed to this mismatch in albedo amplitude.

Albedo phase

Having a look onto the time of appearance of the albedo maximum in figure 6.2 and its minimum in figure 6.3 for α_{SL4R} 0.088° , α_{amap} 0.05° , α_{SL4R} 0.5° α_{modis} 0.5° reveals major differences as well.

Similarities between the parameterized albedo values and the observed ones are rare in details. Comparing both observation data sets MODIS and AMAP on the right side (these plots are already shown in section 4.1), albedo maximum and minimum appear mostly in the same month, in contrast to α_{SL4R} .

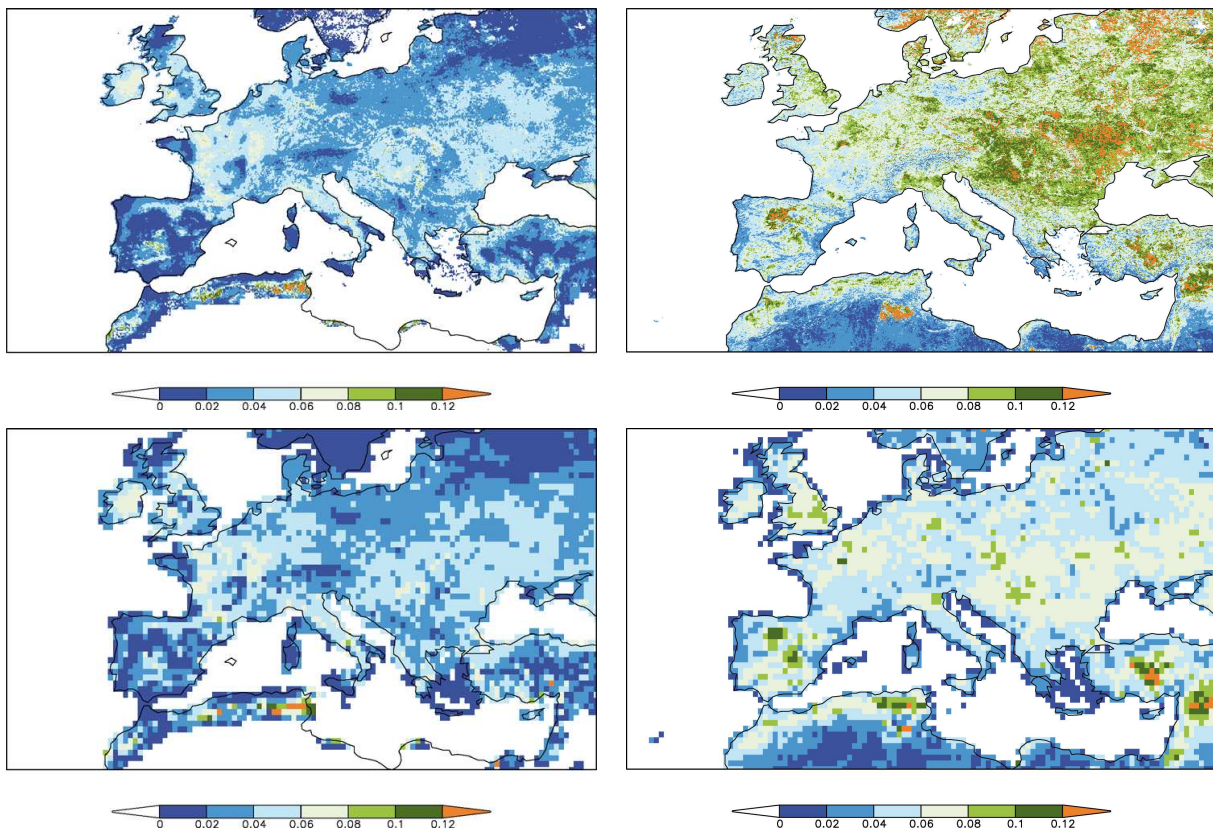


Figure 6.1.: Comparison of the albedo amplitude: α_{SL4R} in 0.088° (upper left), α_{SL4R} in 0.5° (bottom left), α_{omap} 0.05° (upper right), α_{modis} 0.5° (bottom right).

The albedo maximum of SL4R occurs mainly in July (coloured in orange). Nearly every part in Europe shows the same time for the albedo maximum, besides parts of the Mediterranean region. The summer month are also dominating in the observations, but here structured differences occur, which are about one to three month.

The albedo minimum, shown in figure 6.3, demonstrate also only some coherence between observation and SL4R.

Albedo level of absolute minimum

The absolute albedo minimum is a measure of maximum absorbed solar energy. At low albedo more solar energy is absorbed leading to an increase in surface skin temperature. To capture realistic albedo conditions for land use change studies, the minimum albedo level is important. It is also indicator of autochthonous conditions determined by the typical floral, pedological and cultural composition.

The albedo minimum for α_{SL4R} is higher than α_{omap} and α_{modis} for Central and Easter Europe,

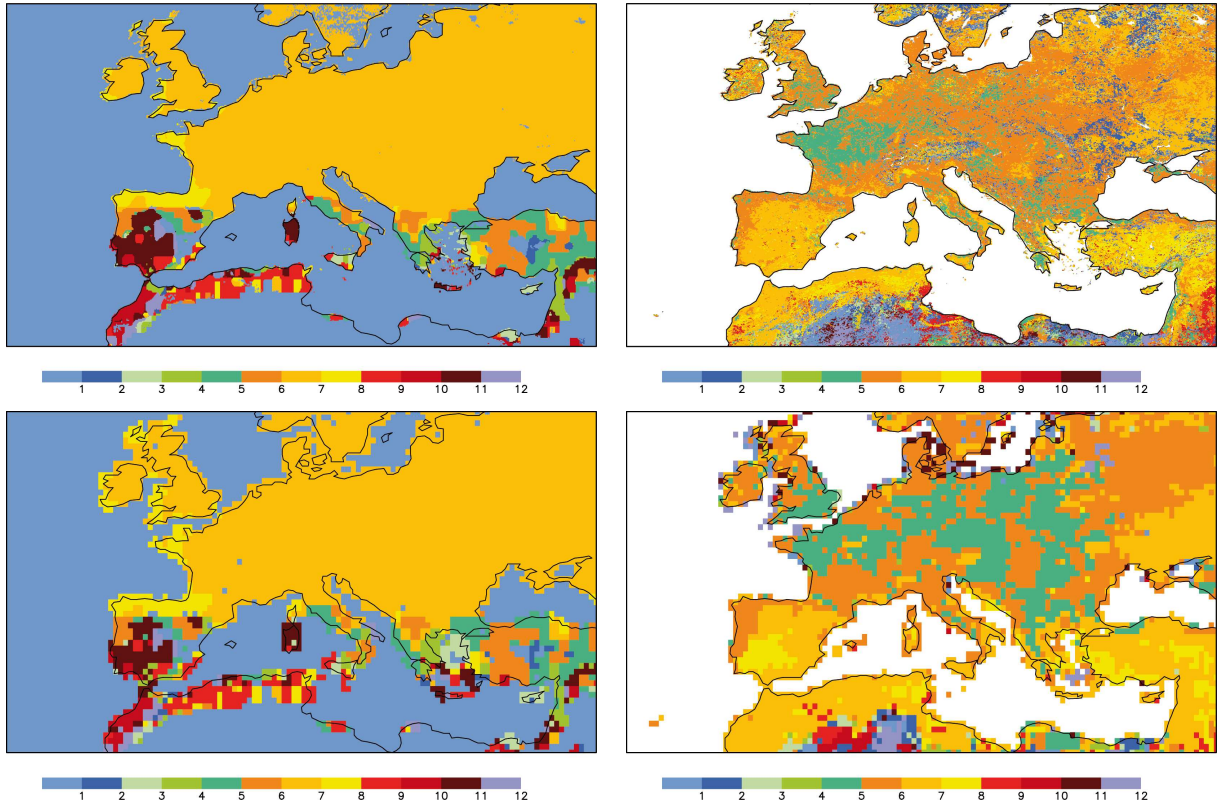


Figure 6.2.: Month with albedo maximum. α_{SLAR} in 0.088° resolution (top left), α_{SLAR} in 0.5° (bottom left), α_{amap} 0.05° (top right), α_{modis} 0.5° (bottom right). [Jan=1,...,Dec=12], colours are attached to seasons: bluish (DFJ), greenish (MAM), yellowish (JJA), reddish (SON).

see figure 6.4. The albedo minimum derived from satellite observations are for Eastern Europe mainly between 0.04 to 0.12. For α_{SLAR} the minimum albedo for Eastern Europe is often > 0.12 , whereby the differences to observation are on average 6% which is as large as the amplitude of the α_{SLAR} annual cycle (compare figure 6.1, left).

The lowest albedo values of α_{SLAR} occur for water and are set to 0.06. In α_{SLAR} an albedo lower than 0.06 can occur on land coincidentally by using equation (2.3). The lowest albedo values over land of MODIS and AMAP are 0.04. Figure 6.4 (right) shows nicely that the lowest observed albedo values occur in areas in the north of the Black Sea. This matches with the distribution of Chernozem (black soil), whereby Kondratyev et al. (1981) are reporting of albedo values of 4% for ploughed Chernozem.

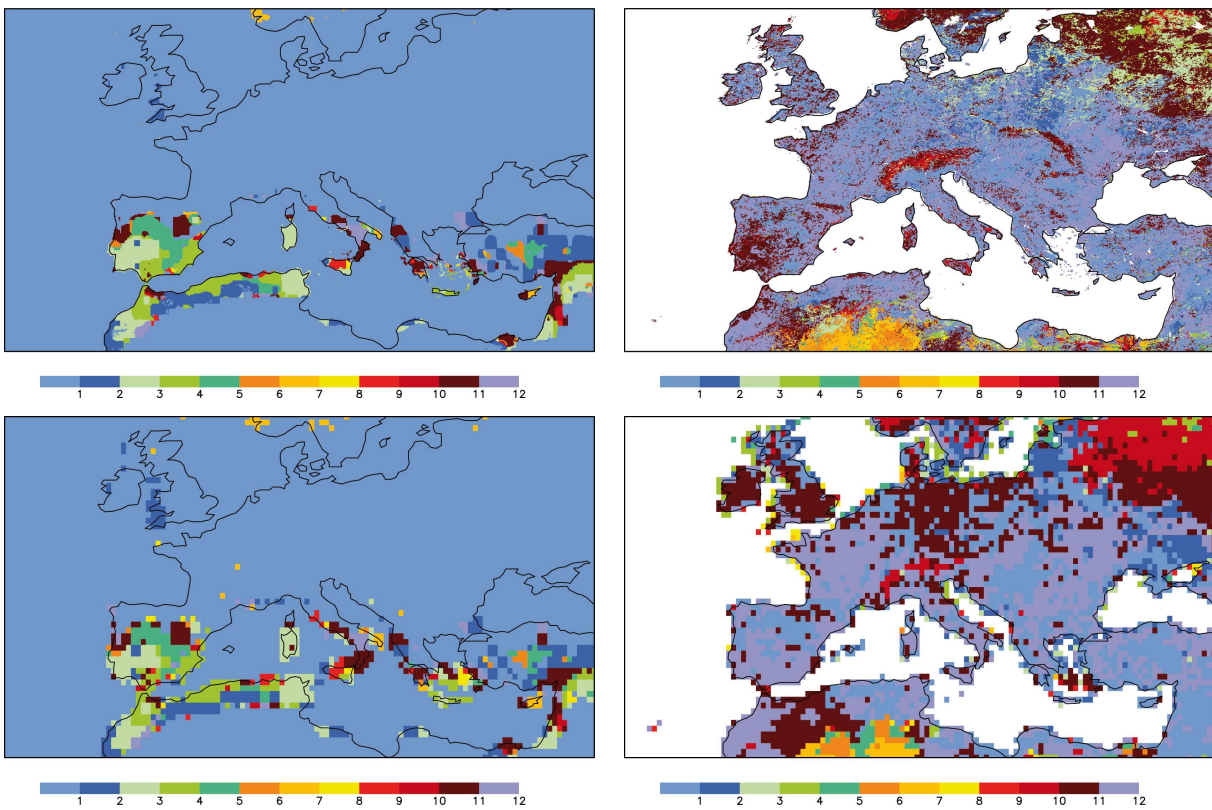


Figure 6.3.: Same as figure 6.2 but appearance of the albedo minimum.

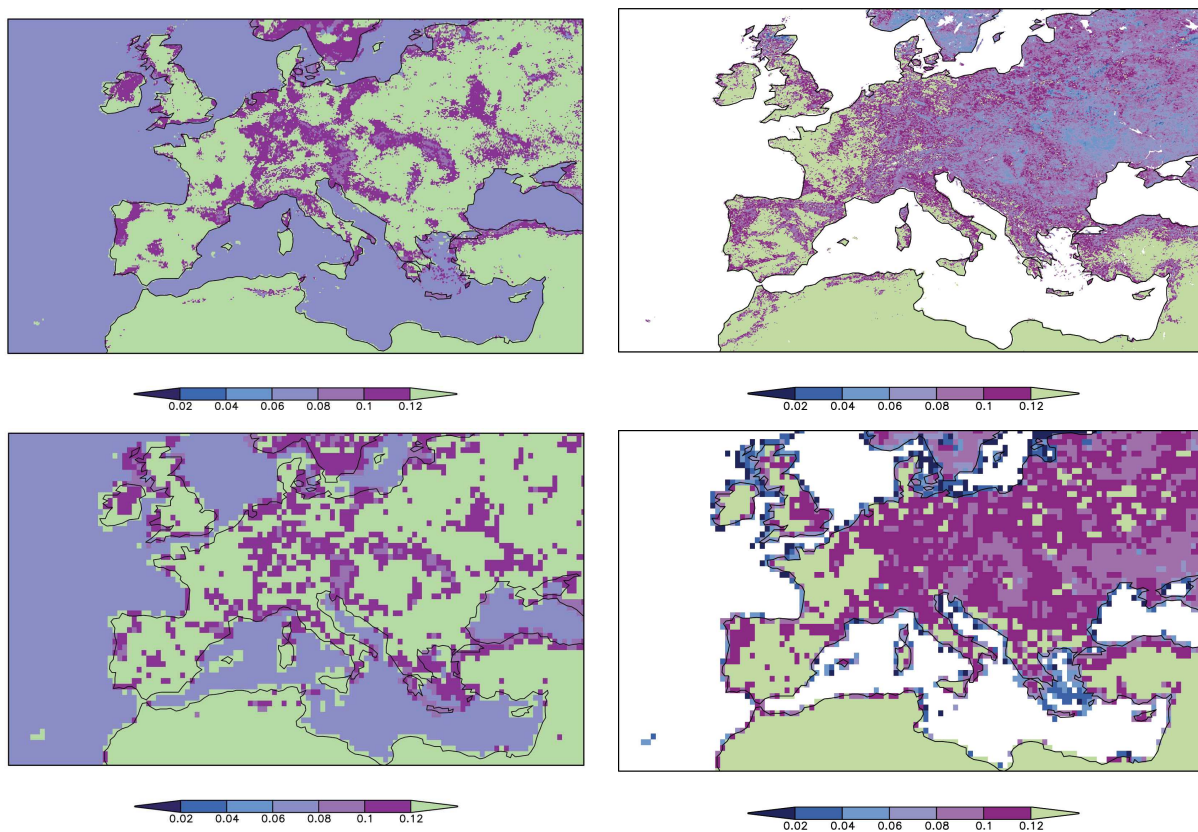


Figure 6.4.: Albedo minimum of α_{SLAR} in 0.088° resolution (upper left), α_{SLAR} in 0.5° resolution (bottom left), α_{amap} 0.05° resolution (upper right) and for α_{modis} 0.5° resolution (bottom right).

6.2. Limitations for the use of SL4R albedo for land use change studies

These limitations are a combination of problems at different levels, resulting in errors when using the SL4R data for land use change studies. Mixtures of data sets, assumptions and parameterizations led to an over-parameterization. This mixture of issues hinders an easy elimination of a certain problematic. Of course, some uncertainty sources can not be avoided, as they are directly linked to the data. In any case, caution is necessary when interpreting of regional vegetation effects on regional climate. Regional in this case can be defined as an area of about 1000 km² to 100,000 km², which is roughly the size of a large city up to the size of Bavaria together with Baden-Wuerttemberg, or e.g. Iceland.

Following the demonstration of the construction scheme in figure 2.7, the table 6.2 lists four levels of uncertainty sources. It also points out, how the chance is seen to reduce that source of uncertainty.

Table 6.2.: Levels and combination of uncertainties

Level	main source of uncertainty	chance
1	subjectivity and arbitrariness of parameter allocation	unavoidable but minimizable
2	blurring, levelling and stretching through interpolation	unavoidable but minimizable
3	rough assumptions for parameterization	avoidable
4	unwanted changes through rearrangement and arbitrary combination of fixed parameters	must be eliminated especially in case of land use change studies

Level one:

This source of uncertainty can be expected by the allocation of parameters to any horizontal land cover distribution information. A validation is hardly possible, but the hypothetical character is described in section 2.3. The subjective adaptation through expert knowledge of the LSP II parameter allocations is also mentioned in Hagemann et al. (1999); Hagemann (2002), and is explained further in appendix A. It is hard to judge which is a good or a correct allocation for a ecosystem class. As an example for errors in allocation table 6.3 compares the Global Ecosystem Types (GET) land surface class Coniferous Forest to the class Conifer Forest.

The values for GET3 and GET27 in table 6.3 seem arbitrary. While looking into the definition for these types in Olson (1994), there is no hint for defining the above parameters.

GET3 (Coniferous Forest) is defined as: “Conifer evergreen forest is here narrowed to areas where Hemlock is locally dominant or widely codominant along with any other conifers.”

GET27 (Conifer Forest) is defined as: “Conifer Forest with little or no snow includes needle-leaf

Table 6.3.: Parameter Values used by Hagemann (2002) - excerpt (For the explanation of the parameters please see section 2.2).

Type	GET Legend	α_s	$z_{0,veg}$	cv_g	cv_d	LAI_g	LAI_d	c_f	W_{ava}	f_{pwp}
3	Coniferous Forest	0.13	1	0.96	0.95	9.2	9.0	0.9	130	0.41
27	Conifer Forest	0.13	1	0.87	0.31	9.7	4.4	0.84	250	0.49

types of mild (oceanic)-to-warm temperate or tropical zones. Trees can use sunlight in all or most month, while metabolism of preceding types is constrained by cold tops or roots, even when winter sunlight might be absorbed by needles.”

GET3 occurs rarely in high latitudes of North America. GET27 occurs around the Gulf of Mexico and in Europe at the Atlantic coast of the Pyrenees. In this case it is unclear, why the Leaf Area Index LAI of GET27 in moderate climates should shrink drastically from 9.7 to 4 in the dormancy season and influence thereby the annual albedo cycle, in contrast to an almost constant LAI for Hemlock dominated coniferous forest areas of higher latitudes.

To minimize the first level of subjectivity and arbitrariness, a detailed look for each region needs do be done. It does not make sense just to adapt values from a table. For every region, it can be checked whether the horizontal distribution of the data does make sense. Corrections of that issue can take a high technical effort. Still the problematic of subjectivity of expert knowledge would remain, and could hardly be validated.

Level two:

One or several remappings are leading to a horizontal blurring. Remapping can cause a levelling of the values, as well as lead to a statistically induced elevation. Remapping must be used for upscaling or downscaling input data, applying different statistical interpolation algorithms, see Jones (1998, 1999).

Very common is so-called conservative remapping keeping e.g. radiation fluxes constant. By using this remapping from a coarser to finer a grid, it can produce very strong but wrong gradients. As it is an area weighted method, the original horizontal pattern of the coarse resolution basically remains. Distance weighted remapping, takes the n nearest neighbours of a point into account. The algorithm for finding the nearest neighbours is based on angular distances.

Figure 6.5 demonstrates the blurring, levelling and elevation effects just due to consecutive interpolation. Shown are the original albedo amplitude of the α_{amap} annual cycle on the upper left. The original data on 0.05° horizontal resolution were conservatively remapped onto a 0.5° grid (not shown). Afterwards it was remapped back to 0.05° horizontal resolution by a distant-weighted method. In the upper right, the horizontal pattern after two consecutive remapping steps, shows homogeneous, clustered patterns. Obvious is a strong increase of the annual albedo amplitude in

the north eastern part. The bottom of figure 6.5 shows the difference in the albedo amplitude. On average the amplitude is lowered by at least 1%. The extreme increase of the albedo amplitude in the north eastern part, is no mistake. Especially the distance weighted method is reacting on the spread of pixels with an annual albedo amplitude higher than 0.12 there.

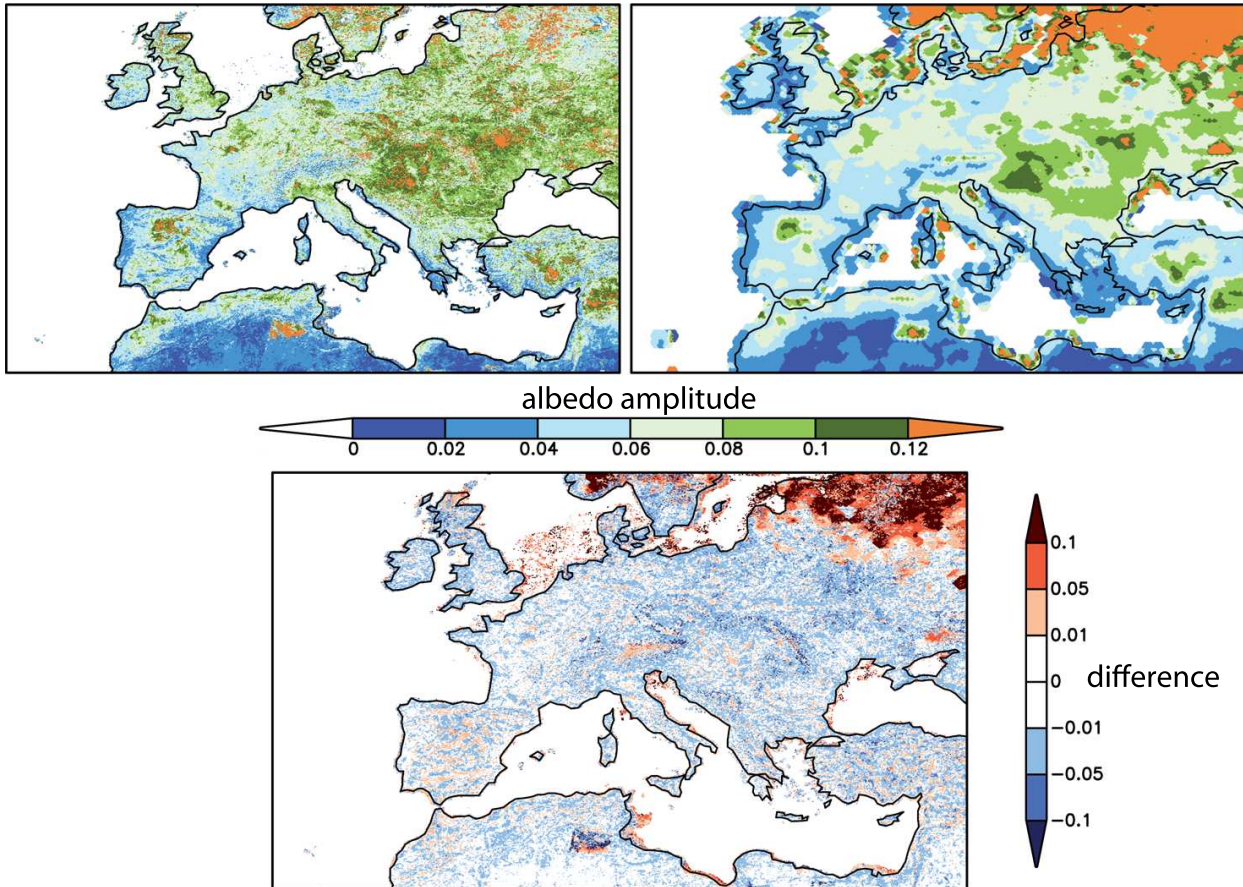


Figure 6.5.: Amplitude and difference of α_{amap} after consecutive remapping. Amplitude original at 0.05° resolution (left), upscaled to 0.5° by conservative remapping, and back to 0.05° horizontal resolution by distance-weighted remapping (right). Bottom: difference of albedo amplitude (remapped-original). No land sea mask is used for this plot to cover observed data over water. The satellite observation over water detects islands, drilling platforms, ship traffic and so on. Remapping methods applied on sparsely distributed grid boxes produces false information. The same methodological effect leads to an enormous albedo amplitude increase for the North-Eastern Region.

Within the soil library, as shown in figure 2.7 interpolations are also applied for the allocations of every ecosystem type as well as for the growing factor and the albedo data. For the derivation of the annual albedo cycle, four interpolation steps are needed, if the target resolution is not in 0.5° resolution (if needed, the interpolation includes also a rotation):

1. The parameters for GET classes at 1 km horizontal resolution parameters are upscaled to the target resolution as mean fraction.

6. Albedo characteristics within the Surface Library for REMO (SLAR)

2. The growing factor is downscaled from 0.5° to target resolution (conservatively remapped).
3. The MODIS albedo and FPAR data sets for receiving the albedo-weights α_{veg} and α_{soil} are upscaled from 0.05° to 0.5° resolution (conservatively remapped).
4. The albedo-weights in 0.5° resolution onto target resolution (interpolated by a distance weighting method).

It is obvious that the subjectively allocated parameter LAI, upscaled to target resolution in combination with a downscaled annual cycle is hardly able to pinpoint an annual cycle of albedo.

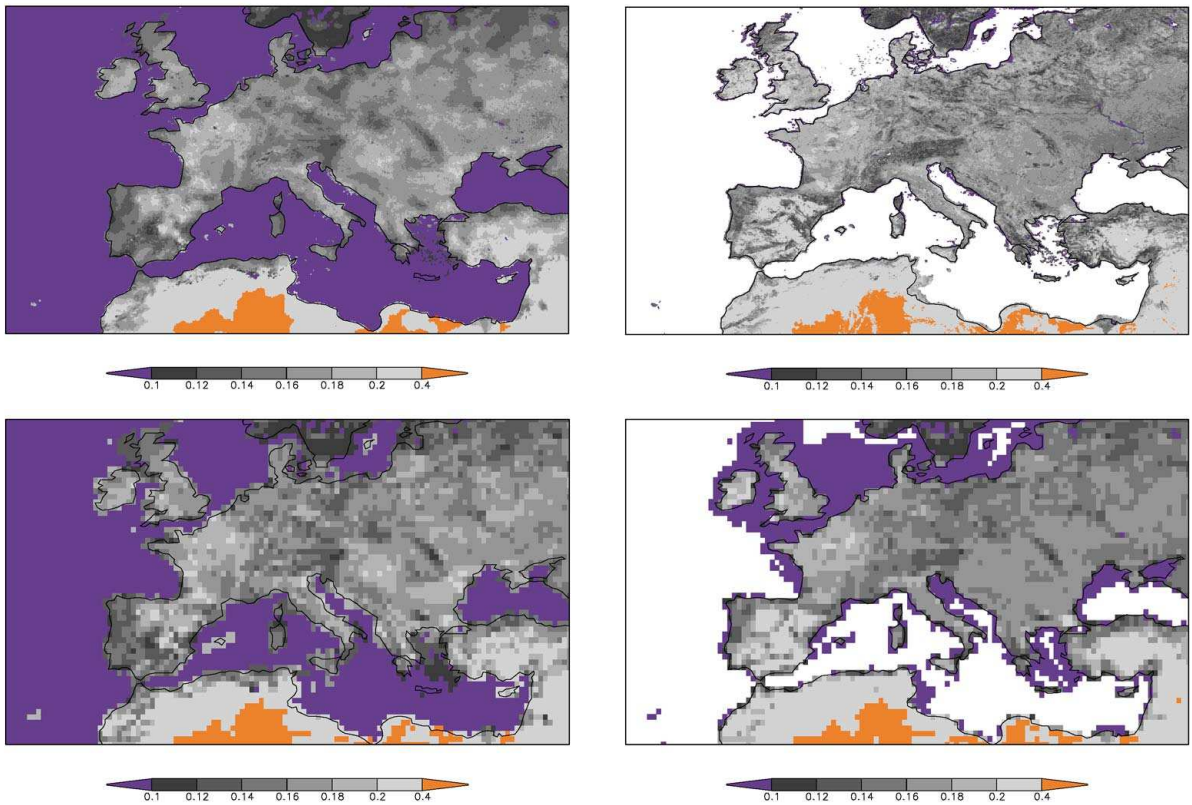


Figure 6.6.: Albedo pattern comparison for the monthly mean of July. On the left side for α_{SLAR} in 0.088° resolution (upper left) and α_{SLAR} in 0.5° resolution (bottom left), satellite observations on the right for α_{omap} 0.05° resolution (upper right) and α_{modis} 0.5° resolution (bottom right).

The blurring of the pattern of α_{SLAR} is shown in figure 6.6 for the month of July. The left part is showing the monthly mean of July for the α_{SLAR} in two resolutions. In the upper part α_{SLAR88} for 0.088° , and the bottom part α_{SLAR5} for 0.5° resolution. It is compared to AMAP α_{omap} in 0.05° and MODIS α_{modis} in 0.5° resolution for July.

Comparing the modelled albedo to the observed albedo, the pattern of the July albedo does not look too bad. However, details are important, for regional aspects, and there are several disagreements.

Looking to the Iberian Peninsula the fine darker stripes are visible in both observations. α_{modis} does also distinguish the Rhone river valley, separating the Massif Central from the Alps, as well as the Rhine Graben with its prominent darker edges of Black Forest and Vosges. The Alps appear identical as a continuous dark stripe for the July albedo mean in both observation data sets. Comparing α_{modis} in 0.5° to α_{SLAR} in 0.5° on the bottom part, the Iberian Peninsula does show a concentration of low albedo in the centre, instead of the three stripes. The south of Portugal and south of Spain re all darker. The Rhone river valley and the Rhine Graben can be distinguished, but the Alps appear in the form of a slightly opened mouth with a brighter spot in its centre.

The blurring through interpolation can be seen well in the top left of figure 6.6 for α_{SLAR} in 0.088° horizontal resolution. The pattern follows exactly the pattern of α_{SLAR} 0.5° (left bottom) and looks as if the coarse one got treated with a smoothing filter. Altogether the horizontal pattern of α_{SLAR} in 0.088° follows strictly the pattern of the 0.5° resolution. This mismatch of α_{SLAR} can be seen in all months, but it is not shown here.

Even if some major patterns can be relocated, it is insufficient for a detailed, regional analysis of albedo effects.

Level three:

The third level comprises the usage of empirical parameterizations. Starting with the phase of the vegetation cycle, it is the growing factor which is controlling the changes in albedo, the vegetation ratio and the Leaf Area Index in the parameterization.

Phase Mismatch due to Growing Factor:

The Growing factor is a product of a combination of two completely different input data sets, and one is not necessarily describing a phenology. The temperature data set was used to account for temperature limited phenology, and for the lack of *fapar* observations for higher latitudes. Within $\pm 40^\circ$ latitude the phenological information of photosynthetic activity is used directly. Water limitation or lack of sunlight are here indirectly involved. Using the temperature curve only for higher latitudes, does not account for water limitation or lack of sunlight.

Missmatch of phase and amplitude due to the assumption of linear relationship between albedo and vegetation

The loss in the absolute maximum and minimum can be attributed to the albedo-weights of the regression method, in combination with the annual LAI cycle. The α_{SLAR} albedo maximum and minimum are depending on the combination of LAI and the given albedo-weights, α_{veg} and α_{soil} , due to the formula for calculating the albedo cycle (equation 6.3.2:

$$\alpha_{SLAR} = \alpha_{veg}(1 - e^{-0.5*LAI}) + (e^{-0.5*LAI})\alpha_{soil}.$$

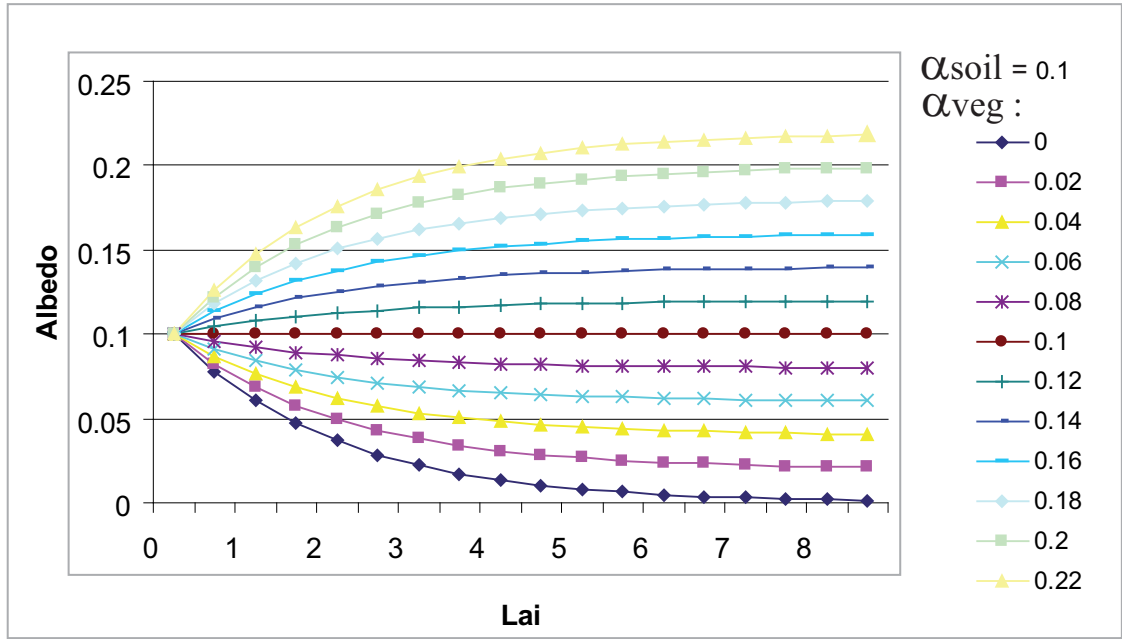


Figure 6.7.: Albedo due to LAI changes following equation 6.3.2 for different α_{veg} -values but fixed $\alpha_{soil}=0.1$.

In the albedo parameterization α_{veg} is the dominant factor for LAI values above 4. For LAI < 4, α_{soil} is dominating in equation 2.3. This can be seen in figure 6.7. For fixed $\alpha_{soil}=0.1$, the possible albedo values for different α_{veg} values, in dependence on the LAI is shown. It helps to derive some essential for the formula given above:

1. the annual cycle of α_{SLAR} is constant, if $\alpha_{veg}=\alpha_{soil}$
2. the annual cycle of α_{SLAR} is nearly constant for LAI>4
3. the annual cycle of α_{SLAR} has a convex annual cycle if $\alpha_{veg}>\alpha_{soil}$
4. the annual cycle of α_{SLAR} has a concave cycle if $\alpha_{veg}<\alpha_{soil}$
5. α_{SLAR} -maximum is a product of the α_{veg} , α_{soil} , LAI combination
6. α_{SLAR} -minimum is a product of the α_{veg} , α_{soil} , LAI combination

In case, the formula would be correct for describing the natural development of the annual cycle of albedo, it is still very unlikely that the exact needed values for α_{veg} , α_{soil} and LAI can be described in the SL4R. As described above in level one and two, the input data sets are already quite uncertain.

Concerning the mismatches in the annual cycle of albedo, another problematic is connected to the same formula. In order to derive the albedo compounds α_{veg} and α_{soil} as weighting factors in the albedo parameterization in the SL4R (albedo-weights), a linear relationship between the annual cycle of albedo and vegetation activity is assumed.

This is contrasting results of a regression of the AMAP data for α_{amap} with the vegetation index VI_{amap} , applied for data pairs over a time period of three years in a 16d mean time interval. In

appendix C, the full results of this regression are shown and discussed. Figure 6.8 summarizes the information of appendix C, by marking in orange grid boxes where a linear correlation may be assumed. In those grid boxes the p-value is lower than 0.05, and, the absolute correlation coefficient $|r_{xy}|$ minus the standard error (se) is > 0.8 . The subtraction of the standard error helps to avoid border cases, for example, cases where the correlation coefficient are exact 0.8. With those conditions, the orange grid boxes indicate where a linear equation is able to reproduce at least 60% of the observed data - but time independent. The correlation coefficient does not take into account a time dependency of the data pairs.

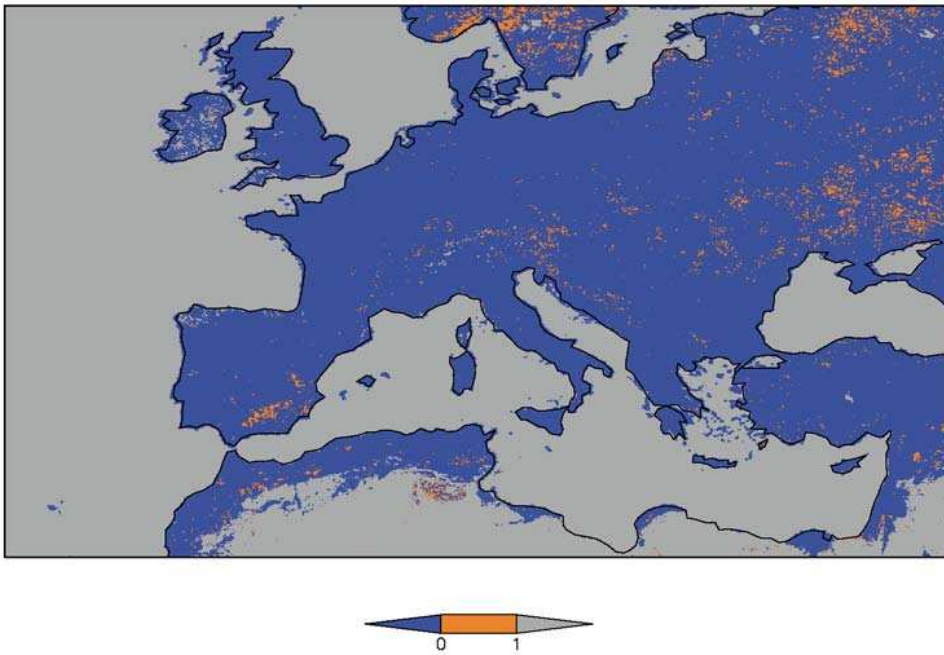


Figure 6.8.: Validity of regression of α_{amaP} to VI_{amaP} for Europe (see appendix C); orange grid boxes: $|r| - se \geq 0.8 \wedge p \leq 0.05$.

Figure 6.8 in numbers:

- total number of grid boxes: 347 950
- number of grid boxes with $|r| - se \geq 0.8 \wedge p \leq 0.05$: 1 239
- fraction of these grid boxes to total grid boxes in percent: 3.56%

Hence, for parts of Europe and North Africa, only for 3.56% of the land cover the interaction of albedo and vegetation cycles can be described with a linear model. If one allows a moderate correlation with $|r| - se \geq 0.5$ a linear model could be used for 36% of the land surface, which is demonstrated in figure 6.9. Please note that a correlation coefficient $0.5 \leq |r| \leq 0.8$ is hardly indicating linear correlations, as discussed in appendix C .

The results show that a linear dependence of AMAP to VI_{amaP} is rare - therefore, it should not be

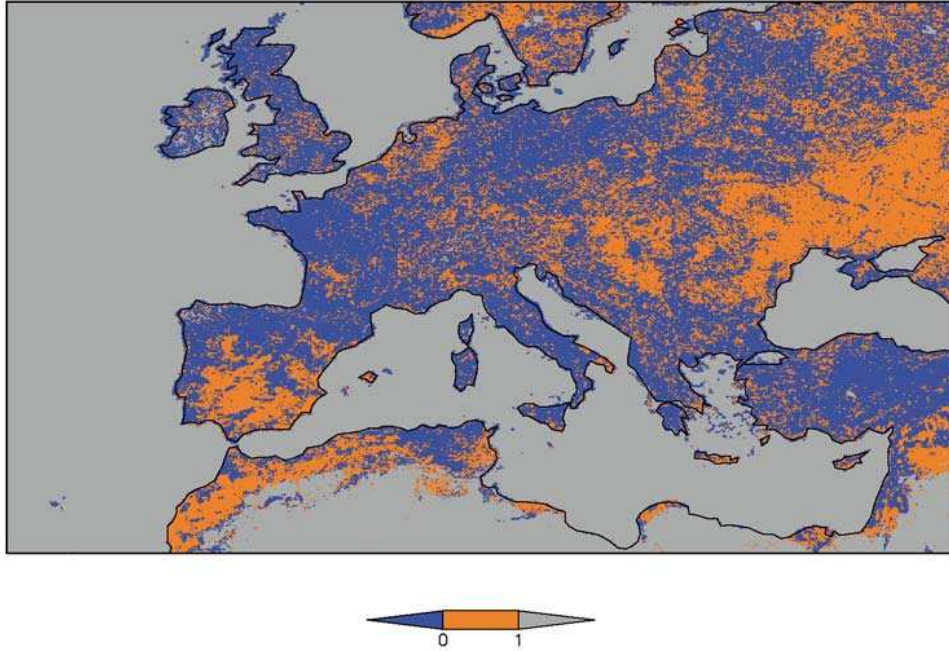


Figure 6.9.: Same as figure 6.8 but orange grid boxes: $|r| - se \geq 0.5 \wedge p \leq 0.05$.

used for a parameterization method. This is the most severe point, and implicates that the idea of using the regression to separate α_{soil} and α_{veg} is questionable.

The used interpretation of the separated parts, one part with active vegetation and one part for non-active vegetation, seems to be not correct for the further issue: the connection to vegetation induced annual cycle. It was a result of an parameterization adaptation due to the observation that the annual albedo cycle is not convex shaped for all regions, especially for parts of Africa, and the Iberian Peninsula (Rechid et al., 2008, 2009). It was suggested that in dry, sparsely vegetated regions, the bare soil fraction is much brighter, than in humid, full vegetated areas with a high humus content. The explanation was that the albedo of bright soils is by vegetation, and for dark soils, vegetation is elevating the albedo. Annual cycle observations of albedo could be interpreted in this sense. Looking at the same time to the development of the vegetation activity, this explanation is not sufficient. As already shown in the figures 5.5 to 5.14, the mean vegetation index variations does not have the same, opposite or any other dependence on the annual cycle of the broadband albedo. Albedo variations are not only depending on vegetation activity. Furthermore the moisture content and even the roughness (e.g. by ploughing) of a surface is influencing the surface albedo in the same amount as observed annual albedo variations (e.g., Kondratyev et al., 1981; Kraus, 1988; von Storch et al., 1999).

The connection of the annual cycle of LAI to the annual cycle of the albedo is a further severe point of critic. As the LAI is a biomass translation of $fapar$ and the $fapar$ correlates to VI_{amap}

(see section 3.2), it can be assumed that the annual cycle for an LAI would be exactly in phase to the VI_{amap} .

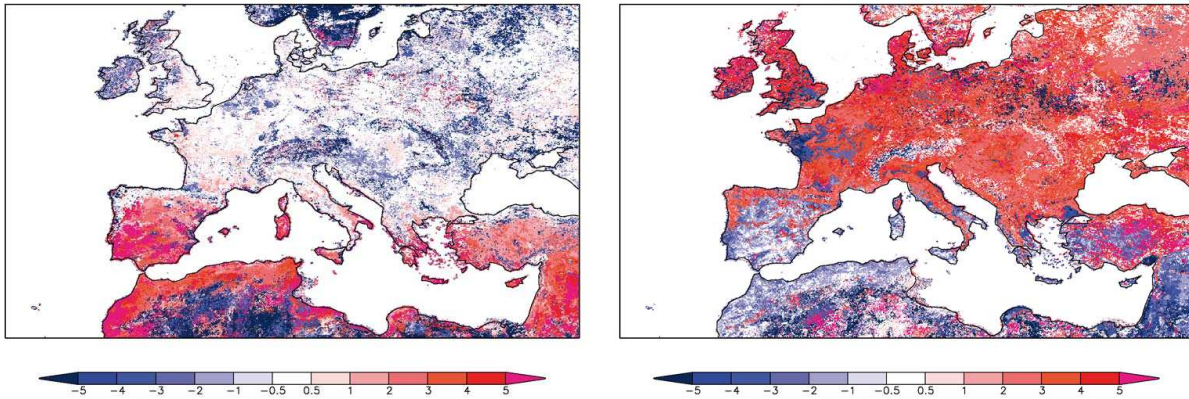


Figure 6.10.: Differences in month of appearance for: α_{amap} maximum versus VI_{amap} maximum (left), α_{amap} maximum versus VI_{amap} minimum (right).

Figure 6.10 shows in white grid boxes, where the monthly albedo cycle is in phase to the vegetation cycle (left), or exactly off phase (right). Positive shifts in month are indicated in shades of red, negative shifts are shown in shades of blue. Although joint maxima exist they are quite rare. Not shown here is that the coexistence of minima is extremely rare as well as the joint appearance of an albedo minimum to a vegetation activity maximum. Over all, the shapes of the annual cycles for broadband albedo and vegetation activity do not match.

To mention here is another point for the unreliable usage of slope and intercept of the regression as surface albedo values with active (α_{veg}) or non-active vegetation (α_{soil}). A linear regression may produce negative values for the y-intercept and slope, as shown in figure C.5 and discussed in appendix C. Negative values did also occur in Rechid et al. (2008), but were excluded.

Level four:

In case of land use change studies, unwanted changes through rearrangement and combination of parameters can be produced. The problematic is again connects to the parameterization of the albedo with equation: $\alpha = \alpha_{veg}(1 - e^{-k*LAI}) + (e^{-k*LAI})\alpha_{soil}$. (equation 6.3.2)

The albedo-weights (α_{veg} , α_{soil}) are fixed maps. Also the growing factor f_i is a fixed map, and is used for the calculation of the LAI cycle. Albedo changes due to land use changes can be taken into account also by changing the LAI, which is given as a maximum and minimum value for each GET, and the horizontal distribution of the GET are again fixed maps.

In a thought experiment, one would like to know the influence of a change in vegetation cover of Coniferous Forest into Conifer Forest and vice versa. The allocation for these two ecosystem classes is already mentioned in table 6.3. Following this table, one could think it is the easiest

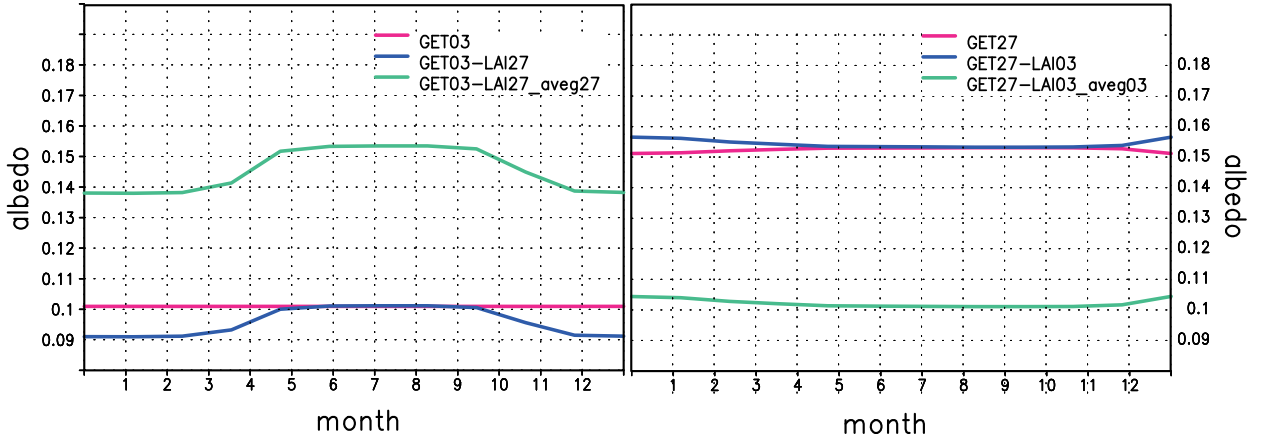


Figure 6.11.: Visualization of uncertainty caused by combination of vegetation class parameters. Left: original for GET_03 in pink, GET_03 with LAI from GET_27 in blue and GET_03 with LAI from GET_27 and additionally with α_{veg} of GET_27 in green. Right side same but vice versa.

to relocate the parameters of GET_03 to GET_27 and vice versa - (and early land use change experiments just exchanged parameters in the LSPII table (see section 6.3.2). The annual albedo cycle for one class would then be calculated with its own growing factor and albedo-weights (α_{soil} , α_{veg}), but would get attributed the LAI_d and LAI_g from the other class. This “production of unwanted changes” is demonstrated in table 6.4 with its visualization in figure 6.11 as examples for the uncertainty caused by a wrong combination.

Table 6.4.: Combination table used for albedo parameterization in figure 6.11. Original combination for land surface classes for GET_03 and GET_27, and two possible land use changes as examples for an uncertainty source originating from a wrong combination.

	LAI_g	LAI_d	α_{soil}	α_{veg}
GET_03	9.2	9.0	0.0979	0.101
GET_27	9.7	4.4	0.0981	0.153
GET_03 with LAI_27	9.7	4.4	0.0979	0.101
GET_27 with LAI_03	9.2	9.0	0.0981	0.153
GET_03 with LAI_27 and α_{veg_27}	9.2	9.0	0.0979	0.153
GET_27 with LAI_27 and α_{veg_27}	9.7	4.4	0.0981	0.101

The with equation 6.3.2 received annual cycle of albedo for the parameters of GET_03 and GET_27 is coloured in magenta. If we want to replace GET_03 by GET_27 or vice versa, it cannot simply be replaced, due to the connection of three independent data sets: Growing Factor (f_i), α_{veg} , α_{soil} . For this plot the α_{soil} , α_{veg} and f_i were carried out by using masks of the GET classes. The values are not exact, because the 0.5° maps got regridded on a 0.05° grid to make it conform with a fractional GET distribution in 0.05° . Anyway, if we just replace the allocated parameters LAI_g and LAI_d for GET_03, with the one for GET_27, and keep the growing factor and both albedo-weights

fixed, we get blue curves. For GET_27 the annual LAI cycle is so high that the addition of the factor α_{soil} transforms the annual albedo cycle to a slightly concave curve instead of an expected convex-shaped one.

To counteract those mismatches one solution is an adapted α_{veg} parameter. This method has e.g. been used in Galos (2010). Adapting α_{veg} and keeping α_{soil} fixed, without adapting the fixed maps of f_i , α_{soil} and α_{veg} , might lead to even larger discrepancies, as it is sketched in figure 6.11. On the other hand, figure 6.12 is visualizing the effect of an unadapted α_{soil} . Changing only α_{veg} and transfer the information as given in table 6.4, the green curves result either elevating or lowering the albedo by about 5%! It is still a question, how to adapt α_{veg} and α_{soil} reasonably.

So far it was not mentioned that influences of land surface changes with according changes in waterholding capacity and roughness length are not investigated for REMO yet. Even though many experiments on the influence of the lower boundary on the model simulations were conducted, still the interaction of the allocated parameters and the model are neither fully traceable nor clear (e.g., Rechid and Jacob, 2006; Göttel et al., 2008; Preuschmann and Jacob, 2008; Paeth et al., 2009; Galos, 2010; Preuschmann and Jacob, 2010).

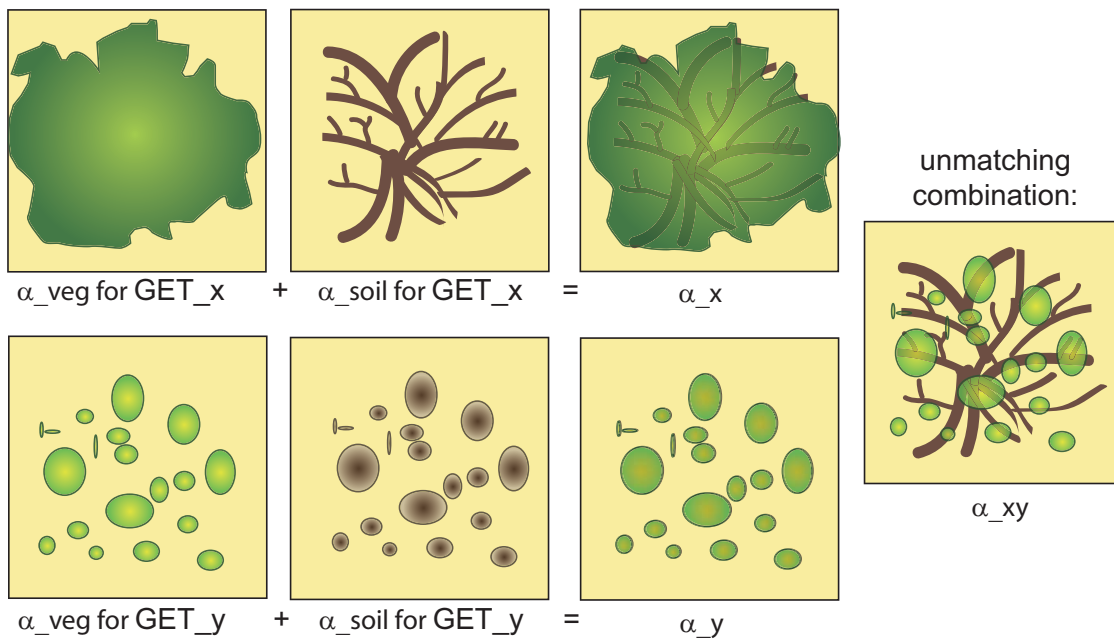


Figure 6.12.: Principle of unwanted albedo change, due to unchanged α_{soil} α_{veg} .

One might think, it should be no problem to allocate the right parameters to the GET and in case of a change in horizontal pattern for one GET the entire information for this vegetation class would be transferred. But what is the “right” parameter, and how could we be sure, if we allocate one that it is globally valid? What ever we do, the whole construction for the albedo parameterization is already extremely sophisticated. Moreover, as demonstrated, the uncertainty can be higher than the real annual albedo cycle.

6.3. Sensitivity studies with REMO for several albedo characteristics

This subchapter investigates the impact of changed albedo characteristics on model output for the regional climate model REMO.

6.3.1. REMO with α_{SLAR} and α_{amap_1}

For this sensitivity study a reference simulation is compared to a simulation with a changed albedo based on satellite observations.

REMO with a horizontal resolution of 0.22° is forced with lateral boundary conditions from the European Centre for Medium Range Weather Forecasts reanalysis (ERA40) (Uppala et al., 2005). Two five year simulation were performed, each with an identical annual albedo cycle composed of monthly means for each simulation year. For the reference simulation α_{SLAR} was used. For the other simulation α_{SLAR} replaced by α_{amap_1} .

For the derivation of α_{amap_1} , there was only a preliminary masking for snow and clouds was used which did not contain the additional condition allowing bright surfaces, if snow can be neglected, as described in chapter 3.3.1. Therefore, this masking excluded all very bright areas in the product version of 16d means for 2003-2005, which is then transformed into an annual cycle and conservatively remapped from 0.05° to 0.22° horizontal resolution. By this procedure most missing data gaps were filled, Remaining missing values were filled by a time interpolation and still remaining missing values (mainly North Africa) were filled by mean albedo values, derived from α_{SLAR} . The albedo over water is also identical to α_{SLAR} .

The simulations are denoted as:

1. REMO_{SLAR}: with monthly mean annual cycle of α_{SLAR}
2. REMO_{amap}: with monthly mean annual cycle of α_{amap_1}

Annual albedo cycle: Amplitude

Almost in every grid box the difference in the albedo amplitude ($\alpha_{amap_1} - \alpha_{SLAR}$) is larger than 1%, shown in figure 6.13. For many regions the amplitude increased by more than 5%, and for some grid boxes the albedo amplitude increased even by 10%, which can be seen on the Iberian Peninsula, North Africa, Turkey and for Scandinavia. The unchanged grid boxes in North Africa appear as continuous white areas. The white area in France however is not related to the missing value exchange procedure.

The mean albedo amplitude over land in the α_{amap_1} annual cycle is about 3.2% (figure 6.14). The mean albedo amplitude from the α_{SLAR} is about 1.8%, indicating a strong underestimation albedo variation.

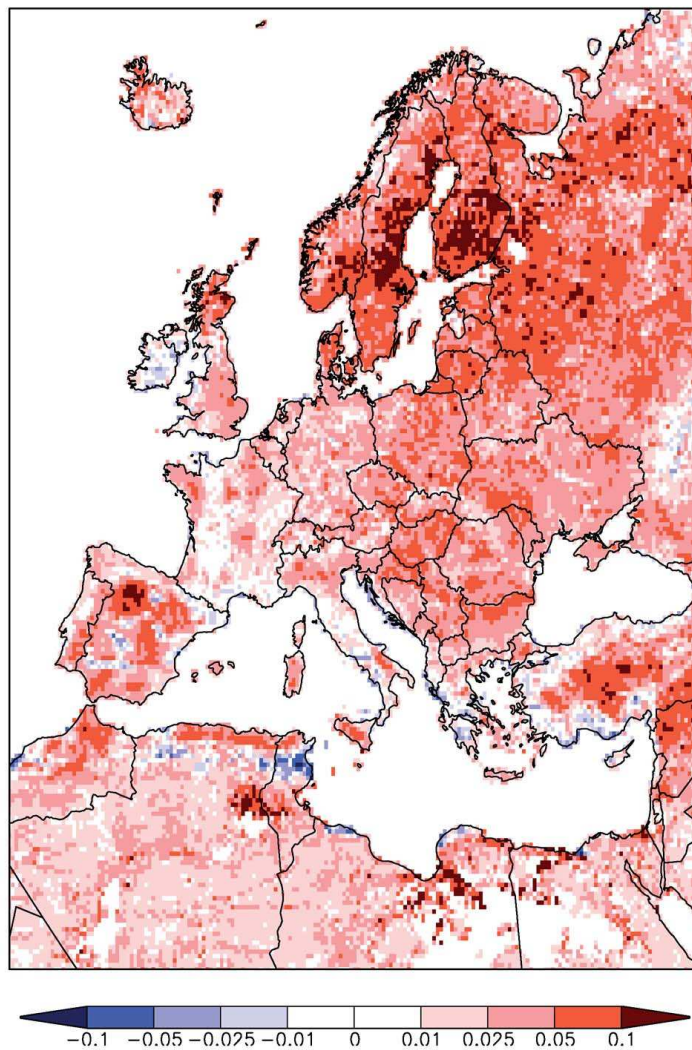


Figure 6.13.: Difference in albedo amplitude: $\alpha_{amap_1} - \alpha_{SLAR}$.

Annual albedo cycle: Phase

The spatial distribution of the month with albedo maxima and minima is shown in figure 6.15. For both simulations, the albedo maximum (top) occurs during the summer months. Compared to α_{SLAR} , the shift for central Europe in α_{amap_1} is about one month. Only for the Mediterranean regions, the differences higher than three month exist. The albedo maximum for the south-western part of the Iberian Peninsula is reached in July for α_{amap_1} , whereas for α_{SLAR} the albedo maximum occurs in November to January.

This is in direct contrast to the albedo minimum for α_{amap_1} , which is reached in the south-western part of the Iberian Peninsula in the winter season, whereas the albedo minimum of α_{SLAR} lies in the spring months. For $REMO_{amap}$ (6.15 bottom left) most grid boxes show an albedo minimum of α_{amap_1} in November and December. This leads to a maximal difference in the mean albedo of

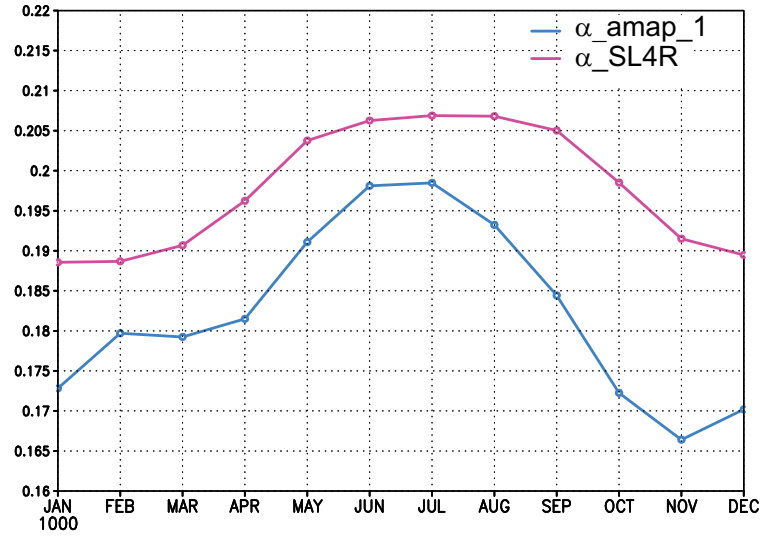


Figure 6.14.: Annual albedo cycle over land for simulation domain of $REMO_{SLAR}$ and $REMO_{amaap}$. Blue: annual cycle of α_{amaap_1} , pink: annual cycle of α_{SLAR} .

about 2.5% for November, in the mean albedo cycles shown in figure 6.14.

Albedo minimum

Dominating is a lowering in the albedo minimum level, shown in figure 6.16. Especially for eastern and north eastern Europe, lower albedo minimum exists for α_{amaap_1} . Referring to figure 6.4 the minimum in α_{SLAR} is always ≥ 0.12 . For α_{amaap_1} the minimum level for the eastern European region is as low as 0.06 or even lower, which is realistic in respect to Chernozem and needle leaf forest covers. As a large area is affected by this difference, it has major consequences for the energy budget. This lowering of the albedo minimum is also causing the shift in the level of the annual albedo cycles, already shown in figure 6.14.

Radiative perturbation

The radiative perturbation, a posterior calculation, shows differences in the energy regime due to background albedo changes under the assumption of a typical amount of incoming solar radiation and excluding snow. The radiative perturbation is calculated by using the global radiation G_{001524} and equation 4.1 of section 4.2:

$$R_{pert} = G_{001524}(\alpha_{amaap_1} - \alpha_{SLAR}) \quad (6.1)$$

The radiative perturbation for all four seasons is shown in figure 6.17. The albedo differences over large areas of Libya and Egypt are causing an energy loss of more than $10 W/m^2$. In the summer months, the Alps, the south of Romania, the Ukraine and south-western Russia also show a lower energy reflection.

A temperature decrease can be expected, if more energy is reflected. This is basically the case, in the spring and summer season for the Iberian Peninsula and from the Moroccan until the Tunisian coast. Here reflected solar radiation is increased, by more than 10 W/m^2 .

For the western and central European continent R_{pert} is rather low for winter. For summer and spring reflection increases. Especially Scandinavia and north-west Russia show higher reflection leading to R_{pert} ranging from 0.5 to 5 W/m^2 . This is in contrast to autumn, where less radiation is reflected (0 to -5 W/m^2).

Significance of simulation results

A two sided mean student t-test was used to check for significant changes on the 2 m temperature for every grid box. The samples are the entries for every grid box over time (i.e. 60 timesteps), and are assumed to be normally distributed. The test decides if the means of the sample populations are different. The test is not sensitive to seasonality. In case of opposite seasonal changes, it might compensate the effect on the total mean. Additionally, a student t-test for a sample number of 15 time steps is too low for checking significant differences in the probability distribution of every season on its own.

The area of the north African region shows significant 2 m temperature changes, as well for most of the Mediterranean coastal areas (figure 6.18). This pattern for significant temperature differences coincides with areas of high albedo differences in every season (shown in figure 6.19), which is explicitly the case for the Mediterranean coastal areas.

In the northern latitudes the effect of background albedo differences is superimposed by snow-albedo effects, which is not part of this study.

The only explicit changed parameter for this sensitivity study is the albedo. Nevertheless, the effects of interacting processes with radiation can also lead to temperature differences at a distance.

Background albedo differences for seasons

The differences in the background albedo for seasonal means is shown in figure 6.19. It reveals all effects of annual albedo cycle amplitude, its phase and minimum level.

The strong increase in the albedo amplitude is clearly affecting the albedo differences for Scandinavia to Russia. The strong decrease in albedo minimum level is dominating the total albedo decrease for some north African regions and eastern European region. Especially for the Iberian Peninsula, all three effects are leading to strong albedo differences in all seasons. As the differences in phase are very high for this region, it also leads in combination with amplitude increase and minimum changes to high discrepancies for every month. For the Iberian Peninsula an albedo increase is dominating.

2 m temperature differences for seasons

Albedo changes are affecting the 2 m temperature within the radiation scheme of REMO. Figure 6.20 shows the five year seasonal mean temperature differences, $REMO_{amap}$ minus $REMO_{SLAR}$. The highest occurring monthly mean temperature differences are ranging from -8 to $6^{\circ}C$, but these are exceptions. The main seasonal differences are much lower, often under $\pm 0.5^{\circ}C$. Since the simulation lasts only for five years, as opposed to usual 30 years, temperature differences up to $\pm 0.5^{\circ}C$ can be related to model internal variability. The uncertainty value is depending among other things, on the grid box distance to the boundary area for the direction of inflowing driving data, which are fed into REMO as lateral boundary information. The closer to the inflow at the boundary, the lower is the model internal variability (Kevin Sieck - personal communication (e.g., Alexandru et al., 2007; Lucas-Picher et al., 2008)). With higher distances from the boundary, particularly the cloud distribution is highly variable, which causes differences in the radiation budget and influences the temperature. To demonstrate tendencies in figure 6.20 seasonally mean temperature differences are illustrated in a specific range i.e. $-0.5, -0.2, -0.02, 0, 0.02, 0.2, 0.5^{\circ}C$. In North Africa, $REMO_{amap}$ leads to higher 2 m temperature values in all seasons $> 0.5^{\circ}C$, mainly due to the lower albedo minimum (compare figure 6.16). Since North Africa is sparsely covered by clouds, this region is less affected by cloud induced model internal variability, and additionally it is close to the boundary area. The same is valid for the Iberian Peninsula; a relation of temperature changes to albedo changes is clearly obvious. For the Iberian Peninsula, the pattern of de-and increase in the albedo minimum level is clearly persistent in the seasonal mean temperature differences. A cooling by $-0.9^{\circ}C$ is reached in summer for the Iberian Peninsula.

The strongly lower albedo minimum level is also clearly leading to a temperature increase for Hungary, Serbia and Romania in the summer season. This can be related to more cloud free days in summer.

The pattern of a summer temperature decrease from Sweden to Finland, is nearly identically to the pattern of a strong albedo amplitude increase.

The cooling from the Baltic states to Russia and the Ukraine, seems to result from an internal effect. There is no clear dependency to albedo changes observable. Long term and remote effects must be investigated by a simulation lasting at least 30 years.

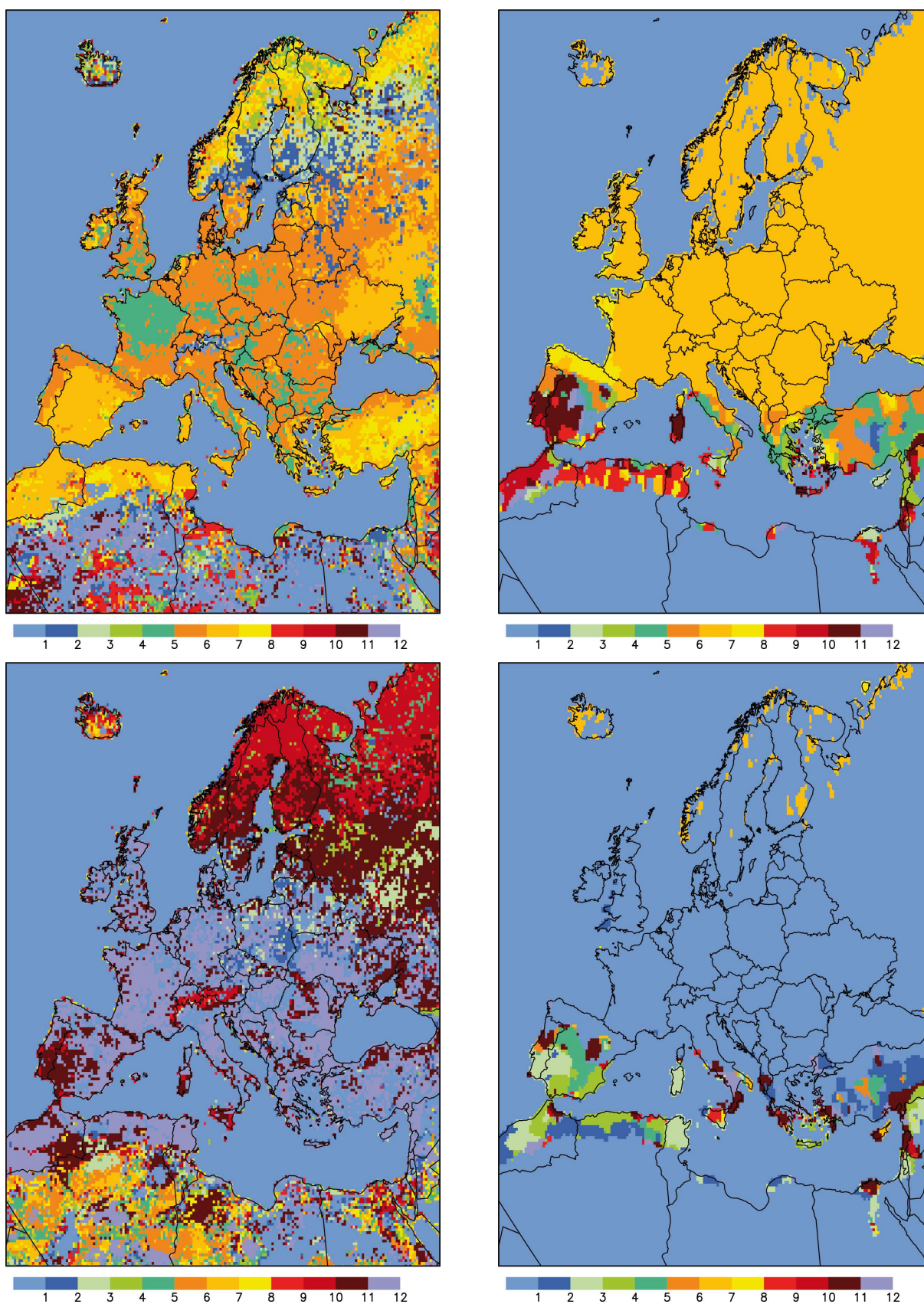


Figure 6.15.: Phase: Month with albedo maximum: α_{omap_1} (top left) α_{SLAR} (top right), bottom: albedo minimum. [Jan=1,...,Dec=12], colours are related to seasons: bluish (DFJ), greenish (MAM), yellowish (JJA), reddish (SON).

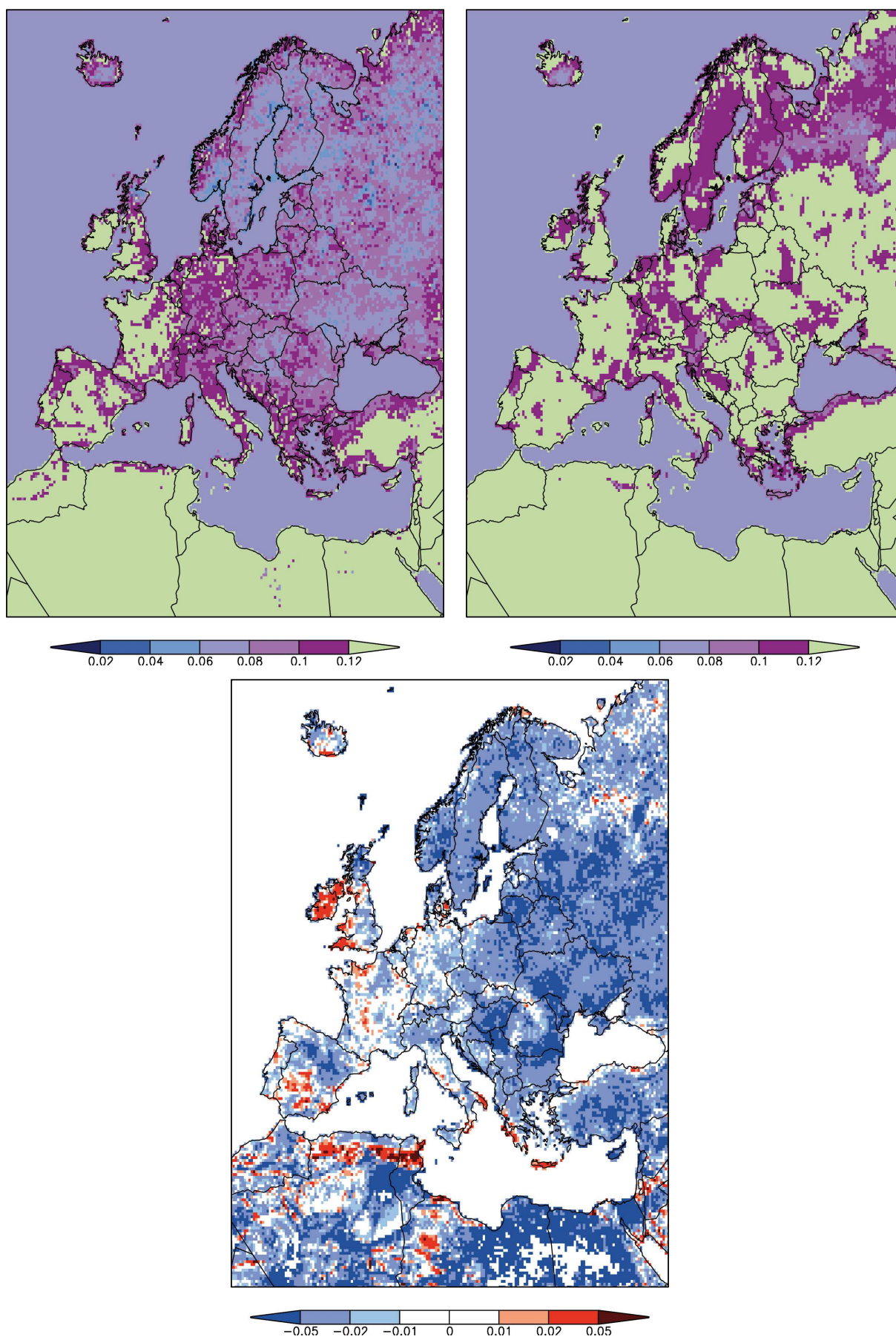


Figure 6.16.: Albedo minimum: α_{ama_1} (top left), α_{SLAR} (top right), bottom: difference in albedo minimum ($\alpha_{ama_1} - \alpha_{SLAR}$)

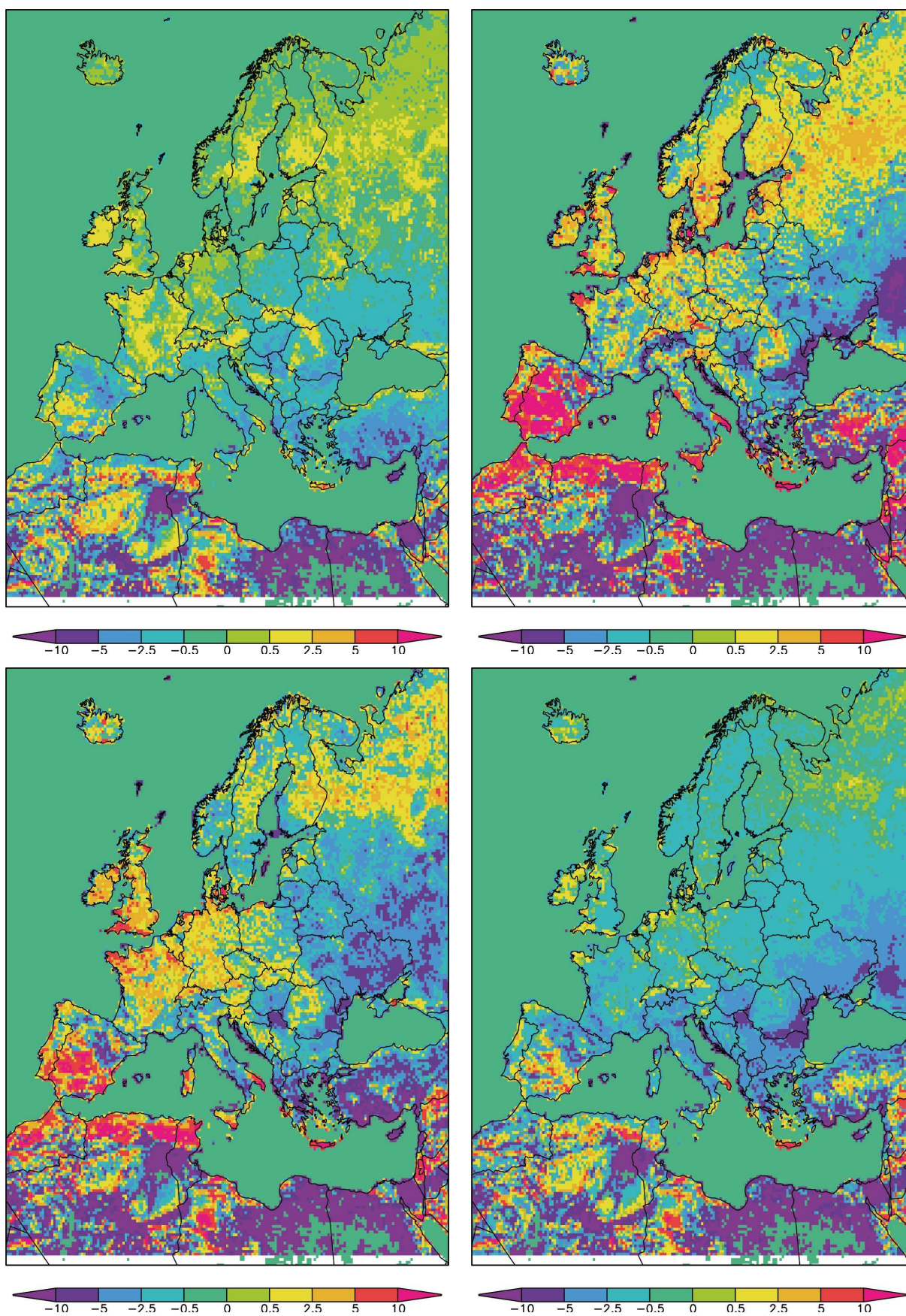


Figure 6.17.: Radiative perturbation (R_{pert}) in W/m^2 caused by albedo differences ($G(\alpha_{amap_1} - \alpha_{SLAR})$) for seasonal means: DJF (top left), JJA (top right), MAM (bottom left), SON (bottom right).

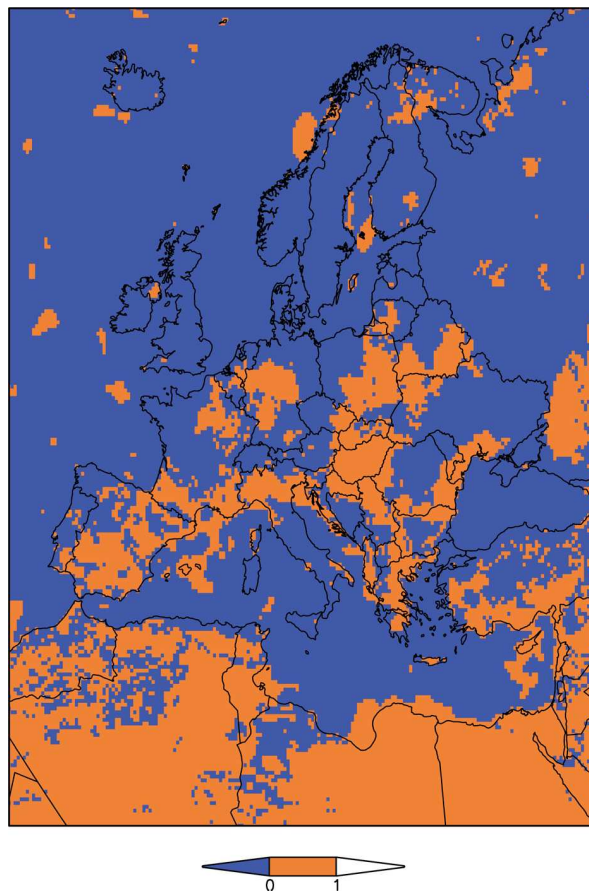


Figure 6.18.: Significance test for 2 m temperature changes in REMO (two sided mean t-test, with a 95% significance level): Orange grid boxes indicate a significant difference.

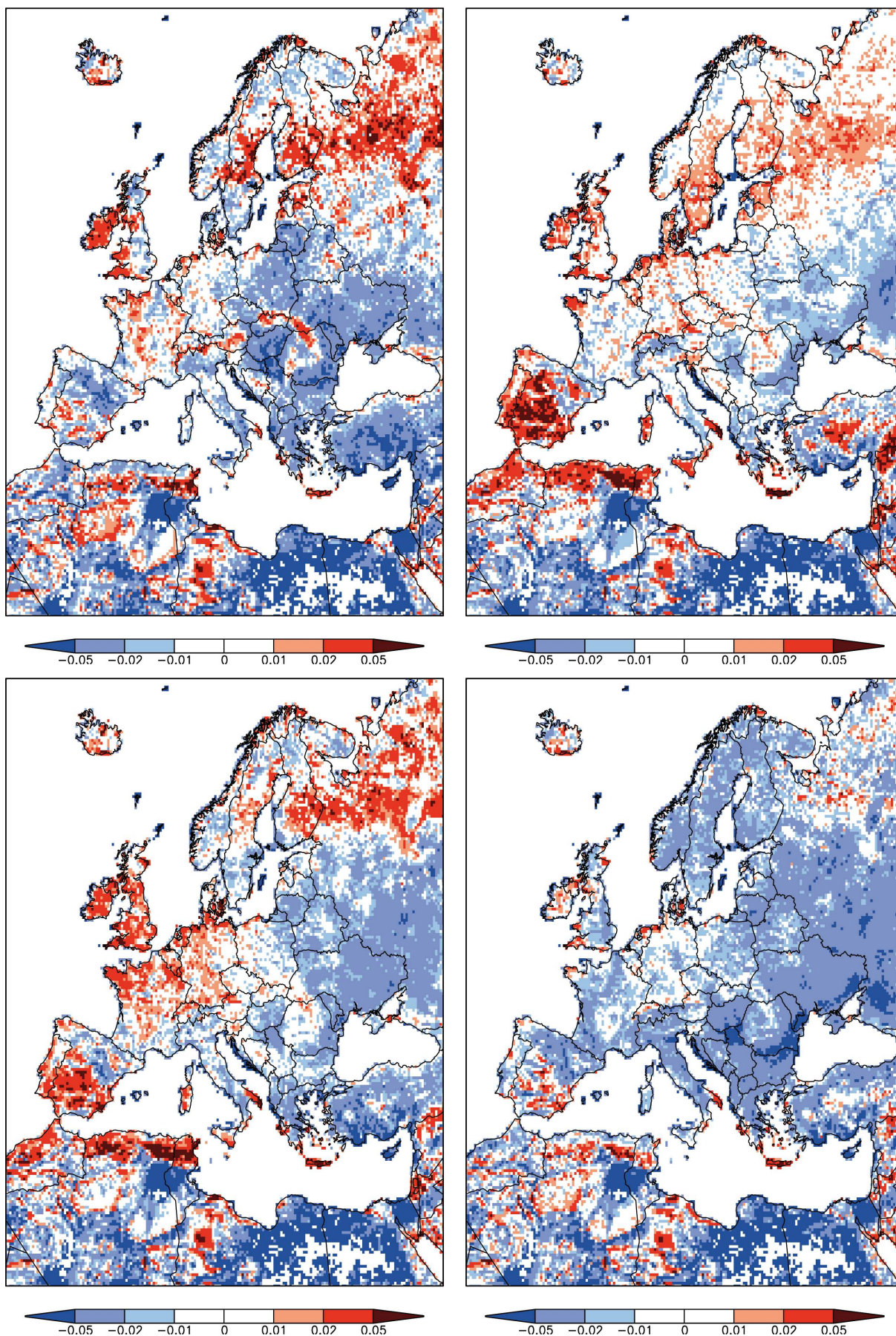


Figure 6.19.: Difference in seasonal mean background albedo ($REMO_{amap} - REMO_{ref}$), averaged over 5 years: DJF (top left), JJA (top right), MAM (bottom left), SON (bottom right).

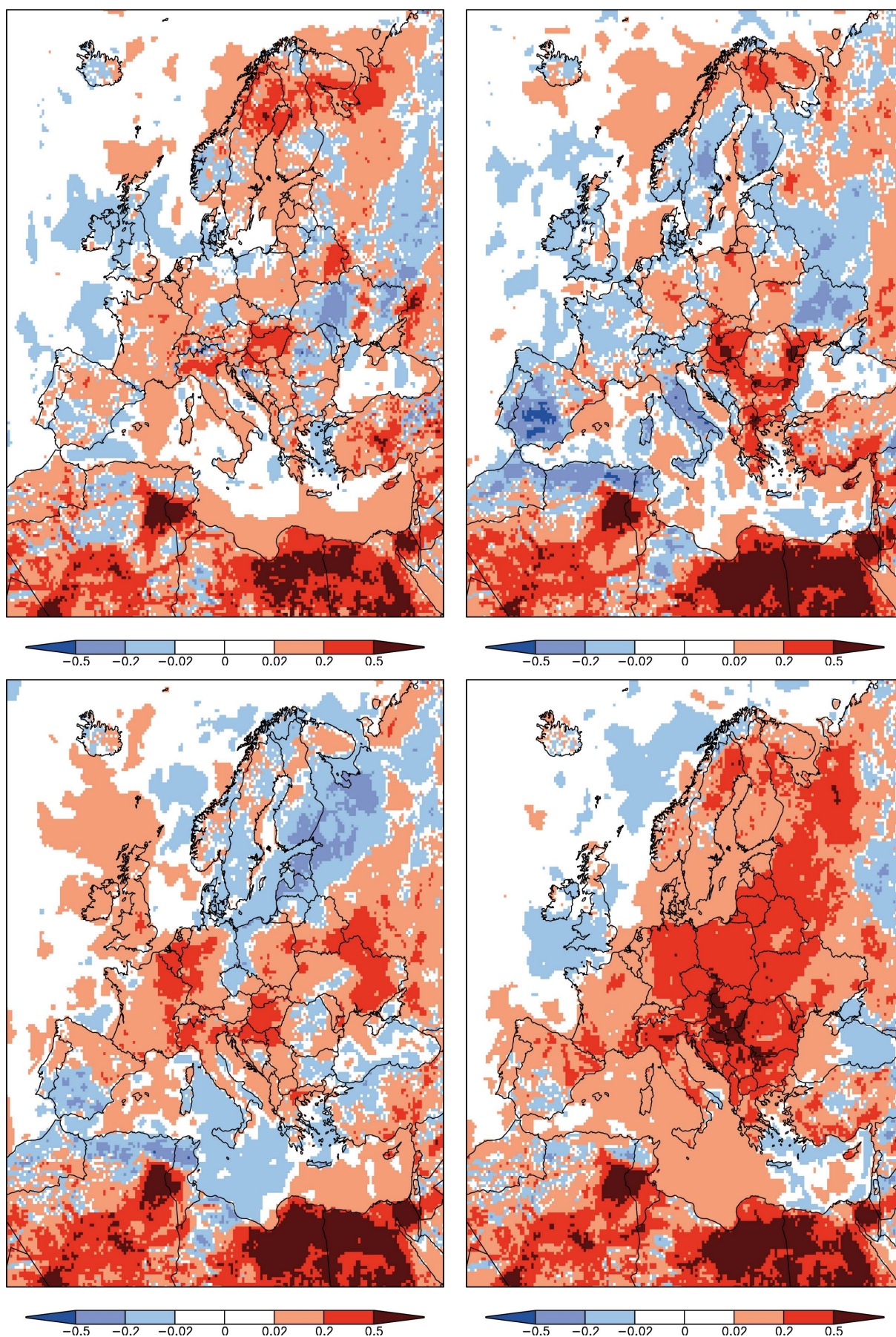


Figure 6.20.: REMO 2 m temperature difference ($REMO_{amap} - REMO_{ref}$), averaged over 5 years for all seasons: DJF (top left), JJA (top right), MAM (bottom left), SON (bottom right).

6.3.2. REMO with changed LAI and thereby changed albedo

Description of the sensitivity study

The sensitivity study's experimental set up domain is Central Europe, equivalent to the UBA domain, with a horizontal resolution of 0.088° ($\approx 10 \times 10$ km), laterally forced over ten years (1991-2000) by ERA40 (Uppala et al., 2005). The UBA simulation carried out for the German Environmental Agency UBA, for the same time period and forcing data was used as reference simulation (Jacob et al., 2008).

The difference to the reference simulation are exchanged LAI_g and LAI_d in LSPII for GET classes, here deciduous forest and needle leaf forest. Following the description of Olson (1994), the forest types of the GETs as used in the LSPII got clustered respectively. The forest fraction for the deciduous and needle leaf forest are shown in figure 6.21.

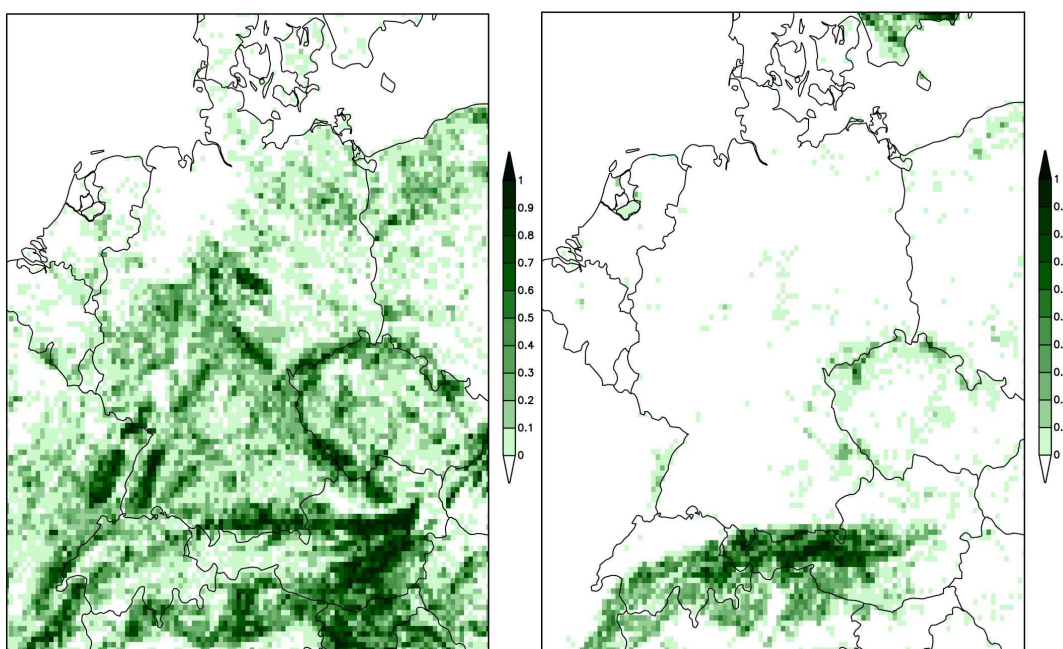


Figure 6.21.: Forest fraction per grid box: Deciduous Forest (left), Needle leaf Forest (right).

As this study was part of the former BMBF project GLOWA-Danube (Ludwig et al., 2003), the LAI for Conifer and Deciduous Forests of the decision support system DANUBIA (Mauser, 2002) was used. The changes, figured in 6.22, led to an increase of the LAI for Coniferous Woods, for LAI_d from 2.5 to 7.8, and for LAI_g from 6.0 to 7.8. For deciduous forests, the LAI_d decreased from 0.7 to 0.0 but increased for LAI_g from 5.2 to 8.0, shown in figure 6.22.

For the albedo calculation within SL4R (equation (6.3.2)) but with changed LAI of the “sensitivity

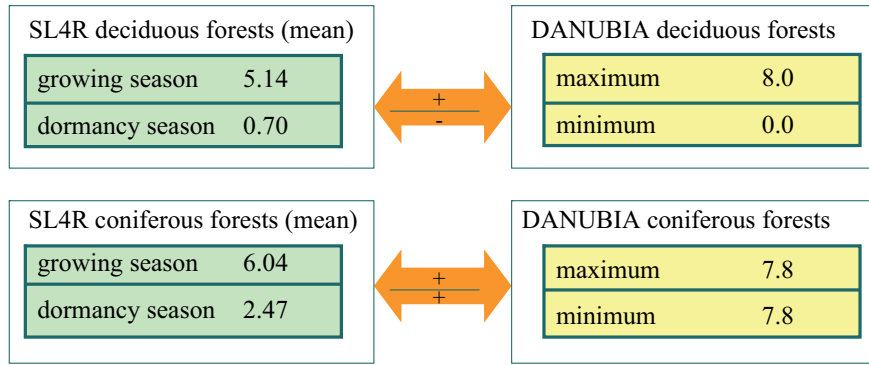


Figure 6.22.: LAI in SL4R and DANUBIA for deciduous and coniferous forests.

study wood”, the changed annual LAI cycle must change the annual albedo cycle (referred as α_{ssw}), even when all other i.e. the albedo-weights α_{veg} , α_{soil} and the growing factor f_i remained unchanged.

The compared experiments will be referred as:

1. REMO_ref: REMO with annual cycle of α_{SL4R}
2. REMO_ssw: REMO with annual cycle of α_{ssw}

Expectations on LAI changes

The LAI differences for both 10 year REMO runs for the winter (DJF) and for summer (JJA) are displayed in figure 6.23. Because the LAI influences interception and stomatal conductance it also influences evaporation (see section 2.2).

The annual albedo cycle is dominated by the LAI cycle. The annual cycle of albedo is a function of the albedo compounds α_{veg} and α_{soil} as weighting factors in the albedo parameterization in the SL4R (albedo-weights) to LAI (see section 2.3). Hence albedo increases with LAI if $\alpha_{veg} > \alpha_{soil}$ (see figure 6.7). This is the case for all grid boxes in this domain, as shown in figure 6.24, even though the albedo-weights pattern looks rather random.

The LAI changes will modify the annual albedo amplitude and will cause albedo minimum level shifts. The lowering of LAI by approximately 0.7 to 0.0 LAI points for deciduous forests and the increase from 2.47 to 7.8 for coniferous forests in the dormancy season has a higher impact than a further increase of LAIs to values above 4.

Annual albedo cycle: Amplitude

The mean albedo for grid boxes with a higher deciduous or coniferous forest fraction than 50% is shown in figure 6.25 for α_{SL4R} , and α_{ssw} respectively. Also mean annual cycle of α_{amap} for the

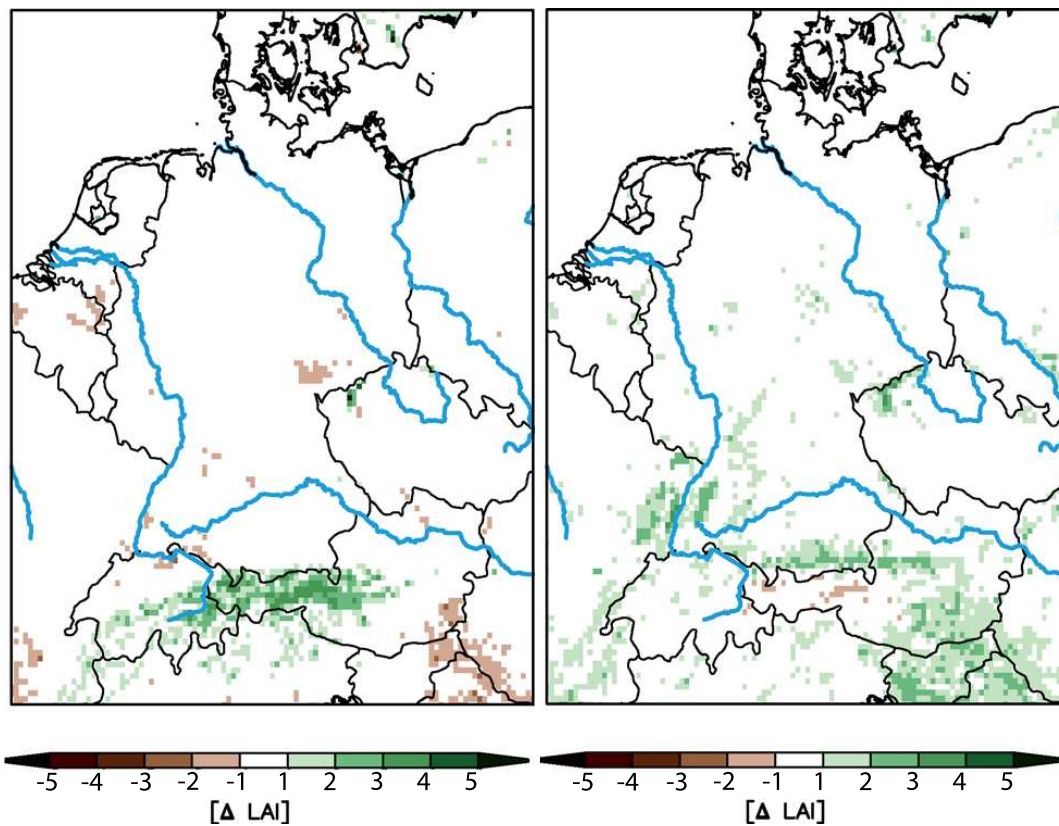


Figure 6.23.: Difference in LAI ($REMO_{ssw}$ minus $REMO_{ref}$). Left: winter season (DJF), right: summer season (JJA).

same regions (conservatively remapped on 0.05°) is plotted in yellow.

The LAI change leads to the expected albedo amplitude spread. The albedo minimum is lowered in winter by about 1%, increased by only 0.02% in summer.

The annual albedo cycle for coniferous forests is more strongly affected by LAI changes. The generally small amplitude is even lowered. In comparison the observation AMAP the annual albedo cycle over coniferous forests, is not as constant as assumed in SL4R. In comparison to figure 5.4 the mean annual albedo cycle has a characteristic shape with two peaks.

The horizontally spread of albedo amplitude differences is dominated by amplitude increases up to 5%, where the LAIs increased in the summer season (figure 6.26).

With the implemented nearly constant cycle of LAI for coniferous forest, the annual albedo cycle is also nearly constant, especially for the Alps. The amplitude's changes fit well to the patterns for LAI increase and decrease for DJF as well as for JJA (compare figure 6.23).

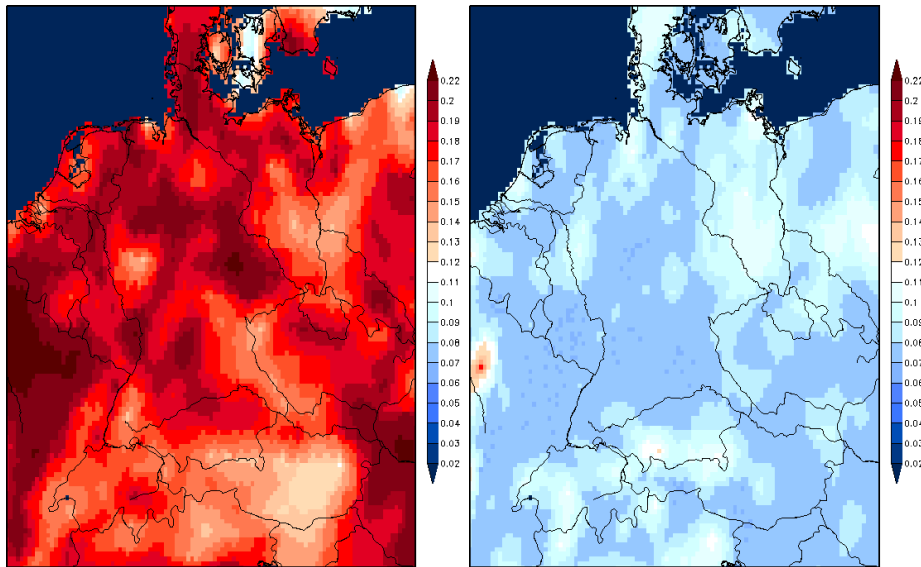


Figure 6.24.: Albedo-weights for Central Europe domain in 0.088° . Left: α_{veg} , right: α_{soil} . Note: $\alpha_{veg} > \alpha_{soil}$ for this domain and the random pattern comes from consecutive interpolation.

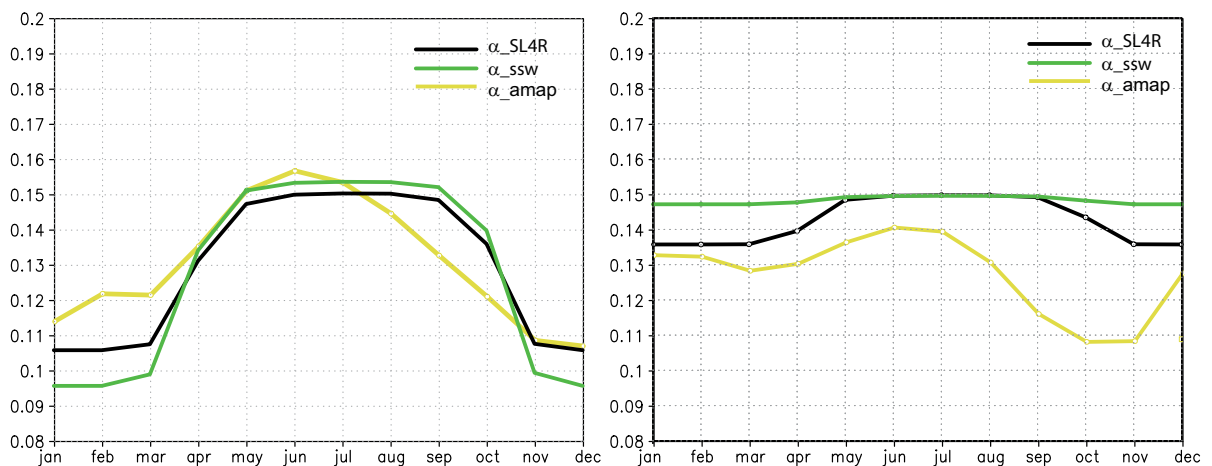


Figure 6.25.: Annual albedo cycle for deciduous forest with (left), coniferous forest (right). Black: α_{SL4R} cycle for $REMO_{ref}$, green: α_{ssw} for $REMO_{ssw}$, yellow: α_{amap} . Only for grid boxes with a forest fraction $> 50\%$.

Annual albedo cycle: Phase

As the growing factor was unchanged, no difference in the phase was expected. The albedo minimum appears in both model runs constantly in January. For the albedo maximum, a slight change can be observed. In the annual albedo cycle of the reference run two grid boxes in Switzerland do not show a cycle at all 6.27 (right). As already mentioned in chapter 6.2, a coincidental combination of

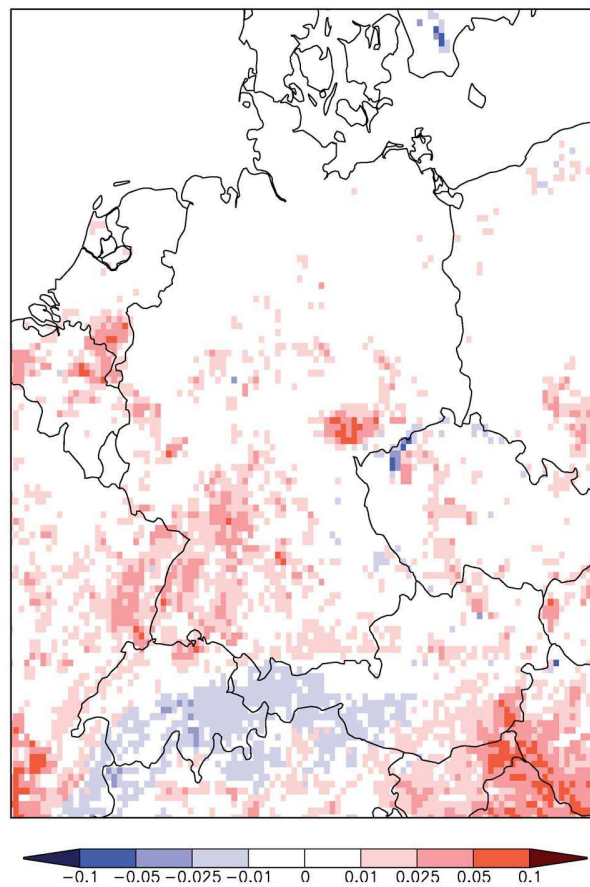


Figure 6.26.: Difference in amplitude: $REMO_{ssw} - REMO_{ref}$.

parameters can lead to an inversion or flattening of the annual albedo cycle. Such a process can be seen for three pixels in Austria, marked with an arrow, in figure 6.27 (left).

Level of albedo minimum

The absolute minimum albedo α_{SLAR} does not fall below 0.08 (figure 6.28, top right). With the implementation of different LAIs the albedo minimum level is widely decreased for southern Germany and for the Austrian, Hungarian, Slovenian and Croatian border region (figure 6.28, top left).

The horizontal pattern for the difference in albedo minimum level (bottom, figure 6.28), is nearly identical to the pattern for the albedo amplitude change, but inverted. For areas with an albedo amplitude increase, the albedo minimum level is decreased.

However, the albedo minimum decrease is attributed to the strong LAI decrease for the dormancy LAI implemented for deciduous forest, which spreads the amplitude and strongly influences the

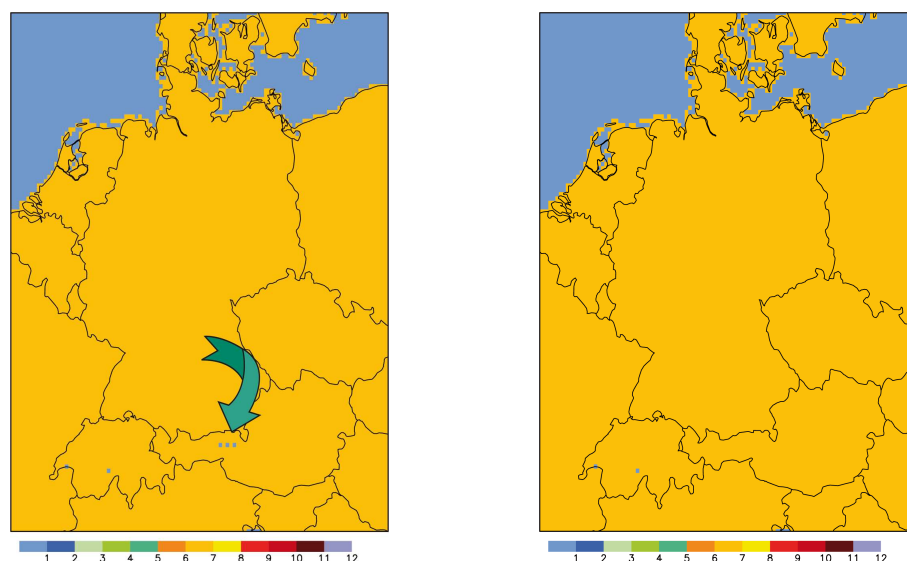


Figure 6.27.: Phase: Month of appearance of the albedo maximum: $REMO_{ssw}$ (left) $REMO_{ref}$ (right). Arrow in left figure points to three pixel of unwanted cycle inversion.

α_{soil} weighting factor in formula . If this decrease of the albedo minimum is realistic compared to the interpretation of LAI changes as an deforestation in winter is not topic of this work.

Radiative perturbation

For calculating the radiative perturbation, the annual cycle of global radiation (G_{001524}) from chapter 4.2 was used. Originally in 0.11° resolution it was conservative remapped to the 0.088° resolution of the Central Europe target domain. The radiative perturbation is again an offline calculation for the background albedo without snow effects.

The seasonal differences of the radiative perturbation for $REMO_{ssw}-REMO_{ref}$ are shown in figure 6.29. For winter (top left), the blue colours indicate that less energy (up to $-5 W/m^2$) can be expected. For the Alps the reflected energy flux density is about $2.5 W/m^2$ higher for $REMO_{ssw}$. The pattern for the spring season is similar to the winter (bottom left). The pattern for summer (top right) is quite homogeneous with a tendency to more reflection up to $2.5 W/m^2$. The autumn season shows almost no differences with predominantly below $\pm 0.5 W/m^2$.

Significance of simulation results

Same as in section 6.3.1 a two sided student t-test, here on 120 monthly means (for each time step) in every grid box, is used to reveal significant differences in the 2 m temperature. Figure 6.30 shows clearly significant differences in the statistical distribution of the 2 m temperature but there is no reasonable pattern.

As the only explicit changed parameter for this sensitivity study is the LAI, it is not clearly explicable if the effect of temperature change is attributable to the LAI changes or the changes in the surface albedo due to the LAI changes. Here as well, processes with teleconnection are involved to explain the temperature differences.

For a seasonal analysis the sample number is with 30 time steps too low for checking significant differences in the probability distribution.

Background albedo differences for seasons

Since the changes in the LAI are more important for $LAI \leq 4$ (compare figure 6.7), it is mainly the albedo for the winter season, which is impacted by the implemented LAI changes for $REMO_{ssw}$, shown in figure 6.32 (top left). This causes also the lowering in the albedo in winter for parts of Austria, Hungary, Slovenia and Croatia.

As $LAI \leq 4$ is typical for the winter season the albedo decreases are comparably strong even though the LAI changes are within ± 1 . This is also explaining, why the albedo changes for the other seasons are only marginal. As can be seen in figure 6.31, the albedo is almost constant for LAI changes above 4. LAI changes from 5 to 6 do not impact considerably on the albedo calculated in SL4R.

2 m temperature differences for seasons

The seasonally averaged 2 m temperature differences in figure 6.33, are rather coherent with the radiative perturbation pattern, for winter and spring. Areas with a decrease of reflected energy match very well with temperature increases. However, the temperature changes do not exceed -0.2 to $0.5^\circ C$, and are definitely in the range of model internal variability (as explained in 6.3.1). Nevertheless, the changes are significantly. Beyond that, temperature changes are one criterion for climate change simulations concerning land use changes.

Only for the winter season the seasonal mean temperature difference can be related to the influence of changes in the albedo. The temperature differences for the remaining seasons might be strongly influenced by changes in the evaporation differences, triggered by LAI changes.

Altogether for the temperature differences ($REMO_{ssw} - REMO_{ref}$), the winter season and summer season behave differently. There is more warming in winter, in contrast to more cooling in summer. There are no major differences between the spring and autumn seasons. Strikingly is the result for the alpine region, whose temperature for $REMO_{ssw}$ is lower for all seasons, but summer. In addition, the Austrian, Hungarian, Slovenian and Croatian border region is always affected by a temperature increase, besides in summer.

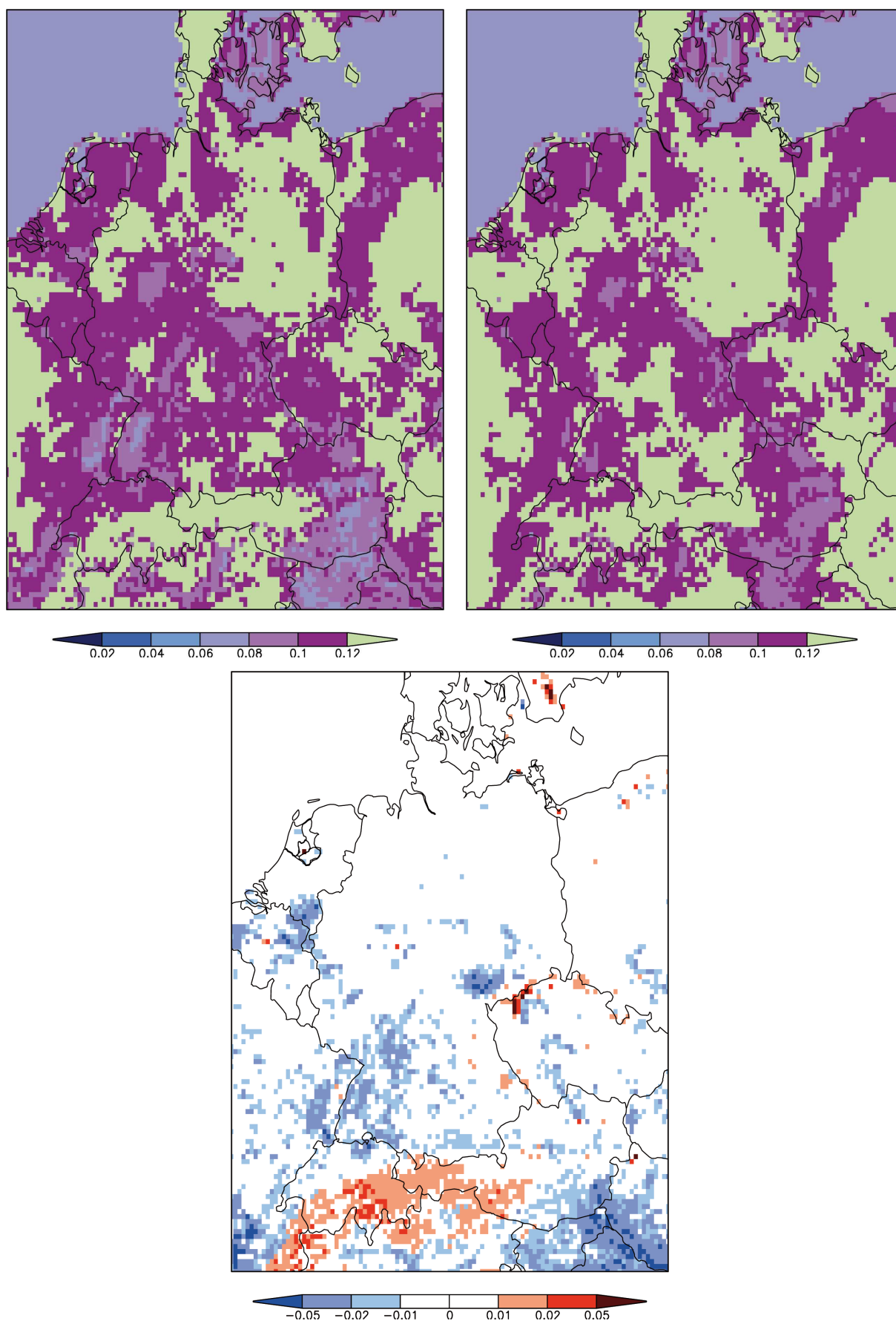


Figure 6.28.: Albedo minimum: $REMO_{ssw}$ (left) $REMO_{ref}$ (right). Difference in albedo minimum (bottom).

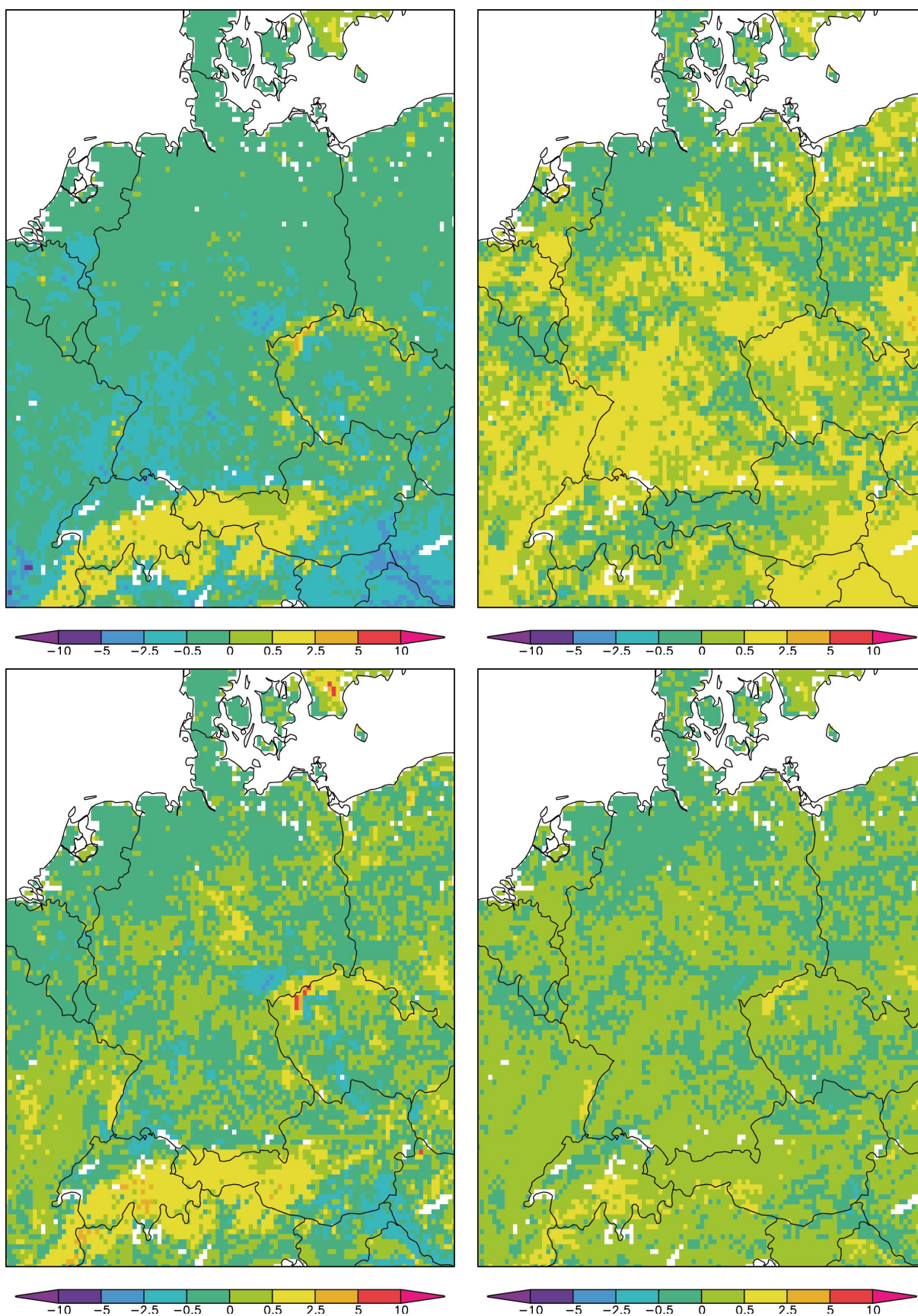


Figure 6.29.: Radiative perturbation caused by LAI changes in $[W/m^2]$, for all seasons: DJF (top left), JJA (top right), MAM (bottom left), SON (bottom right). Water surfaces are indicated in white.

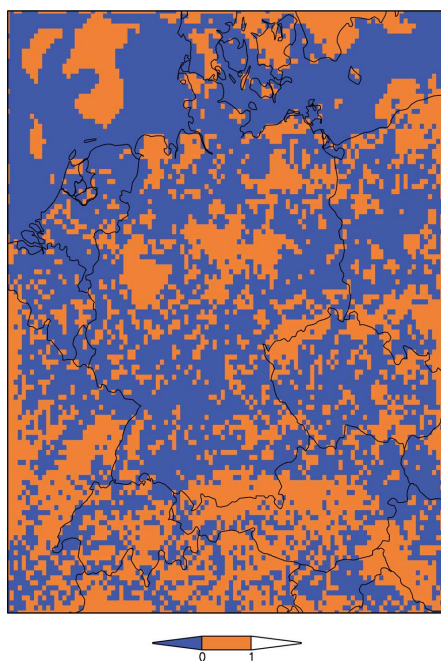


Figure 6.30.: Significance test for 2 m temperature differences of $REMO_{ssw}$ versus $REMO_{ref}$ (two sided mean t-test, with a 95% significance level): Orange grid boxes indicate a significant difference.

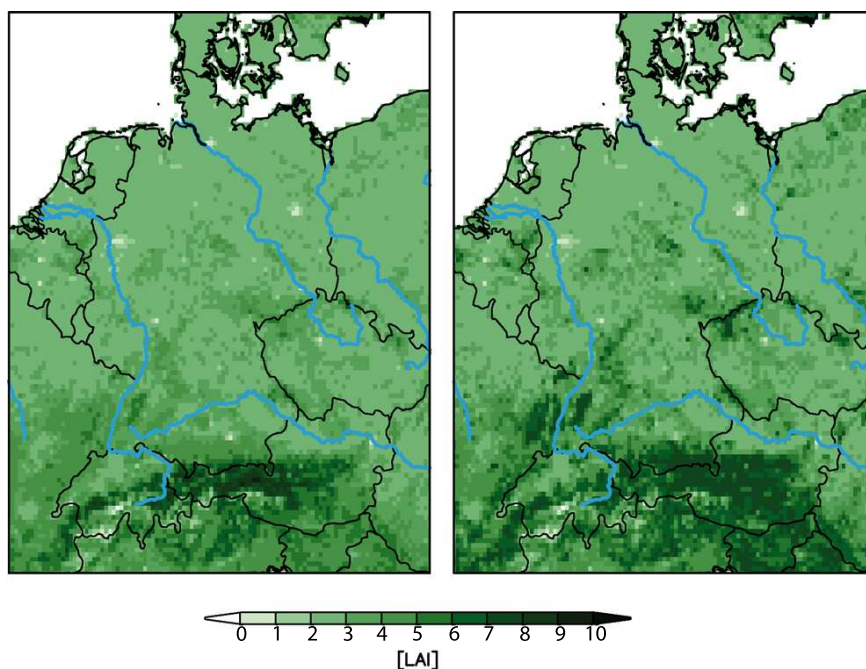


Figure 6.31.: LAI for summer season (JJA): $REMO_{ref}$ (left), $REMO_{ssw}$ (right).

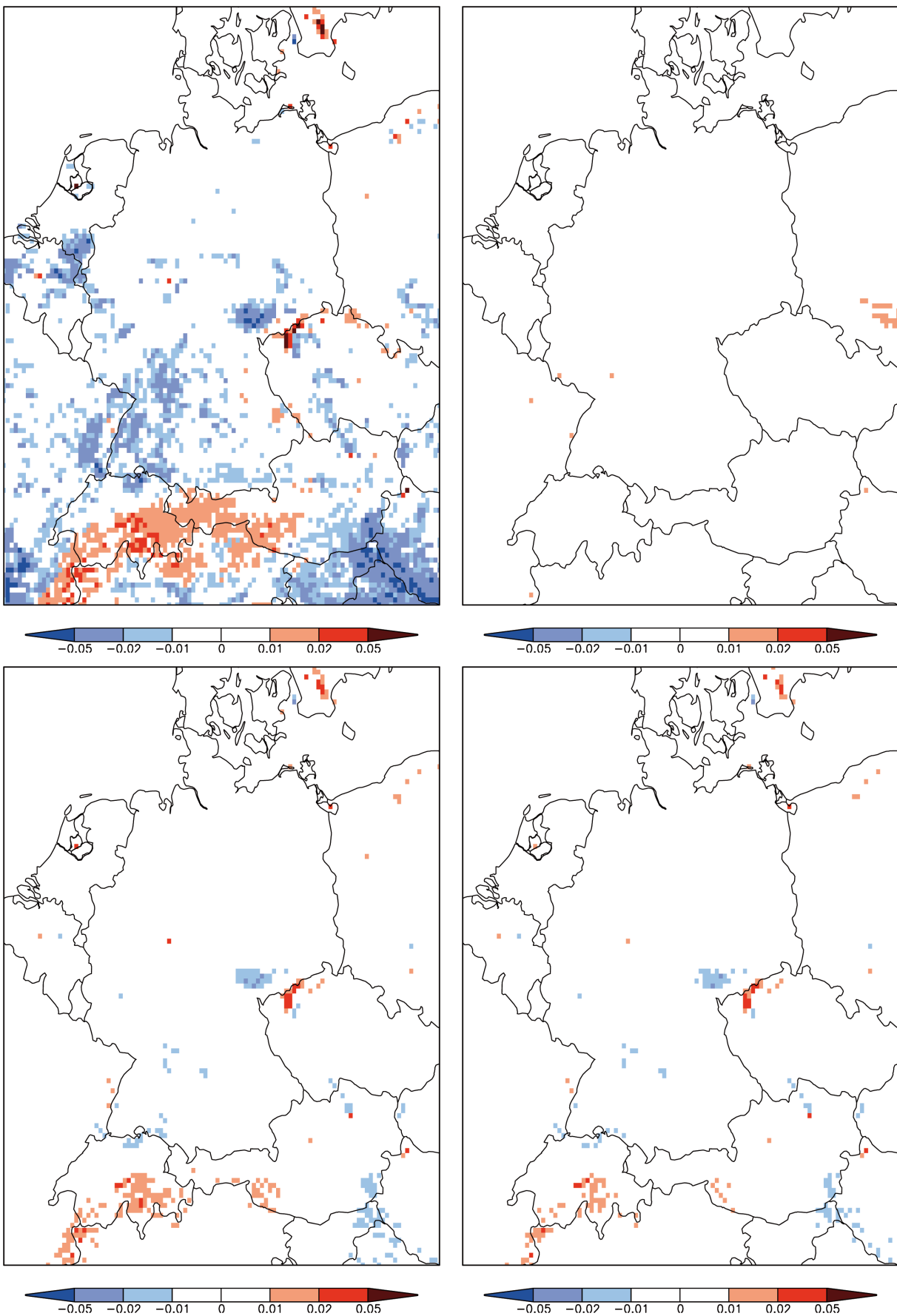


Figure 6.32.: Background albedo difference ($REMO_{ssw} - REMO_{ref}$), averaged over 5 years for all seasons: DJF (top left), JJA (top right), MAM (bottom left), SON (bottom right).

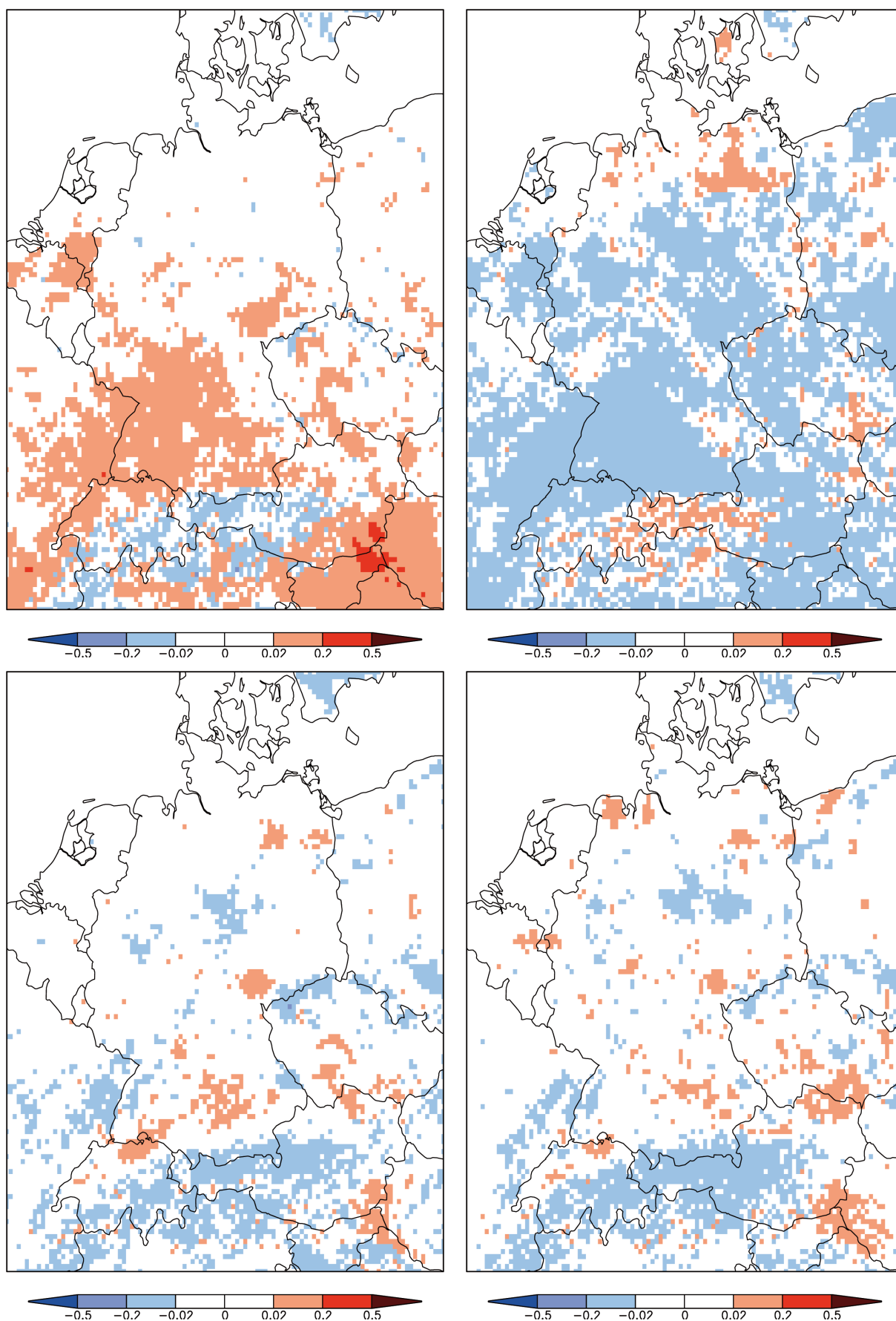


Figure 6.33.: Difference in 2 m temperature over land [$^{\circ}C$] ($REMO_{ssw} - REMO_{ref}$), 5 year seasonal mean: DJF (top left), JJA (top right), MAM (bottom left), SON (bottom right)

6.4. Conclusions for Land Use Change Implementations

As shown in sections 6.3.1 and 6.3.2, the albedo changes caused by different assumptions for different land use classes are significantly influencing the 2 m temperature in REMO. Other processes are as well related to the temperature's development, which might amplify, lower, or offset albedo effects on temperature. Hence, there is no high correlation between albedo and near surface temperature.

The albedo's importance is depending on the scientific question. As REMO is basically an atmospheric limited area model, it is not designed for investigating vegetation feedback mechanisms. However, it is a good tool for investigating the atmosphere's reaction on changes at the lower boundary. Therefore, REMO is also useful to investigate land use changes, as long as they are implemented in a comprehensible manner.

Thus this work is concentrating on the handling of land use changes with respect to realistic vegetation-induced albedo changes. The conclusion by now is that the albedo scheme in SL4R is not suited for the implementation of albedo changes caused by changes in vegetation.

Discussed already in section 6.2, the use of the albedo-weights must not necessarily enhance the approach. Unwanted albedo values are the result, as long as the "real" contrast of α_{veg} and α_{soil} for one vegetation type is not captured, as prerequisite for the use of $\alpha = \alpha_{veg}(1 - e^{-k*LAI}) + (e^{-k*LAI})\alpha_{soil}$ (equation 6.3.2).

Such an albedo contrast retrieval is not trivial. In appendix C it is shown why the method used by Rechid et al. (2008) might be not adequate for land use change studies.

Although the relation between the annual cycle of LAI and albedo must be reconsidered, a more realistic Growing Factor (f_i) by implementing a phenological cycle Rechid (2008) could at least improve the strong offsets of the phase of α_{SL4R} . Although it would not reduce the problematic of unrealistic albedo minimum levels and amplitudes of the annual albedo cycle.

The coupling of a vegetation model, involves the danger of redeploying responsibility. For example, as Jena Scheme for Biosphere-Atmosphere Coupling in Hamburg (JSBACH) is basically using the same dependency of the albedo on LAI, a solution for the albedo problematic is not expectable.

The only conclusion for REMO is: A new approach for land use change studies is needed, as introduced in the next chapter.

7. Implementing Land Use Changes with LUCHS

Investigating the climate's reaction on land use changes in atmospheric models, requires that the parameterized representation of land use classes accurately describes their climate effects. The lower boundary data sets need to contain albedo, LAI, c_v etc. (compare section 2.2). These parameters can be observed. Therefore, investigations of land atmosphere interactions with climate models are depending on the accuracy of this lower boundary data. Especially, when climate change caused by land use changes is the topic of investigation.

Concentrating on the land surface albedo, chapter 5 demonstrated the existence of regional characteristic typical albedo climatologies for specific land use classes. In contrast, chapter 6 showed that regional albedo characteristics are not reproducible within the SL4R.

The aim is to achieve a realistic description for all observable parameters for the entire region of interest. Therefore, the new concept must be based on remote sensing data.

The new method introduced here, for correctly implementing land use changes into the boundary data sets, is called Land Use CHaracter Shifts (LUCHS). Therefore, a recent annual albedo cycle for a certain land cover class in one region (e.g. Central Europe) extracted from the remote sensing data. The extracted annual cycle, represents a characteristic annual albedo cycle for the land cover class in the region. This information can further on be used for spatial transfers, in case of an extension of this land cover class.

As a regional climate model, REMO still has a comparatively low horizontal resolution. For Europe one can assume for a 5 km grid box to observe at least 5 different land use classes. It is not the aim of LUCHS to investigate the interaction of one special plant species, e.g. rye compared to wheat with the atmosphere. LUCHS enables the climate models to investigate the atmosphere's reaction onto albedo changes occurring when land use is changed.

Basid idea

The major aim of this work is, to provide a numerical scheme which allows:

- ▷ a realistic regional representation of the surface albedo
- ▷ an adaptation of albedo values for land use changes.

Land Use CHaracter Shifts (LUCHS), is the name of the new method, which has the described aspects.

To include land surface change scenarios, as for example reforestation, the albedo information for specific land use types needs to be transferable. As already mentioned, regional aspects make it impossible to use globally valid information, because the same forest type in Germany does not

look like the forest in Spain. Therefore, LUCHS uses a recently observed information of a forested area of one region as a master information and is transferring this information onto areas, where an expansion of this forest is expected, but keeps basic autochthonous information as the albedo minimum for this region.

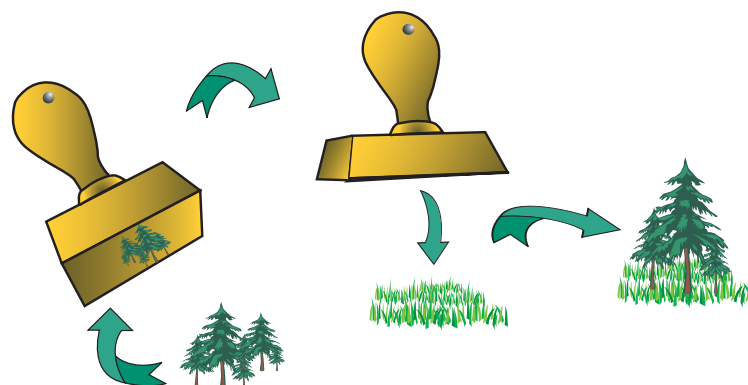


Figure 7.1.: Example for the principle of LUCHS: Coniferous forest characteristics (left) are transferred to crop- or grassland (centre), but the albedo minimum is kept (right).

The principle of copying and stamping is sketched in figure 7.1. To get the master information, surface albedo maps derived from satellites as well as satellite derived land cover maps are used. The transfer for land use change scenarios is a numerical, grid based re-allocation on the highest resolution possible. A remapping, including rotation, onto the target grid can be done afterwards. Assuming that information on albedo characteristics are regionally specific but persistent, LUCHS may transfer albedo characteristic information on land use classes in space and very probably also in time. Of course the transfer of information for future is speculative, also LUCHS is limited onto information which are observable.

7.1. Application of the land use character shifting method

The methods pathway is a composition of nine steps:

1. Select a region
2. Use monthly mean of albedo data derived from satellites
3. Choose masks for land use types to be investigated
4. Compute the annual albedo cycle for these land use types in the region
5. Compute the albedo minimum for the whole region
6. Compute the normalized annual albedo cycle for the whole region
7. Decide about areas of land use changes
8. Replace reference minimum on extension areas with mean of reference minimum and 10th-percentile of considered type

9. Replace the annual albedo cycle on extension areas by the annual albedo cycle or the new land cover type.

Step 1: Select a region

The regional aspect is already discussed in chapter 5. The importance of a regional restriction is connected to the so-called phenological green wave. This is an observable effect of the spatial moving of spring dates (Chen et al., 2000). It is correlated to geographical latitude, continental climate etc., but is also related to a typical regional floral composition. It is impossible to parameterize all these interacting parameters globally with only one formula. Therefore, the regional restriction is needed.

LUCHS is assuming persistence for those regional conditions.

To demonstrate LUCHS, the performance of two European contrasting domains were chosen: The Iberian Peninsula and Central Europe. The orography of both regions has already been shown in figure 5.1.

Step 2: Use annual monthly means of albedo data derived from satellites

The AMAP derived from MERIS Albedomap, as described in 3.3.1, is taken as surface albedo data set.

The method can be applied to every time series, but the horizontal resolution should be higher, than the required model resolution, to avoid information loss when remapping.

Step 3: Choose masks for land use types to be investigated

To analyse the characteristic features of a land use shift, first maps for a recent land use must exist. The optimal version would be a land use distribution from the same year, at the same resolution originating from the same satellites sensor. This is hardly available.

Here, the Global Land Cover 2000 (GLC2000) data is used for present land cover masks. For demonstration, an reforestation of needle leaf forest is considered. Therefore, one of the 22 GLC2000 land cover classes is selected for demonstrating LUCHS:

- GLC70: Closed (>40%) needleleaved evergreen forest (>5m)

The GLC2000 maps with 1 km horizontal resolution were aggregated to a fractional map with 0.05° resolution to get the same resolution as the satellite albedo map. Same as in figures 5.2 and 5.3, figure 7.2 shows the fraction of the GLC2000 class 70 for the Iberian Peninsula and Central Europe. As demonstrated in chapter 5 a fraction of a single land cover class above 50% seems to be sufficient for the analysis in LUCHS. The 50% coverage is at least reached in figure 7.2 for areas marked in light green, yellow and red.

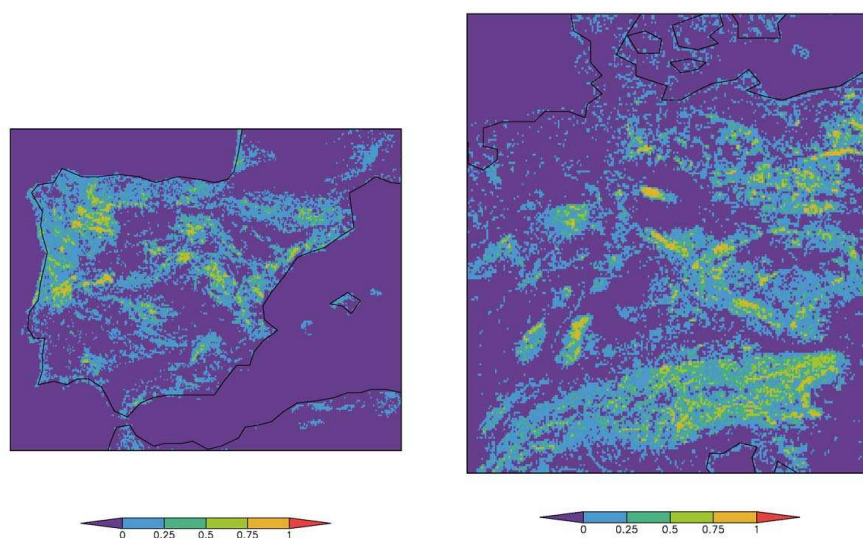


Figure 7.2.: Fractional contribution per 0.05° grid box of GLC70 Needle Leaf for Iberia (left) and Central Europe (right).

Step 4: Compute the annual albedo cycle for these land use types in the region

In LUCHS, the annual albedo cycle of a certain land cover class is extracted from all pixels with a fraction of more than 50%. The retrieved annual albedo cycle is then normalized for every grid box, by subtracting the grid box's absolute albedo minimum. The median for the entire region represents the annual albedo cycle for the land cover class considered. Additionally, the 10th percentile of the albedo minimum is calculated, which will be used later for minimum level adaptations. For the chosen land cover class the normalized annual albedo cycle represented by its monthly means is presented in table 7.1 for Iberia, and in table 7.2 for Central Europe, respectively.

Table 7.1.: Monthly means of the normalized annual albedo cycle caused vegetation for GLC 70 (needle leaf forest) pixels with a fraction above 50%, for Iberia.

GLC 70		Needle Leaf Forest						10 th pctl: 0.1				
jan	feb	mar	apr	may	jun	jul	aug	sep	oct	nov	dec	
0.0053	0.013	0.018	0.022	0.031	0.039	0.039	0.034	0.027	0.014	0.0063	0.0029	

Table 7.2.: Same as table 7.1 but for Central Europe

GLC 70		Needle Leaf Forest						10 th pctl: 0.088				
jan	feb	mar	apr	may	jun	jul	aug	sep	oct	nov	dec	
0.031	0.041	0.023	0.033	0.047	0.053	0.05	0.043	0.032	0.022	0.014	0.013	

Step 5: Compute the albedo minimum for the whole region

For every grid box the absolute minimum over the given time series is calculated. This map of minima is used as the reference albedo minimum (compare figures 7.11 and 7.12 (right)).

Step 6: Compute the normalized annual albedo cycle for the whole region

The absolute minimum of every grid box is now subtracted from the annual albedo cycle in every grid box, in order to get the part of the annual albedo cycle caused mainly by vegetation.

Step 7: Decide about areas of land use changes

The question of choosing relevant land use change scenarios is not part of this work, but a crucial point.

How to get information about where land use changes should take place? As in section 1.1 the Land Use Harmonization Protocol (LUH-P) is mentioned, here again it could be used as information therefore. Although, as already mentioned, this information does not give enough high resolution, as nowadays used in regional circulation models.

Here a very simple method is used, in order to demonstrate the usefulness of LUCHS. Oriented on GLC2000 and fraction of different land classes extension areas for certain land class are chosen to replace another one. Here information of needle leaf forest will be shifted as reforestation on areas of agriculture between 10% to 50%.

The areas where a land use change shall be executed, needs to be masked. By using the example above, figure 7.3 is showing the areas for the desired change, for both test regions.

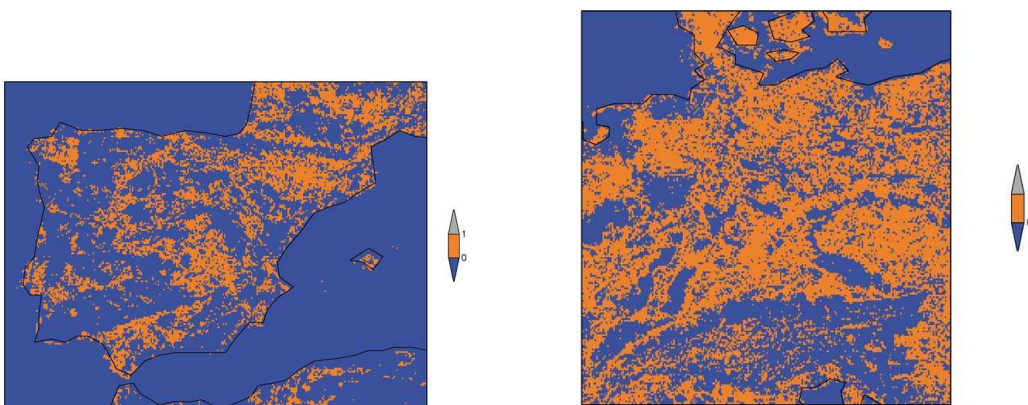


Figure 7.3.: Where to change-masks for Iberia (left) and Central Europe (right) when reforesting agricultural land.

Step 8: Replace reference minimum on extension areas with mean of reference minimum and 10th percentile of considered type

The minimum level of step 5 gets weighted by the albedo minimum 10th percentile (step 4) of the considered extension type. Therefore, the extension areas of step 7 show the grid boxes, where the albedo minimum has to be changed.

This procedure keeps a local component of albedo. The analysis of the albedo minimum level (chapter 5) had demonstrated highly variable albedo minima, attributable to regional specific properties. The above method bears some source of uncertainty, but to avoid replacements with fixed constants, this technique avoids too abrupt changes and keeps a spatial heterogeneity. Also it allows the possibilities of consecutive land use change procedures with LUCHS. In case of further steps, one can use the new minimum map as reference minimum map in the next step.

Step 9: Replace the annual albedo cycle on extension areas by the annual albedo cycle of the new land cover type

To create the new annual cycle of the new land cover type on the extension area, the derived normalized annual albedo cycle from step 4 is transferred to extension grid boxes, defined in step 8. Adding the normalized annual albedo cycle to the weighted minimum level for the extension area results in a new annual albedo cycle for the chosen grid boxes.

For the unchanged grid boxes, the minimum of step 5 is added to the normalized annual albedo cycle of step 6. The final step is to merge the maps of unchanged grid boxes with the new changed ones.

7.2. Results of LUCHS

Evaluating whether LUCHS leads to shifts for land use classes, a slightly adapted inversion method, as described in section 5.3, is applied. In order to proof a shift from Rain-fed Crops into Needle Leaf Forest classification disjunctive levels are chosen. Therefore grid boxes are presumed to belong to the class Needle Leaf Forest, if the absolute maximum is lower than the observed 75th percentile for Needle Leaf Forest in that region. The range lower than the median of the albedo amplitude is chosen as second condition. All remaining classes are summarized to “50 + 150 + 190”. For Iberia/Central Europe the absolute albedo maximum of 0.14/0.15 and for the amplitude of 0.038/0.062 for Needle Leaf Forest are therefore the chosen verification levels. For the regions Iberia/Central Europe values higher than 0.2/0.19 and amplitude values higher than 0.073/0.084 are declared to belong to the Rain-fed Crops class. All values in between are representing all other classes and are indicated in the following figures as Others. Note, the method here is concentrating only on two of 22 possible GLC2000 types, in order to demonstrate the principle only. Grid boxes

with changes but not appearing on the maps after the shift in land use are indicating that the inversion method must be developed further.

The application of the land cover class shift of the characteristic information of the type 70 (Needle Leaf Forest) to areas with Rain-fed Crops implies that mainly those two types should be affected. The land use character shift is done on grid boxes with 10 to 50% fractions of Rain-fed Crops per 0.05° grid box of the original distribution in the GLC2000 class. Therefore, many grid boxes were affected with contributions of all remaining GLC2000 classes, as listed in the tables 5.1 and 5.2. As LUCHS is taking the autochthonous lowest level in every grid box into account, the transferred values might not satisfy the presumed verification conditions.

The results of LUCHS are shown in comparison to the original distribution of the GLC2000 class. In figures 7.4 and 7.5 occurrence of Rain-fed Crops is shown in the top row. The left plot contains the GLC2000 data. The centre plot shows the distribution on α_{amap} using the above described validation levels. The right plot is showing the distribution of the Rain-fed Crops class after the land use class shift from Rain-fed Crops on Needle Leaf Tree. In the same manner the centre row illustrates the distribution of needle leaf forest, and the bottom row the remaining classes Artificial, Sparse Vegetation and Deciduous Forest as well as all not mentioned classes are summarized and declared as Others or “50+150+190” respectively.

The number of grid boxes for Rain-fed Crops is smaller after LUCHS compared to the distribution on the unchanged α_{amap} (figure 7.4). The distribution of the needle leaf forest class is increased, in fact for the Iberian Peninsula in figure 7.4 centre. Hence the chosen validation levels indicate that most of the shifted grid boxes are shifted, but do not satisfy the conditions for needle leaf forest, therefore they are collected into the range of the remaining classes (Others). The visualisation of the shifting method depends on the chosen validation ranges, chosen here with very rough discretisation.

For Central European figure 7.5 shows the same comparison for re-localisation of GLC2000, α_{amap} and after the application of LUCHS. Here the number of grid boxes satisfying the condition for needle leaf forest is increased, especially for the eastern part of this domain. For Central Europe a decrease in the number of grid boxes for the remaining types Artificial, Sparse Vegetation and Deciduous Forest is also observable. This indicates that the characteristics for those grid boxes are not satisfying anymore the chosen verification ranges.

When choosing the same validation ranges as in section 5.3 for the Artificial land cover class, a major shift into this Artificial class occurs after applying LUCHS, as shown in figure 7.6. As the range of the lower quartile of artificial and upper quartile of Needle Leaf forest is overlapping for maximal albedo values (compare figure 5.15), the insufficient shift might be due to the combination of minimum level and amplitude. In case the autochthonous minimum albedo is comparatively high, the changed minimum level in LUCHS, as a mean value of the 10th percentile and the original minimum value, might still be too high to represent a typical minimum level for needle leaf forest.

Albedo amplitude

Effects for a hypothetical reforestation by using LUCHS are shown in the following.

The lowering in the amplitude due to extension of characteristics from GLC2000 type 70 (needle leaf forest) can be seen in figures 7.7 and 7.8. For both regions, the number of grid boxes with an amplitude range of 0.08 to 0.1 (light green) is reduced, meanwhile the ones with an amplitude range of 0.04 to 0.06 (light blue) is increased. For both regions, grid boxes with an amplitude range between 0.02 to 0.04 (blue) and also some 0 to 0.02 (dark blue) were transferred to the range between 0.04 to 0.06 (light blue). Nevertheless, for both regions the amplitude pattern after the application of LUCHS tends to be more homogeneous in comparison to the amplitude pattern of the original data.

Albedo phase

As LUCHS transfers the whole climatology, shifts in the phase of the annual albedo cycle are included automatically.

Figure 7.9 shows for Iberia an increase of grid boxes where the albedo maximum occurs one month earlier, i.e. in June. The number of grid boxes showing an occurrence of the albedo minimum in November is decreased and appears therefore one month later in december.

For Central Europe in figure 7.10, for large regions the albedo minimum appears one month later after the application of LUCHS (from May in green to June in orange). The changes for the appearance of the minimum is more drastically. The Alps show after the application of LUCHS a severe shift by about four month (from autumn season to winter season). Shifts of about one month earlier, i.e. from January to December, is widely observable.

Albedo minimum

The pattern of the albedo minimum, is shown in figures 7.11 and 7.12. For the Iberian Peninsula, a decrease in the albedo minimum level is observable, besides an increase for some grid boxes where in the original data has a very low albedo ranging between 0 to 0.1.

For Central Europe the number of grid boxes with an originally low albedo minima between 0.04 to 0.06 show an albedo minimum increase after LUCHS. An albedo minimum decrease is observable for those grid boxes with an original albedo minimum higher than 0.12.

Radiative Perturbation

Seasonal means of the differences for radiative perturbation (see chapter 6.3) after the application of LUCHS, reveal no major changes for the winter for both regions, shown in figure 7.13 and 7.14.

For the Iberian Peninsula, less radiation is reflected after LUCHS in summer and spring, occasionally by more than -10 W/m^2 . The reforestation therefore would enhance surface temperature warming for those seasons.

As grid boxes with an albedo minimum increase after the application of LUCHS have higher albedo values in summer, these grid boxes show higher reflection of the incoming global radiation, which might lead to temperature decrease.

The amount of radiative perturbation for spring and autumn is less pronounced, but similar to the summer.

For Central Europe, the summer season is widely affected by the implemented albedo changes, shown in figure 127. In summer a decrease up to 10 W/m^2 occurs while at the same time an increase up to 10 W/m^2 is observable mainly for the Alps and Mecklenburg-Vorpommern.

While in spring again a less pronounced but similar pattern to summer occurs, the patterns for winter and autumn show only very low differences in the reflected global radiation.

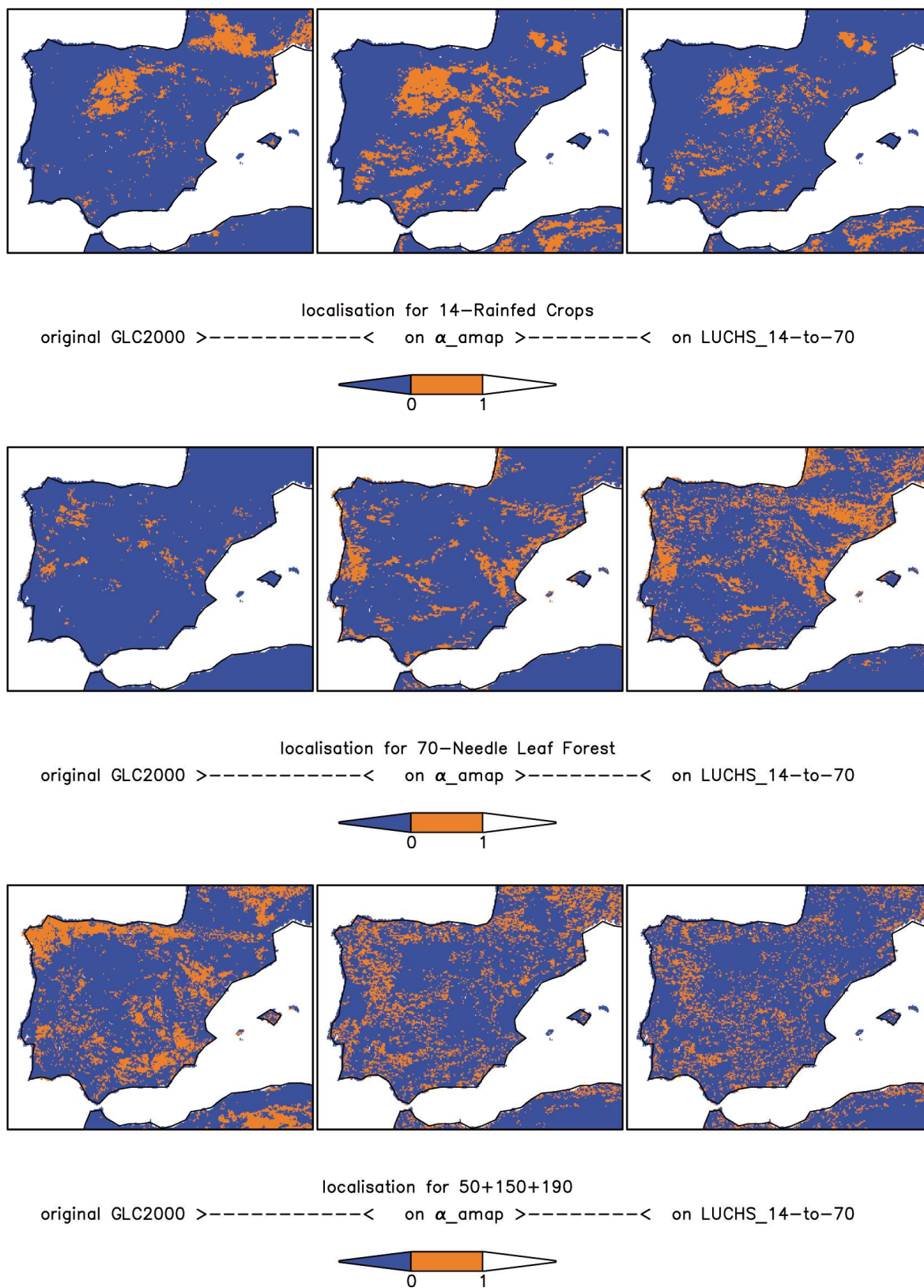


Figure 7.4.: Localisation of Rain-fed Crops (top), Needle Leaf Forest (centre), Others (bottom) on Iberian Peninsula: Left original GLC2000, centre presumed distribution on α_{omap} , right presumed distribution after LUCHS.

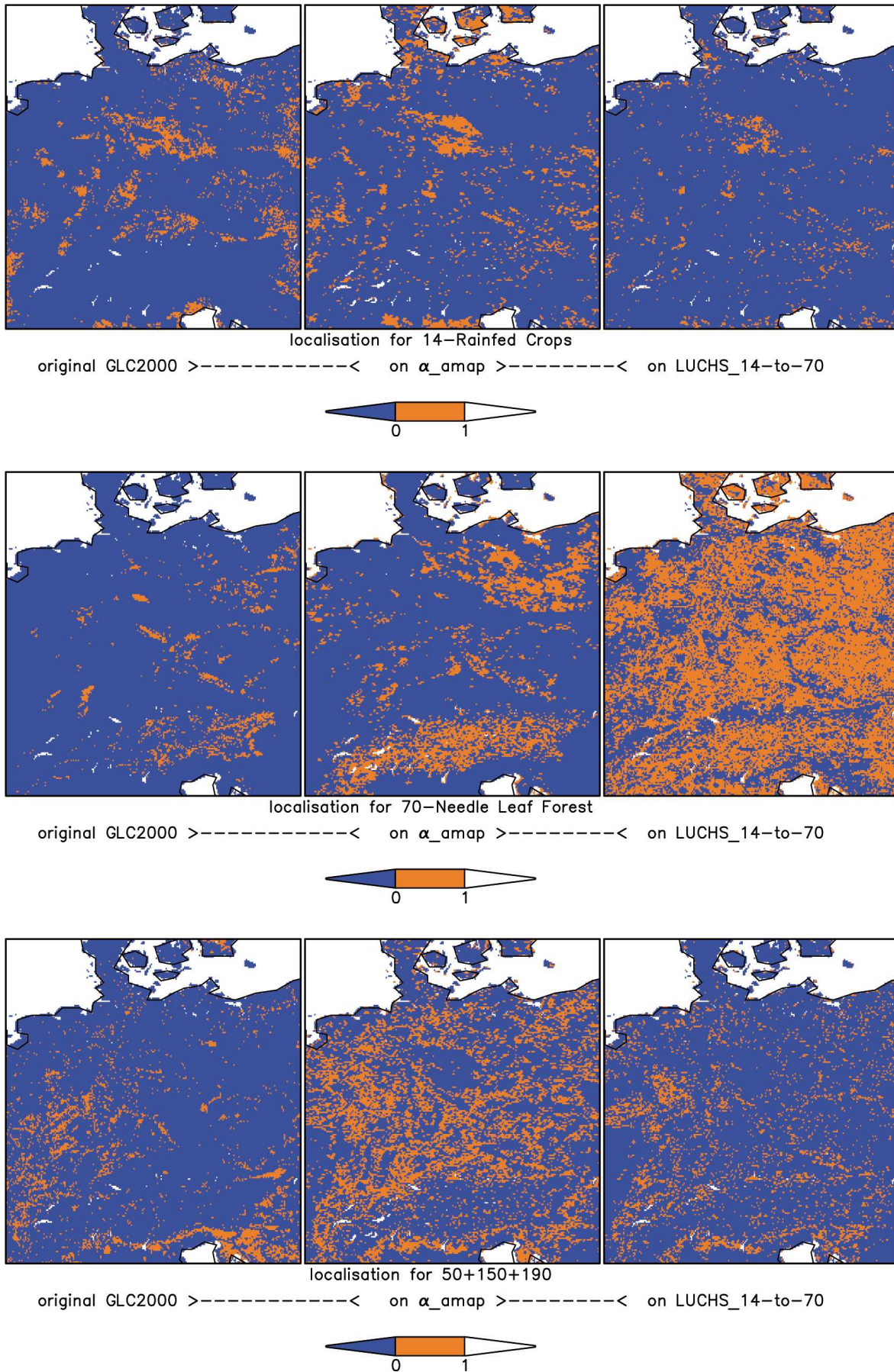


Figure 7.5.: Localisation of Rain-fed Crops (top), Needle Leaf Forest (centre), Others (bottom) in Central Europe: Left original GLC2000, centre presumed distribution on α_{omap} , right presumed distribution after LUCHS.

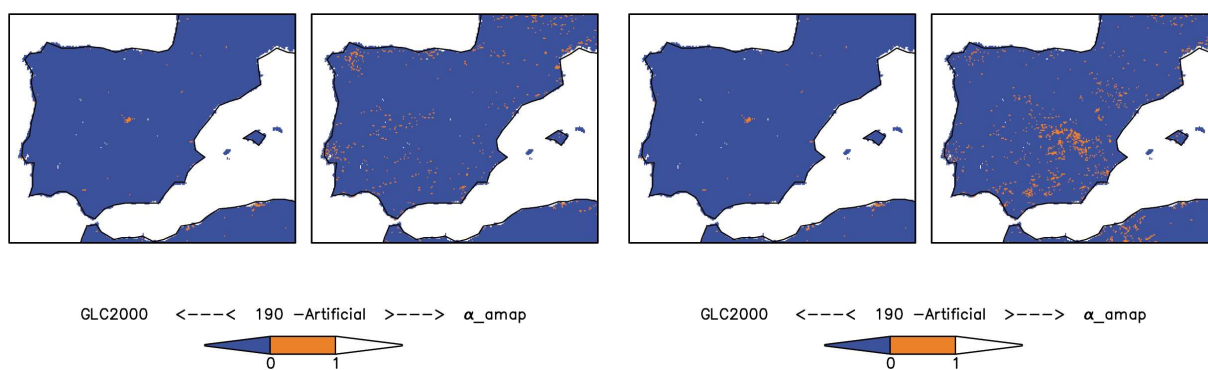


Figure 7.6.: Insufficient shift due to strong overlapping of characteristics.

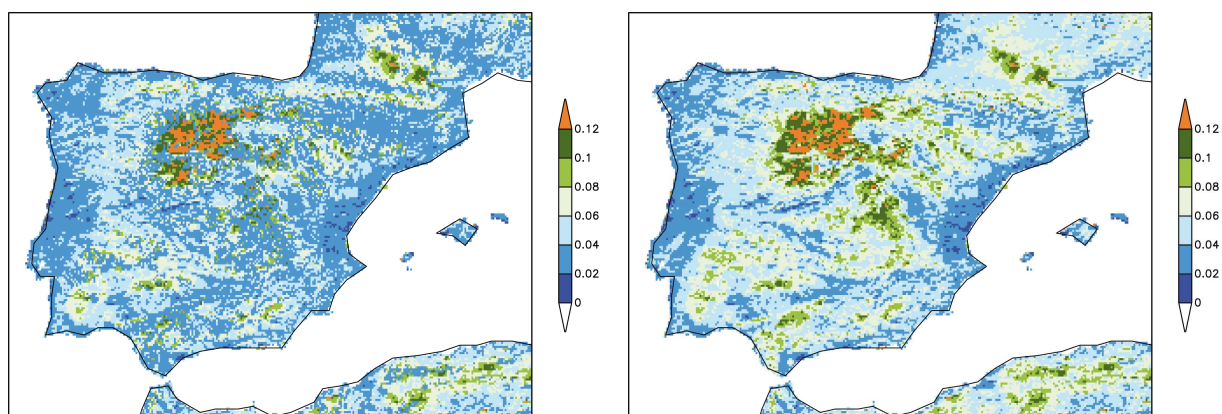


Figure 7.7.: New distribution of amplitude for Iberia domain (left), original amplitude on domain (right).

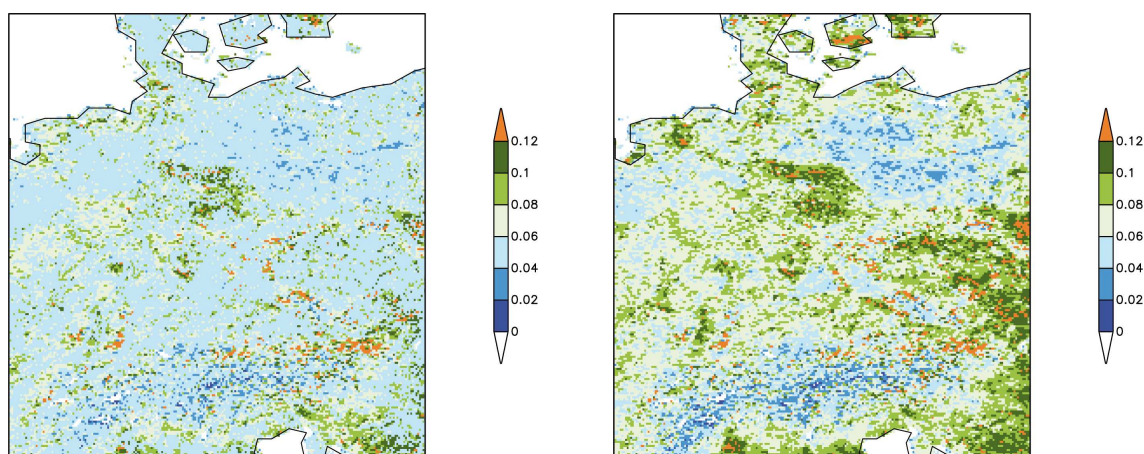


Figure 7.8.: New distribution of amplitude for Central Europe domain (left), original amplitude on domain (right).

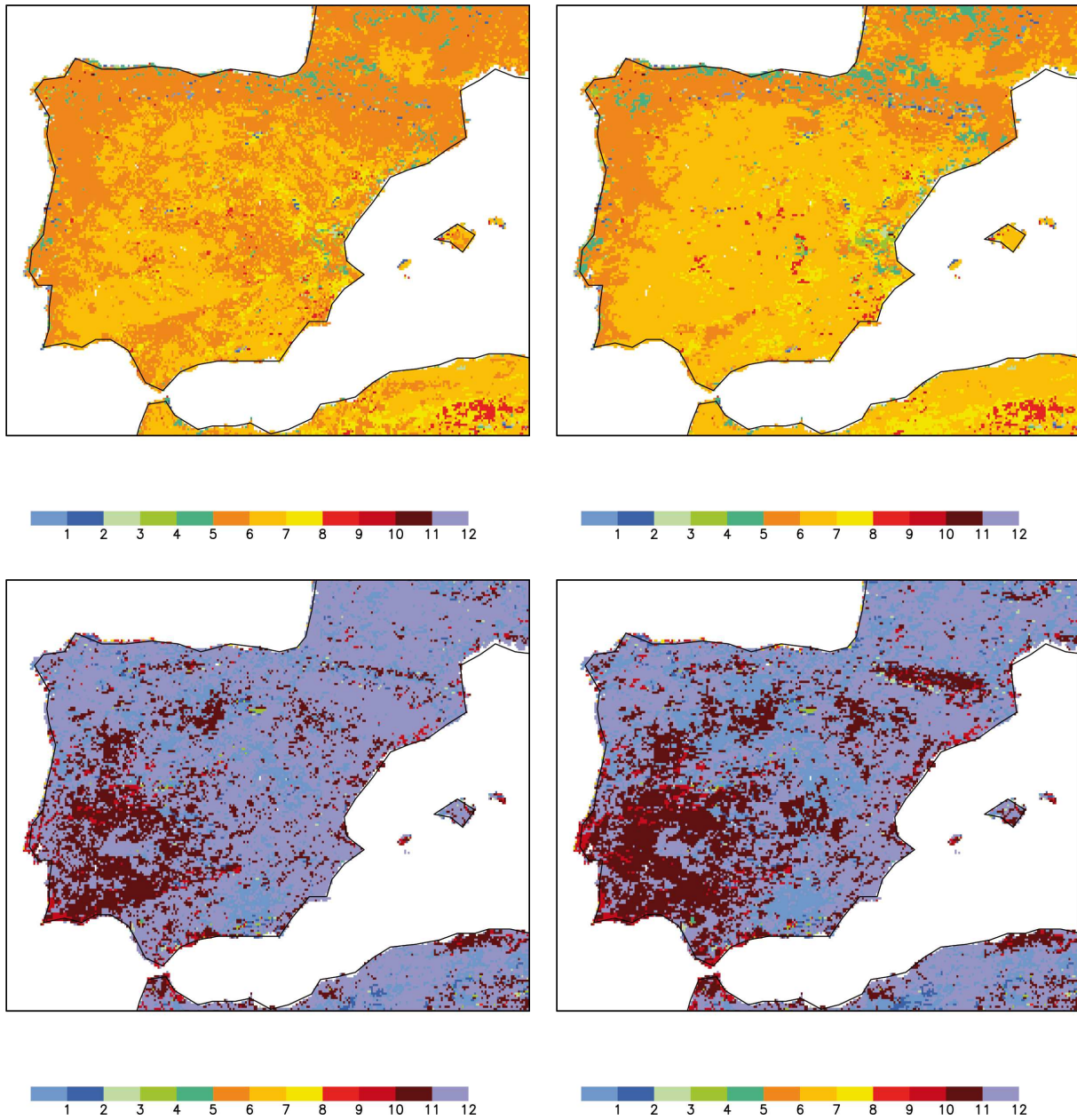


Figure 7.9.: Phase: Top date of maximum, bottom date of minimum for Iberia, after application of LUCHS (left), original (right). [Jan=1,...,Dec=12], colours are attached to seasons: bluish (DFJ), greenish (MAM), yellowish (JJA), reddish (SON).

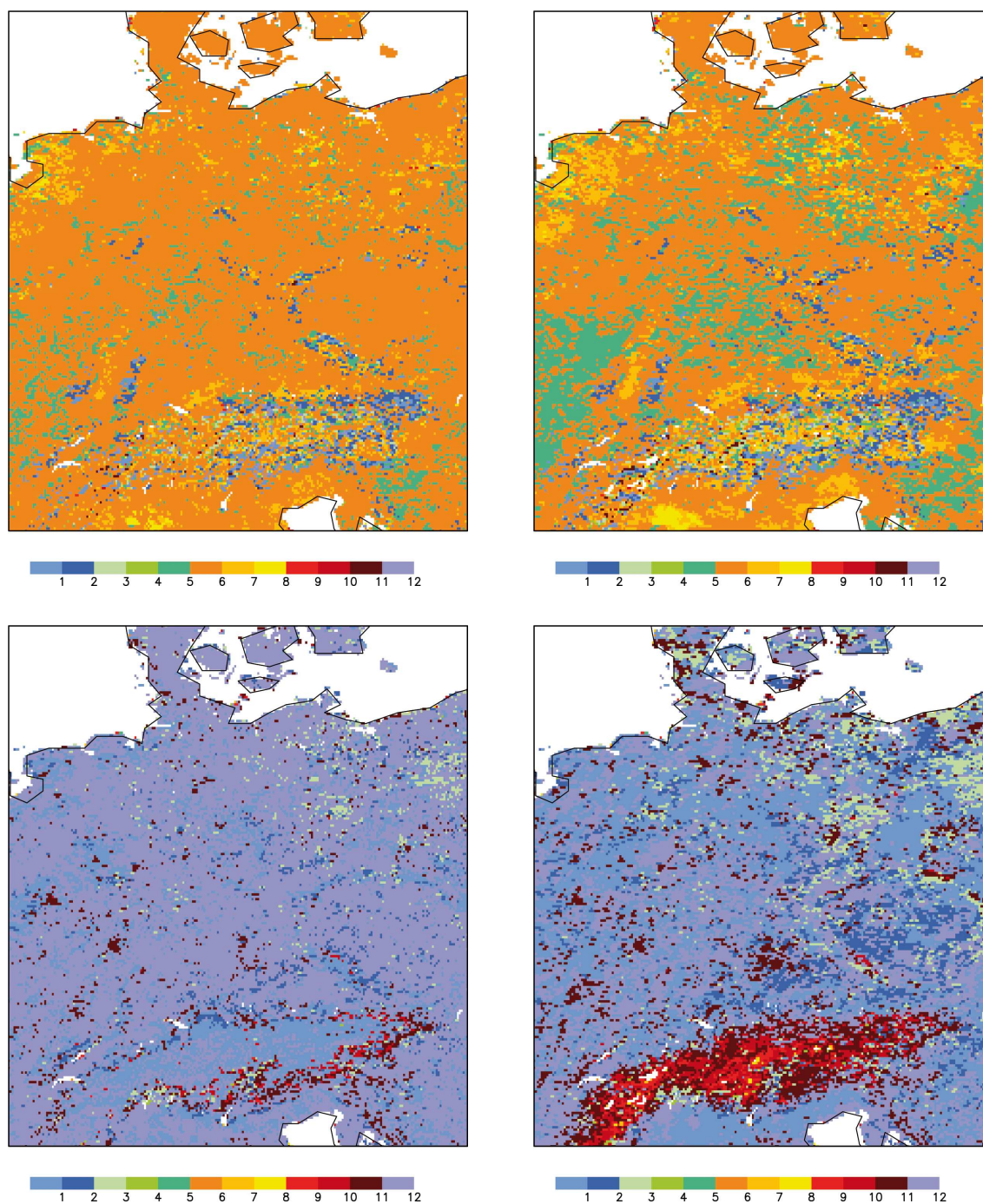


Figure 7.10.: Phase: Top date of maximum, bottom date of minimum for Central European, after application of LUCHS (left), original (right). [Jan=1,...,Dec=12], colours are attached to seasons: bluish (DJF), greenish (MAM), yellowish (JJA), reddish (SON).

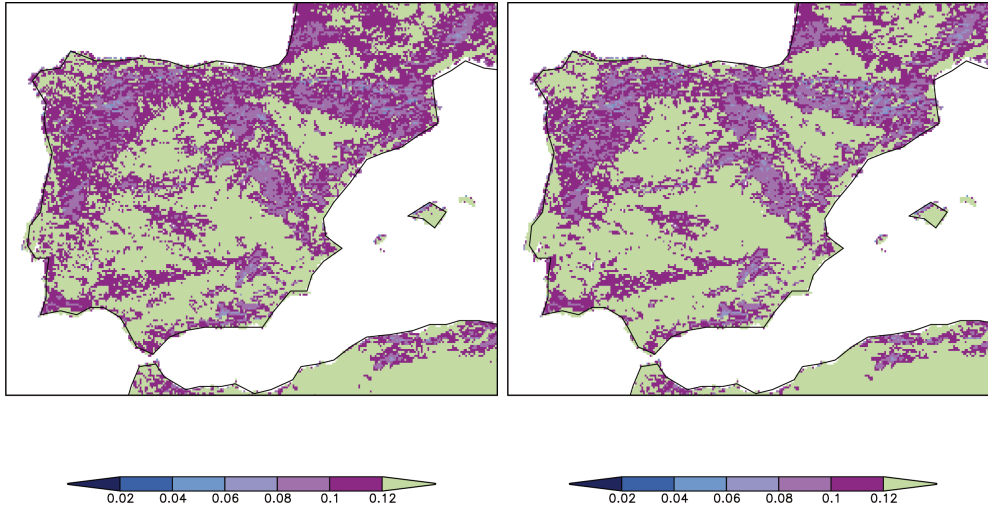


Figure 7.11.: Distribution of albedo minimum for Iberia domain: New distribution of LUCHS (left), original (right).

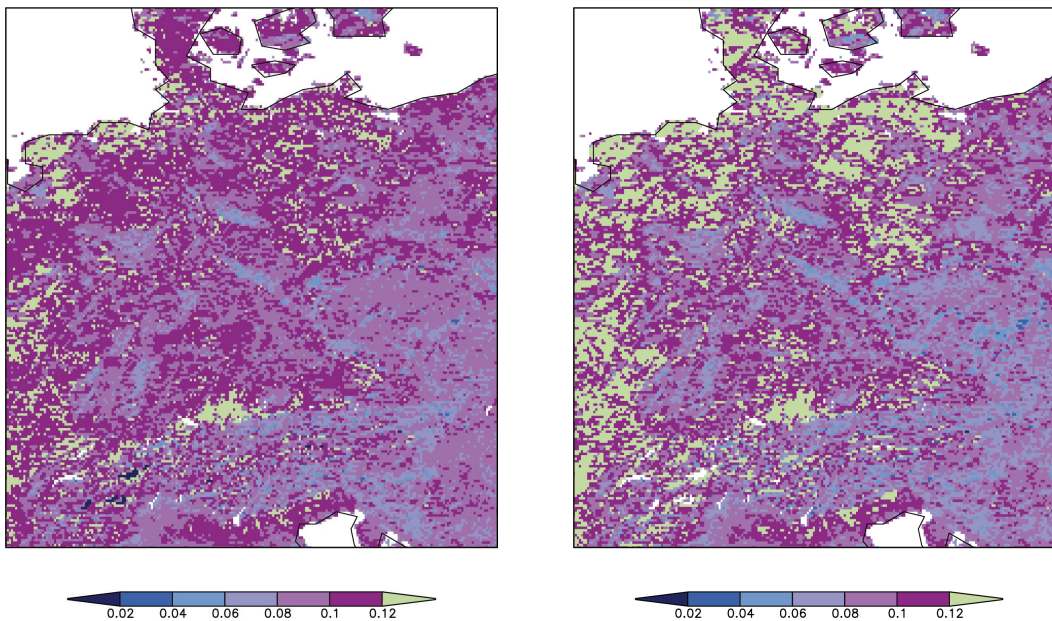


Figure 7.12.: Distribution of albedo minimum for Central European domain: New distribution of LUCHS (left), original (right).

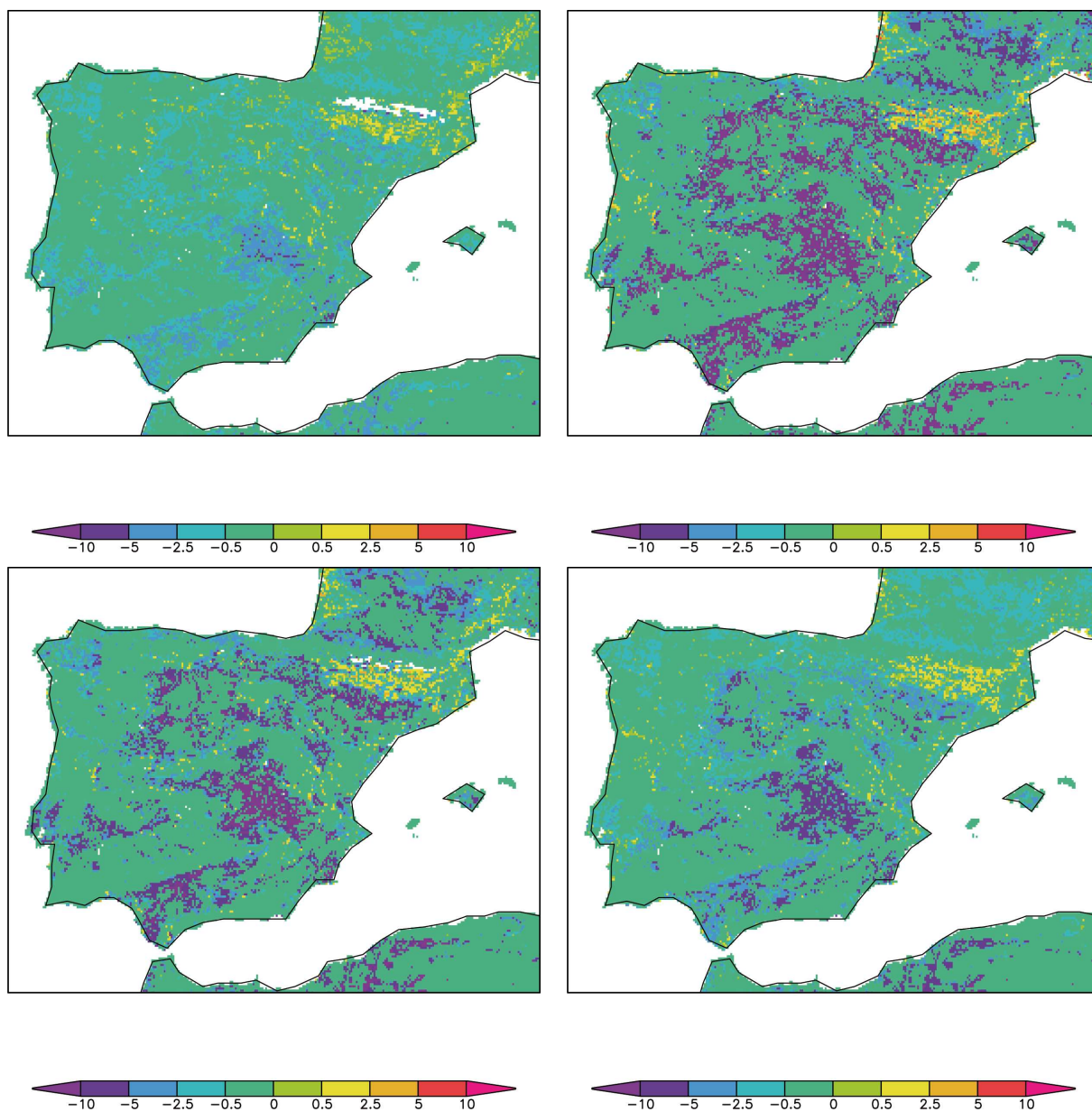


Figure 7.13.: Radiative perturbation in $[W/m^2]$, Iberian Peninsula, seasonal mean: DJF (top left), JJA (top right), MAM (bottom left), SON (bottom right).

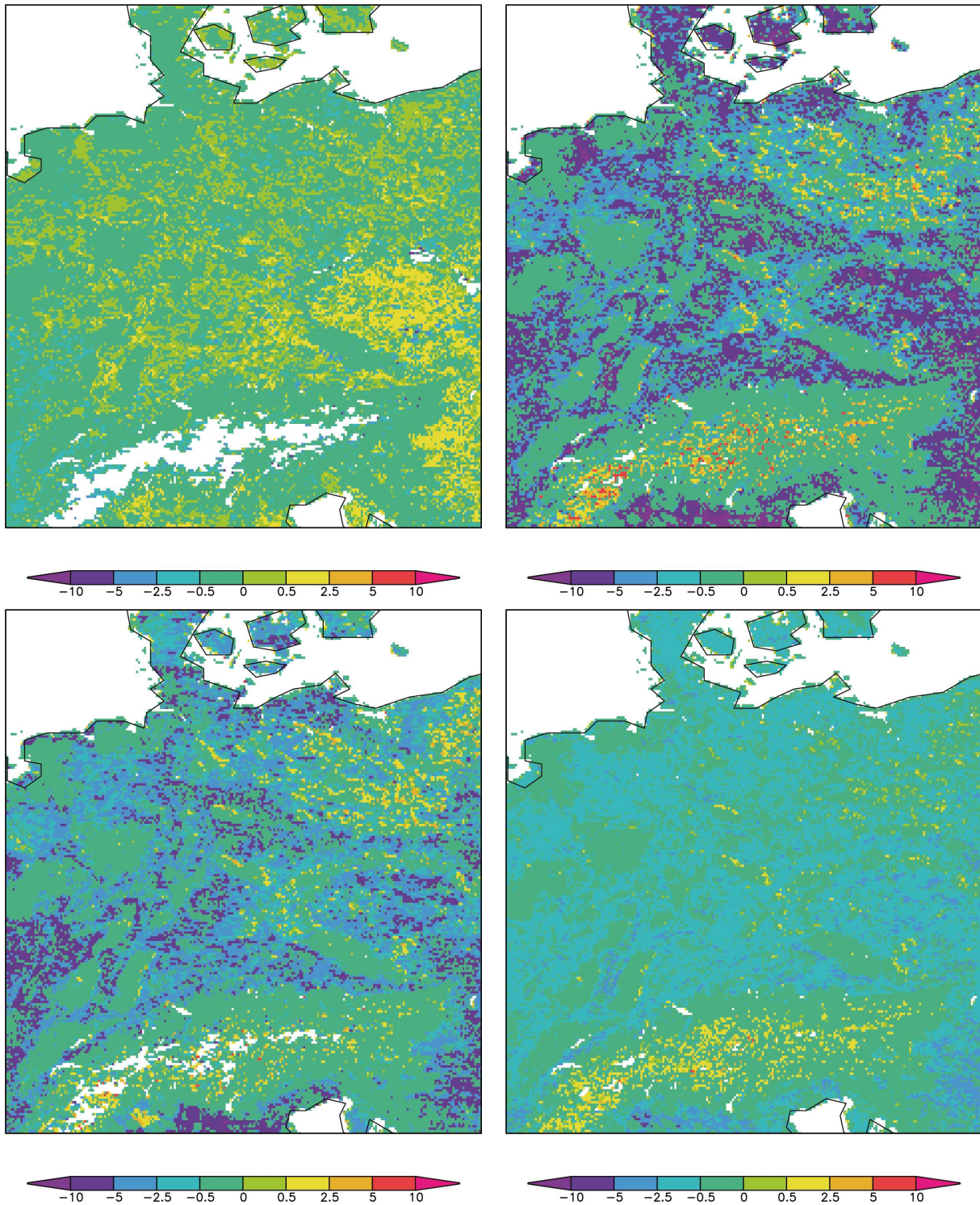


Figure 7.14.: Radiative perturbation in $[W/m^2]$, Central Europe, seasonal mean: DJF (top left), JJA (top right), MAM (bottom left), SON (bottom right).

8. Conclusions and Outlook

8.1. Conclusions

To investigate regional aspects of land-atmosphere interactions, the lower boundary description for climate models should be able to represent a realistic annual cycle of the parameters albedo, Leaf Area Index and vegetation ratio.

For the annual cycle of albedo a new approach is developed in order to provide

- realistic annual cycle of albedo
- realistic regional specification of the albedo
- transfer of observed albedo information in space
- transfer of observed albedo information in time

Changes in the albedo have a strong influence on climate simulations. This is shown by results of the sensitivity studies here, and is also documented (e.g., Rechid and Jacob, 2006; Pongratz et al., 2009a; Vamborg et al., 2011). Following the concept of radiative perturbation, changes of albedo values below 5% may effect the reflected global radiation by in the order of $\pm 10 W/m^2$.

A new concept for the albedo description for REMO is needed, as the lower boundary in REMO (Surface Library for REMO (SL4R)) shows discrepancies compared to observations i.e. the annual cycle of albedo. In comparison to satellite observations, the amplitude and phase of the annual albedo cycle are showing a too homogeneous pattern. Additionally in case of land use change studies, the parameterization scheme uses different constant data sets. Changes in one of them can lead to unexpected values in the composite albedo. These aspects are demanding a new approach for describing the albedo within the lower boundary conditions instead of an adaptation of the albedo scheme within the SL4R.

With the new approach called Land Use CHaracter Shifts (LUCHS), techniques from remote sensing are combined with climate model techniques. Land cover maps derived from satellite data are used to receive information for each land cover type. Therefore, a normalized annual cycle of albedo can be extracted for every land cover type, which includes the regional-dependent amplitude and phase of the annual albedo cycle. By using the annual albedo characteristics for one certain land use type as master information, the land use shift is then transferring this information onto areas, where an expansion of this land use type is considered. In order to keep regionally specific conditions, a combination of a land use type characteristic and a recent minimum albedo as autochthonous information is integrated within LUCHS. This results in new distributions of albedo annual cycles, reflecting characteristics of the transferred land cover type, which are implicitly attached to regional

floral, soil and cultural specifications. LUCHS is not free of assumptions and uncertainties, but by directly using observations, it is parameterization-independent.

There is no obvious dependence of the vegetation on the albedo, but the other way around: The vegetation status can be detected by observing the albedo. In any case LUCHS is usable for describing changes in the vegetation indices LAI and vegetation Ratio. For time ranges in the order of ± 100 years, we can expect that the plants albedo, LAI and vegetation ratio characteristics does not change drastically.

I propose and recommend to rely on observed climatologies with a small uncertainty caused by shifting, than on unrealistic but fully parameterized annual cycles of those parameters.

Technical application

LUCHS is no model internal programme, therefore the performance of REMO keeps unchanged. The procedure of LUCHS itself is very fast and of low computational costs. If the ingoing data sets for LUCHS, an observed albedo data set and the needed land cover maps on the same horizontal resolution, are not available, the preparation of those is the main time consuming part, besides a needed storage capacity for globally highly resolved albedo data of about 5 TB.

It must be said that for land use change scenario simulations by using LUCHS includes a recalculation of the reference simulation, the so-called “control run”, as the albedo differences within the albedo of SL4R and the observed albedo used for LUCHS is to high.

For the calculation for the control period the albedo data set needs to be replaced only in the start option of REMO. For land use change scenarios an automatic integration of the albedo maps with changed albedo will have to be integrated.

One major advantage of using LUCHS for investigation of land use changes is the usage of existing albedo data in high horizontal resolution. For receiving the surface albedo information in the model target resolution interpolation is needed, which increases uncertainties. LUCHS prepares the information on the highest resolution possible. The final albedo maps need only one step of interpolation while remapping onto the target resolution.

LUCHS is perfectly usable for fine resolution, as for example in the new version of a non hydrostatic REMO.

Comparisons of REMO simulations with land use change scenarios by LUCHS to existing simulations with the albedo of SL4R should only be done for model internal validation of REMO.

8.2. Outlook

LUCHS is not fully tested yet. First a long-term simulation comparable to the control period is needed in order to evaluate the impact of the observed albedo data within REMO simulations.

Afterwards, LUCHS can be applied for land use change scenarios as given by the Land Use Harmonization Protocol (LUH-P), of the Global Ecosystem Laboratory, University of New Hampshire (Hurt et al., 2006) (see also section 1.1).

Further an application of LUCHS in other models could be of interest. As the approach for the annual albedo cycle within JSBACH is similar to the SL4R, the problematic of choosing the correct albedo-weights (α_{soil} and α_{veg}) is the same.

Comparisons of albedo observation of MODIS to annual albedo cycles including snow in the MPI-OM Earth System Model (including JSBACH) reveal offsets in albedo values of several percent and inverse phases of the annual albedo cycles for many river basins over the world (Hagemann et al.: Evaluation of land surface water and energy fluxes, in preparation for Journal of Advances in Modeling Earth Systems (JAMES).)

This implies that the parameterized albedo in JSBACH is also not able to represent realistic annual cycles of the albedo without snow. LUCHS gives also an option for validating and investigating the albedo within JSBACH.

A. Historical development of MPI-M land surface.

The surface library got developed over long time and was adapted several times. Its historical basis is described in Claussen et al. (1994), and was originally created for ECHAM4 as a quick integration of vegetation in a global Earth system model before a full coupling with a vegetation model was available. For the horizontal distribution of plants, a catalogue of ecosystem types, described by Olson and Allison (1983) was used, whereby to each class a static based allocation of the vegetation parameters albedo, leaf area index, vegetation ratio, roughness length was done. With Wieringa (1992) and Wierenga (1993) a roughness length for the simple surface types was possible.

According to Henderson-Sellers et al. (1986), annual mean albedo values for thirteen classes of simple surface types of the were available. A translation table, given in Claussen et al. (1994), is assigning albedo values to each Ecosystem Type as fractional combination of simple surface types. The combination of fractional mean albedo values was taken as a mean albedo in case of a complete cover through the ecosystem type. The same procedure was done for roughness length. A maximal and minimal value (growing and dormancy seasons) for the LAI and vegetation ratio, collected by Lieth and Esser (unpublished) for their own vegetation cover classes, was used, by allocating Lieth and Esser vegetation classes to the Olson ecosystem types.

The first main adaptation of GCM, namely the ECMWF model in the MPI-M Hamburg version. (ECHAM) lower boundary data due to vegetation of Claussen et al. (1994), was made by Hagemann et al. (1999). Therefore, a new version of the Global Ecosystem Types (GET) of Olson (1994) was included. The U.S. Geological Survey (USGS) National Center for Earth Resources Observation and Science (EROS) the University of Nebraska-Lincoln (UNL) and the Joint Research Centre of the European Commission (JRC) distributed a 1 km homolosine projected data set (U.S.Geological-Survey, 2001). The 74 of the 94 ecosystem classes were derived from NDVI data (see also chapter 3) of NOAA AVHRR for the period April 1992 to March 1993.

In the satellite derived land cover maps 70 of 94 possible Olson ecosystem types were provided. As only 45 different types were used in Claussen et al. (1994), referring to the description of Olson and Allison (1983). For the remaining unclassified 30 new ecosystem types a guessed allocations due to type similarities was done by Hagemann et al. (1999). It included also a correction of Leaf Area Index (LAI) and Vegetation Ratio (c_v) by using a 0.5° satellite derived vegetation indicating data set (LASUR GVI¹) (Berthelot et al., 1994). This vegetation index data set, basically an

¹Land Surface Reflectance (LASUR) is a postprocessing of the NOAA/AVHRR Global Vegetation Index (GVI) product.

atmospheric corrected NDVI, was used as an *fapar* data set by Hagemann et al. (1999). Even though the GVI data set of Berthelot et al. (1994) is used for the LAI and c_v correction as well as for the derivation of the growing factor between 40° north and south, the two information are independent.

For the recalculation of an LAI and vegetation ratio of the GVI data, the assumption is used that *fapar*, LAI and vegetation ratio are related by following formula:

$$fapar = cv * (1 - e^{-\frac{0.5 * LAI}{cv}}) \quad (A.1)$$

In fact this formulation is a simplified assumptions of three arguments: First by Monsi and Saeki (1953) concerning an adaptation of the Beer-Lambert Law to absorption within plant stocks (for details, see equation B.1 in appendix B). Second, by the idea that the albedo is a linear combination of the reflection over vegetation and the reflection of the remaining part. Third case is a method to include the fact of a so-called “clumped vegetation” due to the effect that vegetation is occurring in spatial concentrations.

Expressing the *fapar* as a combination of Beer-Lambert law expressed for vegetation with the assumption of a disjunct separation of the albedo and *fapar*, drawn to the vegetated part, and a clumped LAI is resulting in equation A.1. It is a highly theoretical interrelationship. And it is not invertible to obtain only one fitting pair of values for LAI and vegetation Ratio at one point, as shown in figure A.1.

Here, the plotted surface in figure A.1 is indicating all possible pairs of Leaf Area Index and Vegetation Ratio values, (LAI | c_v), for obtaining a *fapar*, following the equation A.1 with an extinction coefficient of $K = 0.5$. A simple inversion of the equation to reveal LAI and Vegetation Ratio out of a *fapar* data set is impossible. Therefore, Hagemann et al. (1999) used as second requirement: the difference of the obtained result to the LAI and Vegetation Ratio as given in the expanded list of ecosystem types with its allocations from Claussen et al. (1994) and the extension of guessed similar values, should be minimal.

The method is described in Hagemann et al. (1999) but it should be noted here that a correlation of the maximal and minimal *fapar* value to grid boxes of different content amounts (60%, 70%, 80% and 90%) of a to 0.5° upscaled ecosystem Types map was done. Therewith it is also assumed that a maximal Leaf Area Index and maximal Vegetation Ratio is correlating to a maximal fraction of absorbed photosynthetic radiation and vice versa. Several studies have shown that satellite derived vegetation indices as NDVI and *fapar* or matching indices, have a quite low sensitivity for LAI values beyond 3 (e.g., Myneni et al., 1997; Carlson and Ripley, 1997; Tian et al., 2000). Therewith, the signal for *fapar* (or NDVI) might be already saturated, whereby the maximal leaf area is still in a growing phase.

The corrections to the allocations of Claussen and its enhancement are reaching for the LAI from a reduction of around 5 LAI points to an elevation of about 3 LAI points. The changes are mainly about 0.09 for the growing season and 0.07 for the dormancy season. The changes in the vegetation

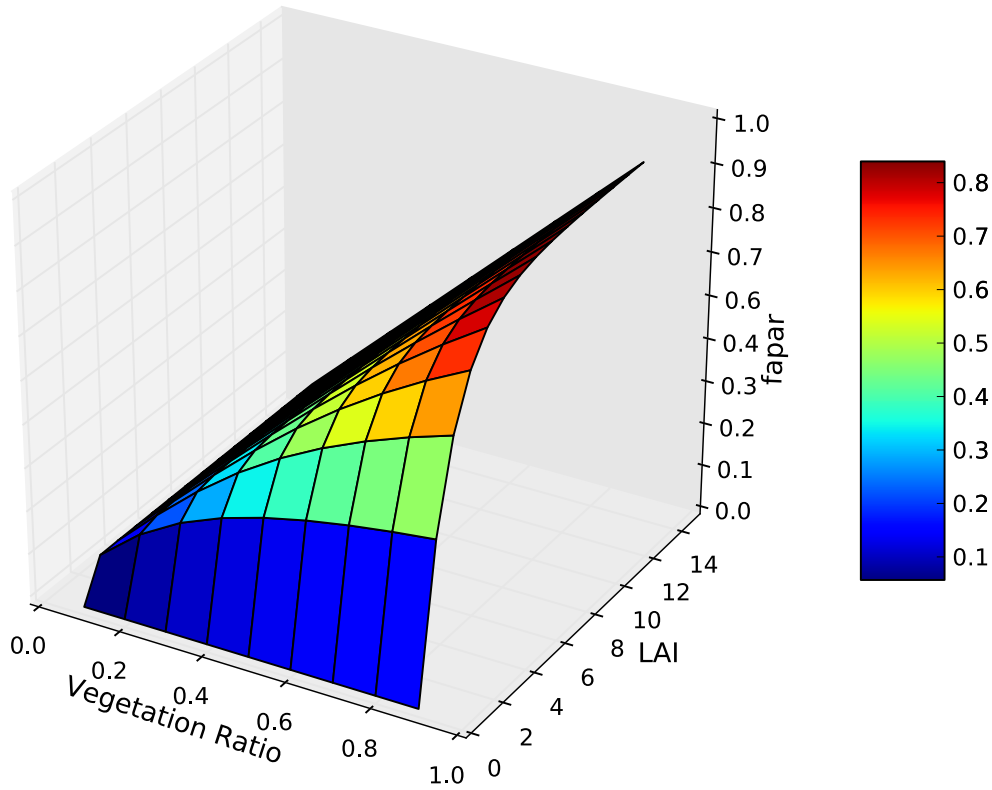


Figure A.1.: f_{apar} in dependency to LAI and Vegetation Ratio as formulated in equation A.1.

ratio show the same behaviour spanning from -0.66 to 0.55. The mean change for the growing season is a reduction of -0.02 and a mean enlargement of the vegetation ratio of 0.01.

All the explained assumptions and procedures are resulting in a look up table, in which every ecosystem type of the Global Ecosystem Types (GET), a Leaf Area Index for growing season $\Leftrightarrow LAI_{max}$ (LAI_g) and Leaf Area Index for dormancy season $\Leftrightarrow LAI_{min}$ (LAI_d), as well as a c_{vg} and c_{vd} is allocated. Neglecting at this point the methods for the allocation of the remaining parameters such as forest ratio, field capacity, soil texture, the procedure of transferring the GET attributed information to a spatial distribution is now explained.

Also, it should be remembered that the ingoing GVI data set of Berthelot et al. (1994) is used for the correction of the LAI and c_v in a resolution of 0.5° . The detour by allocation to a 1 km data set and the following upscaling, does not improve the accuracy of information. Additionally it must be clarified that the horizontal distribution of each parameter is technically hypothetical. It is using the assumption that the attributed value of the parameters of each GET is globally valid.

For the further development of the surface library, a first attempt for separating an albedo for

A. Historical development of MPI-M land surface.

vegetation albedo and a remaining albedo was used, while combining ERBE² albedo satellite observation data. The linkage to the virtual vegetated albedo and the observation data was created by using the disjunctive formula:

$$\alpha = \alpha_{ERBE} * (1 - cv) + \alpha_{virtuell} * cv \quad (\text{A.2})$$

The vegetation distribution was available on 0.5° resolution based on look up tables. As vegetation is usually not to 100% dense and appears often in multi layers as mixtures of different vegetations types, the combination with observed albedo data made sure that an albedo diversity on non vegetated and sparse vegetated surfaces was not equalized through one standard value for bare soils.

²Earth Radiation Budget Experiment

B. Explanations to the usage of Beer-Lambert Law and Vegetation Albedo

Monsi and Saeki (1953) showed that in a vertical column of vegetation layer the light absorption through vegetation is following the absorption within liquids described by the Beer-Lambert law, whereby the extinction coefficient can be assumed being a product of the leaf area and a plant specific extinction coefficient k .

$$I_1 = I_0 * e^{-k*LAI} \quad (B.1)$$

I_1 is the remaining radiation at the canopy bottom and I_0 the incoming radiation at top of canopy. They distinguished different extinction coefficients k different plant types. For $k = 0.3-0.5$ for plants belonging to Grass Types, and $k \approx 0.7$ for plants belonging to Leaf Types (herbaceous perennial plants). Under isotropic conditions, if incoming and outgoing radiation is equally distributed in all directions, and additionally assuming a non clumped and spacial equal distributed and orientated leaves, it is common to use $k = 0.5$ as extinction factor (Dickinson, 1983).

To bring the vertical information of vegetation absorption derived from Monsi and Saeki (1953) into a horizontal information, another theoretical assumption is used. Therefore, the Beer-Lambertian law with its formulation for vegetation in equation B.1 is used to conclude the albedo of pure vegetation:

$$\alpha_{vegetation} = \frac{I_1}{I_0} \quad (B.2)$$

$$\alpha_{vegetation} = \frac{I_0 * e^{-k*LAI}}{I_0} \quad (B.3)$$

$$\alpha_{vegetation} = e^{-k*LAI} \quad (B.4)$$

The formulation of B.4 is of course a very crude assumption. For a vertical column it could be retraced that as more layers of leaves are covering the surface as less light can pass the vertical column. Incoming solar radiation gets absorbed by top leaves, transmitted light gets absorbed by leaves underneath. Shadow effects are further reducing the radiation until it reaches the surface. For reflections of top of canopy, the vertical mass of leaves which is represented by the LAI, does not necessarily matter. “If all the transmitted light were subsequently absorbed and all the light reflected from the upper leaf surfaces were to escape the canopy, the canopy albedo would correspond to the leaf albedo” (Dickinson, 1983). For high amounts of biomass or so-called dense vegetation as Rainforest, it is only the top vegetation layer dominating the albedo of the vegetation cover.

Different species have different colours, also same species may have different colours for example: a red cooper beech and a green beech. As shown in chapter 3 the plant colour is determined by

different absorption rates in the visible spectra. Albedo observation of uniform filled grid boxes are determined by the plant specific albedo of this grid box. The albedo for grid boxes showing sparse, clumped vegetation the underlying surfaces contribute to the albedo in this grid box. This reveals the necessity of an information on fractional vegetation cover.

Gutman and Ignatov (1998) described the ambiguity in simultaneously derivation of a horizontal and vertical vegetation indices by using the NOAA AVHRR NDVI data.

There is no deny that the biomass expressed as leaf area index LAI does play a role, but it is also clear that is is not the controlling factor determining a plant canopy albedo.

This was the driving idea, for mixing partitions of albedos. The second assumption used for the equation A.1 is, the idea of a linear combination of the albedo, in which the total albedo of a grid box is a sum of disjunctive parts. Therefore, it can be separated into the contribution of the vegetation and the remaining parts. The total albedo can be calculated as following:

$$\alpha_{total} = c_v * \alpha_{vegetation} + (1 - c_v) * \alpha_{remains} \quad (B.5)$$

Focussing now on the vegetated part, and assuming that the loss of energy is only coming through the plants photosynthesis, the radiation balance for for a normalized portion of radiation could be formulated for vegetation only as:

$$1 - \alpha_{vegetation} - f_{apar} = 0 \quad (B.6)$$

From the combination and rearrangement of the equations B.6 and B.4 the f_{apar} is assumed to be

$$f_{apar} = 1 - \alpha_{vegetation} \quad (B.7)$$

$$f_{apar} = 1 - e^{-k*LAI} \quad (B.8)$$

The f_{apar} in equation B.8 is in the sense of modelling only valid, if the vegetation is horizontally equal distributed within the grid box. Within Remote Sensing and the development for a method to estimate the f_{apar} out of spectral reflectance Asrar et al. (1992) proposed to use a so-called “clumped” leaf area index, to account to the fact of a sparse vegetation. Knorr (1997) is explaining: “This type of spatial concentration, or *clumping* of vegetation has a strong influence on the dependence of f_{apar} on LAI (Asrar et al. (1992)), and thus on photosynthesis and the energy balance. If one neglects the effect of vegetation height, then the two-flux equations [...] are taken for the fraction f_c of a grid cell alone, with the LAI (Λ), replaced by the “clump” LAI, $\Lambda_c = \Lambda/f_c$. This is the approximation used in the standard model [BETHY]”. In addition the f_{apar} is only valid for vegetated area, which is assigned by the vegetation ratio, c_v (which is assigned with f_c in Knorr (1997)). According to clumped vegetation, equation B.8 changes in:

$$f_{apar} = c_v * (1 - e^{-k*LAI}) \quad (B.9)$$

The major contradiction in the usage of equation B.9 is that f_{apar} is only defined for wavelengths between 0.4-0.7 μm (see section 3.2).

C. Regression of Albedo and Vegetation Index

Presented here is a reproduction of the regression method used in Rechid et al. (2008). Therefore, α_{amap} and VI_{amap} of MERIS Albedomap data got prepared according to the same data preparation. Hence, only data pairs were allowed for the correlation, if:

1. $0.08 \leq VI_{amap} \leq 0.8$
2. $|VI_{amap-max} - VI_{amap-min}| \geq 0.1$
3. $VI_{amap-datacounter} \geq 3$

The Albedomap vegetation index VI_{amap} is not identical with an *fapar* index e.g. of MODIS. Also, the horizontal resolution of the Albedomap data for the regression is finer by a factor of ten. Therefore, figure C.1 shows the comparability of the reproduced regression with Albedomap data to the original regression results of MODIS data. In the center it shows the original outcome of the correlation of MODIS albedo and *fapar*, of Rechid et al. (2008) globally in 0.5° resolution. The Albedomap regression for Europe is shown in the upper part and for Africa in the lower part. In comparison to the original plot, the Albedomap reproductions have similar patterns. For Europe it is evident that the Albedomap regressions show more details but a dominating positive correlation coefficient for central Europe. In contrast, for the Iberian Peninsula a negative correlation coefficient is observable. The detailed differences for the Alps, Dinaric Alps and Carpathian Mountains are not visible in MODIS, due to the upscaled resolution of 0.5° . The patterns of negative and positive correlations for Africa are very similar for both regressions. Therefore, one can conclude that statements about the Albedomap regression are also applicable for the MODIS regression.

Facts for understanding the results of linear correlations

The correlation coefficient r_{xy} is calculated as a Pearson product-moment correlation coefficient of linear correlation. It is the ratio of the sample covariance of the two variables to the product of the two standard deviations, following equation C.1, which is transformed explanatory to an easy ascertainable form, shown in equation C.4. Basically it is a method of a least squares estimation.

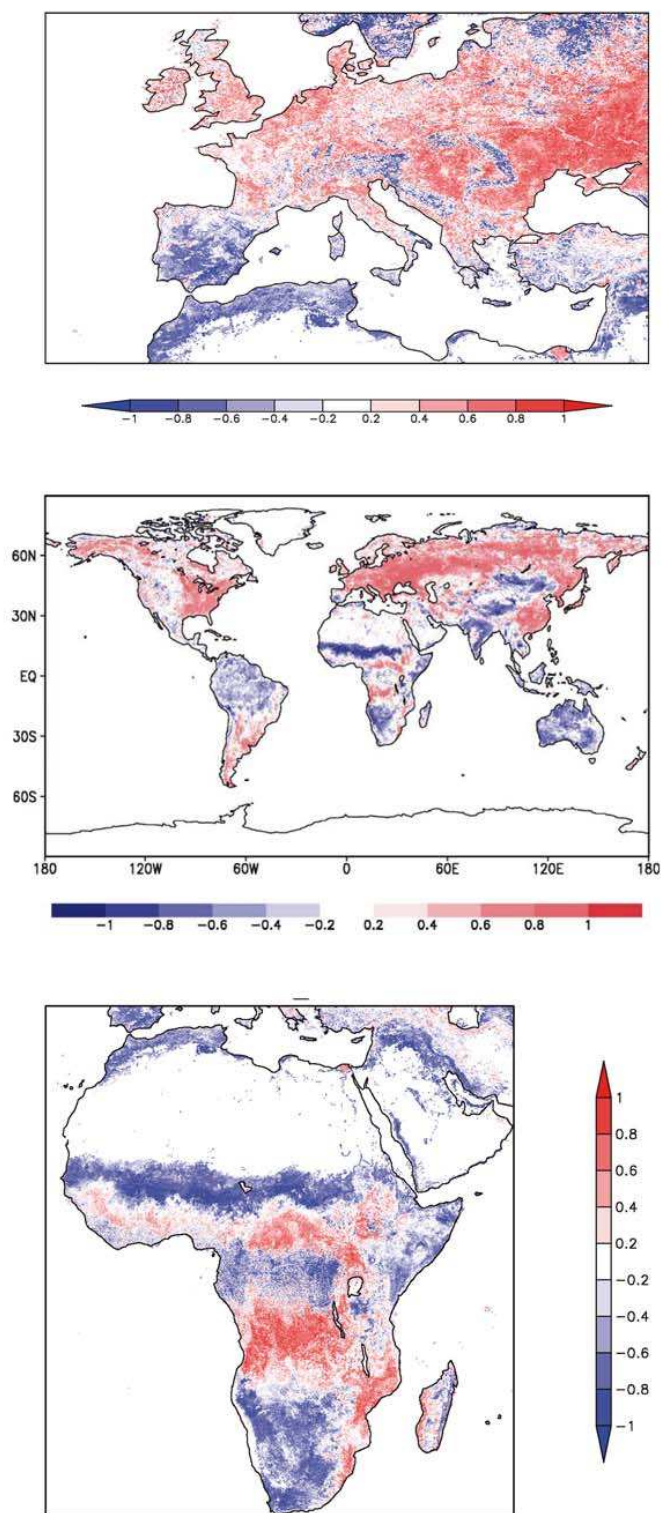


Figure C.1.: Correlation coefficient for correlation of α_{amap} to VI_{amap} in 0.05° horizontal resolution: for Europe (top), for Africa (bottom). Correlation coefficient for correlation of MODIS albedo to f_{apar} in 0.5° global from Rechid et al. (2008) (centre).

$$r_{xy} = \frac{Cov(X, Y)}{s_x s_y} \quad (C.1)$$

$$= \frac{E[(X - \bar{x})(Y - \bar{y})]}{\sqrt{E(X - \bar{x})^2} \sqrt{E(Y - \bar{y})^2}} \quad (C.2)$$

$$= \frac{\frac{1}{n-1} \sum_{i=1}^n [(x_i - \bar{x})(y_i - \bar{y})]}{\sqrt{\left[\frac{1}{n-1} \sum_{i=1}^n (x_i - \bar{x})^2 \right]} \sqrt{\left[\frac{1}{n-1} \sum_{i=1}^n (y_i - \bar{y})^2 \right]}} \quad (C.3)$$

$$= \frac{\sum_{i=1}^n [(x_i - \bar{x})(y_i - \bar{y})]}{\sqrt{\left[\sum_{i=1}^n (x_i - \bar{x})^2 \right]} \sqrt{\left[\sum_{i=1}^n (y_i - \bar{y})^2 \right]}} \quad (C.4)$$

Visualizing the argumentation, several cases of a Pearson product-moment correlation are demonstrated in C.2. The first row shows typical scatter-clouds of two variables and its corresponding Pearson product-moment correlation coefficient. As stronger an elongation of the scatter-cloud can be observed, the correlation coefficient is higher. The coefficient r_{xy} can be used as a measure of how strong the relationship can be seen as a linear process. A perfect linear association is reached, if the value pair's of x and y are describing a line. The correlation coefficient r_{xy} is a value between -1 and 1. A negative correlation coefficient is evident with an inversely arranged linear relationship. Therefore, high values of x correlate with low values of y, and vice versa. It is a matter of definition, but in Fahrmeir et al. (2004) a guideline is given to quantify the absolute linear correlation coefficient in strengths:

- “ weak correlation “ for $|r_{xy}| < 0.5$
- “ moderate correlation “ for $0.5 \leq |r_{xy}| \leq 0.8$
- “ strong correlation “ for $0.8 < |r_{xy}|$.

Following the first line in figure C.2, there is hardly an elongation observable for the scattered value pairs of a correlation coefficient about ± 0.4 .

The correlation coefficient by itself says nothing about the slope of the linear relationship between the two variables. This is demonstrated in the second line of figure C.2, where the correlation is perfect but the slope completely different. For the centre case with a slope of zero and a variance of zero the correlation coefficient is undefined. In the third line of the same figure, one can see that strong correlations, which are not able to be described as a linear process can not be kept by the Pearson product-moment correlation coefficient. For these scatter-clouds, r_{xy} is always zero.

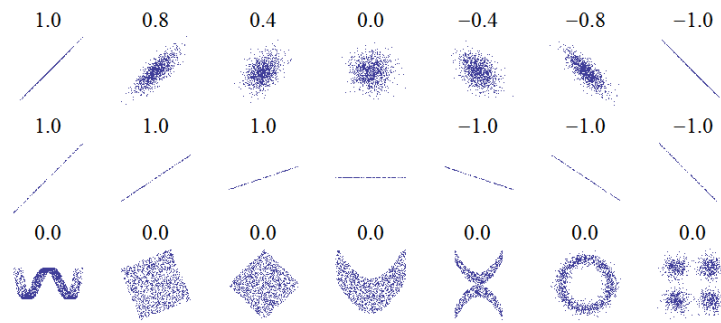


Figure C.2.: Examples for Pearson product-moment correlation coefficients, source: http://en.wikipedia.org/wiki/Pearson_correlation_coefficient, (29 August 2011).

A Pearson product-moment correlation coefficient is neither robust (e.g. for nonlinear correlation) nor resistant to outliers. Therefore, it might give solutions which are just dominated by one extreme outlier value, overwhelming a weaker underlying contrasting linear relationship as it is shown in figure C.3. Wilks (2006) used a data set with a calculated correlation coefficient of $r_{xy} = 0.61$ following the formula C.4. The outstanding outlier, marked with a red arrow, is influencing the correlation coefficient resulting in a moderate, positive correlation, even though it can be assumed via optical validation that the remaining data pairs in this example seem to have a stronger and additionally a negative correlation.

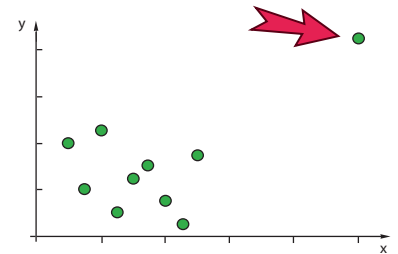


Figure C.3.: Lack of resistance through influence of one single outlying point, with $r_{xy} = 0.61$ (adapted from Wilks (2006)).

The interpretation of a Pearson product-moment correlation coefficient gains with some extra information, as a statistical significance and an estimation of the variability for the resulting correlation. For the statistical significance, a measure for a probability of producing a same result by chance, the so-called p-value, can be calculated. The methods are of high computational costs and differ technically in comparison to classical test statistics and the usage of distribution tables. With the calculation of the p-value no significance level is given in advance. The level of significance can be chosen arbitrary afterwards, but is commonly about 5% or $p < 0.05$. As well as for classical tests, the calculation of a p-value is based on a hypothesised distribution for the test statistic, which can be represented as the correlation coefficient itself. The corresponding p-value is representing the tailed area under the hypothesised distribution of the test statistic. The p-value is the probability of producing the same result by chance under the permission the null hypothesis is true.

The term r^2 specifies the proportion of the variability and can be seen as a measure of how well the linear regression is describing the data. As better a linear regression is, as smaller are the distances (residuals) of the data points to the regression model. As the correlation coefficient is more or less

representing a measure to quantify the amount of the x and y values having a similar distance to its means, the squared r_{xy} product indicates how many of the data pairs can be described with the assumed linear model. A perfect correlation would result in a r^2 equal to one. A r^2 of 0.6 can be interpreted that 60% of the data pairs can be described by the linear regression. It is obvious, that for a high amount of data a strong correlation of $r_{xy} = 0.8$ is evident with an $r^2 = 0.64$. Nevertheless, the r^2 -value is quite intuitive and has some advantages for quick interpretations of the goodness of the correlation.

The range of uncertainty for the correlation coefficient is represented by the standard error. In its calculation the variances of the ingoing data are used. The calculated error rises, if one the variances rises.

Within this work the offered method of the program `scipy.stats` called `linregress`¹ is used, to calculate the referred statistical parameters. In `linregress` the null hypothesis is the assumption that there is no slope within the linear regression, or in other words, that x and y are unrelated. The p-value is calculated as a two-sided test, using the inverse cumulative student-t distribution function assuming $n - 2$ degrees of freedom. As lower the p-value (e.g. 0.05 for a 5% significance level) as likely a linearity can be assumed, or the hypothesis that there is no slope can be rejected.

The results of the used Pearson product-moment correlation, with Albedomap data VI_{amap} versus α_{amap} for Europe are shown in figures C.4 and 6.9. The correlation coefficient is shown for the correlation levels as given from Fahrmeir et al. (2004). The blueish colours are indicating a negative and the yellowish colours a positive correlation. A strong correlation with a correlation coefficient of more than ± 0.8 is rarely to observe in figure C.4. A moderate correlation with $0.5 \leq |r_{xy}| \leq 0.8$ is occurring, but is rare. A weak correlation with a coefficient of ± 0.5 in yellow and turquoise colours is dominating. The r^2 -value, shown in figure C.4, is marking in orange and red, where more than 60% of the data pairs can be described by a linear equation, independent of its location parameters, which is not occurring often.

The corresponding p-value with a significant level of $p \leq 0.05$ is marked in blue in figure C.4. Some purple pixel in south of the Iberian Peninsula need to be pointed out. They do have a p-value of zero, but are corresponding with a correlation coefficient of -0.8 in the figure above.

The standard error for the residuals of the correlation coefficient is shown in figure C.4. Here an error estimation between 0.025 and 0.05 is dominating for the region of Europe. Some regions e.g. Ireland, the west coast of Great Britain and also the Alps and the northern part of the Iberian Peninsula, are showing higher error estimates for r_{xy} . The estimation for the standard error is calculated as

$$stderr_{estimation} = \sqrt{\frac{(1 - r^2) \left[\frac{1}{n-1} \sum_{i=1}^n (y_i - \bar{y}) \right]}{n - 2 \left[\frac{1}{n-1} \sum_{i=1}^n (x_i - \bar{x}) \right]}} \quad (C.5)$$

¹<http://docs.scipy.org/doc/scipy/reference/generated/scipy.stats.linregress.html>

Even though it includes all variances (the covariance, variance of albedo, and variance of the vegetation index), a major impact on elevating the error estimation is connected to a low data sample number n , which is in this case the number of valid 16d mean observations per pixel but is not shown here. A high standard error can also be a hint to outliers, but is no guarantee or a measure for outliers. Also it is not a method to give confidence intervals, but it can be used as an indicator of uncertainty in the estimation of the regression coefficient. It is not easy to judge which offset is tolerable.

A typical albedo difference for forest in comparison to agricultural land is about 0.05. In comparison, the magnitude of the error band with ± 0.05 is higher than typical differences of land use classes. An error offset or uncertainty band, of even ± 0.1 is in the same range as the amplitude of the mean annual albedo cycle for Europe itself (see table 6.1).

The threshold levels for the Standard Error in figure C.4 are indicating in yellow and reddish colours where the magnitude of the uncertainty band is in the same amount as the estimated albedo by a linear equation.

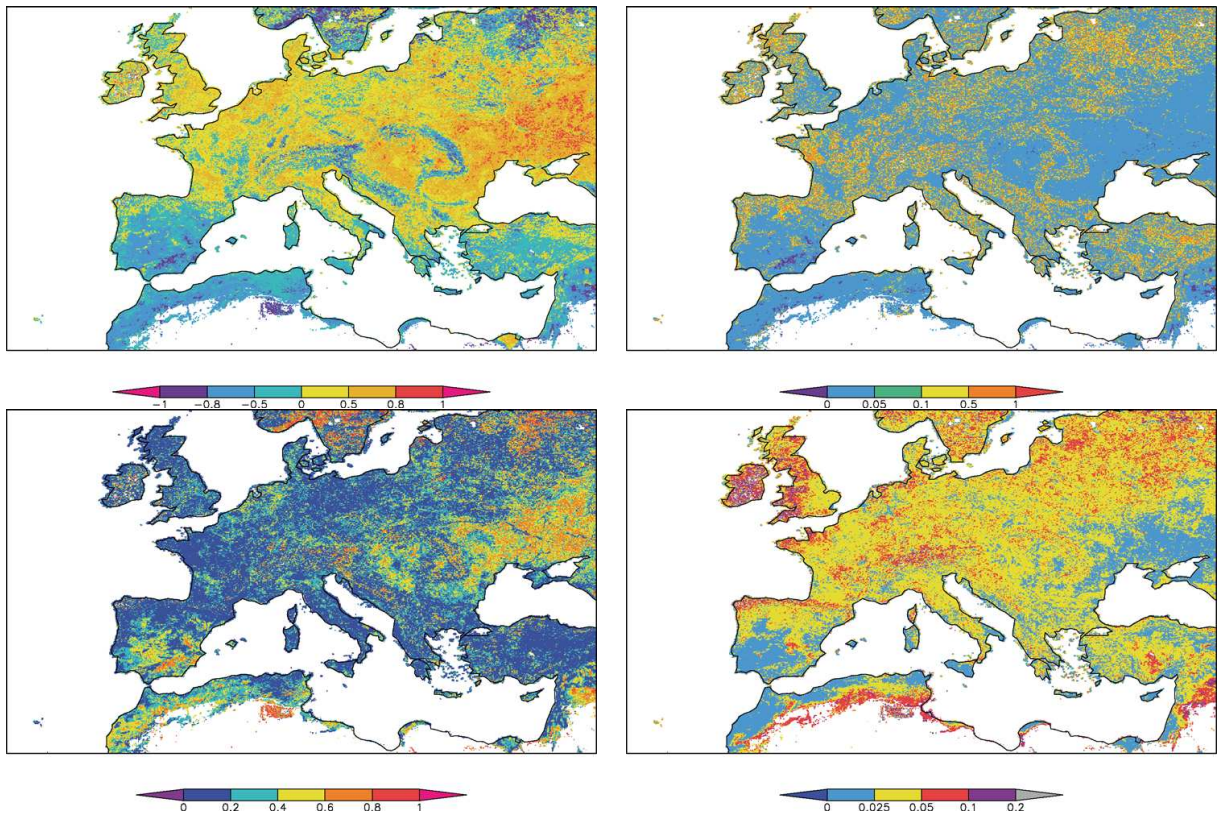


Figure C.4.: Top left: Correlation coefficient r_{xy} ; α_{omap} versus VI_{omap} . Top right: Probability of null hypothesis p-value; α_{omap} versus VI_{omap} . Bottom left: Variability of regression r^2 ; α_{omap} versus VI_{omap} . Bottom right: Standard Error of estimated r_{xy} ; α_{omap} versus VI_{omap} .

Equivalentents to Albveg and Albsoil

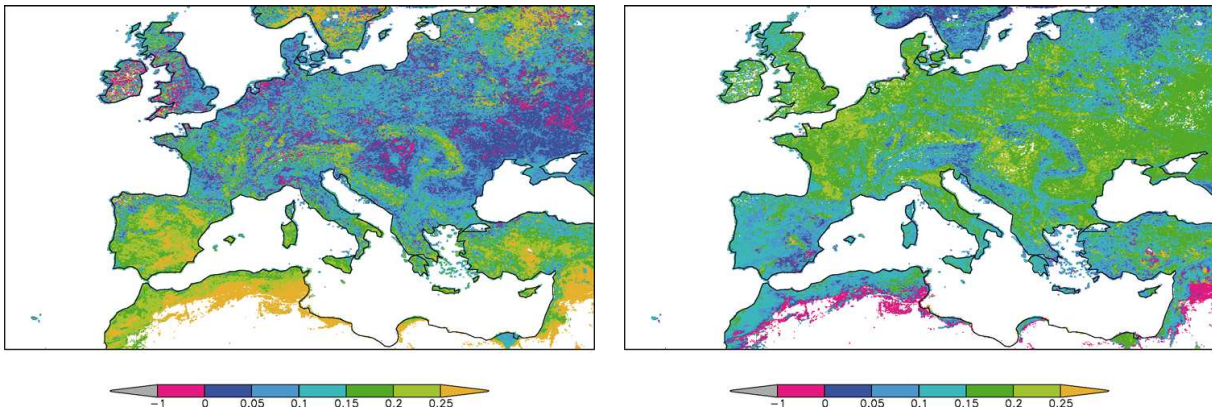


Figure C.5.: Left: “AMAP Soil Albedo”: regression intercept, including negative values. Right: “AMAP Vegetation Albedo”: regression intercept plus slope, including negative values.

In a regression, negative values for slope and intercept may occur. For the method, described in Rechid et al. (2008), those negative values were excluded, and replaced by suggestions (Thomas Raddatz, personal communication).

The amount of valid intercept values would shrink additionally if those values are excluded, as listed in table C.1. The valid data number in case of the $r_{xy} \geq 0.8$ would shrink from 3.56% to 3.2% or in case of a level for $r_{xy} \geq 0.5$ it would shrink from 36% in which one can assume a linear correlation down to 32.8%.

	number of negative pixels	fraction to total pixel in %
All	1 4677	4.22
$ r - se \geq 0.8 \wedge p \leq 0.05$	1314	0.37
$ r - se \geq 0.5 \wedge p \leq 0.05$	11117	3.20

Table C.1.: Negative Slope pixel

Still it is questionable if the intercept, even if negative values are erased, is able to represent an albedo value, especially a surface albedo with non-active vegetation. Also it is questionable, if slope plus intercept is representing a surface albedo in case of fully developed vegetation. A slope for linear equations is not necessarily between 0 and 1, it can exceed an inclination greater than ± 1 . Negative slope values can be as low that an added intercept does not exceed the negative range. Although those values can be excluded by definition, logically the production of negative values is a strong argument to rethink the validity of the interpretation of the regression results as albedo values.

Correlation for Africa

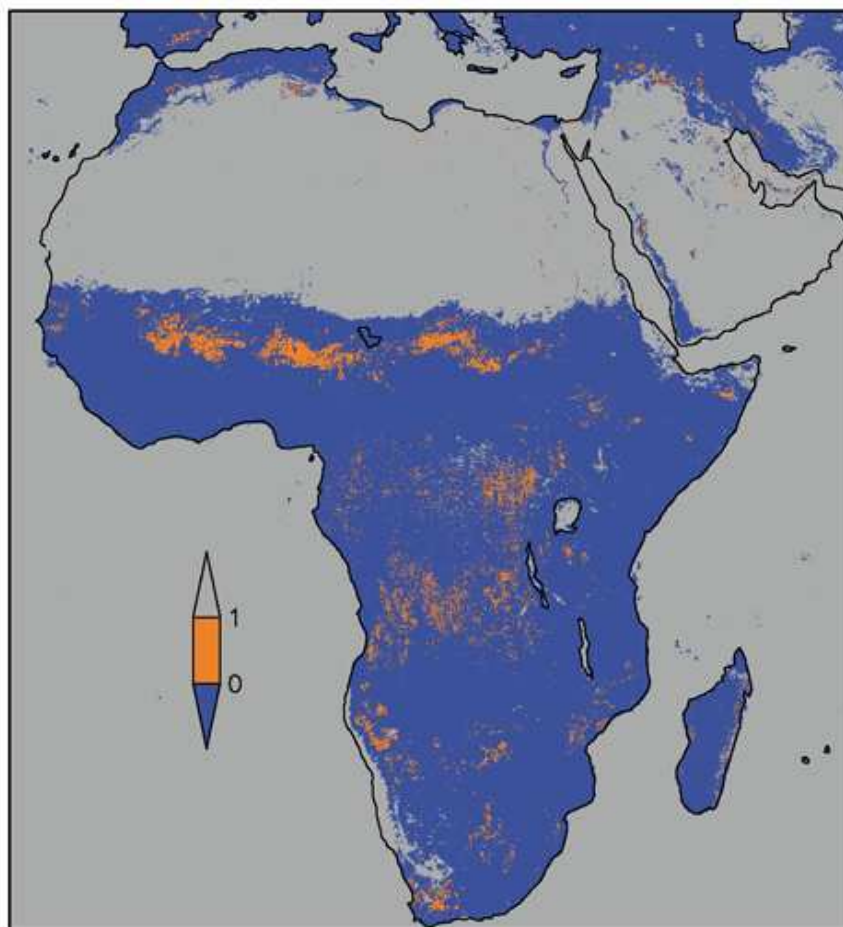


Figure C.6.: Orange: $|r| - se \geq 0.8 \wedge p \leq 0.05$ for Africa with Albedomap data α_{amap} versus VI_{amap} .

The summary of correlation results for Africa is shown in figure C.6. Even not in the Sahel a continuous band would allow a linear model to describe the relationship of vegetation and albedo. For the area around the Kongo basin, some pixels show the requirements of $|r| - se \geq 0.8 \wedge p \leq 0.05$ as true, but it has a very scattered appearance and does not imply a common validity.

References

- Alexandru, A., R. De Elia and R. Laprise (2007): Internal variability in regional climate downscaling at the seasonal scale. *Monthly Weather Review*, 135(9), 3221–3238.
- Asrar, G., R. Myneni and B. Choudhury (1992): Spatial heterogeneity in vegetation canopies and remote sensing of absorbed photosynthetically active radiation: A modeling study. *Remote Sensing of Environment*, 41(2-3), 85–103.
- Bartholome, E. and A. S. Belward (2005): GLC2000: a new approach to global land cover mapping from Earth observation data. *International Journal of Remote Sensing*, 26(9), 1959–1977.
- Berthelot, B., G. Dedieu, F. Cabot and S. Adam (1994): Estimation of surface reflectance and vegetation index using NOAA/AVHRR: Methods and results at global scale. In: *Communication for the 6th international symposium of physical measurements and signatures in remote sensing, ISPRS, Wal d'Isere, France, 17-21 Jan..*
- Betts, A. K., J. H. Ball, A. C. M. Beljaars, M. J. Miller and P. A. Viterbo (1996): The land surface-atmosphere interaction: A review based on observational and global modeling perspectives. *Journal of Geophysical Research-Atmospheres*, 101(D3), 7209–7225.
- Betts, R. A., P. D. Falloon, K. K. Goldewijk and N. Ramankutty (2007): Biogeophysical effects of land use on climate: Model simulations of radiative forcing and large-scale temperature change. *Agricultural and Forest Meteorology*, 142(2-4), 216–233.
- Brovkin, V., J. Bendtsen, M. Claussen, A. Ganopolski, C. Kubatzki, V. Petoukhov and A. Andreev (2002): Carbon cycle, vegetation, and climate dynamics in the Holocene: Experiments with the CLIMBER-2 model. *Global Biogeochemical Cycles*, 16(4), 1139. doi: 0.1029/2001GB001662.
- Brovkin, V., M. Claussen, E. Driesschaert, T. Fichefet, D. Kicklighter, M. F. Loutre, H. D. Matthews, N. Ramankutty, M. Schaeffer and A. Sokolov (2006): Biogeophysical effects of historical land cover changes simulated by six Earth system models of intermediate complexity. *Climate Dynamics*, 26(6), 587–600.
- Carlson, T. N. and D. A. Ripley (1997): On the relation between NDVI, Fractional Vegetation Cover, and Leaf Area Index. *Remote Sensing of Environment*, 62, 241–252.
- Chen, X. Q., Z. J. Tan, M. D. Schwartz and C. Xu (2000): Determining the growing season of land vegetation on the basis of plant phenology and satellite data in Northern China. *International Journal of Biometeorology*, 44, 7–101.

- Claussen, M., V. Brovkin and A. Ganopolski (2001): Biogeophysical versus biogeochemical feedbacks of large-scale land cover change. *Geophysical Research Letters*, 28, 1011–1014. doi: 0.1029/2000GL012471.
- Claussen, M., U. Lohmann, E. Roeckner and U. Schulzweida (1994): A Global Data Set Of Land-Surface Parameters. *Max-Planck-Institut für Meteorology - Report*, 135, 30 pp.
- Crowley, T. J. and S. K. Baum (1997): Effect of vegetation on an ice-age climate model simulation. *Journal of Geophysical Research*, 102, 16463–16480. doi: 0.1029/97JD00536.
- de Haan, J., J. Hovenier, J. Kokke and H. van Stokkom (1991): Removal of atmospheric influences on satellite-borne imagery: A radiative transfer approach. *Remote Sensing of Environment*, 37(1), 1–21. doi: 0.1016/0034-4257(91)90046-9.
- d’Entremont, R. P., C. B. Schaaf, W. Lucht and A. H. Strahler (1999): Retrieval of red spectral albedo and bidirectional reflectance using AVHRR HRPT and GOES satellite observations of the New England region. *Journal of Geophysical Research*, 104(D6), 6229–6239.
- Dickinson, R. E. (1983): Land surface processes and climate - surface albedos and energy balance. *Advances in Geophysics*, 25, 305–353.
- Dixon, R. K., S. Brown, J. F., R. A. Houghton, A. M. Solomon, M. C. Trexler and J. Wisniewski (1994): Carbon pools and flux of global forest ecosystems. *Science*, 263(5144), 185–190. doi: 0.1126/science.263.5144.185.
- DKRZ (1993): The ECHAM3 Atmospheric General Circulation Model. *Technical Report*, 6 (Revision 2), 184.
- Eltahir, E. A. B. (1996): Role of vegetation in sustaining large-scale atmospheric circulations in the tropics. *Journal of Geophysical Research-Atmospheres*, 101(D2), 4255–4268.
- Epiphanio, J. C. N. and A. R. Huete (1995): Dependence of NDVI and SAVI on sun/sensor geometry and its effect on fAPAR relationships in Alfalfa. *Remote Sensing of Environment*, 51(3), 351 – 360. doi: 0.1016/0034-4257(94)00110-9.
- Fahrmeir, L., R. Künster, I. Pigeot and G. Tutz (2004): Statistik - Der Weg zur Datenanalyse. Springer Verlag.
- FAO (1971-1981): The FAO-Unesco Soil Map of the World. Legend and 9 volumes. Unesco, Paris.
- Fell, F. and J. Fischer (2001): Numerical simulation of the light field in the atmosphere-ocean system using the matrix-operator method. *Journal of Quantitative Spectroscopy and Radiative Transfer*, 69(3), 351–388.
- Fischer, J., R. Preusker, J.-P. Muller and M. Zühlke (2007): ALBEDOMAP-Validation Report - ESA AO/1-4559/04/I-LG. *online*.

- Galos, B. (2010): Analysis of forest-climate interactions applying the regional climate model REMO. PhD thesis, University of West-Hungary, Sopron.
- Gao, F., C. Schaaf, Y. Jin, W. Lucht and A. Strahler (2003): Deriving albedo from coupled MERIS and MODIS surface products. In: *Proc. MERIS User Workshops, Frascati, Italy, 10-13 November 2003, ESA SP-549, May 2004*.
- Giorgi, F. (2005): Climate change prediction. *Climatic Change*, 73(3), 239–265.
- Gobron, N., O. Ausedat, B. Pinty, M. Taberner and M. M. Verstraete (2004): Medium Resolution Imaging Spectrometer (MERIS) - An optimized FAPAR Algorithm - Theoretical Basis Document. *Institute for Environment and Sustainability*, EUR Report No.21 386 EN, 20 pp.
- Gobron, N., B. Pinty, M. Verstraete and J.-L. Widlowski (2001): Development of spectral indices optimized for the VEGETATION Instrument. Proceedings of the VEGETATION 2000 conference. www.spot-vegetation.com.
- Gobron, N., B. Pinty, F. Melin, M. Taberner, M. Verstraete, M. Robustelli and J. Widlowski (2007): Evaluation of the MERIS/ENVISAT FAPAR product. *Advances in Space Research*, 39(1), 105–115.
- Gobron, N., B. Pinty, M. Taberner, F. Melin, M. Verstraete and J.-L. Widlowski (2005): Monitoring the photosynthetic activity of vegetation from remote sensing data. *Advances in Space Research*, 38(10), 2196–2202.
- Goldewijk, K. K. (2001): Estimating global land use change over the past 300 years: The HYDE database. *Global Biogeochemical Cycles*, 15, 417–434. doi: 0.1029/1999GB001232.
- Göttel, H., J. Alexander, E. Keup-Thiel, D. Rechid, S. Hagemann, T. Blome, A. Wolf and D. Jacob (2008): Influence of changed vegetations fields on regional climate simulations in the Barents Sea Region. *Climate Change*, 87, 35–50. doi: 10.1007/s10584-007-9341-5.
- Gutman, G. and A. Ignatov (1998): The derivation of the green vegetation fraction from NOAA/AVHRR data for use in numerical weather prediction models RID F-5594-2010. *International Journal of Remote Sensing*, 19(8), 1533–1543. doi: 0.1080/014311698215333.
- Hagemann, S. (2002): An improved land surface parameter data set for global and regional climate models. In: *Report*, Vol. 336, p. 28. Max Planck Institute for Meteorology Hamburg, Germany.
- Hagemann, S., M. Botzet, L. Dümenil and B. Machenhauer (1999): Derivation of global GCM boundary conditions from 1 km land use satellite data. In: *Report*, Vol. 289, p. 34. Max Planck Institute for Meteorology Hamburg, Germany.
- Hagemann, S., M. Botzet and B. Machenhauer (2001): The summer drying problem over south-eastern Europe: sensitivity of the limited area model HIRHAM4 to improvements in physical

- parameterization and resolution. *Physics and Chemistry of the Earth, Part B: Hydrology, Oceans and Atmosphere*, 26(5-6), 391–396.
- Haggett, P. (1991): *Geographie - Eine moderne Synthese*. UTB für Wissenschaften. Ulmer, 2nd edition. Aus dem Englischen mit Adaptionen von Rudi Hartmann.
- Henderson-Sellers, A., M. Wilson and R. Dickinson (1986): Current global land-surface data sets for use in climate -related studies. *NCAR Technical Report*, 272. Boulder Colorado.
- Hurt, G. C., S. Frohling, M. G. Fearon, B. Moore, E. Shevliakova, S. Malyshev, S. W. Pacala and R. A. Houghton (2006): The underpinnings of land-use history: three centuries of global gridded land-use transitions, wood-harvest activity, and resulting secondary lands. *Global Change Biology*, 12(7), 1208–1229.
- IPCC (2001): *Climate Change 2001: The Scientific Basis*. Contribution of Working Group I to the Third Assessment Report of the Intergovernmental Panel on Climate Change. Cambridge University Press, Cambridge, United Kingdom and New York, NY, USA,. IPCC, 2001: *Climate Change 2001: The Scientific Basis*. Contribution of Working Group I to the Third Assessment Report of the Intergovernmental Panel on Climate Change [Houghton, J.T., Y. Ding, D.J. Griggs, M. Noguer, P.J. van der Linden, X. Dai, K. Maskell, and C.A. Johnson (eds.)]. Cambridge University Press, Cambridge, United Kingdom and New York, NY, USA, 881pp.
- IPCC (2007a): *Climate Change 2007: Impacts, Adaptation and Vulnerability*. Contribution of Working Group II to the Fourth Assessment Report of the Intergovernmental Panel on Climate Change. Cambridge University Press, Cambridge, UK, 976 pp.
- IPCC (2007b): *Climate Change 2007: The Physical Science Basis*. Contribution of Working Group I to the Fourth Assessment Report of the Intergovernmental Panel on Climate Change, Vol. Cambridge, United Kingdom and New York, NY, USA. Cambridge University Press, Cambridge, United Kingdom and New York, NY, USA.
- Jacob, D. (2009): *Regional Climate Models: Linking Global Climate Change to Local Impact*. In: *Encyclopaedia of Complexity and Systems Science*, pp. 7591–7602. Springer Verlag.
- Jacob, D., L. Baerring, O. Christensen, J. Christensen, M. de Castro, M. Deque, F. Giorgi, S. Hagemann, M. Hirschi, R. Jones, E. Kjellström, G. Lenderink, B. Rockel, E. Sanchez, C. Schär, S. Seneviratne, S. Somot, A. van Ulden and B. van den Hurk (2007): An inter-comparison of regional climate models for Europe: model performance in present-day climate. *Climatic Change*, 81(0), 31–52.
- Jacob, D., H. Göttel, S. Kotlarski, P. Lorenz and K. Sieck (2008): *Klimaauswirkungen und Anpassung in Deutschland - Phase 1: Erstellung regionaler Klimaszenarien für Deutschland*. In: *Climate Change - Forschungsbericht 204 41 138, UBA-FB 000969*. Umweltbundesamt.

- Jones, P. W. (1998): A User's Guide for SCRIP: A Spherical Coordinate Remapping and Interpolation Package. Theoretical Division, Los Alamos National Laboratory. Version 1.4.
- Jones, P. W. (1999): First- and Second-Order Conservative Remapping Schemes for Grids in Spherical Coordinates. *Monthly Weather Review*, 127, 2204–2210.
- Keshava, N. and J. F. Mustard (2002): Spectral unmixing. *IEEE Signal Processing Magazine*, 19(1), 44–57. doi: 0.1109/79.974727.
- Kleidon, A., K. Fraedrich and M. Heimann (2000): A green planet versus a desert world: Estimating the maximum effect of vegetation on the land surface climate. *Climatic Change*, 44(4), 471–493.
- Knorr, W. (1997): Satellite Remote Sensing and Modelling of the Global CO Exchange of Land Vegetation: A Synthesis Study. PhD thesis, Faculty of Earth Sciences of the University of Hamburg.
- Knorr, W., K. G. Schnitzler and Y. Govaerts (2001): The role of bright desert regions in shaping North African climate. *Geophysical Research Letters*, 28(18), 3489–3492.
- Knyazikhin, Y., J. Glassy, J. L. Privette, Y. Tian, A. Lotsch, Y. Zhang, Y. Wang, J. T. Morisette, P. Votava, R. Myneni, R. R. Nemani and S. W. Running (1999): MODIS Leaf Area Index (LAI) and Fraction of Photosynthetically Active Radiation Absorbed by Vegetation (FPAR) Product (MOD15). Algorithm Theoretical Basis Document. <http://eosps0.gsfc.nasa.gov/atbd/modistables.html>.
- Kondratyev, K. Y., V. I. Korzov, V. V. Mukhenberg and L. N. Dyachenko (1981): The Shortwave Albedo and the Surface Emissivity, pp. 463 – 514, in: Eagleson, P. S. (ed.): Land surface processes in atmospheric general circulation models. Cambridge University Press.
- Kraus, K. (1988): Fernerkundung, Band 1, Physikalische Grundlagen und Aufnahmetechniken. Dümmler, Bonn.
- Kriebel, K. T. and P. Koepke (1985): Reflexion und Emission natürlicher Oberflächen. *Promet*, 15, 19–25.
- Lambers, H., F. S. Chapin and T. L. Pons (1998): Plant physiological ecology. Springer-Verlag.
- Lawrence, D. and J. Slingo (2004): An annual cycle of vegetation in a GCM. Part II: global impacts on climate and hydrology. *Climate Dynamics*, V22(2), 107–122.
- Legates, D. R. and C. J. Willmott (1990): Mean seasonal and spatial variability in global surface air temperature. *Theoretical and Applied Climatology*, V41(1), 11–21.
- Liang, S., A. H. Strahler and C. W. Walthall (1999): Retrieval of land surface albedo from satellite observations: A simulation study. *Journal of Applied Meteorology*, 38, 712–725.

- Lorenz, P. and D. Jacob (2005): Influence of regional scale information on the global circulation: A two-way nesting climate simulation. *Geophysical Research Letters*, 32(18), L18706.
- Lucas-Picher, P., D. Caya, R. Elia and R. Laprise (2008): Investigation of regional climate models' internal variability with a ten-member ensemble of 10-year simulations over a large domain. *Climate Dynamics*, 31(7-8), 927–940.
- Lucht, W., C. B. Schaaf and A. H. Strahler (2000): An algorithm for the retrieval of albedo from space using semiempirical BRDF models RID G-2180-2011. *IEEE Transactions on Geoscience and Remote Sensing*, 38(2), 977–998. doi: 0.1109/36.841980.
- Ludwig, R., W. Mauser, S. Niemeyer, A. Colgan, R. Stolz, H. Escher-Vetter, M. Kuhn, M. Reichstein, J. Tenhunen, A. Kraus, M. Ludwig, M. Barth and R. Hennicker (2003): Web-based modelling of energy, water and matter fluxes to support decision making in mesoscale catchments - the integrative perspective of GLOWA-Danube. *Physics and Chemistry of the Earth, Parts A/B/C*, 28(14?15), 621 – 634. doi: 0.1016/S1474-7065(03)00108-6. <ce:title>Design and application of decision-support systems for integrated water management: lessons to be learned</ce:title>.
- Maignan, F., F. M. Breon and R. Lacaze (2004): Bidirectional reflectance of Earth targets: Evaluation of analytical models using a large set of spaceborne measurements with emphasis on the Hot Spot. *Remote Sensing of Environment*, 90(2), 210–220. doi: 0.1016/j.rse.2003.12.006.
- Manninen, T., L. Korhonen, P. Voipio, P. Lahtinen and P. Stenberg (2009): Leaf Area Index (LAI) Estimation of Boreal Forest Using Wide Optics Airborne Winter Photos. *Remote Sensing*, 1(4), 1380–1394.
- Mauser, W. (2002): GLOWA-DANUBE Integrative Techniken, Szenarien und Strategien zum Globalen Wandel des Wasserkreislaufs am Beispiel des Einzugsgebiets der Oberen Donau Präambel GLOWA-Danube Antrag auf 2. Förderphase. www.glowa-danube.de.
- McCree, K. J. (1972): Action Spectrum, Absorptance and Quantum Yield of Photosynthesis In Crop Plants. *Agricultural Meteorology*, 9(3-4), 191–&.
- Minguez, M., M. Ruiz-Ramos, C. Diaz-Ambroña, M. Quemada and F. Sau (2007): First-order impacts on winter and summer crops assessed with various high-resolution climate models in the Iberian Peninsula. *Climatic Change*, 81(0), 343–355.
- Monsi, M. and T. Saeki (1953): Über den Lichtfaktor in den Pflanzengesellschaften und seine Bedeutung für die Stoffproduktion. *Japanese Journal of Botany*, 14, 22–52.
- Myhre, G. and A. Myhre (2003): Uncertainties in radiative forcing due to surface albedo changes caused by land-use changes RID A-3598-2008. *Journal of Climate*, 16(10), 1511–1524. doi: 0.1175/1520-0442-16.10.1511.
- Myneni, R. and D. Williams (1994): On the relationship between FAPAR and NDVI. *Remote Sensing of Environment*, 49(3), 200–211.

- Myneni, R. B., S. Hoffman, Y. Knyazikhin, J. L. Privette, J. Glassy, Y. Tian, Y. Wang, X. Song, Y. Zhang, G. R. Smith, A. Lotsch, M. Friedl, J. T. Morisette, P. Votava, R. R. Nemani and S. W. Running (2002): Global products of vegetation leaf area and fraction absorbed PAR from year one of MODIS data. *Remote Sensing of Environment*, 83(1-2), 214–231.
- Myneni, R. B., R. R. Nemani and S. W. Running (1997): Estimation of global leaf area index and absorbed par using radiative transfer models. *IEEE Transactions on Geoscience and Remote Sensing*, 35(6), 1380–1393.
- Oleson, K. W., G. B. Bonan, S. Levis and M. Vertenstein (2004): Effects of land use change on North American climate: impact of surface datasets and model biogeophysics. *Climate Dynamics*, V23(2), 117–132.
- Olson, J. S. (1994): Global ecosystem framework-definitions. *USGS EROS Data Center Internal Report, Sioux Falls, SD*, 0, 31.
- Olson, J. W., J.S. and L. Allison (1983): Carbon in Live Vegetation of Major World Ecosystems (Olson Vegetation Dataset). *Technical Report - ORNL-5862 - Oak Ridge National Laboratory*, 4.
- Paeth, H., K. Born, R. Girmes, R. Podzun and D. Jacob (2009): Regional climate change in tropical and northern Africa due to greenhouse forcing and land use changes. *Journal of Climate*, 22(1), 114–132.
- Paschinger, V. (1911): Snow Line and Climate. *Petermanns Mitteilungen*, 57(2), 57–60.
- Pielke, R. A., J. Adegoke, A. Beltran-Przekurat, C. A. Hiemstra, J. Lin, U. S. Nair, D. Niyogi and T. E. Nobis (2007): An overview of regional land-use and land-cover impacts on rainfall. *Tellus Series B-chemical and Physical Meteorology*, 59(3), 587–601.
- Pitman, A. J. (2003): The evolution of, and revolution in, land surface schemes designed for climate models RID A-7353-2011. *International Journal of Climatology*, 23(5), 479–510. doi: 0.1002/joc.893.
- Pongratz, J., T. Raddatz, C. H. Reick, M. Esch and M. Claussen (2009a): Radiative forcing from anthropogenic land cover change since AD 800. *Geophysical Research Letters*, 36, L02709.
- Pongratz, J., C. Reick, T. Raddatz and M. Claussen (2009b): Effects of anthropogenic land cover change on the carbon cycle of the last millennium. *Global Biogeochemical Cycles*, 23, GB4001.
- Preuschmann, S. and D. Jacob (2008): Sensitivity study for parameterization of woods in the regional climate model REMO. *Geophysical Research Abstracts, EGU General Assembly 2008*, Vol. 10, SRef-ID: 1607-7962/gra/EGU2008-A-0861.
- Preuschmann, S. and D. Jacob (2010): Analysis of regional albedo characteristics and its influence in the regional climate model REMO. *Proceedings of Earth Observation for Land-Atmosphere Interaction Science*.

- Probeck, M., R. Ludwig and W. Mauser (2004): Spectral unmixing of sub-scale land cover from multitemporal NOAA-AVHRR imagery using a combined GIS- and fuzzy logic approach. *Analysis of Multi-temporal Remote Sensing Images*, 3, 80–88. doi: 0.11429789812702630_0008.
- Ramankutty, N. and J. A. Foley (1999): Estimating historical changes in global land cover: Croplands from 1700 to 1992. *Global Biogeochemical Cycles*, 13, 997–1028. doi: 0.1029/1999GB900046.
- Ranson, K. J., J. R. Irons and C. S. T. Daughtry (1991): Surface albedo from bidirectional reflectance. *Remote Sensing of Environment*, 35(2-3), 201–211.
- RCP-Database (2009): Available at: <http://www.iiasa.ac.at/web-apps/tnt/RcpDb>.
- Rechid, D. (2008): On biogeophysical interactions between vegetation phenology and climate simulated over Europe. PhD thesis, Department Geowissenschaften der Universität Hamburg.
- Rechid, D., S. Hagemann and D. Jacob (2009): Sensitivity of climate models to seasonal variability of snow-free land surface albedo. *Theor. Appl. Climatol.*, DOI 10.1007/s00704-007-0371-8, 45.
- Rechid, D. and D. Jacob (2006): Influence of monthly varying vegetation on the simulated climate in Europe. *Meteorologische Zeitschrift*, 15(1), 99–116.
- Rechid, D., T. Raddatz and D. Jacob (2008): Parameterization of snow-free land surface albedo as a function of vegetation phenology based on MODIS data and applied in climate modelling. *Theoretical and Applied Climatology*, DOI 10.1007/s00704-008-0003-y.
- Reick, C. H., T. Raddatz, J. Pongratz and M. Claussen (2010): Contribution of anthropogenic land cover change emissions to pre-industrial atmospheric CO₂. *Tellus Series B-Chemical And Physical Meteorology*, 62(5), 329–336.
- Reuter, M. (2005): Identification of cloudy and clear sky areas in MSG SEVIRI images by analyzing spectral and temporal information. PhD thesis, Fachbereich Geowissenschaften der Freien Universität Berlin.
- Roeckner, E., K. Arpe, L. Bengtsson, M. Christoph, M. Claussen, L. Dünemil, M. Esch, M. Giorgetta, U. Schlese and U. Schulzweida (1996): The Atmospheric General Circulation Model ECHAM-4: Model Description and Simulation of Present-Day Climate. Technical report, Max-Planck-Institut für Meteorologie - Report, No. 218.
- Rouse, J. W., R. Haas, J. Schell and D. Deering (1973): Monitoring vegetation systems in the Great Plains with ERTS. *Third ERTS Symposium, NASA SP-351*, 1, 309 – 317. In NASA. Goddard Space Flight Center 3d ERTS-1 Symp., Vol. 1, Sect. A p 309-317 (SEE N74-30705 20-13) 1974.
- Schaaf, C. B., F. Gao, A. Strahler, T. Tsang, W. Lucht, N. Strugnell, X. Li, J.-P. Muller, P. Lewis, M. Barnsley, P. Hobson, M. Disney, M. Dunderdale and G. Roberts (2000): The MODerate Resolution Imaging Spectroradiometer (MODIS) BRDF and Albedo Product: Preliminary Results,. *Proc. Int. Geosci. Remote Sens. Symp.*, IGARSS 00.

- Schaaf, C. B., F. Gao, A. H. Strahler, W. Lucht, X. W. Li, T. Tsang, N. C. Strugnell, X. Y. Zhang, Y. F. Jin, J. P. Muller, P. Lewis, M. Barnsley, P. Hobson, M. Disney, G. Roberts, M. Dunderdale, C. Doll, R. P. d'Entremont, B. X. Hu, S. L. Liang, J. L. Privette and D. Roy (2002): First operational BRDF, albedo nadir reflectance products from MODIS RID G-2180-2011 RID E-3208-2010 RID C-1588-2008 RID C-1889-2008 RID G-7807-2011. *Remote Sensing of Environment*, 83(1-2), 135–148. doi: 0.1016/S0034-4257(02)00091-3.
- Schroeder, T., R. Preusker, M. Schaale and F. J. (2005): Aerosol Correction. *MERIS Global Land Surface Albedo Maps, Algorithm Theoretical Basis Document - Atbd 1.3*.
- Sellers, P. J. (1987): Canopy reflectance, photosynthesis, and transpiration 2. The role of biophysics in the linearity of their interdependence. *Remote Sensing of Environment*, 21(2), 143–183.
- Simmons, S. D. D. K. S., A.; Uppala (2006): ERA-Interim: New ECMWF reanalysis products from 1989 onwards. *ECMWF Newsletter*, 110, 25?35.
- Stensrud, D. J. (2007): Parameterization schemes: keys to understanding numerical weather prediction. Cambridge University Press, Cambridge, United Kingdom and New York, NY, USA.
- Strugnell, N. C. and W. Lucht (2001): An algorithm to infer continental-scale albedo from AVHRR data, land cover class, and field observations of Typical BRDFs. *Journal of Climate*, 14(7).
- Tian, Y. H., Y. Zhang, Y. Knyazikhin, R. B. Myneni, J. M. Glassy, G. Dedieu and S. W. Running (2000): Prototyping of MODIS LAI and FPAR algorithm with LASUR and LANDSAT data. *IEEE Transactions on Geoscience and Remote Sensing*, 38(5), 2387–2401.
- Uppala, S. M., P. W. Kållberg, A. J. Simmons, U. Andrae, V. da Costa Bechtold, M. Fiorino, J. K. Gibson, J. Haseler, A. Hernandez, G. A. Kelly, X. Li, K. Onogi, S. Saarinen, N. Sokka, R. P. Allan, E. Andersson, K. Arpe, M. A. Balmaseda, A. C. M. Beljaars, L. van de Berg, J. Bidlot, N. Bormann, S. Caires, F. Chevallier, A. Dethof, M. Dragosavac, M. Fisher, M. Fuentes, S. Hagemann, E. Hólm, B. J. Hoskins, L. Isaksen, P. A. E. M. Janssen, R. Jenne, A. P. McNally, J. F. Mahfouf, J. J. Morcrette, N. A. Rayner, R. W. Saunders, P. Simon, A. Sterl, K. E. Trenberth, A. Untch, D. Vasiljevic, P. Viterbo and J. Woollen (2005): The ERA-40 re-analysis. *Quarterly Journal of the Royal Meteorological Society*, 131, 2961–3012.
- U.S.Geological-Survey (1996): A Global Digital Elevation Model (DEM). Horizontal grid spacing of 30 arc seconds.
- U.S.Geological-Survey (2001): Global land cover characteristics data base version 2.0.
- Vamborg, F. S. E., V. Brovkin and M. Claussen (2011): The effect of a dynamic background albedo scheme on Sahel/Sahara precipitation during the mid-Holocene. *Climate Of The Past*, 7(1), 117–131.

- Vermote, E. F., D. Tanre, J. L. Deuze, M. Herman and J. J. Morcrette (1997): Second Simulation of the Satellite Signal in the Solar Spectrum, 6S - An overview. *IEEE Transactions on Geoscience and Remote Sensing*, 35(3), 675–686.
- von Storch, H., S. Güss and M. Heimann (1999): Das Klimasystem und seine Modellierung: eine Einführung. Berlin; Heidelberg; New York; Barcelona; Hongkong; London ; Mailand; Paris; Singapur; Tokio Springer.
- Wang, Q., S. Adiku, J. Tenhunen and A. Granier (2005): On the relationship of NDVI with leaf area index in a deciduous forest site. *Remote Sensing of Environment*, 94(2), 244–255.
- Whittow, J. B. (2000): The Penguin Dictionary of Physical Geography (second edition). Penguin Books.
- Wieringa, J. (1993): Representative roughness parameters for homogeneous terrain. *Boundary-Layer Meteorology*, 63(4), 323–363.
- Wieringa, J. (1992): Updating the Davenport roughness classification. *Journal of Wind Engineering and Industrial Aerodynamics*, 41(1-3), 357–368.
- Wilks, D. S. (2006): Statistical Methods in the Atmospheric Sciences. Elsevier Academic Press.
- Woolley, J. T. (1971): Reflectance and transmittance of light by leaves. *Plant Physiology*, 47(5), pp. 656–662.

Acknowledgement

It is a pleasure to thank those, who made this thesis possible, even though I can not name all of them. I am grateful that Professor Dr. Daniela Jacob made available her support in a number of ways, and never stopped trusting in me. Also I would like to show my gratitude to Dr. Diana Rechid and Dr. Stefan Hagemann for all their patience on my nasty questions about their foregoing work and many helpful comments. I owe my deepest gratitude to Ralf Podzun. He was always available and able to answer any question on REMO - it was horrible to realize that this is not possible anymore, when he died unexpectedly in September 2011. Ralf, I hope you are fine up there.

This work grew by detours, trials and errors, it was overshadowed by weird circumstances and tainted with sadness. Without the help and the advice of the former and current members of the regional climate modelling group at the MPI-M and CSC, it would not have come to this result. Thank you all for a great time, intense discussions and fellowship. Thank you Ute for our nice "Heißgetränk"-ritual.

Also I am happy for having obtained a lot of support and having fruitful discussions by my "adoptive" working group the Land Department of the MPI-M. I always felt like being part of your group and enjoyed the cooperation. Especially I thank Professor Dr. Martin Claußen for his strenuous efforts to support me and to promote the interaction with his department. My thanks also go to Thomas Kleinen. Many thanks are going to Professor Dr. Hartmut Graßl and Barbara Zinecker for their tremendous support.

I would like to thank the staff of CIS for their wonderful help and work which allowed me to work nearly trouble-free concerning all the things which usually happen, and the ZMAW-Library for making things available which are not available for everyone.

So many people were enlightening my life and work at MPI-M, unfortunately I can not mention you all - but I want to thank all of you for just being there and having nice dinners.

Finally, I am deeply thankful to my parents, my sister and my uncle. I am grateful that you never stopped loving me.

Index

- α_{soil} , 25
- α_{veg} , 25
- f_i , 23
- α_{amap} , 40
- VI_{amap} , 40
- α_{SLAR} , 26

- absorbed photosynthetically active radiation, 34
- albedo, 16
- albedo characteristics, 45, 51, 69
- albedo-weights, 25
- Albedomap, 37
- amap, 37
- amplitude, 45
- APAR, 34
- atmospheric correction, 29

- background albedo, 16
- black-sky albedo, 28
- broadband conversion, 37
- bucket scheme, 18

- c_v -cycle, 23
- climate model, 13
- cloud masking, 29, 39
- correlation, 141

- DANUBIA, 97

- evaporation, 17

- fapar, 23, 35
- forest ratio, 16
- FPAR
 - see fapar, 24

- GLC2000, 42
- Global Land Cover 2000, 42
- global radiation, 48
- GLOWA-Danube, 97
- growing factor, 23

- I_{ns} , 48
- inversion method, 63, 116

- LAI, 17, 36
- LAI-cycle, 23
- land cover, 4
- land use, 4
- land use change, 4
- Land Use Character Shifts, 111
- land use characteristics, 54
- LeafArea Index, 17
- lower boundary, 13
- lower boundary condition, 14
- LUCHS, 111
- LUH-P, 4

- minimum level, 45
- model internal variability, 90

- NDVI, 34
- near infrared spectral band, 30
- Net Solar Radiation Surface, 48
- NIR, 30

- PAR, 34
- parameterization, 13
- Pearson product-moment correlation coefficient, 139
- phase, 45
- photosynthetically active radiation, 34

pushbroom imaging spectrometer, 37

radiative perturbation, 48

roughness length, 18

sensitivity study, 86, 97

shortwave broadband albedo, 40

significance, 89, 102

SL4R, 69

snow albedo, 16

snow masking, 39

spectral unmixing, 51

spectrally integrated albedo, 29

surface albedo, 16

surface library for REMO, 69

vegetation annual cycle, 19

vegetation index, 40

vegetation parameterization, 15

vegetation parameters, 15

vegetation ratio, 17

verification, 63, 116

vertical diffusion, 17

VIS, 30

visible spectral band, 30

white-sky albedo, 27, 28

